Design functional catalytic materials from first-principles methods for methanol fuel cells

by

Jiayi Xu

B.S., Kansas State University, 2016

AN ABSTRACT OF A DISSERTATION

Submitted in partial fulfillment of the requirements for the degree

DOCTOR OF PHILOSOPHY

Tim Taylor Department of Chemical Engineering
College of Engineering

KANSAS STATE UNIVERSITY
Manhattan, Kansas

2021

Abstract

Direct methanol fuel cells (DMFCs) offer ample opportunities for high-efficiency and sustainable power generation. However, the lack of cost-efficient electrocatalysts for the kinetically sluggish cathodic oxygen reduction reaction (ORR) hinders the technology advancement. The solutions to solve these fundamental challenges would benefit from unique insights from molecular-level modeling.

The first focus of this thesis aims to construct representative molecular models for a vertically aligned carbon nanofiber (VACNF) architecture as a functional support for the platinum-based ORR catalysts. Density Functional Theory (DFT) combined with classic molecular dynamics was employed to produce two supported composite catalyst nanostructures. Both models revealed the mechanistic and catalytic origins corroborating the observed linear sweeping voltammetry. The Pt nanoparticles supported on VACNF show preferential binding at their exposed low coordinated sites, resulting in a lower ORR limiting potential than on Pt (111) facet. This thesis also explored ORR electrocatalysts consisting of non-platinum group metals (Fe, Co, Ni), atomically dispersed and embedded in 2D materials. The active centers are stable in alkaline ORR conditions and permit a maximal utilization of their metallic sites. The dual-metal centers anchored by six pyridinic nitrogen also exhibit wide-ranging catalytic performance. More importantly, the attached OH ligand will likely further tune the ORR activity by modulating the electronic characters at the active centers.

This thesis also considered methanol production for DMFCs via direct methane-to-methanol processes enabled by the Cu-oxo complexes anchored in a MOR zeolite framework. Again, DFT was used to determine the most likely the active center configurations under reaction conditions, i.e., Cu-trioxo and bis (μ-oxo) dicopper. The Cu-trioxo configuration was then shown to be particularly active toward the critical C-H bond activation.

Design functional catalytic materials from first-principles methods for methanol fuel cells

by

Jiayi Xu

B.S., Kansas State University, 2016

A DISSERTATION

Submitted in partial fulfillment of the requirements for the degree

DOCTOR OF PHILOSOPHY

Tim Taylor Department of Chemical Engineering

College of Engineering

KANSAS STATE UNIVERSITY

Manhattan, Kansas

2021

Approved by:

Major Professor
Bin Liu

Copyright

© Jiayi Xu 2021.

Abstract

Direct methanol fuel cells (DMFCs) offer ample opportunities for high-efficiency and sustainable power generation. However, the lack of cost-efficient electrocatalysts for the kinetically sluggish cathodic oxygen reduction reaction (ORR) hinders the technology advancement. The solutions to solve these fundamental challenges would benefit from unique insights from molecular-level modeling.

The first focus of this thesis aims to construct representative molecular models for a vertically aligned carbon nanofiber (VACNF) architecture as a functional support for the platinum-based ORR catalysts. Density Functional Theory (DFT) combined with classic molecular dynamics was employed to produce two supported composite catalyst nanostructures. Both models revealed the mechanistic and catalytic origins corroborating the observed linear sweeping voltammetry. The Pt nanoparticles supported on VACNF show preferential binding at their exposed low coordinated sites, resulting in a lower ORR limiting potential than on Pt (111) facet. This thesis also explored ORR electrocatalysts consisting of non-platinum group metals (Fe, Co, Ni), atomically dispersed and embedded in 2D materials. The active centers are stable in alkaline ORR conditions and permit a maximal utilization of their metallic sites. The dual-metal centers anchored by six pyridinic nitrogen also exhibit wide-ranging catalytic performance. More importantly, the attached OH ligand will likely further tune the ORR activity by modulating the electronic characters at the active centers.

This thesis also considered methanol production for DMFCs via direct methane-to-methanol processes enabled by the Cu-oxo complexes anchored in a MOR zeolite framework. Again, DFT was used to determine the most likely the active center configurations under reaction conditions, i.e., Cu-trioxo and bis (μ-oxo) dicopper. The Cu-trioxo configuration was then shown to be particularly active toward the critical C-H bond activation.

Table of Contents

List of Figures x

List of Tables xix

Acknowledgements xx

Chapter 1 - Introduction 1

1.1 Catalysts for Oxygen Reduction Reactions 1

1.2 Catalysts Design for Methane Conversion 4

1.3 Principles of Computational Catalyst Design 5

1.4 Scope of this Dissertation 7

1.4.1 Catalysts Considered for ORR 7

1.4.2 Catalysts for Methane Conversion 9

1.5 Organization of the Dissertation 9

References 10

Chapter 2 - Quantum Mechanical Theory and Methods 17

2.1 Density Functional Calculations 17

2.1.1 Kohn-Sham Formulation 17

2.1.2 Plane Wave Basis Set and Pseudopotential 18

2.1.3 Electron Exchange-Correlation Functional 20

2.2 Molecular Dynamics 22

2.3 Reaction Thermodynamics and Free Energy Diagram 23

2.3.1 Free Energy for Oxygen Reduction 23

2.3.2 Free Energy Diagram 24
2.4 Limiting Potentials and Overpotentials 25
2.5 Transition State Search 27
2.5.1 CI-NEB method 28
2.5.2 DIMER method 28
2.6 Empirical Computational Methods 29
2.6.1 Brønsted–Evans–Polanyi Relationship 29
2.6.2 Linear Scaling for Molecular Adsorptions 30
2.7 *d*-Band Theory 31
2.8 Bader Charge Analysis 33
References 35
Chapter 3 - Molecular Models for Platinum ORR Catalyst on Multi-Edged Carbon Supports 39
3.1 Introduction 39
3.2 Computational Details 45
3.2.1 Density Functional Theory 45
3.2.2 Molecular Dynamics Simulation 47
3.2.3 ORR Mechanism 47
3.3 Results and Discussion 49
3.3.1 The Pt/fishbone Model 49
3.3.2 ORR on Bare Fishbone Model 51
3.3.3 ORR over Pt/VACNF 53
3.3.4 Pt Catalyst Supported on the Multi-edged VACNF 55

3.3.5 Adsorptions on Pt_{55}/VACNF 56
3.3.6 ORR on the Pt/VACNF Model 63
3.4 Conclusions 64
References 65
Chapter 4 - Intrinsic Properties of Nitrogen-Rich Carbon Nitride for Oxygen Reduction Reaction 69
4.1 Introduction 69
4.2 Computational Method 71
4.3 Results and Discussion 74
4.3.1 Electronic Properties of g-C_3N_4 74
4.3.2 ORR Intermediates on g-C_3N_4 77
4.3.3 Catalytic Performance of g-C_3N_4 and Heterostructures for ORR 80
4.3.4 g-C_3N_4 with Fe Single Atom Site for ORR 82
4.4 Conclusions 89
References 89
Chapter 5 - Graphene-Based Dual-Metal Sites for Oxygen Reduction Reaction 94
5.1 Introduction 94
5.2 Computational Methods 97
5.3 Results and Discussion 100
5.3.1 Stability of the Dual Metal Configurations 100
5.3.2 ORR at Dual Metal Sites 102
5.3.3 ORR at the Dual Metal Sites Modified by OH Ligands 106

5.4 Conclusions 113

References 114

Chapter 6 - C-H Bond Activation and Oxidation of Alkane over Cu-MOR 121

6.1 Introduction 121

6.2 Computational Methods 125

6.3 Results and Discussion 129

6.3.1 Cu-Oxo Models for C-H Bond Activations 129

6.3.2 CH_4-to-CH_3OH Conversion over Cu-Oxo Complexes 130

6.3.3 C2 and C3 Conversions at Cu-Trioxo Site II 135

6.3.4 Alkane Partial Oxidations over Site I of Cu-Trioxo 138

6.4 Conclusions 144

References 145

Chapter 7 - Conclusions and Future Work 150

References 155

Appendix A - Physical Properties of g-C_3N_4 and Heterostructures 156

Appendix B - Atomic Structures of ORR Intermediates at Dual Metal Centers 162

Appendix C - Stabilities of Cu-Oxo Clusters in 8MR and Free Energy Diagrams of Methane Partial Oxidation at Different Spin Multiplicities 170

Appendix D- Reprint Permissions 180

List of Figures

Figure 1.1. Operation scheme for direct methanol fuel cells. Methanol production via partial methane oxidation is also indicated. 1

Figure 1.2. (a) TEM images of vertically aligned carbon nano fiber, (b) its molecular structure with Pt NPs, (c) carbon nanotube adapted from Ref [44], and (d) graphene adapted from Ref [45]. 3

Figure 1.3. Scheme for catalysts design. Adapted from Ref. [73]. 6

Figure 2.1. Iterative, self-consistent scheme to solve Kohn-Sham equations, adapted from Ref. [1]. 18

Figure 2.2. Pseudopotential compared with all electron potential. The pseudo wavefunction ψ^{ps} and pseudopotential V^{ps} (red) comparing with all electron wavefunction ψ^{ae} and all electron potential V^{ae} (blue) adapted from ref. [5]. 20

Figure 2.3. Free energy diagram of ORR on Pt (111) via the associative mechanism under applied potentials of 0 , 0.78 and 1.23 V, adapted form Ref [17]. 26

Figure 2.4. The transition state (or saddle point) search scheme using (a) NEB method and (b) DIMER method, adapted from Ref. [1] 27

Figure 2.5. Linear scaling within adsorption energies of ORR reaction intermediates adapted from Ref. [34]. 31

Figure 2.6. Schematic illustrations of bond formation between an adsorbate valence level and the s and d states of a transition metal surface, adapted from Ref. [38]. 32

Figure 2.7. Binding energies of atomic carbon as a function of the transition metal d-band centers, adapted from Ref. [40]. 33

Figure 2.8. Bader charge analysis on methane activation over Fe_2O_3 (0001) surface. Charge accumulation and depletion are colored yellow and blue. Adapted from Ref. [46] 34

Figure 3.1. Schematic illustration of Pt/VACNF. Color code: gray-C, blue-Pt. 40
Figure 3.2. FESEM images of VACNF (a), TEM image of VACNF (b) and EDS elemental mapping on Pt/VACNF (c), and linear sweeping voltammetry for ORR over bare-VACNF and Pt/VACNF comparing with Pt/C (d). Adapted from Ref. [22]. 41
Figure 3.3. Relationship between the mean first-shell Pt-Pt coordination number of surface Pt atoms and the number of atoms in supported and isolated Pt particles. Adapted from Ref.[27]. 43
Figure 3.4. Correlations of the adsorption energies of OOH* and OH* with the generalized coordination numbers ($\overline{CN}$). Adapted from Ref. [29]. 44
Figure 3.5. Free energy diagram of depositing Pt atom at OH passivated fishbone edge. Color code: blue-Pt, gray-C, red-O, white-H. 49
Figure 3.6. Formation energies (per Pt atom) for semi-periodic Pt_4, Pt_{12}, Pt_{16}, and Pt_{20} supported on graphene edge. Color code: blue-Pt, and gray-C. 50
Figure 3.7. Side view and front view of Pt_{12}/fishbone. Color code: blue-Pt, and gray-C. 51
Figure 3.8. Free energy diagrams comparing the $2e^-$ associative pathway (red) and $4e^-$ pathway (blue) on the Pt-free fishbone model. (Color code: gray-C, red-O from passivating OH, white-H, and purple-O from reactant. 52
Figure 3.9. (a) Optimized ORR intermediates adsorbed on Pt/fishbone, and (b) free energy diagrams for $4e^-$ ORR pathways on Pt(111) (blue) and Pt/fishbone (red). Color code: blue-Pt, gray-C, red-O, and white-H. 53
Figure 3.10. Free energy diagrams of ORR via the dissociative (dashed line) and associative (solid line) mechanisms on Pt(111) (red) and Pt/fishbone (blue) at respective limiting potentials. 54
Figure 3.11. Equilibrated structures of Pt_{55} (a), Pt_{100} (b), and Pt_{147} (c) supported on VACNF; and (d) the normalized radial distribution functions g(r). The inset figure shows the first peak of each

normalized g(r). The vertical line in the inset figure indicates the location of the first peak of g(r). Color code: blue-Pt, gray-C. 56

Figure 3.12. An DFT optimized Pt_{55}/VACNF system. The initial structure was obtained from MD relaxation at 298K. Color code: blue-Pt, gray-C. 57

Figure 3.13. Adsorption and available binding sites for OOH* on Pt_{55}/VACNF. The first shell of Pt atoms has been colored blue. Color from light blue to dark blue indicates low coordinated sites to high coordinated sights. Color code: blue-Pt, brown-C, red-O, white-H. 58

Figure 3.14. Adsorption and available binding sites for O* on Pt_{55}/VACNF. The first shell of Pt atoms has been colored blue. Color from light blue to dark blue indicates low coordinated sites to high coordinated sights. Color code: blue-Pt, brown-C, red-O, white-H. 59

Figure 3.15. Adsorption and available binding sites for OH* on Pt_{55}/VACNF. The first shell of Pt atoms has been colored blue. Color from light blue to dark blue indicates low coordinated sites to high coordinated sights. Color code: blue-Pt, brown-C, red-O, white-H. 60

Figure 3.16. Adsorption energies of OOH* (blue squares), O* (green triangles), and OH* (red dots) as a function of $\overline{CN}$. 62

Figure 3.17. ORR free energy diagram on Pt/VACNF at U = 0.0 V (green-solid line), 0.41 V (blue-dashed line), and 1.23 V (red-dotted line). 63

Figure 4.1. Optimized (2 × 2) supercells for g-C_3N_4 and its various bilayer heterostructures: (a) g-C_3N_4 monolayer, (b) g-C_3N_4 multilayer, (c) g-C_3N_4/GN, and (d) g-C_3N_4/hBN bilayer. C, N, B atoms are in brown, gray, and green, respectively. Black lines indicate the periodic cell boundaries. The lateral lattice parameters and the interlayer spacing are labeled on each structure. 73

Figure 4.2**.** Density of states (DOS) of (a) g-C_3N_4 monolayer, (b) g-C_3N_4 multilayer, (c) g-C_3N_4/GN, (d) g-C_3N_4/hBN: entire structure (black); C in in g-C_3N_4 (orange); N in in g-C_3N_4 (purple); C in

the GN layer (green); B in the hBN layer (blue); N in the hBN layer (red). Only the up-spin is shown, and the vertical dashed lines indicate the Fermi level. 75

Figure 4.3. Optimized structures of O_2, OOH, O, and OH on g-C_3N_4 monolayer (a-d), g-C_3N_4/GN (e-h), g-C_3N_4/hBN (i-l), and g-C_3N_4 multilayer surface (m-p), respectively. The C, N, B atoms are in brown, blue, and green. 78

Figure 4.4. (a) Free energy diagrams of ORR on g-C_3N_4 monolayer (blue), g-C_3N_4/GN (red), g-C_3N_4/hBN (green), and g-C_3N_4 multilayer (yellow) at 298 K and 1 bar, with zero applied potential (U = 0 V); and (b) comparisons of limiting potentials for these materials. Each charge transfer step, associated with the formation of hydroxide ion, i.e., OH^-(aq), is highlighted in blue. 80

Figure 4.5. Optimized structures of (a) Fe/g-C_3N_4, (b) Fe/g-C_3N_4/GN (with an interlayer spacing of 3.10 Å), and (c) FeN_4 moiety in GN (edge passivated with H), adapted from Ref. [53]. The C, N, B, H atoms are in brown, gray, green, orange, and white, respectively. The black lines indicate the periodic cell boundaries. The distinct Fe–N bond lengths in each structure are labeled. 82

Figure 4.6**.** Projected density of states of (a) Fe/C_3N_4, (b) Fe/C_3N_4/GN, and (c) FeN_4. Only the decomposed sp-orbitals for N_p species (green) and the Fe valence electrons (s- and d-orbitals in red and purple respectively) are shown for clarity. 84

Figure 4.7. Optimized structures of O_2, OOH, O, and OH over Fe/C_3N_4 (a-d), Fe/C_3N_4/GN (e-h), and FeN_4 in GN (i-l). The C, N, B atoms are in brown, blue, and green, respectively. 85

Figure 4.8. (a) Free energy diagrams of ORR on Fe-free g-C_3N_4 monolayer (green), Fe/g-C_3N_4 (yellow), Fe/g-C_3N_4/GN (red), and FeN_4 at 298 K and 1 bar, with zero applied potential; and (b) the limiting potentials (U_{lim}) corresponding to each system. Each charge transfer step, associated with the formation of hydroxide ion, i.e., OH^-(aq), is highlighted in blue. 88

Figure 5.1. Molecular structure of dual-metal active center anchored with six pyridinic nitrogen atoms in a periodic monolayer graphene sheet. Color scheme: brown-graphitic carbon, gray-pyridinic nitrogen, yellow-Metal site 1 (M1), and purple-Metal site 2 (M2). 95

Figure 5.2. Free energy diagrams for six dual-metal sites: (a) Pt-Fe, (b) Pt-Co, (c) Pt-Ni, (d) Pt-Cu, (e) Pd-Ni, and (f) Pt-Pd, at U = 0 V (blue), U_{lim} (red), and U = 1.23 V (green). "*" indicates clean surface. 103

Figure 5.3. Free energy diagrams for ORR over PGM-free dual-metal sites: (a) Fe-Fe, (b) Fe-Co, (c) Fe-Ni, (d) Fe-Cu, (e) Co-Co, (f) Co-Ni, (g) Co-Cu, (h) Ni-Ni, (i) Ni-Cu, and (j) Cu-Cu, at U = 0 V (blue), U_{lim} (red), and U = 1.23 V (green). "*" indicates clean surface. 105

Figure 5.4. Relationship between ΔG_{OH^*} (eV) and the Bader charge (q, in |e|) at the OH binding site. The colored lines are used to guide the trend. Green indicates the relationship for the dual-metal sites without OH ligand, blue indicates the relationship on the same side with OH ligand, and red indicates the relationship on the opposite side of OH ligand. 108

Figure 5.5. Free energy diagrams for (a) Fe-Fe$(OH)_o$, (b) Fe-Co$(OH)_o$, (c) Fe-Ni$(OH)_o$, (d) Fe-Cu$(OH)_o$, (e) Co-Co$(OH)_o$, (f) Co-Ni$(OH)_o$, and (g) Pt-Co$(OH)_o$ at U = 0 V (blue), U_{lim} (red), and U = 1.23 V (green). "*" indicates clean surface. The subscript 'o' indicates ORR happens at the opposite side of OH ligand. 109

Figure 5.6. (a) Linear scaling relationships between ΔG_{OH} and ΔG_O (orange) and G_{OH} and G_{OOH} (blue). (b) Predicted U_{lim} as a function of G_{OH}. Systems associated with the potential-limiting step (PLS), $OH * \rightarrow OH(aq) -$ (left side), are colored in blue; systems associated with the PLS, $O^* \rightarrow OH^*$ or $O_2^* \rightarrow OOH^*$ (middle), are colored in purple; and system associated with the PLS, $O_2(g) \rightarrow OOH^*$ (right side), are colored in green. In addition, the bare dual-metal centers are represented in dots; the dual-metal centers with ORR occurring on the same side with the OH ligand are

represented by squares; and the dual-metal centers with ORR occurring on the opposite side of the OH ligand are represented by diamonds. 111

Figure 6.1. Optimized structures of Cu-oxo clusters. (a) mono (μ-oxo) dicopper, (b) bis (μ-oxo) dicopper, and (c) Cu-trioxo complex. The ball-and-stick style is used to emphasize each active center for C-H bond activation. The line style is used to represent the MOR framework for clarity. (Color code: red-O, purple-Al, yellow-Si, and orange-Cu). 124

Figure 6.2. Optimized MOR zeolite framework structures. (a) the orthogonal MOR unit cell; (b) a view of the 12 MR along the [001] (c-axis) of the monoclinic unit cell cleaved from (a) indicated by dashed line; (c) a view of the 8MR of MOR framework; (d) the supercell of (b) along the z-axis with Al substitutions. (Color code: red-O, yellow-Si, and purple-Al)..... 127

Figure 6.3. Optimized structures of various reaction intermediates. (a)-(d) correspond to methane adsorption, transition state (TS) of methane activation, CH_3+H*, and methanol adsorption over the site II of Cu-trioxo; (e)-(h) correspond to methane adsorption; TS of methane activation, CH_3+H*, and methanol adsorption over mono (μ-oxo) dicopper; (i)-(l) correspond to methane adsorption; TS of methane activation; CH_3+H*; methanol adsorption over bis (μ-oxo) dicopper. (Color code: red-O, yellow-Si, purple-Al, and orange-Cu) 133

Figure 6.4. Potential energy surfaces of methane-to-methanol conversion over site II of Cu-trioxo (blue), mono (μ-oxo) dicopper (red), and bis (μ-oxo) dicopper (yellow), where s, d, t, q, indicates the singlet, doublet, triplet, and quartet spin states. Computational errors are based on the Bayesian error estimation. 134

Figure 6.5. Potential energy surfaces of partial oxidation of methane, ethane, propane forming methanol (yellow), ethanol (blue), 1-propnol (green), and isopropanol (red) over site II of Cu-trioxo. Computational errors are based on the Bayesian error estimation. 136

Figure 6.6. Optimized structure over Cu-trioxo site II. (a)-(d) are ethane adsorption, TS for ethane activation, C_2H_5+H*, ethanol; (e)-(g) illustrates the adsorptions of propane, 1 propanol, and isopropanol. (Color code: red-O, yellow-Si, purple-Al, and orange-Cu) 137
Figure 6.7. Potential energy surfaces for the partial oxidation of methane, ethane, propane forming methanol (yellow), ethanol (blue), 1-propnol (green), and isopropanol (red) over site I of Cu-trioxo, respectively. Computational errors are based on the Bayesian error estimation. 138
Figure 6.8. Optimized structures over Cu-trioxo site I. (a)-(d) correspond to methane adsorption, TS for methane activation, CH_3 + H*, and methanol adsorption; (e)-(h) correspond to ethane adsorption, TS for ethane activation, C_2H_5 + H*, and ethanol adsorption; (i)-(o) correspond to propane adsorption, TS for C-H bond activation at the terminal carbon, $CH_3CH_2CH_2$ + H*, 1-propanol, TS for C-H bond activation at the secondary carbon, CH_3CHCH_3 + H*, and isopropanol adsorption.(Color code: red-O, yellow-Si, purple-Al, and orange-Cu) 140
Figure 6.9. Potential energy surfaces of methane partial oxidation over Cu-trioxo site I at the doublet (yellow), quartet (blue), and sextet (red) spin multiplicities. Computational errors are based on the Bayesian error estimation..... 141
Figure 7.1. Semi-periodic Pt_4 supported on undoped (a), N_p-doped (b), and N_g-doped (c) graphitic edges in a modified fishbone model. The second layer GN network is rendered by grey lines. Numerical values labeled on Pt and edge C atoms are net charges based on Bader charge analyses. Color code: blue-Pt, gray-C, and blue-N. Adapted from Ref [1]. 152
Figure 7.2. Limiting potential volcano plot for different classes of ORR electrocatalysts. The straight line indicates the linear constraint between ΔG_{OOH^*} andΔG_{OH^*}. Adapted from Ref.[7] 153
Figure A.1. Different stacking configurations of g-C_3N_4/GN (a-d) and g-C_3N_4/hBN (e-h). The corresponding cohesive energies are also shown. (Color code: blue-N, green-B, brown-C)..... 157

Figure A.2. Total DOS of g-C_3N_4 at lattice parameter of (a) 7.13 Å, (b) 7.31 Å, and (c) 7.40 Å with the corresponding energy band gap of 2.79 eV, 3.15 eV, and 3.20 eV. 158
Figure A.3. Total DOS of O_2 adsorption over (a) g-C_3N_4 monolayer, (b) g-C_3N_4/GN, (c) g-C_3N_4/hBN, and (d) g-C_3N_4 multilayer. 159
Figure A.4. Optimized structures of Fe at different locations of the g-C_3N_4 substrate. (a) Hollow site coordinated with 4 N_p; (b) hollow site coordinated with 2 N_p; and (3) Fe on top of N_g. The lowest energy structure (a) is set to be at 0 eV. (Color code: blue-N, brown-C, and yellow-Fe) 160
Figure A.5. DOS of O_2 adsorption on (a) Fe/g-C_3N_4 and (b) Fe/g-C_3N_4/GN..... 161
Figure B.1. Optimized dual-metal sites (consisting of PGM) and configurations of O_2, OOH, O, and OH adsorbates. Color code: brown-C, light blue-N, yellow-Fe, dark blue-Co, pink-Ni, purple-Cu, silver-Pt, green-Pd, red-O, and white, H. 162
Figure B.2. Optimized dual-metal sites (consisting of non-PGM only) and configurations of O_2, OOH, O, and OH. Color code: brown-C, light blue-N, yellow-Fe, dark blue-Co, pink-Ni, purple-Cu, red-O, and white, H. 163
Figure B.3.Optimized dual-metal site and configurations O_2, OOH, O, and OH that bind on the opposite side of the pre-adsorbed OH ligand. Color code: brown-C, light blue-N, yellow-Fe, dark blue-Co, pink-Ni, purple-Cu, silver-Pt, red-O, and white-H. 164
Figure B.4. Bader charge analysis of Fe-Fe (a), Fe-Co (b), Fe-Ni (c), Fe-Cu (d), Co-Co (e), Co-Ni (f), and Pt-Co (g) with (right) and without (left) the pre-adsorbed OH ligand. Color code: brown-C, light blue-N, yellow-Fe, dark blue-Co, pink-Ni, purple-Cu, silver-Pt, red-O, and white, H. 165

Figure B.5. Optimized dual-metal site and configurations O_2, OOH, O, and OH that bind on the same side of the pre-adsorbed OH ligand. Color code: brown-C, light blue-N, yellow-Fe, dark blue-Co, pink-Ni, purple-Cu, silver-Pt, red-O, and white-H. 166

Figure B.6. Free energy diagrams of ORR over (a) Fe-Fe$(OH)_s$, (b) Fe-Co$(OH)_s$, (c) Fe-Ni$(OH)_s$, (d) Fe-Cu$(OH)_s$, (e) Co-Co$(OH)_s$, (f) Co-Ni$(OH)_s$, and (g) Pt-Co$(OH)_s$ at the same side of OH ligand. "*" indicates clean surface. 167

Figure B.7. The relationship between the adsorptions of OH and O_2 (i.e., ΔG_{OH^*} and $\Delta G_{O_2^*}$). .. 168

Figure C.1. Phase diagram (a) of Cu-oxo active centers as a function of μ_{H_2O} and μ_O, and (b) the most stable active center configuration (indicated by the red triangle) from the bottom view. . 170

Figure C.2. Energetics of methane partial oxidation over (a) site II of Cu-trioxo, (b) mono (μ-oxo) dicopper, and (c) bis (μ-oxo) dicopper with different spin multiplicities. Computational errors are based on the Bayesian error estimation. 171

Figure C.3. Potential energy surfaces of respective ethane and propane conversions into ethanol (a), 1-propanol (b), and isopropanol (c) over site II of Cu-trioxo active site at doublet (yellow), quartet (blue), and sextet (red) spin multiplicities. Computational errors are based on the Bayesian error estimation. 172

Figure C.4. Potential energy surfaces of respective ethane and propane conversions into ethanol (a), 1-propanol (b), and isopropanol (c) over site I of Cu-trioxo active site at doublet (yellow), quartet (blue), and sextet (red) spin multiplicities. Computational errors are based on the Bayesian error estimation. 173

Figure C.5. Methane C-H bond activation considering doublet (yellow), quartet (blue), and sextet (red) spin multiplicities. The energy barriers (in eV) are also labeled numerically. 174

List of Tables

Table 3.1. Adsorptions of OOH*, O*, and OH* on Pt_{55}/VACNF: Binding sites, $\Delta G_{ads,}$ based on eqs. 2.12-2.15 in Chapter 2, and $\overline{CN}$. 61

Table 4.1. Lattice parameters and interlayer spacing for g-C_3N_4, g-C_3N_4/GN, and g-C_3N_4/hBN. The PBE-D2 calculations from this work are highlighted in bold numbers. 72

Table 4.2. Binding energies (BE_A in eV) of ORR intermediates on g-C_3N_4 monolayer, g-C_3N_4 multilayer, g-C_3N_4/GN, and g-C_3N_4/hBN. 77

Table 4.3. Binding energies (BE_A in eV) of ORR intermediates on Fe/g-C_3N_4, Fe/g-C_3N_4/GN, and FeN_4. 86

Table 5.1**.** Adsorption energies (in eV) of O_2, OOH, O, and OH, the dual-metal site formation energies (ΔG_f in eV), the limiting potentials (U_{lim} in V), and the corresponding PLS. 101

Table 5.2. Adsorption energies (in eV) of O_2, OOH, O, and OH, limiting potentials (U_{lim} in V), and the corresponding PLS for M1-M2$(OH)_o$. Subscription "o" indicates binding sites are on the opposite side of the OH ligand. 106

Table 6.1. Selected theoretical works on C-H bond activation by Cu-oxo complexes in ZSM-5 or MOR frameworks. 123

Table 6.2. Lattice Parameters of MOR 126

Table B.1**.** Adsorption free energies (in eV) of ORR intermediates and onset potential (U_{lim} in V) on the same side of pre-adsorbed OH. 169

Table C.1. Lattice parameters and magnetic moments of bulk CuO. 174

Table C.2. Bond distance and band angles of optimized Cu-oxo clusters. 175

Table C.3. Spin densities of each active sites at different spin multiplicities 176

Acknowledgements

I would like to express my thanks to my advisor, Prof. Bin Liu, for encouraging, guiding, teaching, and supporting my Ph.D. studies. I appreciate all his dedications and ideas sharing with me to make my Ph.D. experience productive. His advice on both research and career have been priceless, which allows me to grow as a researcher. I would also like to thank my committee members, Prof. Jun Li, Prof. James Edgar, and Prof. Chuancheng Duan served as my committee, along with the time, attention, and guidance they have provided.

I am also grateful to the members of the Liu's former and current group members: Dr. Song Liu, Dr. Mingxia Zhou, Dr. Nannan Shan, Narges Manavi, and Chaoran Huang, whom I had a great time to work with, as well as the discussion and sharing of valuable research ideas.

I'm also thankful for Prof. Jun Li's group: Ayyappan Elangovan, Prof. Keith Hohn's group: Fan Zeng and Quangxing Zheng, Dr. Dong Ding's group: Lucun Wang, and Dr. Dongxia Liu's group: Su Cheun Oh for their experimental collaborations.

I truly appreciate Professor Christin Aikens and her group members: Dr. Fahri Alkan, Gowri Udayangani, Pratima Pandeya, Zhen Liu, Olivia Hull, Yuchen Wang, and Shana Haveridge for the joint research group meetings and discussion.

I would also like to express my gratitude to my dear friends, Rachel and Erik Gfeller, Jane and Rod Fox, Fan Qiu, Shuai Cao, Esther and Andrew Craigo, Oscar Ramos, Sharon and George Gardener, Brian Anderson, Mark Nussbaumer, Doug Gurgel, Ben Lemmons, Ben Meyer, Marci Felbush, Dakota German, Joe Wright, Kyle Reighard, Tyler Gleason, Fan Liu, Hai Yu and Jibin Sun for their friendship.

Last but not least, I am greatly indebted to my family, especially my parents, Wei Xu and Bin Wu, for all of the sacrifices they made on my behalf. I would like to express appreciation to my beloved wife, Shijiao Chen, who has always been my support along the way, as well as my three sweetest little kids, Kevin Xu, Kelly Xu, and Kyler Xu, who have always brought many kinds of surprises to my life.

Chapter 1 - Introduction

Fuel cells will play a major role in mitigating our dependence on fossil fuels and combating climate change with efficient and versatile power delivery.[1] Direct methanol fuel cells (DMFCs) attract broad attention due to their simplicity and efficiency; theoretically, the efficiency can achieve up to 96.5%.[2,3] As shown in Figure 1.1, methanol (e.g., produced via methane partial oxidation) is directly fed to the anode side of DMFC for oxidation in an alkaline environment producing power and the water by-product. On the cathode side, oxygen is reduced to hydroxide (OH^-) via the oxygen reduction reaction (ORR). A closed circuit in the full cell illustrated below enables a complete cycle of chemical energy-to-electricity conversion.

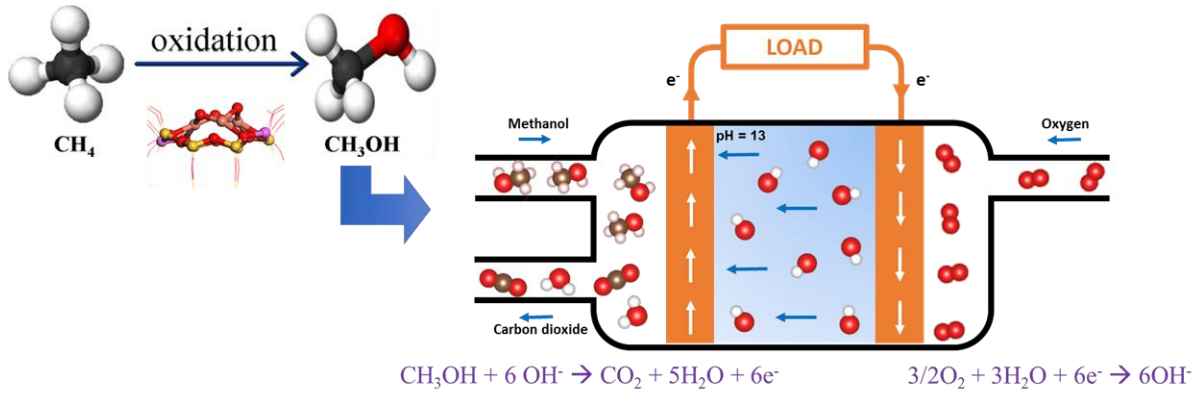


Figure 1.1. Operation scheme for direct methanol fuel cells. Methanol production via partial methane oxidation is also indicated.

1.1 Catalysts for Oxygen Reduction Reactions

As illustrated in Figure 1.1, the equilibrium potentials of methanol oxidation reaction (anode side) and ORR (cathode site) under alkaline conditions are -0.81 V and 0.402 V, respectively.[4,5] Hence, the overall DMFC potential (i.e., 1.21 V). Despite the low activity of methanol oxidation reaction at the anode side, the slow reaction kinetics of ORR at cathode side can also limit the

performance of DMFC.[6–8] Therefore, in order to improve the performance of DMFCs, finding optimal catalysts to enhance cathodic ORR performance is crucial.

Platinum (Pt) catalysts supported on high surface area Vulcan carbon (or carbon black), denoted as Pt/C, have long been recognized as the standard ORR electrocatalysts.[9,10] However, the high manufacturing cost of Pt-based fuel cell devices undermines their competition against current fossil energy conversion and transportation technologies.[11] Pt/C catalysts are also susceptible to carbon support corrosion, resulting in catalyst sintering and catalyst dissolution.[9,12,13] Moreover, Pt cathodes are notoriously sensitive to crossover methanol and CO poisoning.[13] Overall, the ultimate goal of the design and development of next-generation ORR catalysts are driven to increase ORR activity, to improve the resistance to crossover methanol and CO, and to significantly lower the fuel cell production cost.[14,15]

There are two main strategies to overcome these challenges: (1) stabilize and boost Pt catalytic performance by utilizing novel catalyst supports;[13] and (2) develop catalytic materials that are Pt free.[14,15] Well-dispersed Pt catalysts on suitable supports can withstand electrochemical oxidation/reduction cycles without the loss of their intrinsic properties.[13] There has also been numerous success in using Fe, Ni, and Co as substitutes for Pt ORR catalysts.[15–20] Materials that are completely free from metals were also considered.[21–27] All these materials show appeal in resisting crossover methanol and CO poisoning.[14,15]

Graphitic carbon nanostructures, such as graphene (GN)[28–30], carbon nanotubes (CNT)[31,32], and carbon nanofibers (CNFs)[33–35], remain stable under oxidizing environment. Debe *et al.*[36,37] employed vertically aligned organic whiskers loaded 0.1-0.22 mg Pt/cm^2 and achieved higher ORR activity than Pt/C by at least 3 folds and better durablility.[36,37] Vertically aligned carbon nanofibers (VACNFs), as shown in Figure 1.2a, is another unique structural variation for the

preparation of Pt ORR catalysts. As illustrated by Figure 1.2b, the stacked 3D conical architecture of VACNF displays high edge density ready to anchor the deposited Pt NPs.[38] When using CNT (Figure 1.2c) and GN (Figure 1.2d) as catalyst supports, Pt NPs are also distributed at the wall, basal plane, or defect sites.[39–43]

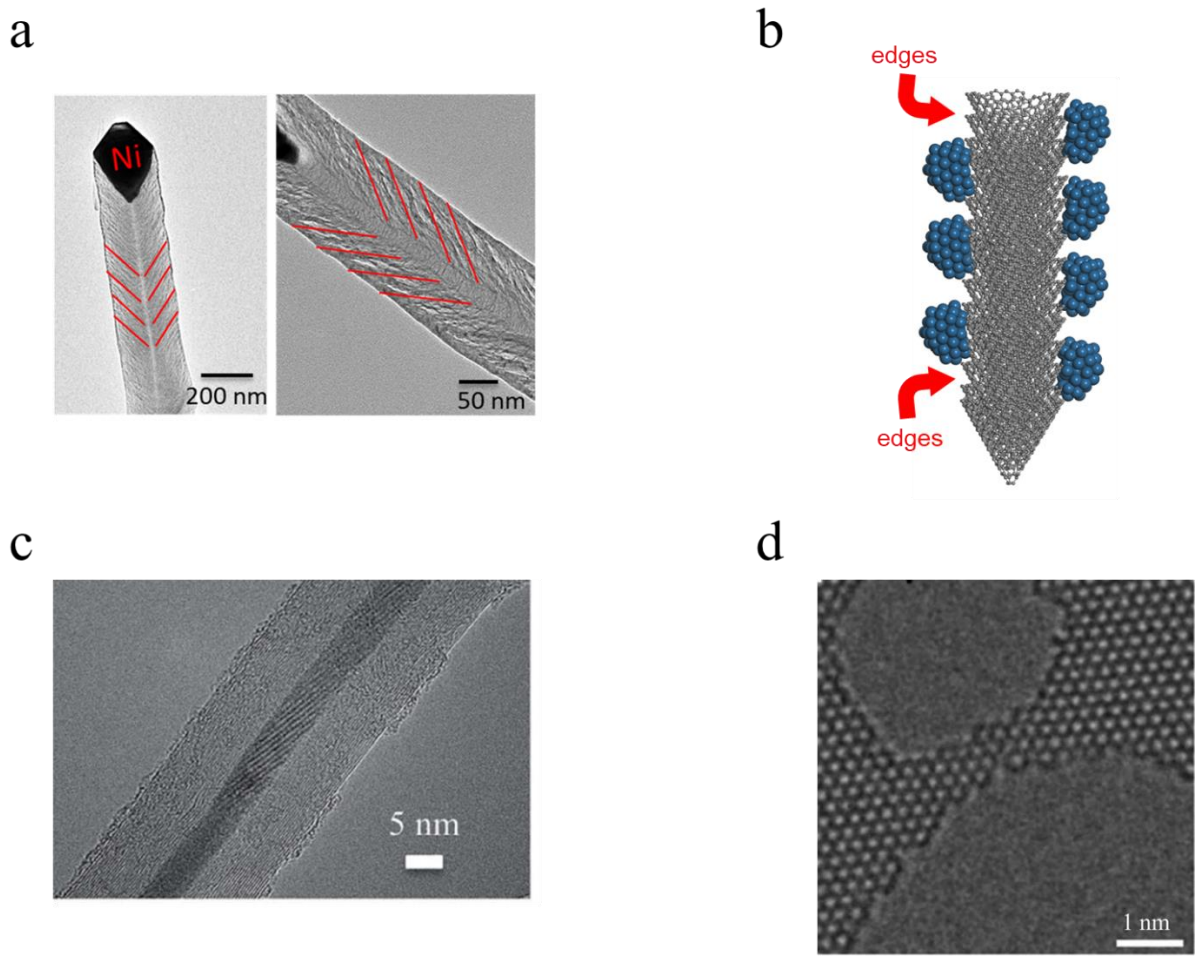


Figure 1.2. (a) TEM images of vertically aligned carbon nano fiber, (b) its molecular structure with Pt NPs, (c) carbon nanotube adapted from Ref [44], and (d) graphene adapted from Ref [45].

To significantly lower metal usage, single-atom catalysts (SACs) have recently gained momentum for several electrochemical reactions such as ORR, oxygen evolution reaction (OER), and nitrogen reduction reaction (NRR).[15] Atomically dispersed Fe, Co, Mn in SAC systems exhibit

competitive ORR performance.[14–16,46–50] The most representative ORR SAC consist of the characteristic Metal-Nitrogen-Carbon (M-N-C) moieties.[14,15,46,50–53] The active centers of SAC catalysts display rich variations in terms of elemental species and compositions of metallic centers, as well as ligand configurations. Besides SACs represented by lone atom active centers, dual-metal sites, composed of two adjacent identical or distinct transition metal species, emerged as extended forms augmenting the SAC selection repertoire.[15] Dual-metal sites enable charge redistribution via *d-d* orbital hybridizations, and open up new opportunities to fine-tune ORR activity. Moreover, the ORR efficacy is also exceptionally sensitive to the heteroatom co-dopants such as B,[48] P,[54] S,[47] and the external ligands (e.g., OH,[55] Cl[56]) directly associated with the active center.

1.2 Catalysts Design for Methane Conversion

The methanol fuel for DMFC operation is produced primarily from methane, a major component of natural gas.[57,58] On the industrial scale, the synthesis of methanol proceeds via steam reforming of methane forming syngas (CO and H_2), followed by catalytic hydrogenation step that converts syngas to methanol. Such a conventional process is both expensive and sensitive to sulfur poisoning.[59] Hence, alternative pathways for methane-to-methanol conversion are needed to realize more sustainable chemical production.

The C–H bond strength is 104 kcal/mol,[60] so methane oxidation at low temperature is not feasible due to its chemical inertness. At high temperatures (e.g., 537 ºC), methane will likely be completely oxidized into CO_2 and H_2O.[58,61] Hence, a challenge to this reaction is to efficiently activate the C–H bond without over-oxidizing the hydrocarbon into CO_2. In nature, selective C–H bond activation is catalyzed by soluble methane monooxygenase (sMMO), or particulate methane monooxygenase (pMMO). The diiron center in sMMO and tri- and dicopper centers in pMMO are

all capable of producing methanol at high selectivity with their bridging oxygen at room temperature.[62–68]

Inspired by the catalytic functionality of the above biocatalysts, Groothaert and co-workers found that Cu-exchanged zeolites, e.g., ZSM-5 and mordenite (MOR), both show good catalytic activity and selectivity towards methane partial oxidation, with Cu-MOR being more superior.[69] However, there are on-going debates regarding the exact active center structures and accompanying reaction mechanisms. This issue is further complicated by various computational approaches proposed to target the relevant catalyst systems.

1.3 Principles of Computational Catalyst Design

Catalysts play a critical role in accelerating the rates of chemical and energy conversions and is the main driving force advancing the solutions to the issues mentioned above. Optimal catalysts invariably display high activity and long-term stability behaviors. Understanding the structure of active catalysts has always been important in catalyst development and optimization.[70,71] Studies elucidate the active site arrangements, density of states, charge transfer, *d*-band center, spin density, adsorption energies, and reaction energy barriers. Over the course of intensive catalysis research in the past decades, these wide-ranging topics can be explored through both experimental and theoretical strategies.[14,15,72]

As depicted in Figure 1.3, the characterization and experimental testing of synthesized catalysts provide testing bed for catalyst modeling based on Density Functional Theory (DFT). To a great extent, this has been achieved by advances in quantum mechanical modeling techniques and computational toolsets. By carrying out DFT calculations, atomic/molecular geometries,

binding energies can be routinely obtained. Then, reaction mechanisms and catalytic trends will be deduced and understood.

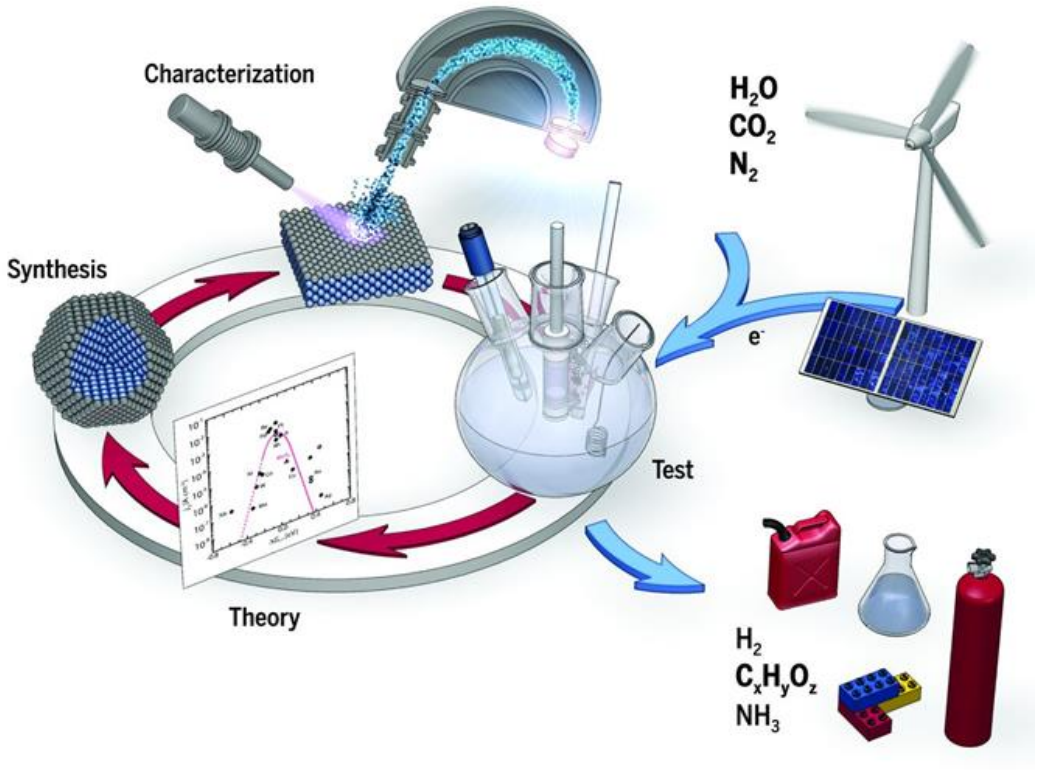


Figure 1.3. Scheme for catalysts design. Adapted from Ref. [73].

With extensively accumulated knowledge, descriptor (i.e., atomic structure, electronic properties, quantifiable thermodynamic values) driven catalyst design paradigms have become a dominant force in modern catalysis. Such an approach will be demonstrated in the following chapters of this dissertation. With DFT, electronic structures and charge distributions can also be conveniently obtained as complementary knowledge for deep understanding of catalytic behaviors.

In this thesis, established molecular modeling tools will be utilized to tackle the frontier issues directly related to catalyst designs for chemical conversions in DMFC systems. Specifically, we emphasize the construction of representative model catalysts to help gain insights into catalytic reactivities and stabilities. The governing molecular mechanisms, and their relationships to catalyst geometric and electronic structures will be investigated and understood.

1.4 Scope of this Dissertation

This dissertation focuses on two main reactions: ORR and the methane partial oxidation reaction., both are relevant to DMFC operations. As detailed below, carbon-based VACNF, N-doped GN, and N-rich g-C_3N_4 were considered as various functional catalytic materials to stabilize and promote ORR systems. For methane partial oxidation, the goal is to explore the stable active site structures with high catalytic activity for methane C–H bond activation.

1.4.1 Catalysts Considered for ORR

1.4.1.1 Platinum supported by VACNF

The VACNF architecture has characteristic stacked conical structures, as shown in Figure 1.2b.[13,38,74] VACNFs are conductive, and remain stable under oxidizing environment.[13] As discussion in Section 1.1 Debe *et al.*,[36,37] has demonstrated that the vertically aligned architecture is capable of stabilizing the sputtered Pt NPs at its ample edge sites throughout the fiber length. As such, the high edge density is a desirable feature and opens up opportunities as ideal catalyst supports. This work is built on promising experimental evidence showing that VACNF structures stabilize well dispersed Pt NPs and will eventually lower the Pt usage without significant performance loss. However, Pt catalysts supported on VACNF is rather complex. Its molecular structure is not well understood. Electrochemical measurements revealed that the half-wave potential for ORR obtained from Pt/VACNF catalysts left-shifted by 0.04 V compared to

commercial Pt/C catalysts, indicating the subtle but non-neglectable impact of the VACNF support on Pt catalysts. Therefore, a thorough investigation at the molecular level should be called upon elucidate the ORR process.

1.4.1.2 Graphitic carbon nitride (g-C_3N_4) as functional ORR catalysts

Graphitic carbon nitride (g-C_3N_4) is a two-dimensional (2D) nitrogen rich semiconductor, consisting of both graphitic (N_g) and pyridinic (N_p) nitrogen species. With an energy band-gap of 2.7 eV, g-C_3N_4 has been extensively employed as photocatalytic and photoelectrochemical devices.[75–79] Recently, g-C_3N_4 were explored in electrochemical ORR systems.[21,22,71,80,81] In this dissertation, the ORR reactivity of g-C_3N_4 were probed. Moreover, the lattice of g-C_3N_4 (7.13 Å) is compatible with GN (7.31 Å) and hexagonal boron nitride (hBN) (7.40 Å) monolayers, giving rise to the possibility of forming in-plane heterostructures. Studies have shown that the electronic structures in 2D materials can be modulated this way.[82,83] Hence, modifications to g-C_3N_4 via the decoration of ORR-active metal ions (i.e., single-atom Fe) and heterostructure engineering with graphene and hBN were considered.

1.4.1.3 Dual-metal sites for ORR

Dual-metal active centers can be regarded as a variation to the emerging SACs, with two single atom sites located in close proximity.[15] The embedded synergistic effects (i.e., intermetallic interaction and charge polarization) between two neighboring metal atoms allows increased ORR activity, and enhanced the structural stability.[15] Meanwhile, the charge redistribution at the dual-metal site also lowers the O-O bond dissociation energy barrier to promote alternative ORR pathways. Thus, a broad screening will likely generate new insights into this new class of SAC materials. Furthermore, the strongly bounded OH ligand that is directly generated from alkaline condition or as an ORR intermediate can also modulate the electronic structure of the active center

to fine-tune the ORR activity. Therefore, in this dissertation, the potential of the dual metal sites consisting of both PGM (Pt and Pd) and non-PGM(Fe, Co, Ni, and Cu) coordinated with six pyridinic N atoms embedded in GN framework with and without OH ligand as ORR catalysts were considered and discussed in Chapter 5.

1.4.2 Catalysts for Methane Conversion

In this dissertation, the stabilities and catalytic activities for methane-to-methanol conversion of mono(μ-oxo) dicopper, two Cu atoms connected by a bridging oxygen atom, bis(μ-oxo) dicopper, two Cu atoms connected by two bridging oxygen atoms, and Cu-trioxo, three Cu atoms inter-connected by three bridging oxygen atoms, are investigated.[57,69,84] Despite the intensive previous study[57,69,84], the active center responsible for the high catalytic activity is still under debate. In Chapter 6, theoretical modeling was carried out to evaluate the stability of these active centers anchored inside of the 8-membered ring (8MR) of MOR framework, along with the re-examination of C-H bond activation of methane at different spin multiplicity. Later, the activities of partial oxidation of ethane and propane were also modeled.

1.5 Organization of the Dissertation

The contents of this dissertation are organized in seven chapters. Chapter 1 (this chapter) provides an overview of the research background and scope of this dissertation. Chapter 2 describes the theory, methodology, and reaction mechanisms relevant to this dissertation. Chapter 3 discusses the construction and evaluation of Pt catalysts supported on VACNF model catalysts for ORR. Chapter 4 investigated graphitic carbon nitride (g-C_3N_4) as a potential ORR catalyst. Chapter 5 broadly screened atomically dispersed dual-metal centers as another alternative ORR catalyst. Chapter 6 presents a theoretical study of direct methane-to-methanol conversion over Cu loaded MOR zeolitic framework. Research conclusions and outlook are summarized in Chapter 7.

References

(1) Strasser, P.; Koh, S.; Anniyev, T.; Greeley, J.; More, K.; Yu, C.; Liu, Z.; Kaya, S.; Nordlund, D.; Ogasawara, H.; Toney, M. F.; Nilsson, A. Lattice-Strain Control of the Activity in Dealloyed Core–Shell Fuel Cell Catalysts. *Nat. Chem.* **2010**, *2* (6), 454–460.

(2) Zou, L.; Fan, J.; Zhou, Y.; Wang, C.; Li, J.; Zou, Z.; Yang, H. Conversion of PtNi Alloy from Disordered to Ordered for Enhanced Activity and Durability in Methanol-Tolerant Oxygen Reduction Reactions. *Nano Res.* **2015**, *8* (8), 2777–2788.

(3) Tiwari, J. N.; Tiwari, R. N.; Singh, G.; Kim, K. S. Recent Progress in the Development of Anode and Cathode Catalysts for Direct Methanol Fuel Cells. *Nano Energy* **2013**, *2* (5), 553–578.

(4) Yu, E. H.; Krewer, U.; Scott, K. Principles and Materials Aspects of Direct Alkaline Alcohol Fuel Cells. *Energies* . 2010.

(5) Lee, C. H. Theoretical Basis of Electrocatalysis; Pati, S. U. L. E.-A. R. E.-I. M. E.-R. K., Ed.; IntechOpen: Rijeka, 2018; p Ch. 1.

(6) Wu, G.; More, K. L.; Johnston, C. M.; Zelenay, P. High-Performance Electrocatalysts for Oxygen Reduction Derived from Polyaniline, Iron, and Cobalt. *Science.* **2011**, *332* (6028), 443 LP – 447.

(7) Steele, B. C. H.; Heinzel, A. Materials for Fuel-Cell Technologies. *Nature* **2001**, *414* (6861), 345–352.

(8) Gong, K.; Du, F.; Xia, Z.; Durstock, M.; Dai, L. Nitrogen-Doped Carbon Nanotube Arrays with High Electrocatalytic Activity for Oxygen Reduction. *Science.* **2009**, *323* (5915), 760 LP – 764.

(9) Nie, Y.; Li, L.; Wei, Z. Recent Advancements in Pt and Pt-Free Catalysts for Oxygen Reduction Reaction. *Chem. Soc. Rev.* **2015**, *44* (8), 2168–2201.

(10) Katsounaros, I.; Cherevko, S.; Zeradjanin, A. R.; Mayrhofer, K. J. J. Oxygen Electrochemistry as a Cornerstone for Sustainable Energy Conversion. *Angew. Chemie Int. Ed.* **2014**, *53* (1), 102–121.

(11) Yang, C.-J. An Impending Platinum Crisis and Its Implications for the Future of the Automobile. *Energy Policy* **2009**, *37* (5), 1805–1808.

(12) Yu, X.; Ye, S. Recent Advances in Activity and Durability Enhancement of Pt/C Catalytic Cathode in PEMFC: Part I. Physico-Chemical and Electronic Interaction between Pt and Carbon Support, and Activity Enhancement of Pt/C Catalyst. *J. Power Sources* **2007**, *172* (1), 133–144.

(13) Elangovan, A.; Xu, J.; Brown, E.; Liu, B.; Li, J. Fundamental Electrochemical Insights of Vertically Aligned Carbon Nanofiber Architecture as a Catalyst Support for ORR. *J. Electrochem. Soc.* **2020**, *167* (6), 66523.

(14) He, Y.; Liu, S.; Priest, C.; Shi, Q.; Wu, G. Atomically Dispersed Metal–Nitrogen–Carbon Catalysts for Fuel Cells: Advances in Catalyst Design, Electrode Performance, and

Durability Improvement. *Chem. Soc. Rev.* **2020**.

(15) Zhu, Y.; Sokolowski, J.; Song, X.; He, Y.; Mei, Y.; Wu, G. Engineering Local Coordination Environments of Atomically Dispersed and Heteroatom-Coordinated Single Metal Site Electrocatalysts for Clean Energy-Conversion. *Adv. Energy Mater.* **2019**, *n/a* (n/a), 1902844.

(16) Xu, J.; Liu, B. Intrinsic Properties of Nitrogen-Rich Carbon Nitride for Oxygen Reduction Reaction. *Appl. Surf. Sci.* **2020**, *500*, 144020.

(17) Wang, J.; Huang, Z.; Liu, W.; Chang, C.; Tang, H.; Li, Z.; Chen, W.; Jia, C.; Yao, T.; Wei, S.; Wu, Y.; Li, Y. Design of N-Coordinated Dual-Metal Sites: A Stable and Active Pt-Free Catalyst for Acidic Oxygen Reduction Reaction. *J. Am. Chem. Soc.* **2017**, *139* (48), 17281–17284.

(18) Wang, J.; Liu, W.; Luo, G.; Li, Z.; Zhao, C.; Zhang, H.; Zhu, M.; Xu, Q.; Wang, X.; Zhao, C.; Qu, Y.; Yang, Z.; Yao, T.; Li, Y.; Lin, Y.; Wu, Y.; Li, Y. Synergistic Effect of Well-Defined Dual Sites Boosting the Oxygen Reduction Reaction. *Energy Environ. Sci.* **2018**, *11* (12), 3375–3379.

(19) Zhang, L.; Fischer, J. M. T. A.; Jia, Y.; Yan, X.; Xu, W.; Wang, X.; Chen, J.; Yang, D.; Liu, H.; Zhuang, L.; Hankel, M.; Searles, D. J.; Huang, K.; Feng, S.; Brown, C. L.; Yao, X. Coordination of Atomic Co–Pt Coupling Species at Carbon Defects as Active Sites for Oxygen Reduction Reaction. *J. Am. Chem. Soc.* **2018**, *140* (34), 10757–10763.

(20) Meng, Y.; Yin, C.; Li, K.; Tang, H.; Wang, Y.; Wu, Z. Improved Oxygen Reduction Activity in Heteronuclear FeCo-Codoped Graphene: A Theoretical Study. *ACS Sustain. Chem. Eng.* **2019**, *7* (20), 17273–17281.

(21) Lyth, S. M.; Nabae, Y.; Moriya, S.; Kuroki, S.; Kakimoto, M.; Ozaki, J.; Miyata, S. Carbon Nitride as a Nonprecious Catalyst for Electrochemical Oxygen Reduction. *J. Phys. Chem. C* **2009**, *113* (47), 20148–20151.

(22) Zheng, Y.; Jiao, Y.; Chen, J.; Liu, J.; Liang, J.; Du, A.; Zhang, W.; Zhu, Z.; Smith, S. C.; Jaroniec, M.; Lu, G. Q. (Max); Qiao, S. Z. Nanoporous Graphitic-C3N4@Carbon Metal-Free Electrocatalysts for Highly Efficient Oxygen Reduction. *J. Am. Chem. Soc.* **2011**, *133* (50), 20116–20119.

(23) Guo, D.; Shibuya, R.; Akiba, C.; Saji, S.; Kondo, T.; Nakamura, J. Active Sites of Nitrogen-Doped Carbon Materials for Oxygen Reduction Reaction Clarified Using Model Catalysts. *Science (80-.).* **2016**, *351* (6271), 361 LP – 365.

(24) Zhang, L.; Niu, J.; Dai, L.; Xia, Z. Effect of Microstructure of Nitrogen-Doped Graphene on Oxygen Reduction Activity in Fuel Cells. *Langmuir* **2012**, *28* (19), 7542–7550.

(25) Qu, L.; Liu, Y.; Baek, J.-B.; Dai, L. Nitrogen-Doped Graphene as Efficient Metal-Free Electrocatalyst for Oxygen Reduction in Fuel Cells. *ACS Nano* **2010**, *4* (3), 1321–1326.

(26) Choi, C. H.; Chung, M. W.; Kwon, H. C.; Park, S. H.; Woo, S. I. B, N- and P, N-Doped Graphene as Highly Active Catalysts for Oxygen Reduction Reactions in Acidic Media. *J. Mater. Chem. A* **2013**, *1* (11), 3694–3699.

(27) Chen, Z.; Higgins, D.; Chen, Z. Nitrogen Doped Carbon Nanotubes and Their Impact on the Oxygen Reduction Reaction in Fuel Cells. *Carbon N. Y.* **2010**, *48* (11), 3057–3065.

(28) Seo, M. H.; Choi, S. M.; Kim, H. J.; Kim, W. B. The Graphene-Supported Pd and Pt Catalysts for Highly Active Oxygen Reduction Reaction in an Alkaline Condition. *Electrochem. commun.* **2011**, *13* (2), 182–185.

(29) Zhu, C.; Dong, S. Recent Progress in Graphene-Based Nanomaterials as Advanced Electrocatalysts towards Oxygen Reduction Reaction. *Nanoscale* **2013**, *5* (5), 1753–1767.

(30) Shao, Y.; Zhang, S.; Wang, C.; Nie, Z.; Liu, J.; Wang, Y.; Lin, Y. Highly Durable Graphene Nanoplatelets Supported Pt Nanocatalysts for Oxygen Reduction. *J. Power Sources* **2010**, *195* (15), 4600–4605.

(31) Tang, H.; Chen, J. H.; Huang, Z. P.; Wang, D. Z.; Ren, Z. F.; Nie, L. H.; Kuang, Y. F.; Yao, S. Z. High Dispersion and Electrocatalytic Properties of Platinum on Well-Aligned Carbon Nanotube Arrays. *Carbon.* **2004**, *42* (1), 191–197.

(32) Wang, D.-W.; Su, D. Heterogeneous Nanocarbon Materials for Oxygen Reduction Reaction. *Energy Environ. Sci.* **2014**, *7* (2), 576–591.

(33) Bessel, C. A.; Laubernds, K.; Rodriguez, N. M.; Baker, R. T. K. Graphite Nanofibers as an Electrode for Fuel Cell Applications. *J. Phys. Chem. B* **2001**, *105* (6), 1115–1118.

(34) Li, W.; Waje, M.; Chen, Z.; Larsen, P.; Yan, Y. Platinum Nanopaticles Supported on Stacked-Cup Carbon Nanofibers as Electrocatalysts for Proton Exchange Membrane Fuel Cell. *Carbon N. Y.* **2010**, *48* (4), 995–1003.

(35) Lee, K.; Zhang, J.; Wang, H.; Wilkinson, D. P. Progress in the Synthesis of Carbon Nanotube- and Nanofiber-Supported Pt Electrocatalysts for PEM Fuel Cell Catalysis. *J. Appl. Electrochem.* **2006**, *36* (5), 507–522.

(36) Debe, M. K.; Schmoeckel, A. K.; Vernstrom, G. D.; Atanasoski, R. High Voltage Stability of Nanostructured Thin Film Catalysts for PEM Fuel Cells. *J. Power Sources* **2006**, *161* (2), 1002–1011.

(37) Debe, M. K. Nanostructured Thin Film Electrocatalysts for PEM Fuel Cells - A Tutorial on the Fundamental Characteristics and Practical Properties of NSTF Catalysts. *ECS Trans.* **2012**, *45* (2), 47–68.

(38) Cheng, H.; Zhu, Y.-A.; Chen, D.; Åstrand, P.-O.; Li, P.; Qi, Z.; Zhou, X.-G. Evolution of Carbon Nanofiber-Supported Pt Nanoparticles of Different Particle Sizes: A Molecular Dynamics Study. *J. Phys. Chem. C* **2014**, *118* (41), 23711–23722.

(39) Lim, D.-H.; Wilcox, J. Mechanisms of the Oxygen Reduction Reaction on Defective Graphene-Supported Pt Nanoparticles from First-Principles. *J. Phys. Chem. C* **2012**, *116* (5), 3653–3660.

(40) Lim, D.-H.; Wilcox, J. DFT-Based Study on Oxygen Adsorption on Defective Graphene-Supported Pt Nanoparticles. *J. Phys. Chem. C* **2011**, *115* (46), 22742–22747.

(41) Jin, N.; Han, J.; Wang, H.; Zhu, X.; Ge, Q. A DFT Study of Oxygen Reduction Reaction

Mechanism over O-Doped Graphene-Supported Pt4, Pt3Fe and Pt3V Alloy Catalysts. *Int. J. Hydrogen Energy* **2015**, *40* (15), 5126–5134.

(42) Verga, L. G.; Aarons, J.; Sarwar, M.; Thompsett, D.; Russell, A. E.; Skylaris, C.-K. Effect of Graphene Support on Large Pt Nanoparticles. *Phys. Chem. Chem. Phys.* **2016**, *18* (48), 32713–32722.

(43) Zhang, J.; Chen, C.; Chen, S.; Hu, Q.; Gao, Z.; Li, Y.; Qin, Y. Highly Dispersed Pt Nanoparticles Supported on Carbon Nanotubes Produced by Atomic Layer Deposition for Hydrogen Generation from Hydrolysis of Ammonia Borane. *Catal. Sci. Technol.* **2017**, *7* (2), 322–329.

(44) Gowda, P.; Mukherjee, S.; Reddy, S. K.; Ghosh, R.; Misra, A. Giant Actuation in Bulk Carbon Nanotubes under Coupled Electric and Magnetic Fields. *RSC Adv.* **2015**, *5* (33), 26157–26162.

(45) Robertson, A. W.; Warner, J. H. Atomic Resolution Imaging of Graphene by Transmission Electron Microscopy. *Nanoscale* **2013**, *5* (10), 4079–4093.

(46) Zhao, J.; Wang, W.; Qu, X.; Meng, Y.; Wu, Z. M-Porphyrin (M = Mn, Co) Carbon Materials as Oxygen Reduction Catalysts from Density Functional Studies. *Mol. Phys.* **2019**, 1–9.

(47) Mun, Y.; Lee, S.; Kim, K.; Kim, S.; Lee, S.; Han, J. W.; Lee, J. Versatile Strategy for Tuning ORR Activity of a Single Fe-N4 Site by Controlling Electron-Withdrawing/Donating Properties of a Carbon Plane. *J. Am. Chem. Soc.* **2019**, *141* (15), 6254–6262.

(48) Saputro, A. G.; Fajrial, A. K.; Maulana, A. L.; Fathurrahman, F.; Agusta, M. K.; Akbar, F. T.; Dipojono, H. K. Dissociative Oxygen Reduction Reaction Mechanism on the Neighboring Active Sites of a Boron-Doped Pyrolyzed Fe–N–C Catalyst. *J. Phys. Chem. C* **2020**, *124* (21), 11383–11391.

(49) Liu, K.; Wu, G.; Wang, G. Role of Local Carbon Structure Surrounding FeN4 Sites in Boosting the Catalytic Activity for Oxygen Reduction. *J. Phys. Chem. C* **2017**, *121* (21), 11319–11324.

(50) Lee, D. H.; Lee, W. J.; Lee, W. J.; Kim, S. O.; Kim, Y.-H. Theory, Synthesis, and Oxygen Reduction Catalysis of Fe-Porphyrin-Like Carbon Nanotube. *Phys. Rev. Lett.* **2011**, *106* (17), 175502.

(51) Lefèvre, M.; Proietti, E.; Jaouen, F.; Dodelet, J.-P. Iron-Based Catalysts with Improved Oxygen Reduction Activity in Polymer Electrolyte Fuel Cells. *Science (80-.).* **2009**, *324* (5923), 71 LP – 74.

(52) Zitolo, A.; Goellner, V.; Armel, V.; Sougrati, M.-T.; Mineva, T.; Stievano, L.; Fonda, E.; Jaouen, F. Identification of Catalytic Sites for Oxygen Reduction in Iron- and Nitrogen-Doped Graphene Materials. *Nat. Mater.* **2015**, *14* (9), 937–942.

(53) Hossen, M. M.; Artyushkova, K.; Atanassov, P.; Serov, A. Synthesis and Characterization of High Performing Fe-N-C Catalyst for Oxygen Reduction Reaction (ORR) in Alkaline Exchange Membrane Fuel Cells. *J. Power Sources* **2018**, *375*, 214–221.

(54) Ma, T. Y.; Ran, J.; Dai, S.; Jaroniec, M.; Qiao, S. Z. Phosphorus-Doped Graphitic Carbon Nitrides Grown In Situ on Carbon-Fiber Paper: Flexible and Reversible Oxygen Electrodes. *Angew. Chemie Int. Ed.* **2015**, *54* (15), 4646–4650.

(55) Yang, Y.; Zhang, H.; Liang, Z.; Yin, Y.; Mei, B.; Song, F.; Sun, F.; Gu, S.; Jiang, Z.; Wu, Y.; Zhu, Z. Role of Local Coordination in Bimetallic Sites for Oxygen Reduction: A Theoretical Analysis. *J. Energy Chem.* **2020**, *44*, 131–137.

(56) Han, Y.; Wang, Y.; Xu, R.; Chen, W.; Zheng, L.; Han, A.; Zhu, Y.; Zhang, J.; Zhang, H.; Luo, J.; Chen, C.; Peng, Q.; Wang, D.; Li, Y. Electronic Structure Engineering to Boost Oxygen Reduction Activity by Controlling the Coordination of the Central Metal. *Energy Environ. Sci.* **2018**, *11* (9), 2348–2352.

(57) Woertink, J. S.; Smeets, P. J.; Groothaert, M. H.; Vance, M. A.; Sels, B. F.; Schoonheydt, R. A.; Solomon, E. I. A [Cu2O]2+ Core in Cu-ZSM-5, the Active Site in the Oxidation of Methane to Methanol. *Proc. Natl. Acad. Sci.* **2009**, *106* (45), 18908 LP – 18913.

(58) Zhao, Z.-J.; Kulkarni, A.; Vilella, L.; Nørskov, J. K.; Studt, F. Theoretical Insights into the Selective Oxidation of Methane to Methanol in Copper-Exchanged Mordenite. *ACS Catal.* **2016**, *6* (6), 3760–3766.

(59) Gesser, H. D.; Hunter, N. R.; Prakash, C. B. The Direct Conversion of Methane to Methanol by Controlled Oxidation. *Chem. Rev.* **1985**, *85* (4), 235–244.

(60) Vanelderen, P.; Snyder, B. E. R.; Tsai, M.-L.; Hadt, R. G.; Vancauwenbergh, J.; Coussens, O.; Schoonheydt, R. A.; Sels, B. F.; Solomon, E. I. Spectroscopic Definition of the Copper Active Sites in Mordenite: Selective Methane Oxidation. *J. Am. Chem. Soc.* **2015**, *137* (19), 6383–6392.

(61) Robinson, C.; Smith, D. B. The Auto-Ignition Temperature of Methane. *J. Hazard. Mater.* **1984**, *8* (3), 199–203.

(62) Lieberman, R. L.; Rosenzweig, A. C. Crystal Structure of a Membrane-Bound Metalloenzyme That Catalyses the Biological Oxidation of Methane. *Nature* **2005**, *434* (7030), 177–182.

(63) Rosenzweig, A. C. The Metal Centres of Particulate Methane Mono-Oxygenase. *Biochem. Soc. Trans.* **2008**, *36* (6), 1134–1137.

(64) Rosenzweig, A. C.; Frederick, C. A.; Lippard, S. J.; Nordlund, P. auml;r. Crystal Structure of a Bacterial Non-Haem Iron Hydroxylase That Catalyses the Biological Oxidation of Methane. *Nature* **1993**, *366* (6455), 537–543.

(65) Chan, S. I.; Wang, V. C.-C.; Lai, J. C.-H.; Yu, S. S.-F.; Chen, P. P.-Y.; Chen, K. H.-C.; Chen, C.-L.; Chan, M. K. Redox Potentiometry Studies of Particulate Methane Monooxygenase: Support for a Trinuclear Copper Cluster Active Site. *Angew. Chemie Int. Ed.* **2007**, *46* (12), 1992–1994.

(66) Liakos, D. G.; Neese, F. Interplay of Correlation and Relativistic Effects in Correlated Calculations on Transition-Metal Complexes: The (Cu2O2)2+ Core Revisited. *J. Chem. Theory Comput.* **2011**, *7* (5), 1511–1523.

(67) Snyder, B. E. R.; Bols, M. L.; Schoonheydt, R. A.; Sels, B. F.; Solomon, E. I. Iron and Copper Active Sites in Zeolites and Their Correlation to Metalloenzymes. *Chem. Rev.* **2018**, *118* (5), 2718–2768.

(68) Hori, Y.; Shiota, Y.; Tsuji, T.; Kodera, M.; Yoshizawa, K. Catalytic Performance of a Dicopper–Oxo Complex for Methane Hydroxylation. *Inorg. Chem.* **2018**, *57* (1), 8–11.

(69) Groothaert, M. H.; Smeets, P. J.; Sels, B. F.; Jacobs, P. A.; Schoonheydt, R. A. Selective Oxidation of Methane by the Bis(μ-Oxo)Dicopper Core Stabilized on ZSM-5 and Mordenite Zeolites. *J. Am. Chem. Soc.* **2005**, *127* (5), 1394–1395.

(70) Duan, J.; Chen, S.; Jaroniec, M.; Qiao, S. Z. Heteroatom-Doped Graphene-Based Materials for Energy-Relevant Electrocatalytic Processes. *ACS Catal.* **2015**, *5* (9), 5207–5234.

(71) Jin, H.; Guo, C.; Liu, X.; Liu, J.; Vasileff, A.; Jiao, Y.; Zheng, Y.; Qiao, S.-Z. Emerging Two-Dimensional Nanomaterials for Electrocatalysis. *Chem. Rev.* **2018**, *118* (13), 6337–6408.

(72) Schwarz, H.; González-Navarrete, P.; Li, J.; Schlangen, M.; Sun, X.; Weiske, T.; Zhou, S. Unexpected Mechanistic Variants in the Thermal Gas-Phase Activation of Methane. *Organometallics* **2017**, *36* (1), 8–17.

(73) Seh, Z. W.; Kibsgaard, J.; Dickens, C. F.; Chorkendorff, I.; Nørskov, J. K.; Jaramillo, T. F. Combining Theory and Experiment in Electrocatalysis: Insights into Materials Design. *Science (80-.).* **2017**, *355* (6321), 4998.

(74) Poveda, R. L.; Gupta, N. Carbon Nanofibers: Structure and Fabrication. In *Carbon Nanofiber Reinforced Polymer Composites*; Springer International Publishing: Cham, 2016; pp 11–26.

(75) Xiang, Q.; Yu, J.; Jaroniec, M. Preparation and Enhanced Visible-Light Photocatalytic H2-Production Activity of Graphene/C3N4 Composites. *J. Phys. Chem. C* **2011**, *115* (15), 7355–7363.

(76) Low, J.; Cao, S.; Yu, J.; Wageh, S. Two-Dimensional Layered Composite Photocatalysts. *Chem. Commun.* **2014**, *50* (74), 10768–10777.

(77) Dai, K.; Lu, L.; Liu, Q.; Zhu, G.; Wei, X.; Bai, J.; Xuan, L.; Wang, H. Sonication Assisted Preparation of Graphene Oxide/Graphitic-C3N4 Nanosheet Hybrid with Reinforced Photocurrent for Photocatalyst Applications. *Dalt. Trans.* **2014**, *43* (17), 6295–6299.

(78) Li, H.; Wu, Y.; Li, C.; Gong, Y.; Niu, L.; Liu, X.; Jiang, Q.; Sun, C.; Xu, S. Design of Pt/t-ZrO2/g-C3N4 Efficient Photocatalyst for the Hydrogen Evolution Reaction. *Appl. Catal. B Environ.* **2019**, *251*, 305–312.

(79) Tian, J.; Liu, Q.; Ge, C.; Xing, Z.; Asiri, A. M.; Al-Youbi, A. O.; Sun, X. Ultrathin Graphitic Carbon Nitride Nanosheets: A Low-Cost, Green, and Highly Efficient Electrocatalyst toward the Reduction of Hydrogen Peroxide and Its Glucose Biosensing Application. *Nanoscale* **2013**, *5* (19), 8921–8924.

(80) Mansor, N.; Miller, T. S.; Dedigama, I.; Jorge, A. B.; Jia, J.; Brázdová, V.; Mattevi, C.; Gibbs, C.; Hodgson, D.; Shearing, P. R.; Howard, C. A.; Corà, F.; Shaffer, M.; Brett, D. J.

L.; McMillan, P. F. Graphitic Carbon Nitride as a Catalyst Support in Fuel Cells and Electrolyzers. *Electrochim. Acta* **2016**, *222*, 44–57.

(81) An, S.; Zhang, G.; Wang, T.; Zhang, W.; Li, K.; Song, C.; Miller, J. T.; Miao, S.; Wang, J.; Guo, X. High-Density Ultra-Small Clusters and Single-Atom Fe Sites Embedded in Graphitic Carbon Nitride (g-C3N4) for Highly Efficient Catalytic Advanced Oxidation Processes. *ACS Nano* **2018**, *12* (9), 9441–9450.

(82) Li, X.; Dai, Y.; Ma, Y.; Han, S.; Huang, B. Graphene/g-C3N4 Bilayer: Considerable Band Gap Opening and Effective Band Structure Engineering. *Phys. Chem. Chem. Phys.* **2014**, *16* (9), 4230–4235.

(83) Ghosh, D.; Periyasamy, G.; Pati, S. K. Transition Metal Embedded Two-Dimensional C3N4–Graphene Nanocomposite: A Multifunctional Material. *J. Phys. Chem. C* **2014**, *118* (28), 15487–15494.

(84) Grundner, S.; Markovits, M. A. C.; Li, G.; Tromp, M.; Pidko, E. A.; Hensen, E. J. M.; Jentys, A.; Sanchez-Sanchez, M.; Lercher, J. A. Single-Site Trinuclear Copper Oxygen Clusters in Mordenite for Selective Conversion of Methane to Methanol. *Nat. Commun.* **2015**, *6* (1), 7546.

Chapter 2 - Quantum Mechanical Theory and Methods

2.1 Density Functional Calculations

Density functional theory (DFT) has proven to be a powerful method to extract accurate geometric, electronic, and catalytic information for energy and catalysis applications. DFT has already been used broadly to predict ground state molecular structures, total energies, charges, and many other physical properties of a targeted molecules or materials.[1] The discussion presented in this thesis focuses on the most relevant theoretical background, and the computational methods derived from DFT.

2.1.1 Kohn-Sham Formulation

Density functional theory (DFT) developed within the Kohn-Sham formulation (eq. 2.1),[2] including the effective potential term, v_{eff} (eq. 2.2), will be presented as the underlying theoretical foundation. In the K-S formulation, the total energy of an interacting inhomogeneous electron gas, in the presence of an external potential, is a function of the electron density, denoted as $\rho(r)$. Therefore, the calculation begins with an assumption of initial electron density for the calculations of the effective potential, followed by the construction of the Coulombic and exchange correlation potential in the Hamiltonian, which can be used to solve for a new electron density and total energy. Such a process is called self-consistent field, as indicated by Figure 2.1 by Shan et al.[1]

$$\left[-\frac{\hbar^2}{2m}\nabla_i{}^2 + v_{eff}(r)\right]\Psi_i(r) = \varepsilon_i\Psi_i(r) \tag{2.1}$$

$$v_{eff} = V_{en}(r) + \int \frac{\rho(r')}{|r-r'|}dr' + V_{xc}[\rho(r)] \tag{2.2}$$

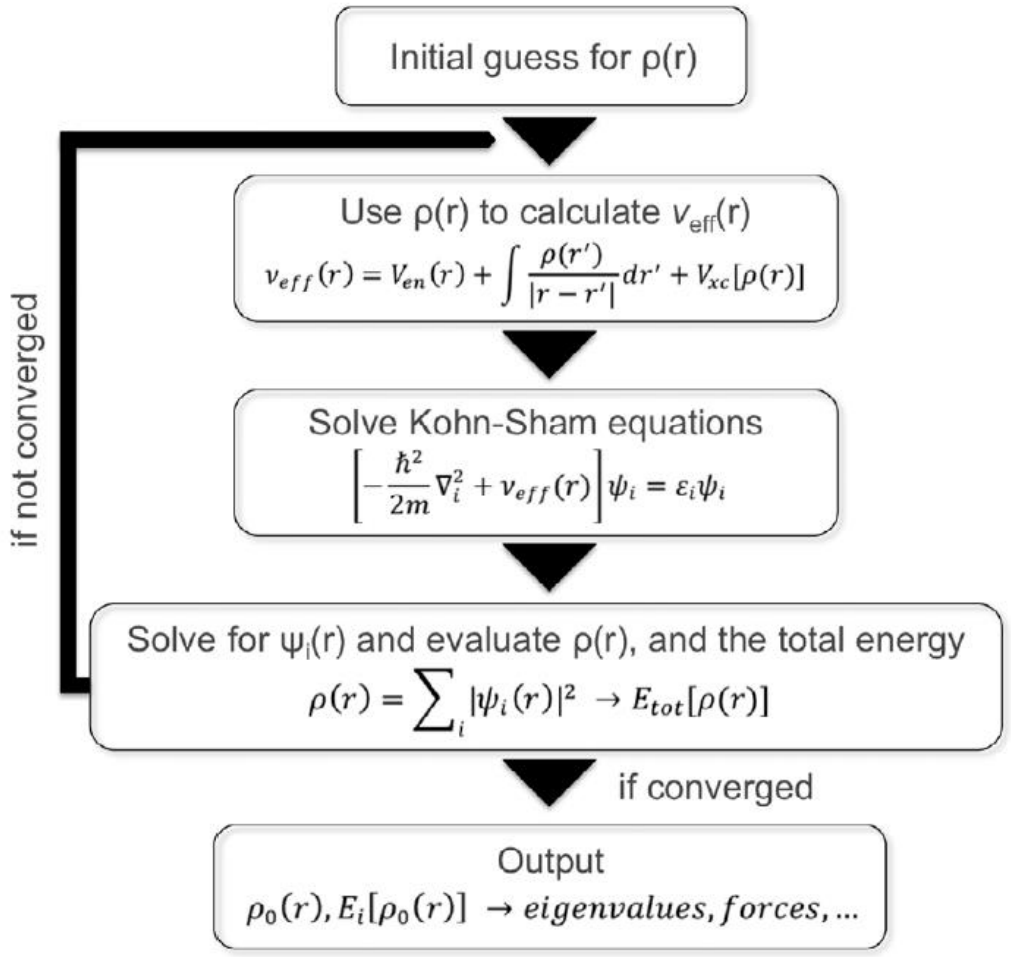


Figure 2.1. Iterative, self-consistent scheme to solve Kohn-Sham equations, adapted from Ref. [1].

2.1.2 Plane Wave Basis Set and Pseudopotential

In solid crystal systems, in order to manage the infinite number of interacting electrons in the static field of an infinite number of ions, Bloch's theorem is used to represent the wavefunction of an electron occupying a state of *k* in the first Brillouin zone of the crystal unit cell.[3] Therefore, the plane wave basis set is employed, which uses periodic functions to represent the wavefunctions in a periodic crystal lattice structure. Thus, the wavefunctions and can be written as eq. 2.3, where

$u_{\vec{k}}(\vec{r})$ is the periodic part of the wavefunction. In the reciprocal space, the wavefunctions can be further expanded to a finite number of plane waves whose wave vectors are reciprocal lattice vectors of the crystal, thus, the electronic wavefunction is written as a sum of plane waves, shown by eq. 2.4, where $\vec{G}$ is the lattice vector in the reciprocal space, $C_{i\vec{k}}(\vec{G})$ is the expansion coefficient corresponding to vector $\vec{G}$.

$$\psi_{\vec{k}}(\vec{r}) = e^{i\vec{k}\cdot\vec{r}} u_{\vec{k}}(\vec{r}) \tag{2.3}$$

$$\psi_{\vec{k}}(\vec{r}) = \sum_{\vec{G}} C_{i\vec{k}}(\vec{G})\, e^{i(\vec{k}+\cdot\vec{G})\cdot\vec{r}} \tag{2.4}$$

As seen in Figure 2.2, near the nuclei, the electron wavefunctions oscillate rapidly. Therefore, the all-electron calculations with full Coulombic potential can be extremely expensive. Since the chemical bonding and physical properties are dominated by the valence electrons, which are bonded more weakly than the core electrons, the assumption of frozen core and pseudopotential such as the projector augmented-wave method (PAW) method[4], can be adopted. As illustrated in Figure 2.2, the pseudopotential still represents all electron potential in the valance electron region (beyond r_c), which is important to obtain accurate atomic properties. The pseudopotential method dramatically decreases the number of plane wave basis sets needed to expand the wavefunction, which makes DFT calculations more manageable.

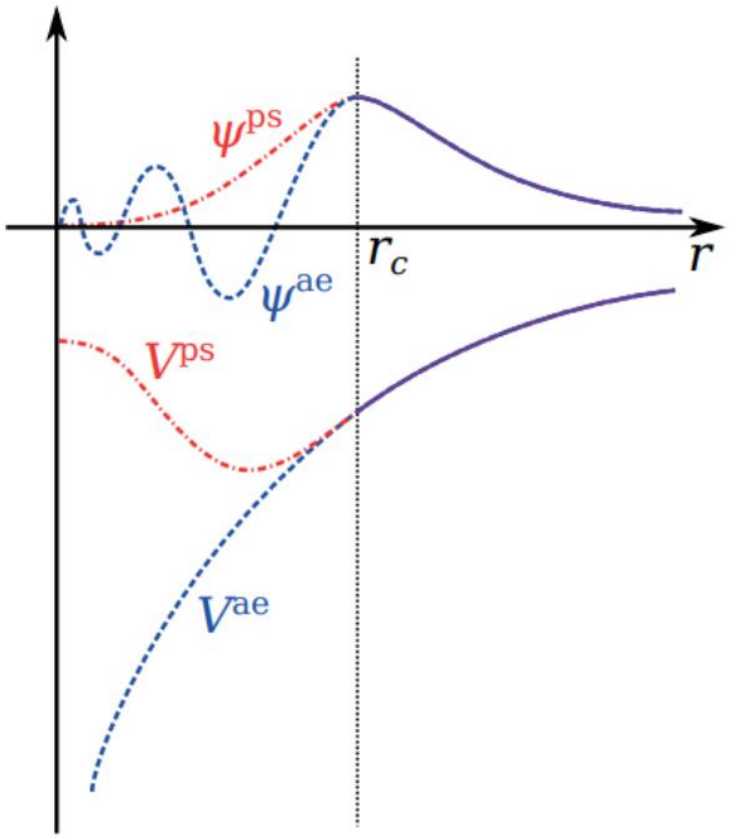


Figure 2.2. Pseudopotential compared with all electron potential. The pseudo wavefunction ψ^{ps} and pseudopotential V^{ps} (red) comparing with all electron wavefunction ψ^{ae} and all electron potential V^{ae} (blue) adapted from ref. [5].

2.1.3 Electron Exchange-Correlation Functional

To solve the Hohn-Sham equation (eq. 2.1), the electron exchange-correlation term (V_{xc}) in eq. 2.2 needs to be approximated. This term represents the interacting electronic kinetic energy and the corrections of Coulombic self-interactions.[1] Most commonly, the electron exchange-correlation effect can be accounted adequately using the generalized gradient approximation (GGA) theory,[6] which includes both the local electron density and the local gradient of electron density.

The gradient of electron density can be treated with several mathematical and physical variations, including Perdew-Burke-Ernzerhof (PBE),[6] Perdew-Wang (PW91)[7], and so on.

The PBE functional is very popular due to high accuracy to cost ratio for many systems, such as transition metals, surfaces, and interphases.[8] However, the PBE functional does not include long range dispersion forces, i.e. van der Waals interaction, which leads to significantly spurious self-interaction errors.[8] Thus in this thesis, the modified version of PBE functional with long range dispersion forces (PBE-D2[9] and PBE-D3[10]) and Bayesian error estimation functional with van der Waals (BEEF-vdW)[8] are employed.

Both PBE-D2 and PBE-D3 are modified version of PBE functional with an add-on energy term within Grimme's DFT-D2 and DFT-D3 methods. The DFT-D2 method considers all pairs of atoms,[9] while the DFT-D3 method further expand to account for the three-body effects[10]. In the study of ORR over Pt/VACNF (Chapter 3) and dual metal sites (Chapter 5), the DFT-D3 method was employed. However, in the investigation of ORR over g-C_3N_4 and its derived hetero-structures, DFT-D2 method was employed due to better interlayer spacing estimations compared with experimental values.

The BEEF-vdW functional is relatively new, and was derived using machine-learning methods to avoid pitfalls of semiempirical density functional development.[8] The development of this functional is based on regularization of a very flexible polynomial GGA exchange expansion. BEEF-vdW was generated using several training data set including solid state physics, surface chemistry, and vdW dominated interactions.[8] According to Zhao et al, [11] the quality of the calculated binding energies using BEEF-vdW shows comparable results to those obtained by a higher level of theory (hybrid HSE06), thus, BEEF-vdW is expected to be much more accurate than PBE coupled with DFT-D2 or the D3 method. Such functional also leads to an ensemble of

functionals around the optimum results, allowing an estimation of the computational error.[8] For the study of methane-to-methanol conversion in Chapter 6, the BEEF-vdW was employed to account for the primary interactions (i.e., van der Waals) during methane adsorption.

2.2 Molecular Dynamics

Molecular dynamics (MD) simulations can be employed to obtain the relaxed structure at nanometer length scale with much higher level of structural complexity. The structure of Pt NPs supported on VACNF was simulated using reactive MD simulation.

MD techniques describe atomic or molecular motion in classical N-particle systems by integrating Newton's equation of motion, as described by eq. 2.5, where $F_i(t)$ and $r_i(t)$ are the force and position vectors of particle *i* and time *t*. m_i represents the particle mass. This equation can be solved by using the velocity-Verlet algorithm,[12] to directly obtain the particle velocity and position at the next time step, $t + \Delta t$, as expressed by eqs. 2.6 and 2.7.

$$F_i(t) = m_i \frac{d^2 r_i(t)}{dt^2}, i = 1,2, \dots, N \tag{2.5}$$

$$v_i(t + \Delta t) = v_i(t) + \frac{F_i(t+\Delta t)+F_i(t)}{2m_i}\Delta t \tag{2.6}$$

$$r_i(t + \Delta t) = r_i(t) + v_i(t)\Delta t + \frac{F_i(t)}{2m_i}\Delta t^2 \tag{2.7}$$

The accuracy of the prediction from MD simulation highly depends on the accuracy of the force field. To model the chemical reactivity involving bond formation and breaking, the conventional force fields, such as UFF (Universal force field)[13] and AMBER (assisted model building and energy refinement)[14], are insufficient. Therefore, the ReaxFF[15] force field, which is a bond-order-based potential, will be employed in the MD simulations presented in this thesis (see Chapter 3).

2.3 Reaction Thermodynamics and Free Energy Diagram

The Gibbs free energy of each reaction intermediate can be estimated using eq. 2.8, where E_{DFT}, ZPE, and TS are the total energy obtained from DFT calculations, the zero-point energy, and the entropic term, respectively.[1] ZPE is essentially the ground state energy at 0 K in the vacuum[16], and it's normally expressed by eq. 2.9. The entropic term can be calculated using statistical mechanics, as suggested by McQuarrie[16]. Further, the adsorption energy and reaction free energy are calculated using eq. 2.10 and 2.11:

$$G = E_{DFT} + ZPE - TS \tag{2.8}$$

$$ZPE = \frac{1}{2}\sum_i hcv_i \tag{2.9}$$

$$\Delta G_{ad} = G_{total} - (G_{surf} + G_{gas}) \tag{2.10}$$

$$\Delta G = \sum G_{Products} - \sum G_{Reactants} \tag{2.11}$$

In this thesis work, ZPE and the entropic contribution was included to compute free energies for gas phase species; however, for the chemisorbed molecules (or states) the entropic contribution is small, hence it is neglected.

For heterogeneous catalysis, i.e. the selective oxidation of methane, the reactants, initially in the gas phase, are adsorbed onto solid catalysts. At the catalyst surface, eqs 2.10 and 2.11 can be directly used to calculate adsorption and reaction energies. However, for electrocatalysis, the pH effect, as well as the applied potential bias, needs to be considered.

2.3.1 Free Energy for Oxygen Reduction

For electrocatalysis, using oxygen reduction reaction (ORR) as an example, note that the adsorption free energies of O_2*, OOH*, O*, and OH*, denoted by $\Delta G_{O_2^*}$, ΔG_{OOH^*}, ΔG_{O^*}, and ΔG_{OH^*} were calculated based on eqs. (2.12 – 2.15), using μ_{H_2O} and μ_{H_2} as references:

$$\Delta G_{O_2^*} = E_{O_{2^*}} - E_* - (2\mu_{H_2O} - 2\mu_{H_2}) \quad (2.12)$$

$$\Delta G_{OOH^*} = E_{OOH^*} - E_* - (2\mu_{H_2O} - \frac{3}{2}\mu_{H_2}) \quad (2.13)$$

$$\Delta G_{O^*} = E_{O^*} - E_* - (\mu_{H_2O} - \mu_{H_2}) \quad (2.14)$$

$$\Delta G_{OH^*} = E_{OH^*} - E_* - (\mu_{H_2O} - \frac{1}{2}\mu_{H_2}) \quad (2.15)$$

ORR is a multistep process that takes place at the catalyst surface with charge transfer involved in each elementary step; therefore, the computational hydrogen electrode (CHE), proposed by Nørskov *et al.*,[17] was employed to account for the energy of proton-electron pairs. As indicated by eq. 2.16, the chemical potential of the proton-electron pair, $\mu(H^+ + e^-)$, is equivalent to the chemical potential of ½H_2 in gas phase, (i.e., ½$\mu(H_{2(g)})$), at all pH values, temperatures, and pressures. Also, the eU term accounts for the free energy resulting from the applied potential bias.

$$\mu(H^+ + e^-) = \frac{1}{2}\mu(H_{2(g)}) - eU \quad (2.16)$$

In order to account for the pH effect, eq. 2.17 is used.[17] Further, the reaction free energy involves applied potential and pH of the solvent can be calculated by eq. 2.18.

$$\Delta G_{pH} = -k_B T ln10 \times pH \quad (2.17)$$

$$\Delta G_{rxn} = \Delta G + neU + \Delta G_{pH} \quad (2.18)$$

2.3.2 Free Energy Diagram

All these computed adsorption energies and reaction energies are used to generate the reaction energy profile called the free energy diagram (FED), which can directly show the reaction thermodynamics of each elementary reaction step. According to the reaction thermodynamics presented by FED, it is possible to compare the catalytic activity of different catalyst materials on

the same chemical reaction, and it is also possible to predict the preferred byproduct of a chemical reaction as well.

2.4 Limiting Potentials and Overpotentials

To assess the ORR catalyst performance, the limiting potential (U_{lim}), also referred as the working potential[18–20] (or onset potential[21,22]), was employed in this thesis. U_{lim} represents the highest applied potential that keeps the reaction exothermic. Generally speaking, the higher the limiting potential, the higher the electrocatalytic activity.[17,18] As defined in eq. 2.19, U_{lim} can be found using the highest value for free energy change (or the least exothermic step involving charge transfer) divided by the number of charges being transferred during that elementary step. Furthermore, the overpotential (η_{lim}) can then be expressed by eq. 2.20, where $E_{eq,ORR}$ is the equilibrium potential for ORR, 1.23 V in acidic condition or 0.402 V in alkaline condition.[23]

$$U_{lim} = -\frac{max[\Delta G_1, \Delta G_2, \Delta G_3, \Delta G_{4,\dots}]}{ne} \tag{2.19}$$

$$\eta_{lim} = E_{eq,ORR} - U_{lim} \tag{2.20}$$

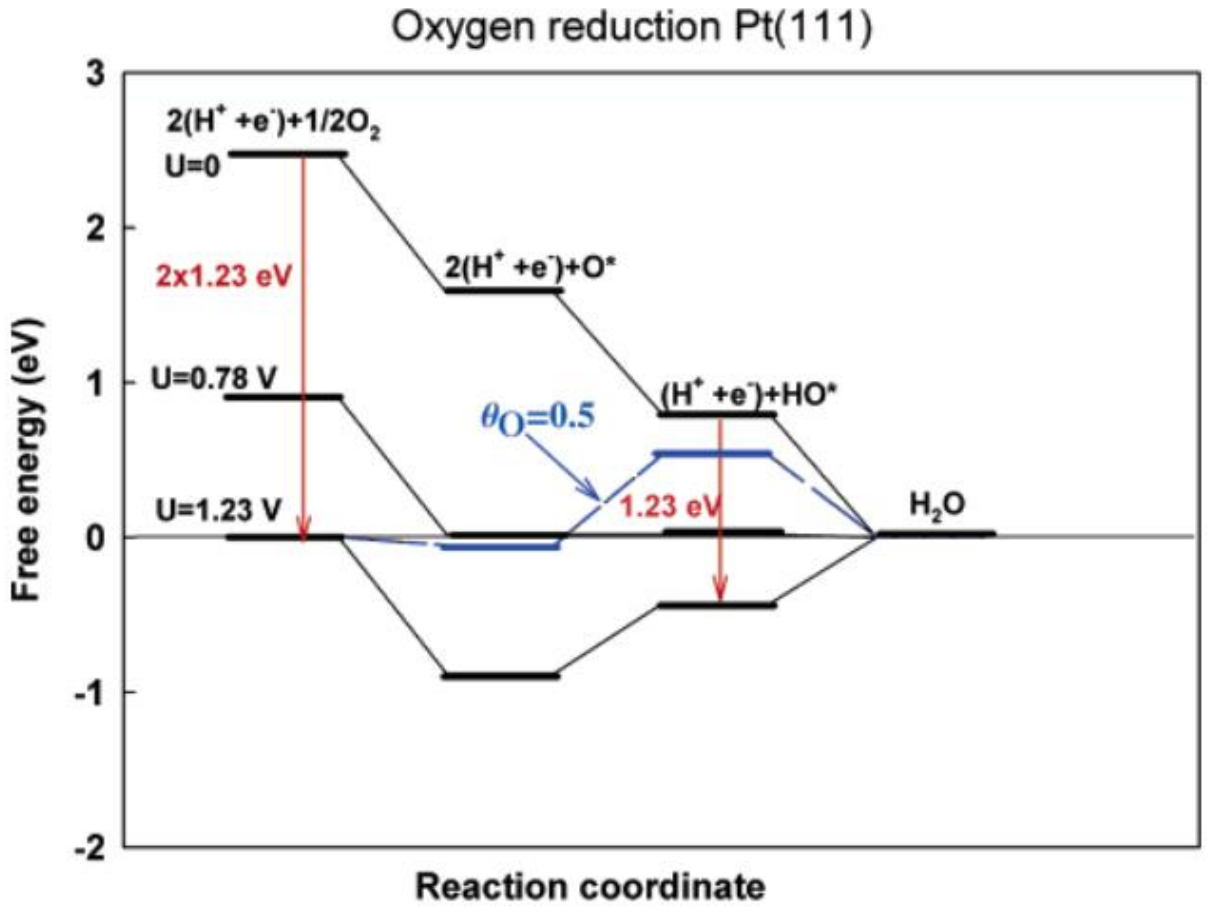


Figure 2.3. Free energy diagram of ORR on Pt (111) via the associative mechanism under applied potentials of 0 , 0.78 and 1.23 V, adapted form Ref [17].

As shown in Figure 2.3, ORR over Pt surfaces, when the free energy contribution from applied potential is not considered, where U = 0 V, the charge transfer steps are exothermic. However, by applying a positive potential bias (according to eq. 2.18), each elementary reaction step involves charge transfer become less exothermic. At U = 0.78 V, the reaction step of converting O* to OH* becomes thermal neutral, indicating 0.78 V is the limiting potential, according to eq. 2.19, since it is the highest applied potential that keeps the overall reaction exothermic. By employing eq. 2.20, the overpotential is estimated to be 1.23 - 0.78 = 0.45 V. At

the theoretical equilibrium potential, U = 1.23 V, the FED shows two endothermic steps involves charge transfer, indicating the reaction is not favored.

2.5 Transition State Search

A number of transition state search techniques are available and have been summarized by Henkelman et al.[24] If the initial and final states of an elementary step are given, the climbing image nudged elastic band (CI-NEB)[25], and coupled with the DIMER method[26], can be employed for the transition state search to obtain the energy barrier. The reaction energy barriers reported in this thesis were all done using this strategy.

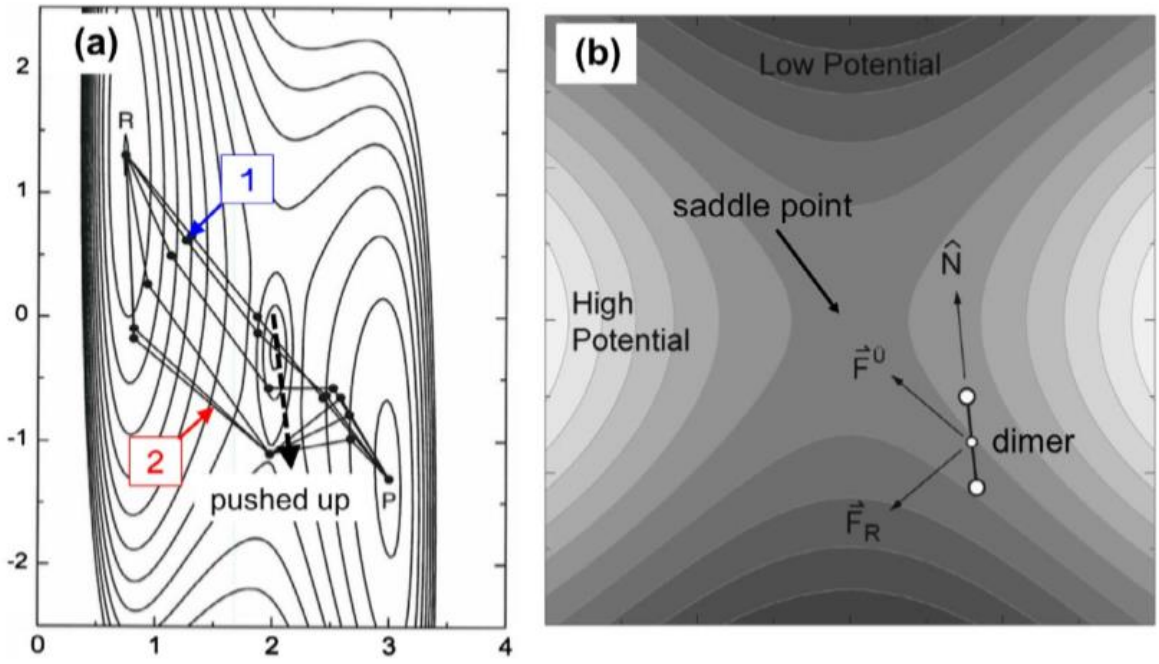


Figure 2.4. The transition state (or saddle point) search scheme using (a) NEB method and (b) DIMER method, adapted from Ref. [1]

2.5.1 CI-NEB method

NEB method is typically used to optimize a string of images (or geometric interpolations) between the known reactant (R) and product (P). As shown in Figure 2.4a, the initial structures are generated using simple linear interpolation of R and P; and subsequent optimization, NEB method, will be used to relax this series of structures to find its real minimum energy pathways and converge to the saddle point (transition state). The CI-MEB method constitutes a small feature compare to regular NEB, that is, during the relaxation, CI-NEB can move the highest energy image towards the energy uphill, with the tangential forces turned off. Thus, the image with the highest energy maximizes its energy along the tangential direction of the band, while minimizing the energies in all other directions. As the CI-NEB method completes, the image for the transition state converges to the saddle point.

However, CI-NEB is computationally expensive. In this thesis, CI-NEB method is only used to perform transition state search to obtain an estimated transition state, then, the DIMER method is used to calculate the transition state energy and energy barrier.

2.5.2 DIMER method

Finding saddle point using DIMER method requires two images of the system (or a 'dimer'). Such method is developed based on the eigenvector-following theory, while using only the first derivatives of the potential energy.[1,26] During the saddle point search, the dimer is moved uphill on the potential energy surface; along the way, the dimer is rotated to find the lowest curvature mode ($\widehat{N}$) of the potential energy where the saddle point is located. As illustrated by Figure 2.4b, the dimer image is moved to the saddle point by an effective force ($\vec{F}^u$), which is caused by the true force ($\vec{F}_g$) and $\widehat{N}$.

The DIMER method does not require evaluations of the Hessian matrix; therefore, the computational cost is much lower than the NEB method. As a matter of fact, the DIMER method provides a convenient solution to find the minimum energy pathway and transition state energy. Thus, the coupled CI-NEB and DIMER has become a more efficient approach for transition state search, where CI-NEB provides the initial guess of the transition state; then DIMER uses the initial guess to reveal the true transition state.

2.6 Empirical Computational Methods

For the purpose of catalyst design, the empirical scaling relationships are very important. Such scaling relationship can be used as a guidance to fast screen, design, and develop highly efficient catalysts.[19] By employing scaling relationships, it is feasible to explore a broad range of materials at low cost; for this reason, this approach has been established and well-integrated in computational catalysis. These relationships can also be helpful to construct and understand the kinetic-based volcano plot.

2.6.1 Brønsted–Evans–Polanyi Relationship

In computational heterogeneous catalysis, the transition state search remains a computationally intensive task. In 2002, Nørskov et al.[27] noted that a linear relationship exist between the reaction energies and the energy barriers during the activation of simple molecules (e.g., CO, O_2, and N_2). Such relationships were quickly established and known as the Brønsted-Evans-Polanyi (BEP) relationship.[28–31] Nørskov et al. also pointed out that, since the transition state structure has already lost its molecular identity, the variations in the transition state energy will follow that of the final state energy, resulting in a linear relationship with a slope close to one.[27]

The BEP relationships have become extremely useful for providing the data needed for kinetic models and offers an empirical approach to estimating kinetic values without performing transition state search using quantum mechanical methods (e.g., NEB or dimer).

2.6.2 Linear Scaling for Molecular Adsorptions

Another type of linear scaling relationship that has been widely employed in computational electrocatalysis is the linear scaling within adsorption energies of reaction intermediates. Such correlation can be used to achieve catalyst design via the descriptor-based approach.[32] The slope of the linear scaling is determined by the bonding types of the chemisorption, which is known as bond order conservation rules.[32,33] For example, the adsorption energies for OOH*, O*, and OH* in ORR are strongly correlated, as shown in Figure 2.5, and change monotonically for different materials. Such strongly correlated linear scaling are due to the adsorbates binding through an O atom.[34] The slope for ΔG_{OOH^*} vs $\Delta G_{OH^*}$is 1, indicating both adsorbates bind to surfaces via metal-oxygen single bond. In contrast, ΔG_{OOH^*} vs ΔG_{O^*} has a slope of 2, meaning O* species binds to metal surface via metal-oxygen double bond. Since, ORR activity evaluation is based on limiting potential, that is derived from adsorption energies, thus, such linear scaling between adsorption energies can provide guidance to future catalyst design and development.

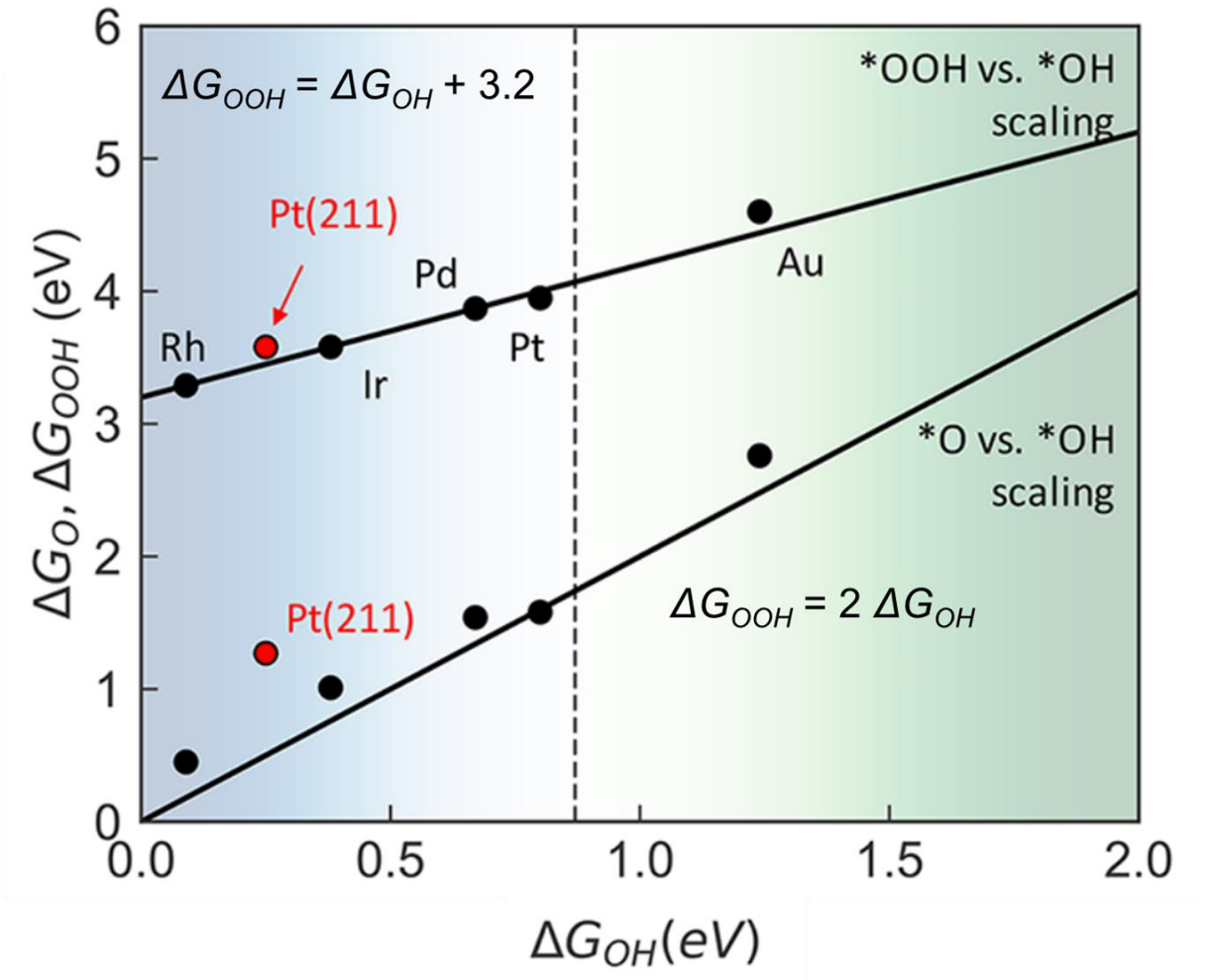


Figure 2.5. Linear scaling within adsorption energies of ORR reaction intermediates adapted from Ref. [34].

2.7 *d*-Band Theory

The electronic structure of transition metal surfaces plays an important role on their catalytic activities.[35–39] According to Nilsson et al.[38], during chemisorption, the valence band will inevitably couple with the *s* states of the metal surface; thus, the different catalytic functions will only rely on the *d* states. As a result, the bonding and antibonding states are formed due to the interactions between the adsorbate electronic states with a narrow distribution of *d*-states, as illustrated in Figure 2.6. When chemisorption takes place on a metal surface, the occupancy of *d*-

state is full, and the bond strength is dependent upon the filling of the antibonding state, which varies with the metal in question.[35,38] Since the antibonding states are always higher than *d*-states, the energy of the *d*-states relative to the Fermi level can be used as an indicator of the bond strength.

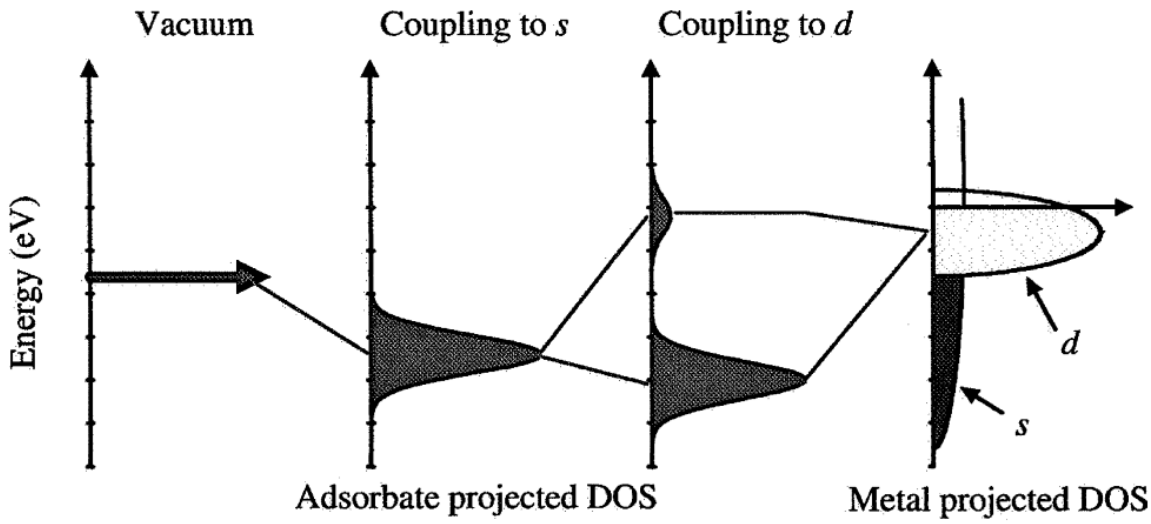


Figure 2.6. Schematic illustrations of bond formation between an adsorbate valence level and the *s* and *d* states of a transition metal surface, adapted from Ref. [38].

The adsorption trend has been established on transition metals according to the *d*-band theory. Figure 2.7 shows that, as the *d*-band center shifts closer to Fermi level, a stronger adsorption energy is expected and vice versa. Hence, the engineering of the *d*-band of catalytic materials has been a primary target to achieve catalyst design.

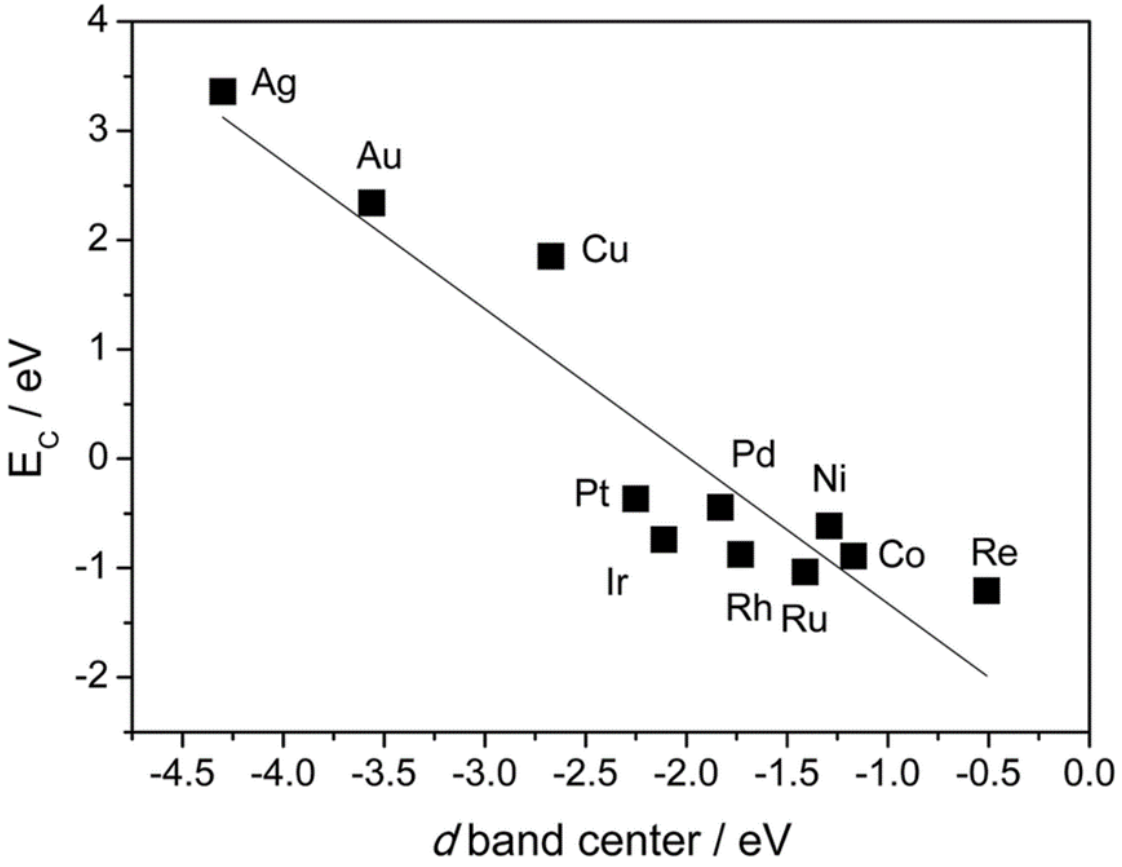


Figure 2.7. Binding energies of atomic carbon as a function of the transition metal *d*-band centers, adapted from Ref. [40].

2.8 Bader Charge Analysis

The charge redistribution at the local environment of the active site can greatly influence the catalytic activity.[41,42] As shown in Figure 2.8, Bader charge analysis[43–45] showed the methane activation over clean α-Fe_2O_3 (0001) surface is facilitated by electron back donation from catalyst surface to H1 (charge accumulation at H1)[46]. Therefore, Bader charge analysis can be used to reveal charge redistribution or charge transfer over a catalyst material, based on the original concept proposed by Richard Bader[47]. Such an approach can approximate the electronic charge density by dividing space within molecular systems into atomic volume using charge density. The electronic charge density can be used to partition molecular system into different sections based

on zero flux surfaces, a 2-D surface with a minimum charge density that is normal to the surface; thus the volume of each section is the occupation volume of each corresponding atomic species. Such approach can reveal the charges carried at the active site, and the interactions with its surrounding local environment. Further, Bader charge may also be used as a descriptor for catalyst screening and design purposes.

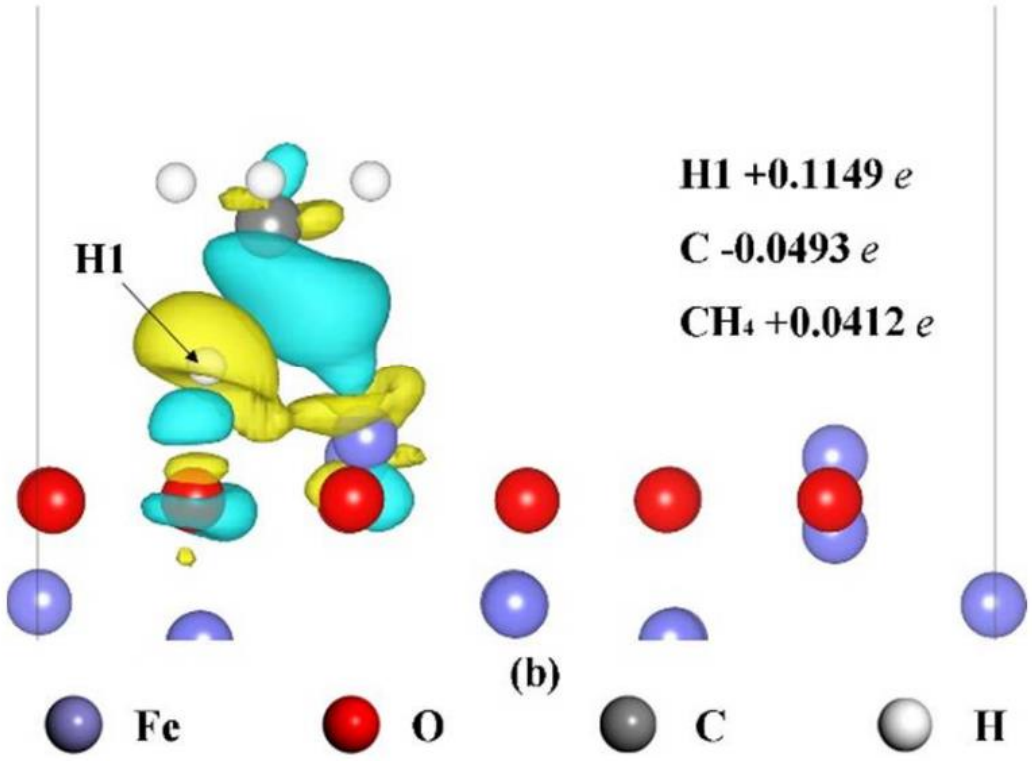


Figure 2.8. Bader charge analysis on methane activation over Fe_2O_3 (0001) surface. Charge accumulation and depletion are colored yellow and blue. Adapted from Ref. [46]

References

(1) Shan, N.; Zhou, M.; Hanchett, M. K.; Chen, J.; Liu, B. Practical Principles of Density Functional Theory for Catalytic Reaction Simulations on Metal Surfaces – from Theory to Applications. *Mol. Simul.* **2017**, *43* (10–11), 861–885.

(2) Kohn, W.; Sham, L. J. Self-Consistent Equations Including Exchange and Correlation Effects. *Phys. Rev.* **1965**, *140* (4A), A1133–A1138.

(3) Fujita, S.; Ito, K. Bloch Theorem BT - Quantum Theory of Conducting Matter: Newtonian Equations of Motion for a Bloch Electron; Fujita, S., Ito, K., Eds.; Springer New York: New York, NY, 2007; pp 85–95.

(4) Kresse, G.; Joubert, D. From Ultrasoft Pseudopotentials to the Projector Augmented-Wave Method. *Phys. Rev. B* **1999**, *59* (3), 1758–1775.

(5) Kocevski, V. *Theory and Modeling of Functional Materials*; 2015.

(6) Perdew, J. P.; Burke, K.; Ernzerhof, M. Generalized Gradient Approximation Made Simple. *Phys. Rev. Lett.* **1996**, *77* (18), 3865–3868.

(7) Perdew, J. P.; Wang, Y. Accurate and Simple Analytic Representation of the Electron-Gas Correlation Energy. *Phys. Rev. B* **1992**, *45* (23), 13244–13249.

(8) Wellendorff, J.; Lundgaard, K. T.; Møgelhøj, A.; Petzold, V.; Landis, D. D.; Nørskov, J. K.; Bligaard, T.; Jacobsen, K. W. Density Functionals for Surface Science: Exchange-Correlation Model Development with Bayesian Error Estimation. *Phys. Rev. B* **2012**, *85* (23), 235149.

(9) Grimme, S. Semiempirical GGA-Type Density Functional Constructed with a Long-Range Dispersion Correction. *J. Comput. Chem.* **2006**, *27* (15), 1787–1799.

(10) Grimme, S.; Antony, J.; Ehrlich, S.; Krieg, H. A Consistent and Accurate Ab Initio Parametrization of Density Functional Dispersion Correction (DFT-D) for the 94 Elements H-Pu. *J. Chem. Phys.* **2010**, *132* (15), 154104.

(11) Zhao, Z.-J.; Kulkarni, A.; Vilella, L.; Nørskov, J. K.; Studt, F. Theoretical Insights into the Selective Oxidation of Methane to Methanol in Copper-Exchanged Mordenite. *ACS Catal.* **2016**, *6* (6), 3760–3766.

(12) Verlet, L. Computer "Experiments" on Classical Fluids. I. Thermodynamical Properties of Lennard-Jones Molecules. *Phys. Rev.* **1967**, *159* (1), 98–103.

(13) Rappe, A. K.; Casewit, C. J.; Colwell, K. S.; Goddard, W. A.; Skiff, W. M. UFF, a Full Periodic Table Force Field for Molecular Mechanics and Molecular Dynamics Simulations. *J. Am. Chem. Soc.* **1992**, *114* (25), 10024–10035.

(14) Weiner, P. K.; Kollman, P. A. AMBER: Assisted Model Building with Energy Refinement. A General Program for Modeling Molecules and Their Interactions. *J. Comput. Chem.* **1981**, *2* (3), 287–303.

(15) van Duin, A. C. T.; Dasgupta, S.; Lorant, F.; Goddard, W. A. ReaxFF: A Reactive Force

Field for Hydrocarbons. *J. Phys. Chem. A* **2001**, *105* (41), 9396–9409.

(16) McQuarrie, D. A. *Statistical Mechanics*, Viva Studn.; Bruce Armbruster, 2011.

(17) Nørskov, J. K.; Rossmeisl, J.; Logadottir, A.; Lindqvist, L.; Kitchin, J. R.; Bligaard, T.; Jónsson, H. Origin of the Overpotential for Oxygen Reduction at a Fuel-Cell Cathode. *J. Phys. Chem. B* **2004**, *108* (46), 17886–17892.

(18) Meng, Y.; Yin, C.; Li, K.; Tang, H.; Wang, Y.; Wu, Z. Improved Oxygen Reduction Activity in Heteronuclear FeCo-Codoped Graphene: A Theoretical Study. *ACS Sustain. Chem. Eng.* **2019**, *7* (20), 17273–17281.

(19) Zhao, J.; Wang, W.; Qu, X.; Meng, Y.; Wu, Z. M-Porphyrin (M = Mn, Co) Carbon Materials as Oxygen Reduction Catalysts from Density Functional Studies. *Mol. Phys.* **2019**, 1–9.

(20) Liu, S.; Cheng, L.; Wang, W.; Li, K.; Wang, Y.; Wu, Z. Fe-Porphyrin Carbon Matrix as a Bifunctional Catalyst for Oxygen Reduction and CO2 Reduction from Theoretical Perspective. *Mol. Phys.* **2019**, *117* (14), 1805–1812.

(21) Nagaprasad Reddy, S.; Krishnamurthy, C. B.; Grinberg, I. First-Principles Study of the Ligand Substituent Effect on ORR Catalysis by Metallocorroles. *J. Phys. Chem. C* **2020**, *124* (21), 11275–11283.

(22) Hunter, M. A.; Fischer, J. M. T. A.; Yuan, Q.; Hankel, M.; Searles, D. J. Evaluating the Catalytic Efficiency of Paired, Single-Atom Catalysts for the Oxygen Reduction Reaction. *ACS Catal.* **2019**, *9* (9), 7660–7667.

(23) Lee, C. H. Theoretical Basis of Electrocatalysis; Pati, Ed.; IntechOpen: Rijeka, 2018; p Ch. 1.

(24) Henkelman, G.; Jóhannesson, G.; Jónsson, H. Methods for Finding Saddle Points and Minimum Energy Paths BT - Theoretical Methods in Condensed Phase Chemistry; Schwartz, S. D., Ed.; Springer Netherlands: Dordrecht, 2002; pp 269–302.

(25) Henkelman, G.; Uberuaga, B. P.; Jónsson, H. A Climbing Image Nudged Elastic Band Method for Finding Saddle Points and Minimum Energy Paths. *J. Chem. Phys.* **2000**, *113* (22), 9901–9904.

(26) Henkelman, G.; Jónsson, H. A Dimer Method for Finding Saddle Points on High Dimensional Potential Surfaces Using Only First Derivatives. *J. Chem. Phys.* **1999**, *111* (15), 7010–7022.

(27) Nørskov, J. K.; Bligaard, T.; Logadottir, A.; Bahn, S.; Hansen, L. B.; Bollinger, M.; Bengaard, H.; Hammer, B.; Sljivancanin, Z.; Mavrikakis, M.; Xu, Y.; Dahl, S.; Jacobsen, C. J. H. Universality in Heterogeneous Catalysis. *J. Catal.* **2002**, *209* (2), 275–278.

(28) Cheng, J.; Hu, P.; Ellis, P.; French, S.; Kelly, G.; Lok, C. M. Brønsted−Evans−Polanyi Relation of Multistep Reactions and Volcano Curve in Heterogeneous Catalysis. *J. Phys. Chem. C* **2008**, *112* (5), 1308–1311.

(29) Liu, Z.-P.; Hu, P. General Trends in CO Dissociation on Transition Metal Surfaces. *J. Chem.*

Phys. **2001**, *114* (19), 8244–8247.

(30) Logadottir, A.; Rod, T. H.; Nørskov, J. K.; Hammer, B.; Dahl, S.; Jacobsen, C. J. H. The Brønsted–Evans–Polanyi Relation and the Volcano Plot for Ammonia Synthesis over Transition Metal Catalysts. *J. Catal.* **2001**, *197* (2), 229–231.

(31) Pallassana, V.; Neurock, M. Electronic Factors Governing Ethylene Hydrogenation and Dehydrogenation Activity of Pseudomorphic PdML/Re(0001), PdML/Ru(0001), Pd(111), and PdML/Au(111) Surfaces. *J. Catal.* **2000**, *191* (2), 301–317.

(32) Wang, Y.; Montoya, J. H.; Tsai, C.; Ahlquist, M. S. G.; Nørskov, J. K.; Studt, F. Scaling Relationships for Binding Energies of Transition Metal Complexes. *Catal. Letters* **2016**, *146* (2), 304–308.

(33) Abild-Pedersen, F.; Greeley, J.; Studt, F.; Rossmeisl, J.; Munter, T. R.; Moses, P. G.; Skúlason, E.; Bligaard, T.; Nørskov, J. K. Scaling Properties of Adsorption Energies for Hydrogen-Containing Molecules on Transition-Metal Surfaces. *Phys. Rev. Lett.* **2007**, *99* (1), 16105.

(34) Kulkarni, A.; Siahrostami, S.; Patel, A.; Nørskov, J. K. Understanding Catalytic Activity Trends in the Oxygen Reduction Reaction. *Chem. Rev.* **2018**, *118* (5), 2302–2312.

(35) Nørskov, J. K.; Abild-Pedersen, F.; Studt, F.; Bligaard, T. Density Functional Theory in Surface Chemistry and Catalysis. *Proc. Natl. Acad. Sci.* **2011**, *108* (3), 937 – 943.

(36) Nørskov, J. K. Electronic Factors in Catalysis. *Prog. Surf. Sci.* **1991**, *38* (2), 103–144.

(37) Hammer, B.; Nørskov, J. K. Electronic Factors Determining the Reactivity of Metal Surfaces. *Surf. Sci.* **1995**, *343* (3), 211–220.

(38) Nilsson, A.; Pettersson, L. G. M.; Hammer, B.; Bligaard, T.; Christensen, C. H.; Nørskov, J. K. The Electronic Structure Effect in Heterogeneous Catalysis. *Catal. Letters* **2005**, *100* (3), 111–114.

(39) Hammer, B.; Norskov, J. K. Why Gold Is the Noblest of All the Metals. *Nature* **1995**, *376* (6537), 238–240.

(40) Zhao, Z.-J.; Chiu, C.; Gong, J. Molecular Understandings on the Activation of Light Hydrocarbons over Heterogeneous Catalysts. *Chem. Sci.* **2015**, *6* (8), 4403–4425.

(41) Zhu, Y.; Sokolowski, J.; Song, X.; He, Y.; Mei, Y.; Wu, G. Engineering Local Coordination Environments of Atomically Dispersed and Heteroatom-Coordinated Single Metal Site Electrocatalysts for Clean Energy-Conversion. *Adv. Energy Mater.* **2019**, 1902844.

(42) He, Y.; Liu, S.; Priest, C.; Shi, Q.; Wu, G. Atomically Dispersed Metal–Nitrogen–Carbon Catalysts for Fuel Cells: Advances in Catalyst Design, Electrode Performance, and Durability Improvement. *Chem. Soc. Rev.* **2020**.

(43) Henkelman, G.; Arnaldsson, A.; Jónsson, H. A Fast and Robust Algorithm for Bader Decomposition of Charge Density. *Comput. Mater. Sci.* **2006**, *36* (3), 354–360.

(44) Sanville, E.; Kenny, S. D.; Smith, R.; Henkelman, G. Improved Grid-Based Algorithm for Bader Charge Allocation. *J. Comput. Chem.* **2007**, *28* (5), 899–908.

(45) Tang, W.; Sanville, E.; Henkelman, G. A Grid-Based Bader Analysis Algorithm without Lattice Bias. *J. Phys. Condens. Matter* **2009**, *21* (8), 84204.

(46) Tang, J.-J.; Liu, B. Reactivity of the Fe2O3(0001) Surface for Methane Oxidation: A GGA + U Study. *J. Phys. Chem. C* **2016**, *120* (12), 6642–6650.

(47) Bader, R. F. W. *Atoms in Molecules: A Quantum Theory*; Clarendon Press, 1994.

Chapter 3 - Molecular Models for Platinum ORR Catalyst on Multi-Edged Carbon Supports

Chapter 2 is partially reproduced with permission from:

Elangovan, A.; Xu, J.; Brown, E.; Liu, B.; Li, Jun., "Fundamental Electrochemical Insights of Vertically Aligned Carbon Nanofiber Architecture as a Catalyst Support for ORR", Journal of the Electrochemical Society, 2020, 167, 066523.

3.1 Introduction

Fuel cells are attractive power generating devices that can convert chemical energy into electricity. The cathodic oxygen reduction reaction (ORR), eqs. 3.1 and 3.2 in both acidic and alkaline conditions, is kinetically sluggish and is a critical rate limiting factor due to the strong O=O bond, 498 kJ/mol.[1] ORR directly limits the overall fuel cell performance, i.e., high over-potential and low power density.[2–4]

$$O_2(g) + 4H^+ + 4e^- \rightarrow 2H_2O, \qquad \Delta G_{Ph=1} = -4.92\ eV \tag{3.1}$$

$$O_2(g) + 2H_2O + 4e^- \rightarrow 4OH^-(aq), \qquad \Delta G_{Ph=13} = -0.402\ eV \tag{3.2}$$

Platinum (Pt) supported on Vulcan carbon (Pt/C) has exhibited one of the highest ORR activities, and is frequently used as a standard bearer for subsequent catalyst development.[5] However, its scarcity hinders wide applications. The Department of Energy (DOE) has thus set a target of less than 0.125 mg/cm^2 for Pt usage since 2015.[6] Driven by this goal, a lot of research also aims to develop effective and functional catalyst supports that better stabilize small Pt particles to reduce Pt usage and also help enhance Pt reactivity.[4,7–10]

At high electrode potentials, carbon support corrosion and catalyst dissolution occurs and result in severe deterioration of ORR performance.[11–13] Graphitic catalyst supports such as graphene, carbon nanotubes, and carbon nanofibers are stable in the presence of oxygen at typical ORR operating conditions.[14–21]

Debe *et al.*[7–9] demonstrated that vertically aligned carbon structures are capable of stabilizing small Pt nanoparticles (NPs). As illustrated in Figure 3.1, vertically aligned carbon nanofibers (VACNFs) are stacked conical architectures with high edge densities. It is hypothesized that these edges support and stabilize sputtered Pt particles (typically on the few-nanometer scale) thanks to the strong Pt–C bonding. The increased stability prolongs Pt lifetime. The dispersity of Pt catalyst particles helps lower the ultimate Pt usage.

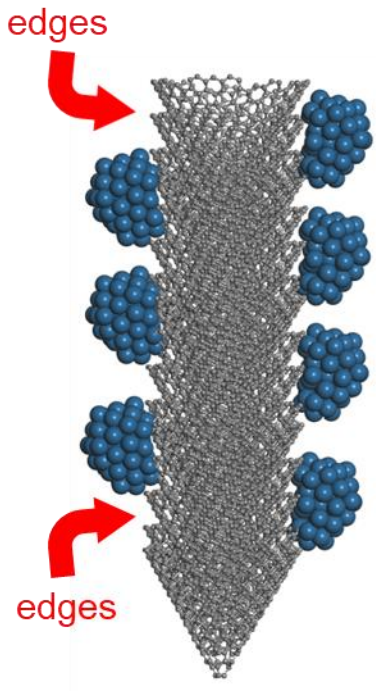


Figure 3.1. Schematic illustration of Pt/VACNF. Color code: gray-C, blue-Pt.

Recently, Elangovan *et al.*[22] synthesized VACNFs (Figure 3.2 a and b) using plasma enhanced chemical vapor deposition (PECVD). Afterwards, Pt particles were deposited using a high-resolution ion beam coater (Figure 3.2 c). The average diameter of these particles is approximately 1.1 nm. Linear sweeping voltammetry (Figure 3.2 d) indicates that the current density (J, mA/cm^2) obtained from Pt/VACNF (dark purple) is higher than Pt/C (magenta). This behavior was later found due to the improved O_2 mass transport facilitated exactly by the vertically stacked conical architecture. However, the half-wave potential ($E_{1/2}$), obtained using Pt/VACNF shifts toward left by 0.04 V (relative to Pt/C), an indication of lower ORR reactivity. This left-shift of half-wave potential, however, cannot be directly understood from electrochemical measurements.

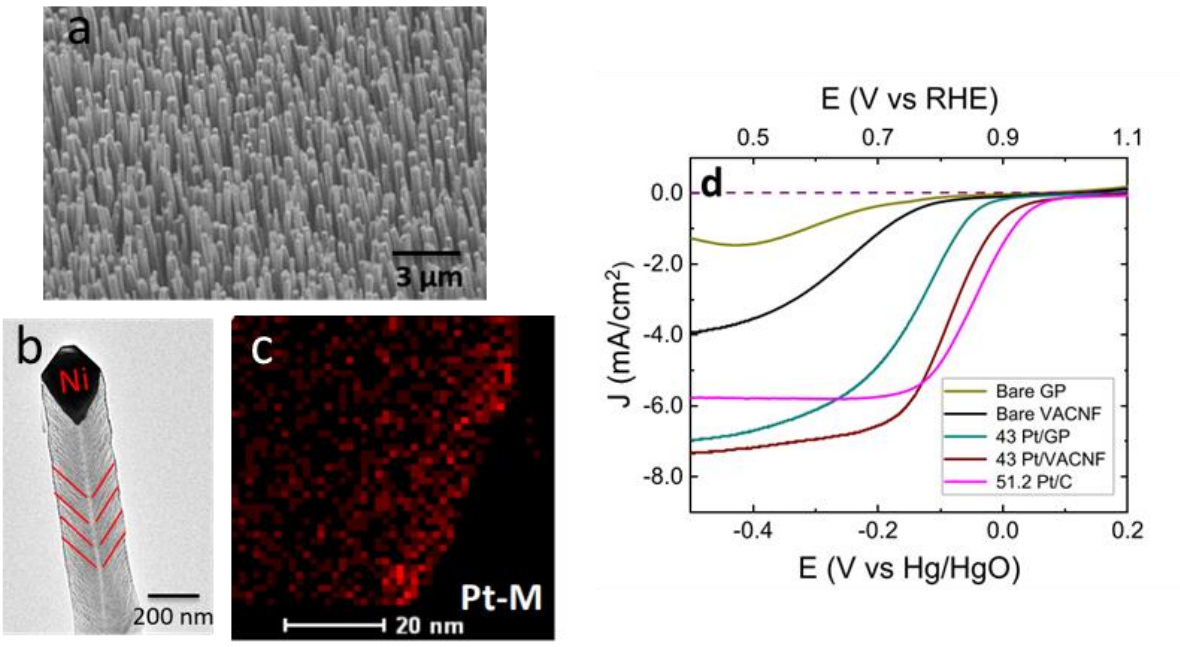


Figure 3.2. FESEM images of VACNF (a), TEM image of VACNF (b) and EDS elemental mapping on Pt/VACNF (c), and linear sweeping voltammetry for ORR over bare-VACNF and Pt/VACNF comparing with Pt/C (d). Adapted from Ref. [22].

Despite the high ORR activity of Pt/C, the nanoparticle size can influence the ORR activity.[23] The specific ORR activity increases by up to several-fold as Pt particles grow from 1.3 nm, then the activity levels off as the particle size reaches ~2.2 nm.[23] Computationally, the Pt(111) plane is considered as the dominant facet that determines the ORR activity with such Pt particles diameters.[23,24] Based on Density Functional Theory (DFT) calculations, Nørskov *et al*.[24] revealed that ORR undergoes the associative mechanism, i.e., O-O bond cleavage upon the formation of OOH*, on its (111) facet. The limiting potential for this process is predicted to be 0.78 V, corresponding to the potential limiting step (PLS) of O*-to-OH* conversion.

For even smaller particles, e.g., sputtered Pt on VACNF, the ORR reactivity could be more sensitive to the surface structures of Pt NPs.[25,26] At such length scale, the VACNF support is also likely to influence ORR occurring on the Pt sites. In fact, the structures of catalyst particles are widely recognized as an influencing factor for catalytic activities. The nano-catalyst size and shape effects that directly influence the chemisorption and catalytic activity were comprehensively summarized by Cuenya *et al*.[25] What remains elusive is how the *chemically stable* carbon support impacts the geometric and catalytic characters of Pt catalysts.

To better understand the Pt-carbon support interactions, Cheng *et al*.[27] employed molecular dynamics (MD) simulations to model Pt NPs of varying sizes mechanically supported on carbon nanofibers. This work revealed that Pt NPs clearly prefer the open carbon edges and confirmed our initial hypothesis. Furthermore, coordination number, defined as the numbers of nearest atoms to an active site, was used for structural analysis. Cheng *et al*.[27] also showed that the average coordination number of the outermost shell increases logarithmically with the particle size increases (Figure 3.3), i.e., a higher fraction of low coordinated surface sites on smaller particles.

These low-coordinated Pt sites typically bind O, OH, and OOH (i.e., the common ORR intermediates) stronger than on flat Pt single crystalline surfaces, e.g., Pt(111).[25,28,29]

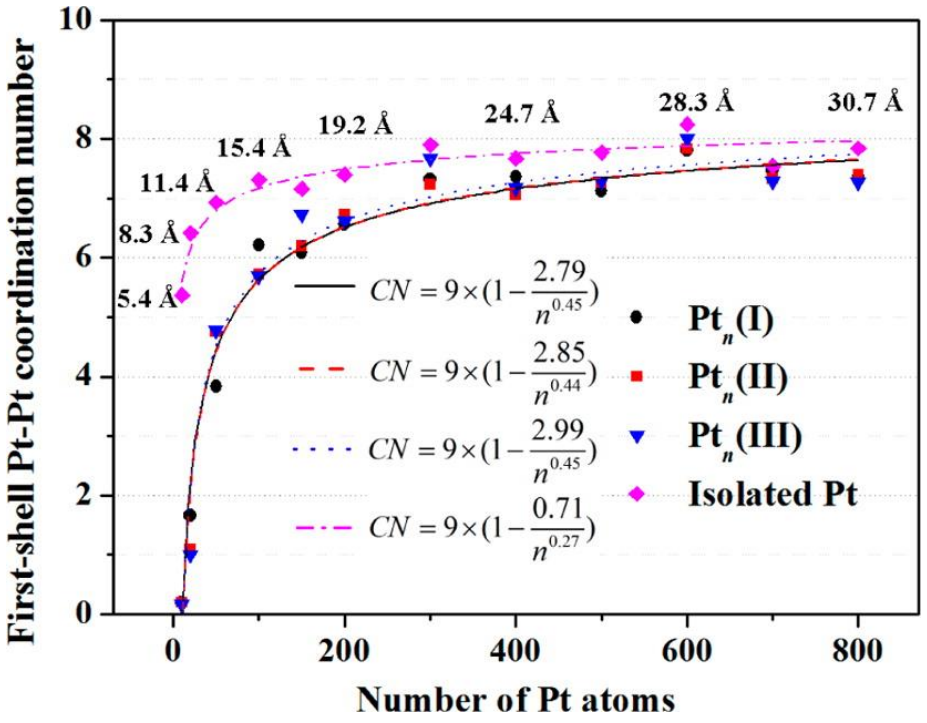


Figure 3.3. Relationship between the mean first-shell Pt-Pt coordination number of surface Pt atoms and the number of atoms in supported and isolated Pt particles. Adapted from Ref.[27].

Recent theoretical work by Calle-Vallejo *et al.*[28,29] further revealed a set of linear correlations to quantify the adsorbate binding energies by introducing the so-called generalized coordination numbers ($\overline{CN}$) concept. As shown in Figure 3.4, the adsorption energies of OOH and OH both follow linear relationships with $\overline{CN}$, as represented by eq. 3.3,

$$\overline{CN}(i) = \sum_{j=1}^{n_i} cn(j)n_j / cn_{max} \qquad (3.3)$$

where the neighboring atom i is accounted with a weight of n_j/cn_{max}. For an fcc crystal, the cn_{max} for the top site is 12. Thus, $\overline{CN}$ for the Pt top site in the (111) facet will be $\overline{CN}$ = (9 × 6 + 12 × 3)/12 = 7.5, meaning that the top site is coordinated by six nearest neighbor atoms (each also having 9 nearest neighbors) in the top layer; and three atoms in the second layer (each now having 12 nearest neighbor atoms). Similarly, for the bridge site, 3-fold site, and the 4-fold sites, the respective cn_{max} are 18, 22, and 26. In this formulation, eq. 3.3 is able to successfully explain the trend that stronger binding (more negative values) will occur at low $\overline{CN}$.

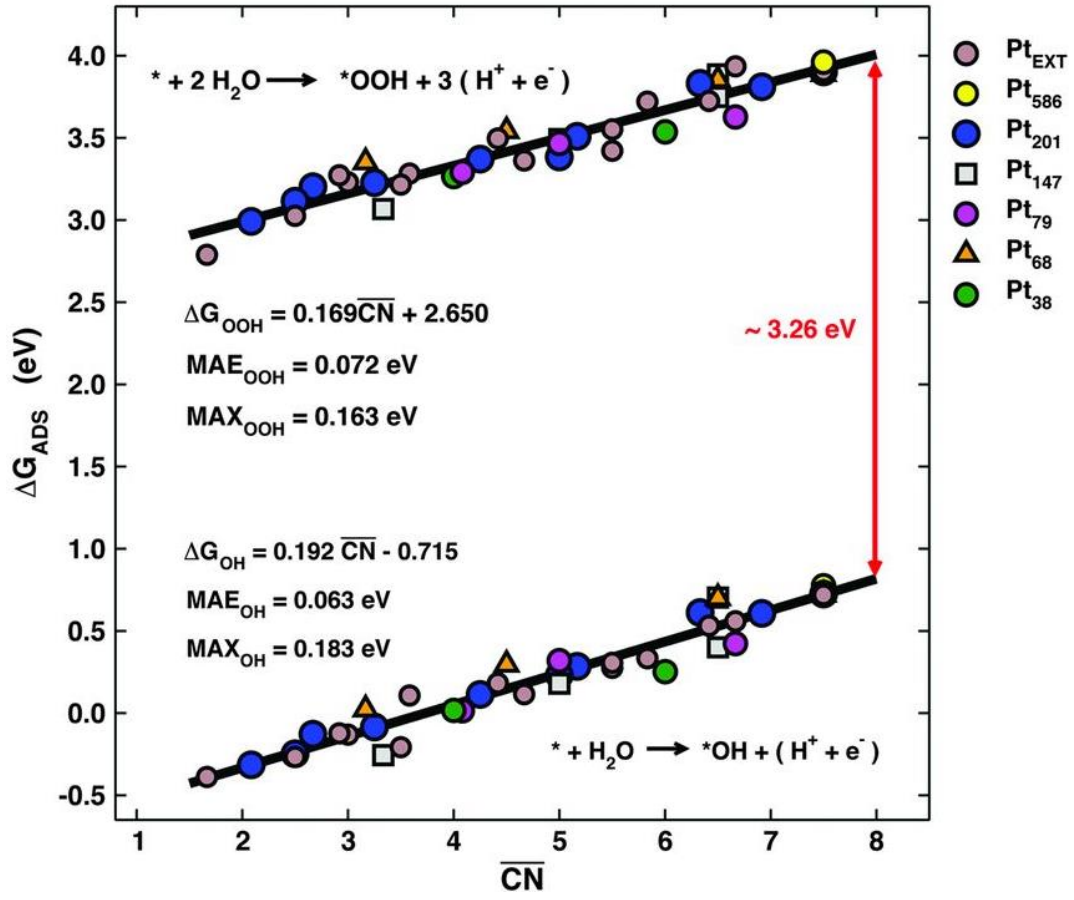


Figure 3.4. Correlations of the adsorption energies of OOH* and OH* with the generalized coordination numbers ($\overline{CN}$). Adapted from Ref. [29].

Recent studies suggest that graphitic carbon structures indeed influence ORR reactivity via strong support and electronic structure modifications. Wang *et al*.[30] employed multiwalled carbon nanotubes (MWCNTs) as the Pt catalyst support and showed that Pt surface area loss for Pt/MWCNT was 37% after 168 hours versus 80% for the Pt/C catalyst. Carbon support also promotes ORR by enhancing beneficial charge transfer. Zhou *et al*.[31] pointed out that the C–N interaction results in stronger binding to Pt and alters the Pt band structures. Lim *et al*.[32] performed DFT calculations to show that defective graphene support promotes charge transfer from Pt to adsorbed O_2 and to reduce O–O bond dissociation energy barrier by 0.21 eV. Ma *et al*.[33] also showed that the ORR activity increased by 2.1-fold (at 0.9 V) using N-doped reduced graphene oxide as a Pt catalyst support in comparison to Pt/C.

In this chapter, molecular models were developed to represent Pt catalyst deposited on the 3D VACNF architecture for ORR. A simple semi-periodic Pt/fishbone model was constructed based on parallel graphene sheets to investigate the ORR mechanisms and the PLS. Also, a sophisticated Pt/VACNF catalyst model on a multi-edged carbon support was built using structures obtained from MD simulations. The ORR performance of these model catalysts was also compared with Pt(111). The lower ORR limiting potential on Pt catalysts originates from the restructuring of Pt NPs on VACNF, exposing more low coordinated sites that binds ORR intermediates stronger at their active sites.

3.2 Computational Details

3.2.1 Density Functional Theory

Spin polarized DFT calculations were carried out using the Vienna ab initio Simulation Package (VASP).[34] The generalized-gradient approximation (GGA) Perdew-Burk-Ernzerhof (PBE) functional was used to account for the Kohn-Sham electron exchange-correlation

interactions.[35] The projector augmented wave (PAW) method was used to represent the ionic cores.[36] A cut-off for the plane wave basis set expansion up to 400 eV was used for all calculations. The break condition for the self-consistent iteration was set to 1×10^{-5} eV. Ionic relaxation was stopped when the forces on all atoms were smaller than 0.05 eV/Å. The Brillouin zone was sampled using $1 \times 4 \times 1$ k-point for semi-periodic Pt/fishbone model and single Γ k-point for Pt/VACNF model.[37] In this work, the Grimme's DFT-D3 theory was employed to account for the van der Waals interactions between adsorbates and substrates.[38]

The semi-periodic *fishbone* models were built by cleaving the graphite layers to represent the VACNF architecture. Given the large diameter of the VACNF (~50 to 250 nm), the small curvature of the VACNF was neglected in this model.[39] The dangling bonds at the broken graphitic edges at the fishbone sidewall were passivated by OH groups, which are energetically favorable in alkaline conditions. Pt structures with different numbers of atoms, from Pt_4 to Pt_{20}, were constructed, and the formation energies of Pt NPs (per Pt atom) were calculated by eq. 3.4,

$$\Delta G_f = \frac{G_{OH^-} + E_{Pt_n/VACNF} - E_{VACNF_{OH}} - nE_{Pt}}{n} \qquad (3.4)$$

where, G_{OH^-} represents chemical potential of OH^-, and $E_{Pt_n/VACNF}$, $E_{VACNF_{OH}}$, and E_{Pt} represent the total energies of Pt supported by fishbone model, fishbone model passivated by OH groups, and total energy of Pt atom.

Both zero-point energy (ZPE) corrections and entropic contributions were estimated based on the simple harmonic approximation.[40] For liquid phase water, $H_2O(l)$, the solvation energies (the free energy difference between their gas-phase and aqueous-phase states) were taken from the handbook by Dean.[41]

3.2.2 Molecular Dynamics Simulation

Molecular dynamics (MD) simulations were carried out using the LAMMPS code.[42] The ReaxFF force field, adapted from the work by Shin *et al*,[43] was employed to represent the C–C, C–Pt atomic interactions in the Pt/VACNF system.[44] This force field has been used to study Pt-Ni NPs.[43]

The VACNF atomic structures were generated using Nanotube Modeler.[45] Materials Studio was then used to convert the VACNF unit into a periodic structure along the z direction. The periodic boundaries were set as 50 Å × 50 Å × 57 Å. Pt NPs in icosahedral of three sizes (Pt_{55}, Pt_{100}, and Pt_{147}) were placed close to the zig-zag edges of VACNF deliberately for structure relaxations. During MD simulations, the temperature was initially set to 600 K using a conical assemble (NVT) for equilibration; then, the temperature was raised to 800 K for 2 ns, to fully sample the structural and energy configurations. For larger Pt_{147}, even higher temperature (1200 K) was attempted for an additional 0.55 ns to ensure that the structure corresponding to the global energy minimum was reached. Then, the temperature was lowered back to 298 K. The timestep was set to be 0.25 fs, and the trajectories were recorded every 400 steps.

3.2.3 ORR Mechanism

To study the ORR activity over Pt(111) and Pt/fishbone model, the dissociative and associative 4-e^- ORR mechanisms in alkaline solution were considered.[24,46,47] As shown by eqs. 3.5-3.8, the dissociative ORR pathway follows a direct O-O bond cleavage of O_2^*. For each dissociated O^*, one H is abstracted from liquid $H_2O(l)$, coupled with the transfer of one electron to form OH^- ion and OH^* (eq. 3.7). The combination of OH* coupled with a second charge forms a second OH^- ion (eq. 3.8).

$$O_2(g) + * \rightarrow O_2^* \quad (3.5)$$

$$O_2^* + * \rightarrow 2O^* \quad (3.6)$$

$$O^* + H_2O(l) + e^- \rightarrow OH^* + OH^-(aq) \quad (3.7)$$

$$OH^* + e^- \rightarrow * + OH^-(aq) \quad (3.8)$$

In the associative mechanism (eqs. 3.9-3.10), O_2^* first abstracts one H atom from liquid $H_2O(l)$ producing OOH^* and OH^- (first charge transfer), followed by the O-O bond cleavage to produce OH^* and O^*. Both O^* and OH^* proceed to form OH^- by following eqs 3.7-3.8.

$$O_2^* + H_2O(l) + e^- \rightarrow OOH^* + OH^-(aq) \quad (3.9)$$

$$OOH^* + * \rightarrow OH^* + O^* \quad (3.10)$$

$$O_2(g) + * + H_2O(l) + e^- \rightarrow OOH^* + OH^-(aq) \quad (3.11)$$

$$OOH^* + e^- \rightarrow * + OOH^-(aq) \quad (3.12)$$

$$OOH^* + 3OH_{edge} \rightarrow 3O_{edge} + 2H_2O(l) \quad (3.13)$$

$$O_{edge} + H_2O(l) + e^- \rightarrow * + OH^-(aq) \quad (3.14)$$

Over the Pt-free fishbone model, both 2-e$^-$ and 4-e$^-$ pathways were considered. According to Choi *et al.*[48] O_2 adsorption is not crucial over graphitic materials because the charge transfer initiating ORR may occur in the outer Helmholtz plane. Thus, the process involving OOH* formation can be summarized by eq. 3.11. In the 2-e$^-$ pathway, OOH* will desorb upon receiving the second electron, as in eq. 3.12. In the 4-e$^-$ pathway, OOH^- further undergoes the O-O bond cleavage to form OH* and O*. At the OH-passivated fishbone edge, the formation of O* is likely to result in H_2O formation from the passivating OH groups, as described by eqs 3.13-3.14, where OH_{edge} and O_{edge} denote the passivating OH and O species at the graphitic edge.

3.3 Results and Discussion

3.3.1 The Pt/fishbone Model

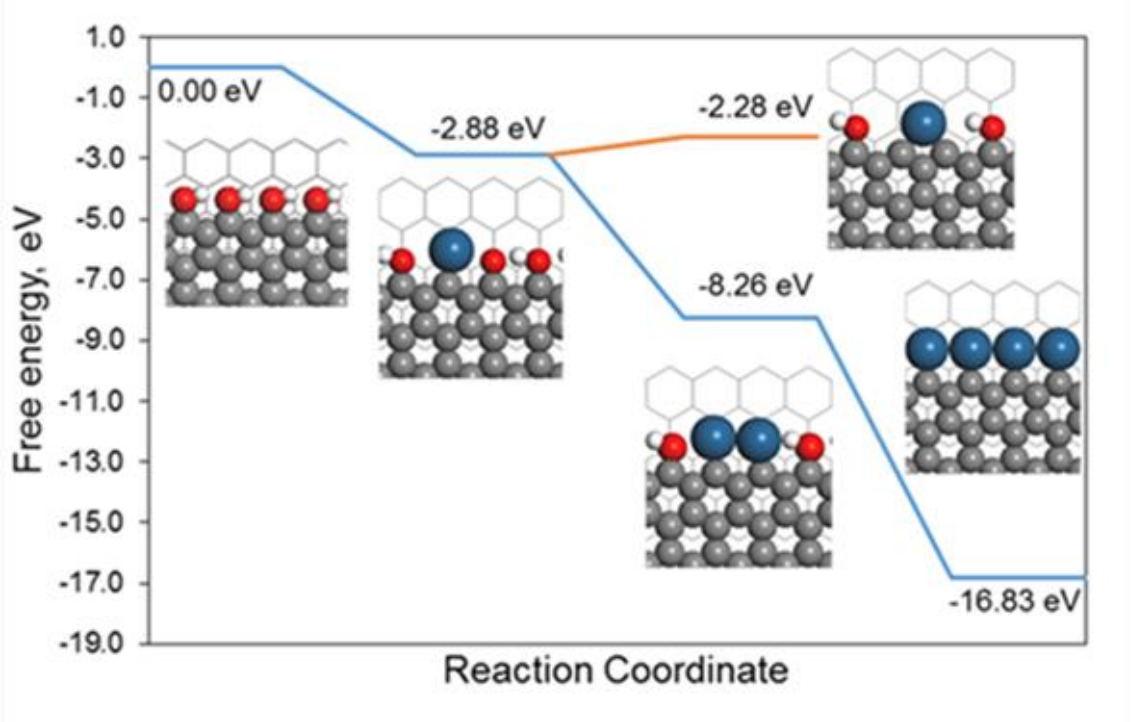


Figure 3.5. Free energy diagram of depositing Pt atoms at the OH passivated fishbone graphite edge. Color code: blue-Pt, gray-C, red-O, white-H.

To model Pt/VACNF, the first question addressed is whether Pt NPs can be directly supported on the open carbon edges. Thus, it is important to learn if the C-Pt bond can be easily formed. According to Figure 3.5 by replacing one OH group with a Pt atom, the reaction is exothermic by -2.88 eV; furthermore, by completely replacing four passivating OH groups with four Pt atoms, the formation energy becomes even more negative, however, by removing OH group and forming another Pt-C bond with the same Pt atom, the reaction is endothermic. Thus, it is reasonable to anticipate that the sputtered Pt species will interact with the open-edge C atoms

preferentially. The newly formed C-Pt bonds are stronger than the C-O bonds, enabling Pt to replace any pre-existing terminating O species at the graphitic edge. Other evidence regarding Pt being directly supported on the carbon edges was also provided from the modeling work by Cheng *et al*.[27,49]

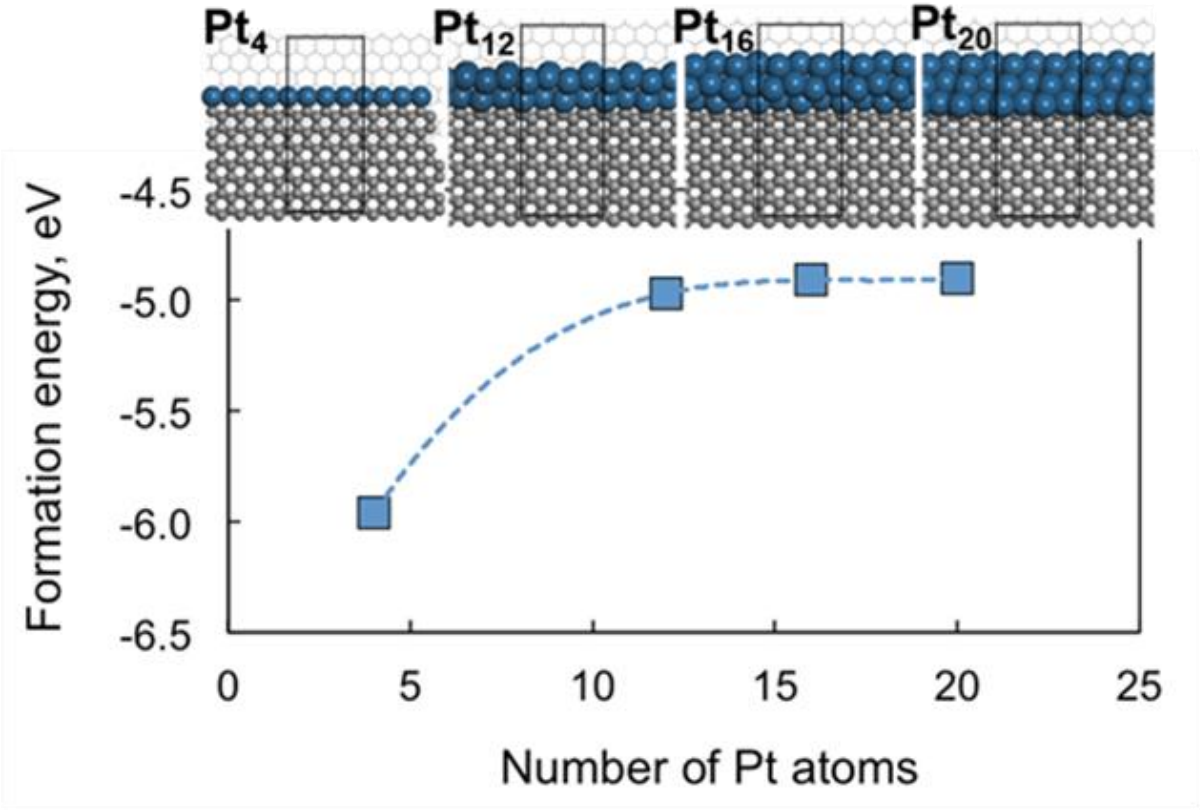


Figure 3.6. Formation energies (per Pt atom) for semi-periodic Pt_4, Pt_{12}, Pt_{16}, and Pt_{20} supported on graphene edge. Color code: blue-Pt, and gray-C.

To determine appropriate representations of Pt catalyst in the Pt/fishbone model, Pt atoms were introduced incrementally as illustrated in Figure 3.6. All structures are periodically bounded parallel to the carbon edge and were optimized. Also shown in Figure 3.6, the formation energies,

eq. 3.4 (per Pt atom) converged within 0.06 eV at Pt_{12}, which was then selected for the modeling of ORR pathways. Detailed side view and front view of the chosen model are shown in Figure 3.7. Upon optimization, the Pt structures become somewhat corrugated and compressed. This is mainly due to the mismatch between Pt (2.81 Å) and graphene lattices (2.51 Å).

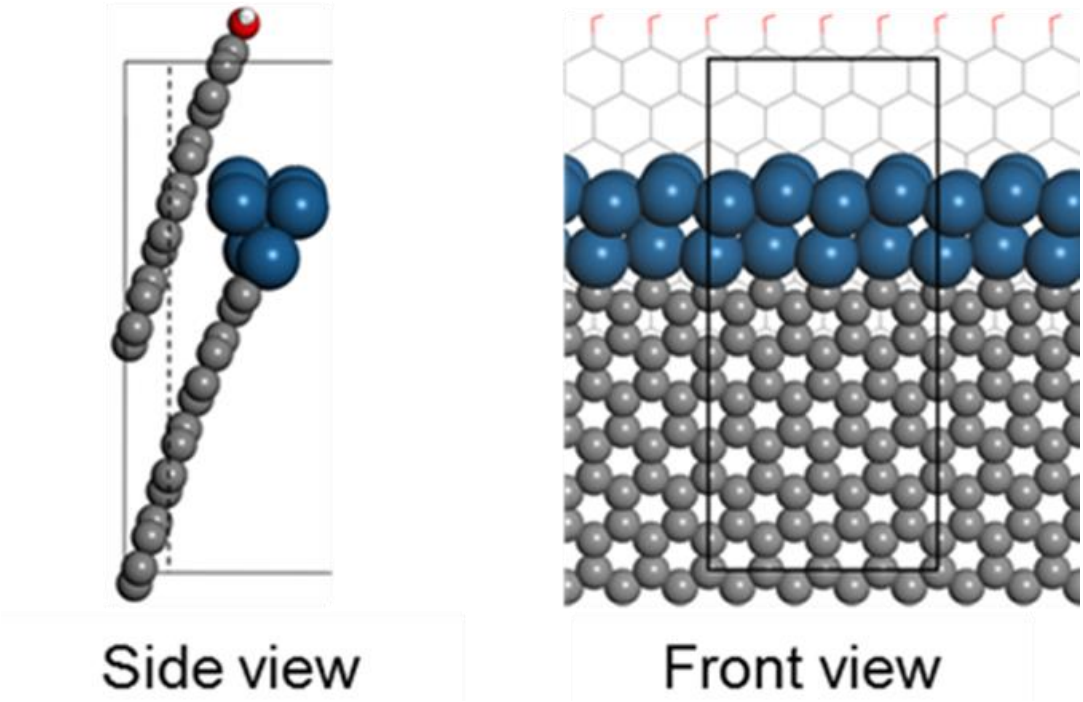


Figure 3.7. Side view and front view of Pt_{12}/fishbone. Color code: blue-Pt, and gray-C.

3.3.2 ORR on Bare Fishbone Model

In fact, Pt-free VACNF exhibits some ORR activities (Figure 3.1 d). The $2e^-$ ORR pathway, producing H_2O_2 (eqs. 3.11-3.12), will likely dominate the process. As shown in Figure 3.8, the dangling bonds at the graphitic edges are passivated by the OH groups. Free energy diagrams corresponding to the $2e^-$ and $4e^-$ ORR pathways are presented in Figure 3.8, along with the configurations of key reaction intermediates such as O_2, O and OH. The formation of OOH^-(aq) from O_2(g) via the elementary steps in eqs. 3.11-3.12 is an exothermic process. In comparison, as

shown by the blue path in Figure 3.8, the 4e$^-$ ORR pathway, upon OOH* formation, O* destabilizes and converts the passivating OH into oxygen atoms according to eq. 3.13. This step is highly exothermic (i.e., -5.19 eV) due to the formations of three edge sites without the passivating H (in purple) as illustrated by the inset figure in Figure 3.5. However, the regeneration of passivating OH groups, following, eq. 3.14, will be endothermic (1.16 eV). Thus, the 2e$^-$ ORR route (shown in red in Figure 3.8) leading to the formation of OOH^- is more competitive, and in good agreement with the experimental results by Elangovan *et al*.[22]

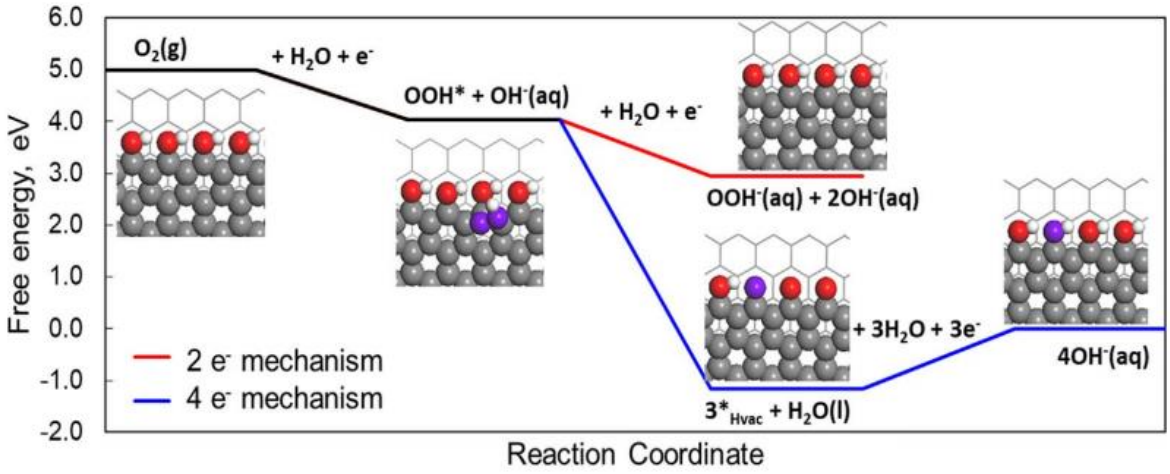


Figure 3.8. Free energy diagrams comparing the 2e$^-$ associative pathway (red) and 4e$^-$ pathway (blue) on the Pt-free fishbone model. (Color code: gray-C, red-O from passivating OH, white-H, and purple-O from reactant.

3.3.3 ORR over Pt/VACNF

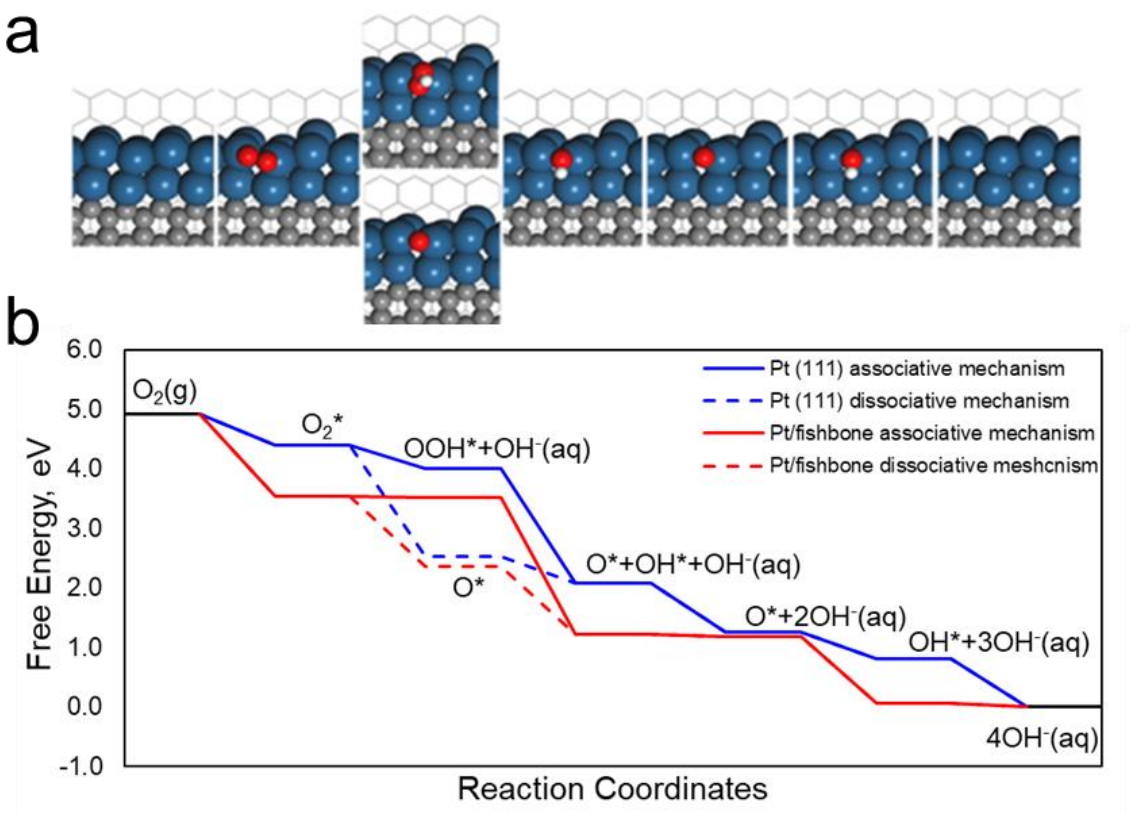


Figure 3.9. (a) Optimized ORR intermediates adsorbed on Pt/fishbone, and (b) free energy diagrams for $4e^-$ ORR pathways on Pt(111) (blue) and Pt/fishbone (red). Color code: blue-Pt, gray-C, red-O, and white-H.

When Pt catalysts are present (Figure 3.9 a), Pt atoms will be the primary active site for ORR, as all ORR intermediates indeed prefer to bind at the Pt-Pt bridge sites even in the presence of the same carbon support. The free energy diagram, Figure 3.9 b, indicates that O_2 adsorption over Pt/fishbone, eq. 3.5, becomes significantly stronger (-1.45 eV) than on Pt(111) (-0.60 eV). Hence, the overall ORR free energy profile corresponding to Pt/fishbone system shifts downward. The O–O bond cleavage, eq. 3.6, is an exothermic step (-1.19 eV). Subsequent formation of OH*

(eq. 3.7) and desorption to form OH^-(aq) (eq. 3.8) are both exothermic at -1.12 eV and -0.05 eV, respectively. In comparison, on Pt/fishbone, the associative mechanism proceeds through the formation of OOH* (eq. 3.9) results in a free energy change of -0.01 eV. In Figure 3.9 b, the formation of atomic O species via the dissociative mechanism would be much more thermodynamically favorable. Interestingly, by applying a bias potential, the OH desorption from Pt/fishbone becomes thermal neutral, indicating that eq. 3.8 is likely the potential limiting step. In comparison with Pt(111), the potential limiting step is the protonation step (eq. 3.7) that converts O* to OH*. This finding agrees with what has been suggested by Nørskov *et al*.[24] Furthermore, the limiting potential for Pt/fishbone is 0.05 V. At this point, we attribute the lower potential (versus 0.45 V on Pt(111)) to the strong OH binding at the low coordinated Pt sites. DFT calculations are consistent with the experimental finding by Elangovan *et al*.[22] This preliminary conclusion will be further verified with the Pt/VACNF model described in the following section.

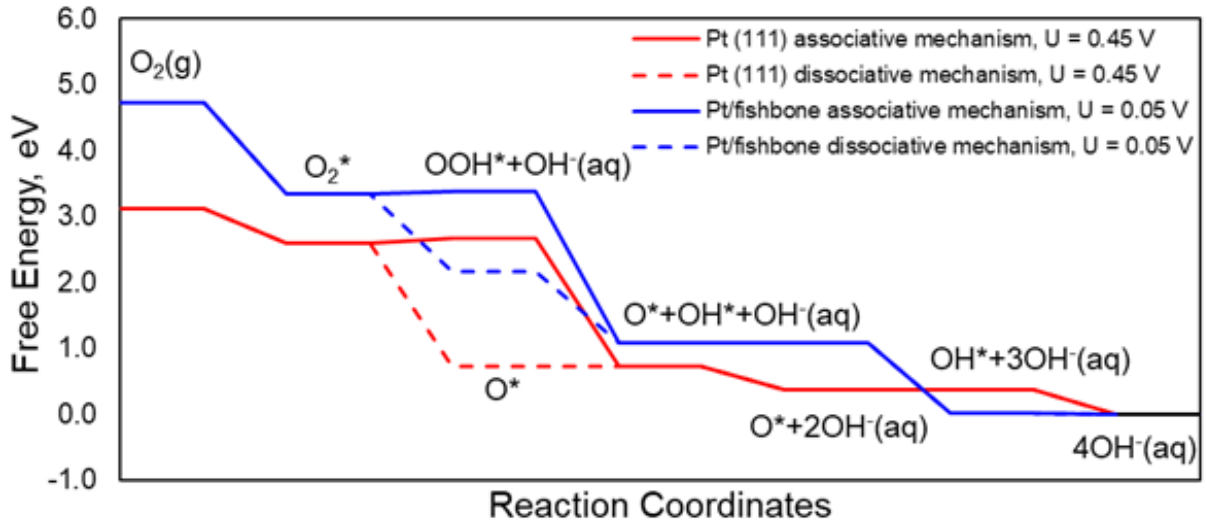


Figure 3.10. Free energy diagrams of ORR via the dissociative (dashed line) and associative (solid line) mechanisms on Pt(111) (red) and Pt/fishbone (blue) at respective limiting potentials.

3.3.4 Pt Catalyst Supported on the Multi-edged VACNF

Despite that experimental measurements can be successfully rationalized with the simple Pt/fishbone model, planar parallel semi-periodic graphene sheets were used to represent circular VACNF edge geometry; hence, the curvature effect was completely neglected.[22] The support geometry will impact the atomic structures of the Pt atoms in the vicinity of catalyst-support interface in the most significant way. Meanwhile, Pt particles were only represented by rows of Pt atoms. Therefore, the descriptions of the Pt particle size, shape, facets and other related geometric characters are inadequate.

In this section, molecular models were constructed with Pt NPs directly supported on stacked carbon nano cone structure (representing VACNF) using a combined DFT and MD approach. Figure 3.11 a-c illustrate three Pt NPs, i.e., Pt_{55}, Pt_{100}, and Pt_{147} anchored along the VACNF wall, spanning across multiple open edges. All three models were allowed to adequately relax during MD simulations at both elevated and room temperatures. These equilibrated structures exhibit bent carbon edges and somewhat distorted NP shapes (from the initial icosahedral geometry). The radial distribution functions (Figure 3.11 d) revealed that as the particle size increase, the particle becomes more and more crystalline, as the first peak becomes narrower and more distinct as Pt NPs increase in size and gradually become Pt bulk-like (black).

The respective average coordination numbers (CN), by simply counted the nearest neighbors of each atoms at the outer most shell, for the first atomic shell of Pt_{55}, Pt_{100}, and Pt_{147} are 4.93, 5.37, and 6.19, with a Pt–Pt cutoff distance of 2.8 Å. A similar criterion was used by Cheng and coworkers.[49] Clearly, all these particles have significant fractions of low coordination sites when compared with Pt(111), in which the CN for each top layer Pt is 9.

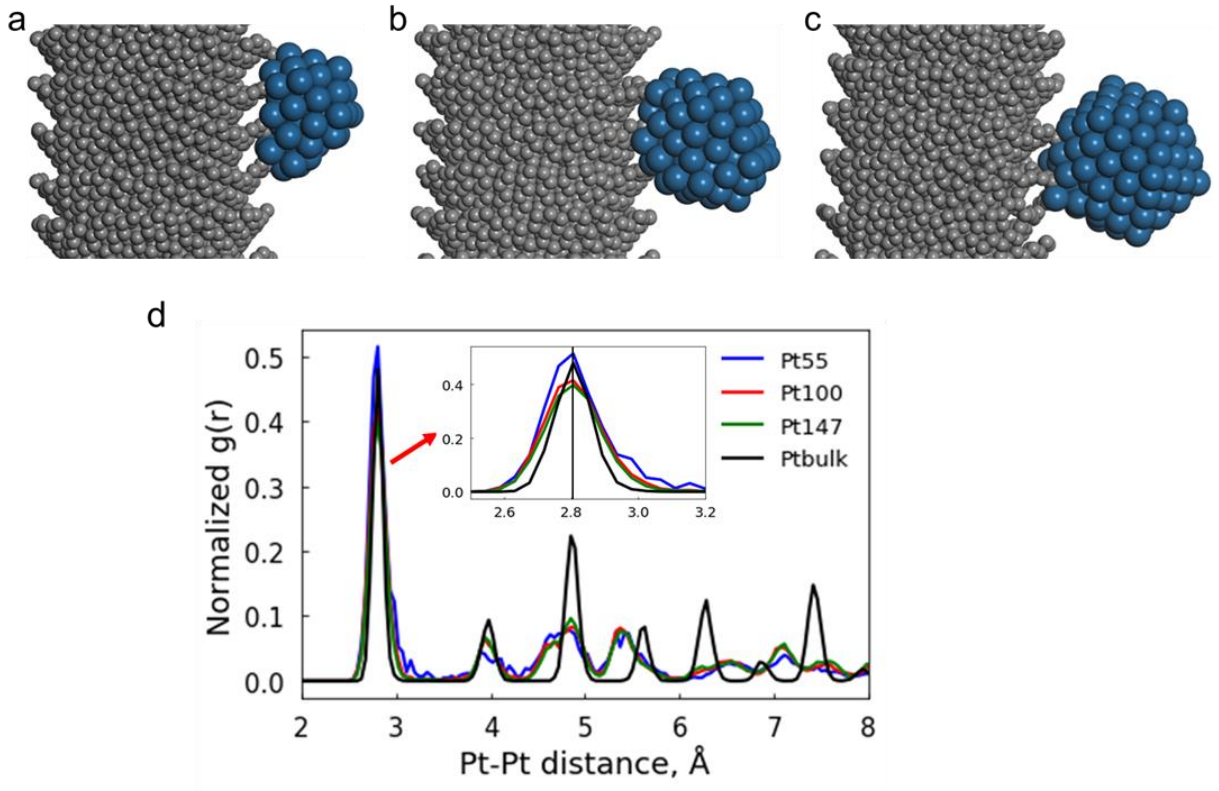


Figure 3.11. Equilibrated structures of Pt_{55} (a), Pt_{100} (b), and Pt_{147} (c) supported on VACNF; and (d) the normalized radial distribution functions g(r). The inset figure shows the first peak of each normalized g(r). The vertical line in the inset figure indicates the location of the first peak of g(r). Color code: blue-Pt, gray-C.

3.3.5 Adsorptions on Pt_{55}/VACNF

The estimated diameter for the Pt_{55} particle is ~1 nm, approximately the same size as the sputtered Pt particles deposited on VACNF experimentally. Moreover, the computational cost is significantly lower than Pt_{100} and Pt_{147}. Hence, the equilibrated Pt_{55} system and C atoms trimmed from the original stacked carbon nano cone structure (Figure 3.12) were subsequently used for DFT calculations.

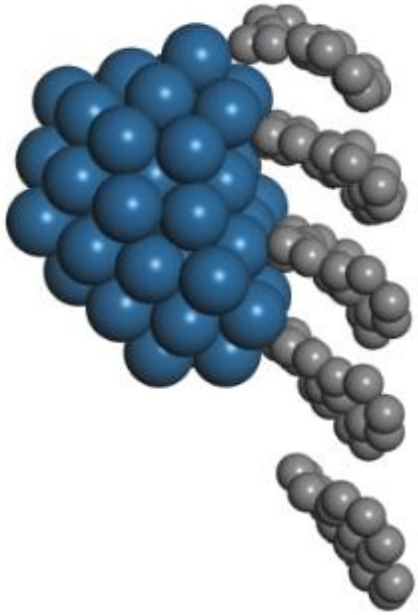


Figure 3.12. An DFT optimized Pt_{55}/VACNF system. The initial structure was obtained from MD relaxation at 298K. Color code: blue-Pt, gray-C.

To characterize the ORR activity of the new model, all possible binding sites for OOH, O, and OH were sampled and the corresponding adsorption energies (ΔG_{ads}), eqs. 2.12-2.15 in Chapter 2, were obtained. The molecular structures and the considered adsorption sites on Pt_{55} are illustrated and summarized in Figures 3.13, 3.14, and 3.15 and Tables 3.1. The corresponding $\overline{CN}$ values were calculated according to eq. 3.3 using the same cutoff distance of 2.8 Å. The darker the Pt atoms in Figures 3.13, 3.14, and 3.15 have higher CN values.

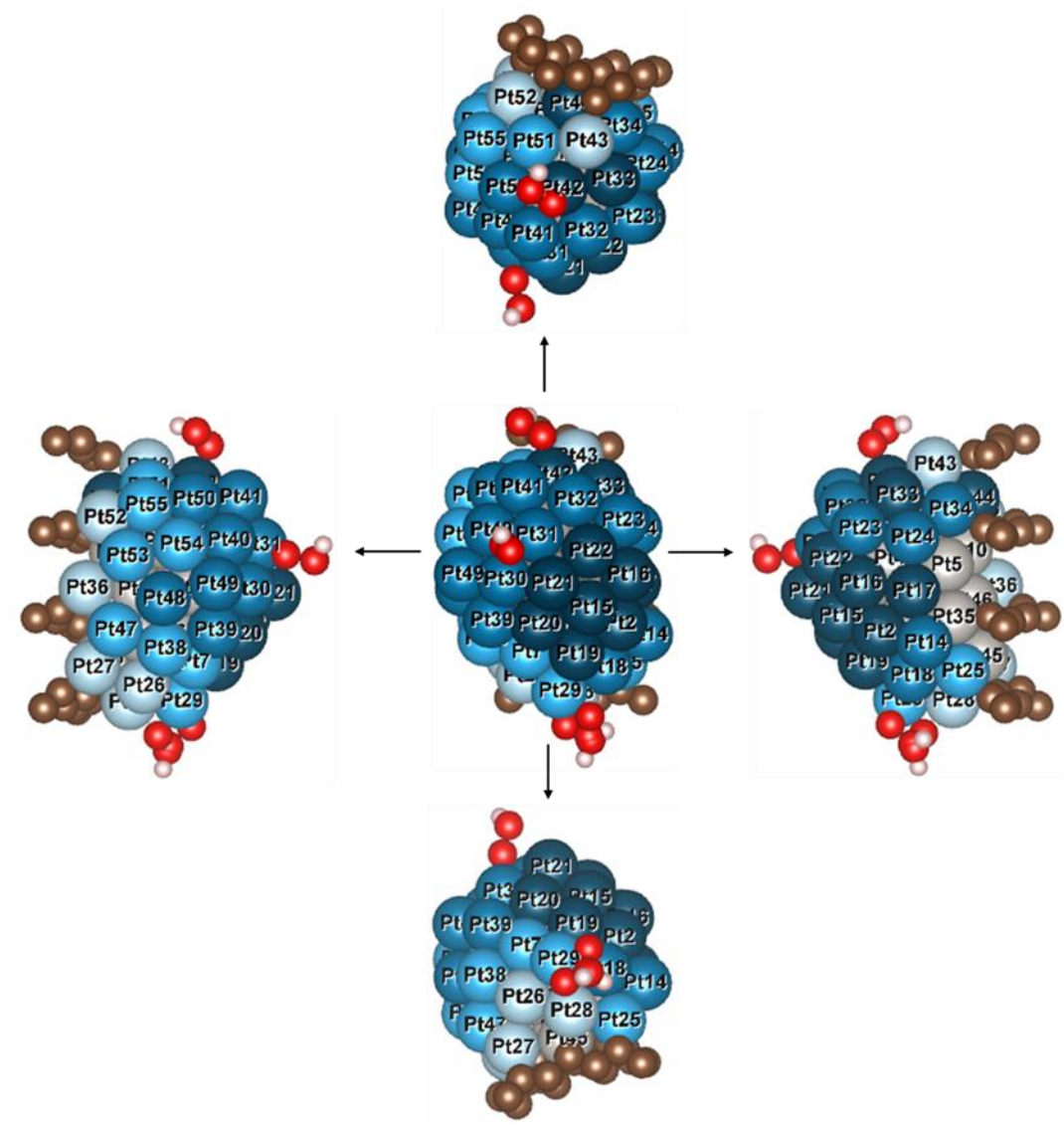


Figure 3.13. Adsorption and available binding sites for OOH* on Pt_{55}/VACNF. The first shell of Pt atoms has been colored blue. Color from light blue to dark blue indicates low coordinated sites to high coordinated sights. Color code: blue-Pt, brown-C, red-O, white-H.

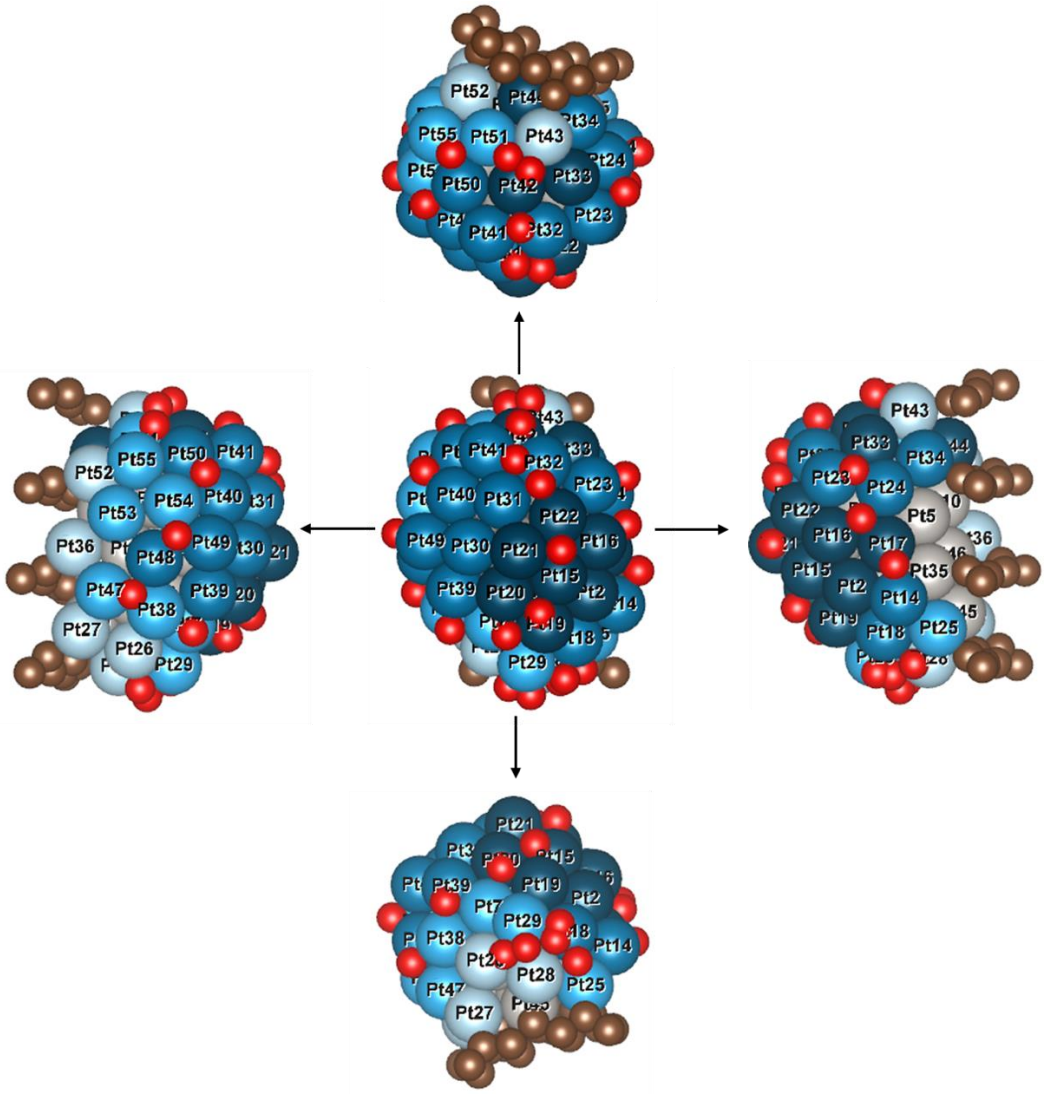


Figure 3.14. Adsorption and available binding sites for O* on Pt_{55}/VACNF. The first shell of Pt atoms has been colored blue. Color from light blue to dark blue indicates low coordinated sites to high coordinated sights. Color code: blue-Pt, brown-C, red-O, white-H.

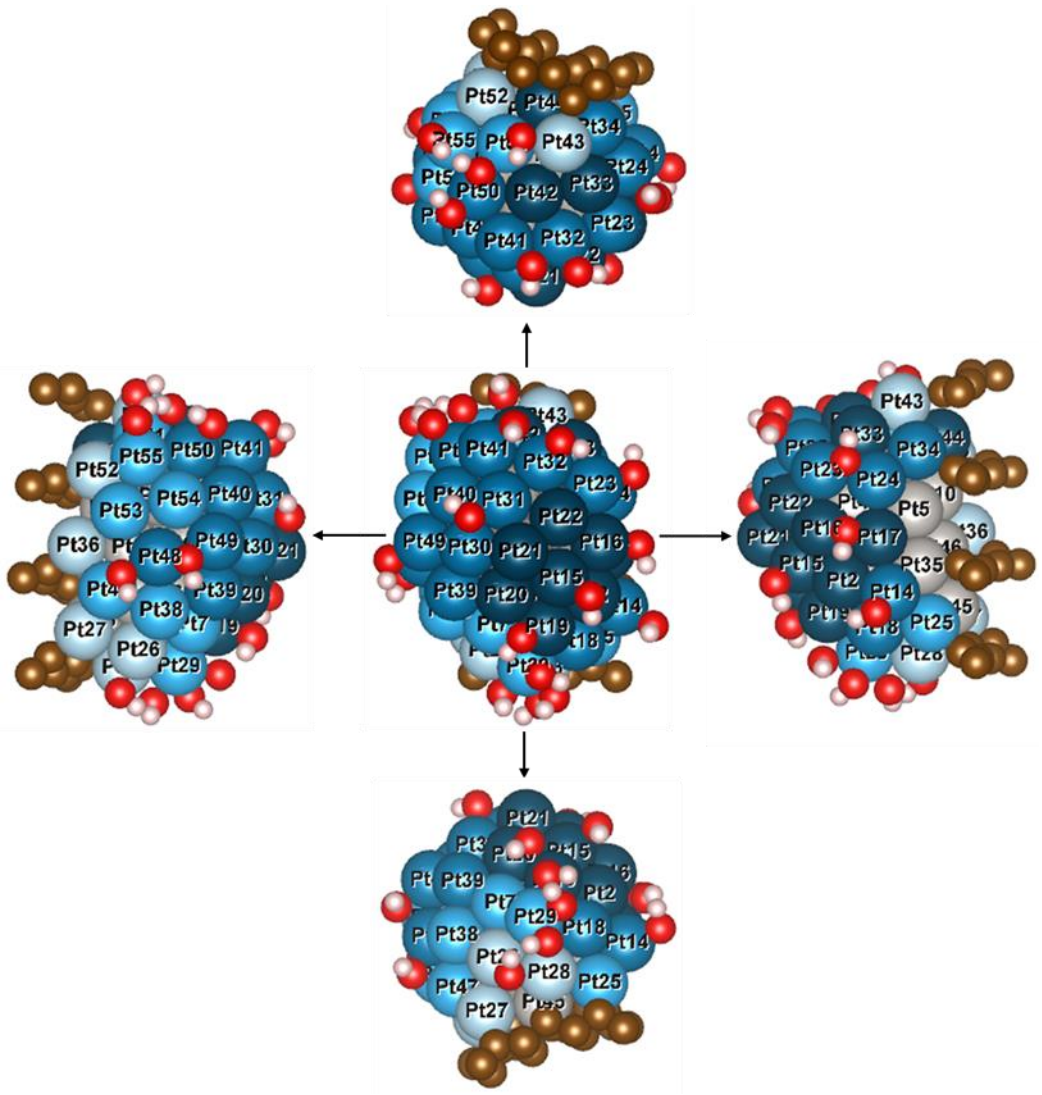


Figure 3.15. Adsorption and available binding sites for OH* on Pt_{55}/VACNF. The first shell of Pt atoms has been colored blue. Color from light blue to dark blue indicates low coordinated sites to high coordinated sights. Color code: blue-Pt, brown-C, red-O, white-H.

Table 3.1. Adsorptions of OOH*, O*, and OH* on Pt_{55}/VACNF: Binding sites, $\Delta G_{ads,}$ based on eqs. 2.12-2.15 in Chapter 2, and $\overline{CN}$.

OOH*			O*			OH*		
Binding Site	$\Delta G_{OOH*,}$ eV	$\overline{CN}$	Binding Site	$\Delta G_{O*,}$ eV	$\overline{CN}$	Binding Site	$\Delta G_{OH*,}$ eV	$\overline{CN}$
29	3.67	2.25	29-28	1.48	1.89	55	0.28	2.08
29-28	3.31	1.89	18-29-28	1.67	2.09	50	0.77	2.83
42	3.87	3.58	18-29	1.78	2.44	31-30	0.98	2.72
30-31	3.82	2.72	29-28-26	1.39	1.82	23-24	0.34	2.33
			31-32-22	1.62	2.59	29-19	0.62	2.56
			41-31-32	1.67	2.27	28-26	0.59	1.39
			43-42	1.61	2.89	28-29	0.34	1.89
			55-50-51	1.32	2.23	51-43	0.55	1.83
			51-43-42	1.56	2.36	29	0.55	2.25
			23-24	1.24	2.33	19-20	0.54	3.06
			17-14	1.35	2.33	32	0.55	2.58
			16-17-24	1.30	2.82	41-32	0.45	2.44
			54-48-49	1.30	2.82	48-47	0.55	2.83
			47-48-38	1.17	2.14	14	0.34	2.58
			21-22-15	1.60	2.64	16-17	0.70	2.67
			20-15-19	1.74	2.77	15	0.86	3.42
			20-7-19	1.62	2.77			
			50-54-40	1.72	2.32			
			41-32-42	1.54	2.59			
			39-38-7	1.51	2.45			

Note that, for Pt sites with similar $\overline{CN}$, the closer Pt atoms are to the C edges, the stronger ORR intermediates bind at such Pt sites. For instance, with similar $\overline{CN}$, 2.83, OH at bridge site of Pt48-Pt47 (Figure 3.15) binds stronger (0.55 eV) than at the top site of Pt50 (0.77 eV) by 0.22 eV. Similarly, O at the Pt55-Pt50-Pt51 3-fold site (Figure 3.14) also binds stronger (1.32 eV) than at the Pt41-Pt31-Pt32 3-fold site of (1.67 eV) by 0.35 eV, even though they share similar $\overline{CN}$, 2.23 vs 2.27, respectively. Therefore, it indicates that carbon edge indeed strengthens the adsorptions of ORR intermediates.

Moreover, linear empirical correlations were established to help elucidate the trends between the adsorption energies and $\overline{CN}$. The results are shown in Figure 3.16. The slopes for ΔG_{OOH^*} or ΔG_{OH^*} vs $\overline{CN}$ are 0.29 and 0.19, respectively. These values are actually quite close to the linear scaling relationships for OH and OOH presented by Calle-Vallejo and coworkers for stand-alone catalyst particles.[28,29] The ΔG_{ads} of all ORR intermediates (OOH*, O*, and OH*) increase (i.e., weaker binding) as $\overline{CN}$ increases. That is to say, overall, Pt NPs with a larger fraction of low $\overline{CN}$ sites tend to bind the ORR intermediates more strongly.[25,28,29]

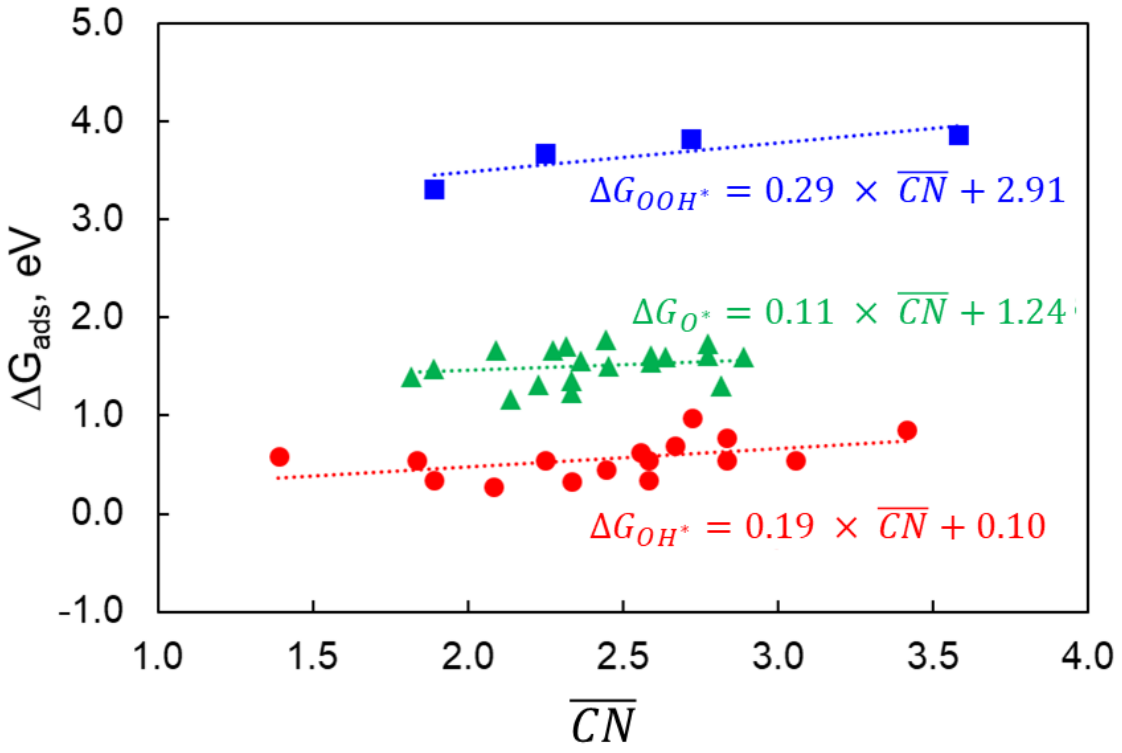


Figure 3.16. Adsorption energies of OOH* (blue squares), O* (green triangles), and OH* (red dots) as a function of $\overline{CN}$.

Using the linear correlations produced in Figure 3.8, the averaged first shell $\overline{CN}$ is 2.67 for Pt_{55} supported by VACNF edge, and the corresponding adsorption energies for OOH*, O*, and OH* are 3.69 eV, 1.54 eV, 0.41 eV, respectively.

3.3.6 ORR on the Pt/VACNF Model

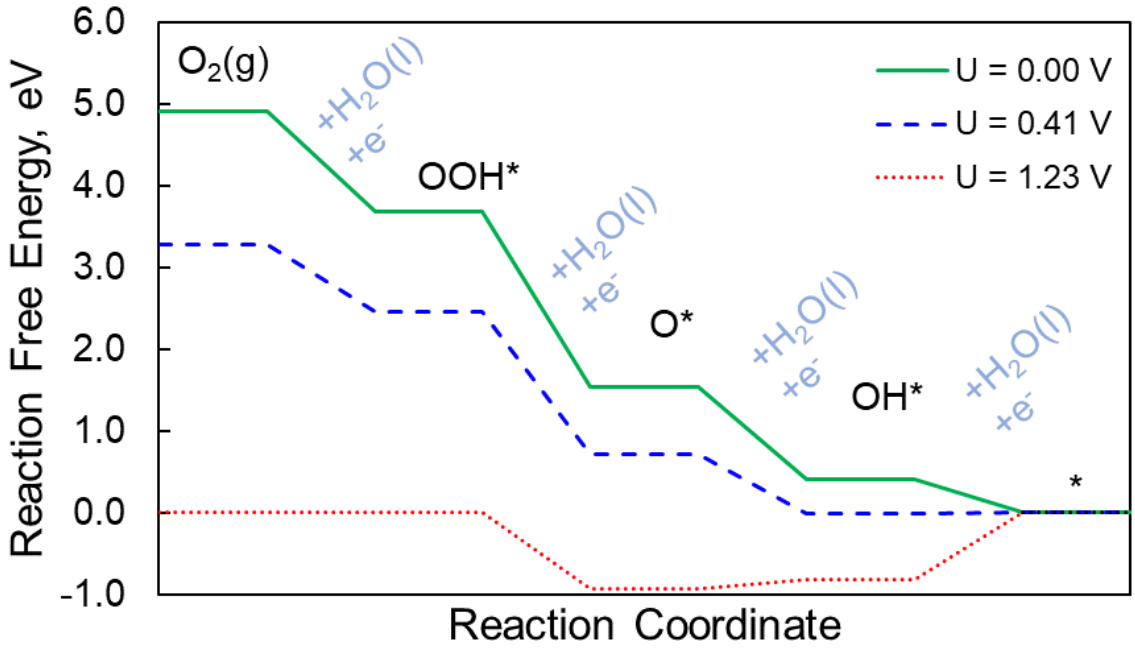


Figure 3.17. ORR free energy diagram on Pt_{55}/VACNF at U = 0.0 V (green-solid line), 0.41 V (blue-dashed line), and 1.23 V (red-dotted line).

Here, the $4e^-$ associative mechanism is considered for ORR. It has been shown in section 3.3 that the ORR PLSs on Pt(111) and Pt/fishbone are the formation of OH* and OH* desorption, respectively. As shown in Figure 3.17, at U = 0 V, the formation of OOH* via the first charge transfer (eq. 3.6) is -3.52 eV, and the O-O bond dissociation step forming OH^-(aq) and O* via the second charge transfer (eq. 3.7) is exothermic by -2.06 eV, which is followed by the protonation of O* with water in the third charge transfer step (eq. 3.4) and is exothermic by -1.05 eV. In the

end, the OH* desorption step via the fourth charge transfer step (eq. 3.5) is -0.41 eV. At an applied potential of 0.41 eV, the thermodynamics barrier for the desorption of OH* is eliminated, yielding a limiting potential of 0.41 V with the OH* desorption as the PLS.

Compared with the findings in section 3.3, the adsorption energies on Pt/VACNF are stronger than on Pt(111), but weaker than on Pt/fishbone. Thus, the ORR limiting potential on Pt/VACNF will be lower than Pt(111), as discussed in section 3.3, by 0.04 V, which is consistent with the 0.04 V left-shift of the half-wave potential from experiment.[22] However, the limiting potential on Pt/VACNF is higher than that on Pt/fishbone by 0.36 V, due to the overall consideration of binding sites with different coordination at different locations (adjacent or away from carbon edges) of Pt_{55}. It is also consistent that the PLS on Pt/VACNF is also the removal of OH, as on Pt/fishbone. Therefore, Pt/VACNF and Pt/fishbone are qualitatively consistent in terms of PLS, but Pt/VACNF model provides better quantitative agreement with the experiment.

3.4 Conclusions

DFT calculations, aided by MD simulations, were carried out to develop catalyst models to better represent Pt catalysts supported on VACNF. The ultimately goal is to thoroughly understand the ORR performance on these catalysts and provide the theory-experiment reconciliation for future catalyst design and preparation.

Two models were presented in this chapter, i.e., the fishbone model and the stacked conical model. DFT calculations revealed that Pt-free fishbone models passivated by OH are active for ORR based on a low-efficiency $2e^-$ mechanism. In addition, Pt will be directly supported on the open carbon edges thanks to the stronger C–Pt bond (versus the C–O bond). With the Pt_{12}/fishbone system, the bindings of ORR intermediates were enhanced, resulting lower limiting potential than

Pt/C catalysts with the removal of OH species as the potential determining step. The Pt_{55}/VANCF permits a more realistic system to study the dependence of ORR performance on the catalyst surface structure. DFT calculations confirmed that, due to the exposure of low coordinated sites, ORR intermediates indeed bind on the Pt sites stronger. The overbinding again will hinder ORR activity. Using VACNF as Pt catalyst support, Pt NPs are stabilized by the formation of C-Pt bond. In this case, little ORR activity lost was observed (0.04 V lower in limiting potential) compared with Pt (111).

References

(1) Ma, R.; Lin, G.; Zhou, Y.; Liu, Q.; Zhang, T.; Shan, G.; Yang, M.; Wang, J. A Review of Oxygen Reduction Mechanisms for Metal-Free Carbon-Based Electrocatalysts. *npj Comput. Mater.* **2019**, *5* (1), 78.

(2) Wu, G.; More, K. L.; Johnston, C. M.; Zelenay, P. High-Performance Electrocatalysts for Oxygen Reduction Derived from Polyaniline, Iron, and Cobalt. *Science.* **2011**, *332* (6028), 443 – 447.

(3) Steele, B. C. H.; Heinzel, A. Materials for Fuel-Cell Technologies. *Nature* **2001**, *414* (6861), 345–352.

(4) Gong, K.; Du, F.; Xia, Z.; Durstock, M.; Dai, L. Nitrogen-Doped Carbon Nanotube Arrays with High Electrocatalytic Activity for Oxygen Reduction. *Science.* **2009**, *323* (5915), 760 – 764.

(5) Yang, C.-J. An Impending Platinum Crisis and Its Implications for the Future of the Automobile. *Energy Policy* **2009**, *37* (5), 1805–1808.

(6) DOE Technical Targets for Polymer Electrolyte Membrane Fuel Cell Components https://www.energy.gov/eere/fuelcells/doe-technical-targets-polymer-electrolyte-membrane-fuel-cell-components.

(7) Debe, M. K.; Schmoeckel, A. K.; Vernstrom, G. D.; Atanasoski, R. High Voltage Stability of Nanostructured Thin Film Catalysts for PEM Fuel Cells. *J. Power Sources* **2006**, *161* (2), 1002–1011.

(8) Debe, M. K. Nanostructured Thin Film Electrocatalysts for PEM Fuel Cells - A Tutorial on the Fundamental Characteristics and Practical Properties of NSTF Catalysts. *ECS Trans.* **2012**, *45* (2), 47–68.

(9) Debe, M. K. Electrocatalyst Approaches and Challenges for Automotive Fuel Cells. *Nature*

2012, *486* (7401), 43–51.

(10) Tian, Z. Q.; Lim, S. H.; Poh, C. K.; Tang, Z.; Xia, Z.; Luo, Z.; Shen, P. K.; Chua, D.; Feng, Y. P.; Shen, Z.; Lin, J. A Highly Order-Structured Membrane Electrode Assembly with Vertically Aligned Carbon Nanotubes for Ultra-Low Pt Loading PEM Fuel Cells. *Adv. Energy Mater.* **2011**, *1* (6), 1205–1214.

(11) Yu, X.; Ye, S. Recent Advances in Activity and Durability Enhancement of Pt/C Catalytic Cathode in PEMFC: Part I. Physico-Chemical and Electronic Interaction between Pt and Carbon Support, and Activity Enhancement of Pt/C Catalyst. *J. Power Sources* **2007**, *172* (1), 133–144.

(12) Yu, X.; Ye, S. Recent Advances in Activity and Durability Enhancement of Pt/C Catalytic Cathode in PEMFC: Part II: Degradation Mechanism and Durability Enhancement of Carbon Supported Platinum Catalyst. *J. Power Sources* **2007**, *172* (1), 145–154.

(13) Nie, Y.; Li, L.; Wei, Z. Recent Advancements in Pt and Pt-Free Catalysts for Oxygen Reduction Reaction. *Chem. Soc. Rev.* **2015**, *44* (8), 2168–2201.

(14) Seo, M. H.; Choi, S. M.; Kim, H. J.; Kim, W. B. The Graphene-Supported Pd and Pt Catalysts for Highly Active Oxygen Reduction Reaction in an Alkaline Condition. *Electrochem. commun.* **2011**, *13* (2), 182–185.

(15) Zhu, C.; Dong, S. Recent Progress in Graphene-Based Nanomaterials as Advanced Electrocatalysts towards Oxygen Reduction Reaction. *Nanoscale* **2013**, *5* (5), 1753–1767.

(16) Shao, Y.; Zhang, S.; Wang, C.; Nie, Z.; Liu, J.; Wang, Y.; Lin, Y. Highly Durable Graphene Nanoplatelets Supported Pt Nanocatalysts for Oxygen Reduction. *J. Power Sources* **2010**, *195* (15), 4600–4605.

(17) Tang, H.; Chen, J. H.; Huang, Z. P.; Wang, D. Z.; Ren, Z. F.; Nie, L. H.; Kuang, Y. F.; Yao, S. Z. High Dispersion and Electrocatalytic Properties of Platinum on Well-Aligned Carbon Nanotube Arrays. *Carbon N. Y.* **2004**, *42* (1), 191–197.

(18) Wang, D.-W.; Su, D. Heterogeneous Nanocarbon Materials for Oxygen Reduction Reaction. *Energy Environ. Sci.* **2014**, *7* (2), 576–591.

(19) Lee, K.; Zhang, J.; Wang, H.; Wilkinson, D. P. Progress in the Synthesis of Carbon Nanotube- and Nanofiber-Supported Pt Electrocatalysts for PEM Fuel Cell Catalysis. *J. Appl. Electrochem.* **2006**, *36* (5), 507–522.

(20) Li, W.; Waje, M.; Chen, Z.; Larsen, P.; Yan, Y. Platinum Nanopaticles Supported on Stacked-Cup Carbon Nanofibers as Electrocatalysts for Proton Exchange Membrane Fuel Cell. *Carbon N. Y.* **2010**, *48* (4), 995–1003.

(21) Bessel, C. A.; Laubernds, K.; Rodriguez, N. M.; Baker, R. T. K. Graphite Nanofibers as an Electrode for Fuel Cell Applications. *J. Phys. Chem. B* **2001**, *105* (6), 1115–1118.

(22) Elangovan, A.; Xu, J.; Brown, E.; Liu, B.; Li, J. Fundamental Electrochemical Insights of Vertically Aligned Carbon Nanofiber Architecture as a Catalyst Support for ORR. *J. Electrochem. Soc.* **2020**, *167* (6), 66523.

(23) Shao, M.; Peles, A.; Shoemaker, K. Electrocatalysis on Platinum Nanoparticles: Particle Size Effect on Oxygen Reduction Reaction Activity. *Nano Lett.* **2011**, *11* (9), 3714–3719.

(24) Nørskov, J. K.; Rossmeisl, J.; Logadottir, A.; Lindqvist, L.; Kitchin, J. R.; Bligaard, T.; Jónsson, H. Origin of the Overpotential for Oxygen Reduction at a Fuel-Cell Cathode. *J. Phys. Chem. B* **2004**, *108* (46), 17886–17892.

(25) Roldan Cuenya, B.; Behafarid, F. Nanocatalysis: Size- and Shape-Dependent Chemisorption and Catalytic Reactivity. *Surf. Sci. Rep.* **2015**, *70* (2), 135–187.

(26) Tuo, Y.-X.; Shi, L.-J.; Cheng, H.-Y.; Zhu, Y.-A.; Yang, M.-L.; Xu, J.; Han, Y.-F.; Li, P.; Yuan, W.-K. Insight into the Support Effect on the Particle Size Effect of Pt/C Catalysts in Dehydrogenation. *J. Catal.* **2018**, *360*, 175–186.

(27) Cheng, H.; Zhu, Y.-A.; Chen, D.; Åstrand, P.-O.; Li, P.; Qi, Z.; Zhou, X.-G. Evolution of Carbon Nanofiber-Supported Pt Nanoparticles of Different Particle Sizes: A Molecular Dynamics Study. *J. Phys. Chem. C* **2014**, *118* (41), 23711–23722.

(28) Calle-Vallejo, F.; Martínez, J. I.; García-Lastra, J. M.; Sautet, P.; Loffreda, D. Fast Prediction of Adsorption Properties for Platinum Nanocatalysts with Generalized Coordination Numbers. *Angew. Chemie Int. Ed.* **2014**, *53* (32), 8316–8319.

(29) Calle-Vallejo, F.; Tymoczko, J.; Colic, V.; Vu, Q. H.; Pohl, M. D.; Morgenstern, K.; Loffreda, D.; Sautet, P.; Schuhmann, W.; Bandarenka, A. S. Finding Optimal Surface Sites on Heterogeneous Catalysts by Counting Nearest Neighbors. *Science.* **2015**, *350* (6257), 185 – 189.

(30) Wang, X.; Li, W.; Chen, Z.; Waje, M.; Yan, Y. Durability Investigation of Carbon Nanotube as Catalyst Support for Proton Exchange Membrane Fuel Cell. *J. Power Sources* **2006**, *158* (1), 154–159.

(31) Zhou, Y.; Neyerlin, K.; Olson, T. S.; Pylypenko, S.; Bult, J.; Dinh, H. N.; Gennett, T.; Shao, Z.; O'Hayre, R. Enhancement of Pt and Pt-Alloy Fuel Cell Catalyst Activity and Durability via Nitrogen-Modified Carbon Supports. *Energy Environ. Sci.* **2010**, *3* (10), 1437–1446.

(32) Lim, D.-H.; Wilcox, J. Mechanisms of the Oxygen Reduction Reaction on Defective Graphene-Supported Pt Nanoparticles from First-Principles. *J. Phys. Chem. C* **2012**, *116* (5), 3653–3660.

(33) Ma, J.; Habrioux, A.; Luo, Y.; Ramos-Sanchez, G.; Calvillo, L.; Granozzi, G.; Balbuena, P. B.; Alonso-Vante, N. Electronic Interaction between Platinum Nanoparticles and Nitrogen-Doped Reduced Graphene Oxide: Effect on the Oxygen Reduction Reaction. *J. Mater. Chem. A* **2015**, *3* (22), 11891–11904.

(34) Kresse, G.; Furthmüller, J. Efficient Iterative Schemes for Ab Initio Total-Energy Calculations Using a Plane-Wave Basis Set. *Phys. Rev. B* **1996**, *54* (16), 11169–11186.

(35) Perdew, J. P.; Burke, K.; Ernzerhof, M. Generalized Gradient Approximation Made Simple. *Phys. Rev. Lett.* **1996**, *77* (18), 3865–3868.

(36) Blöchl, P. E. Projector Augmented-Wave Method. *Phys. Rev. B* **1994**, *50* (24), 17953–17979.

(37) Monkhorst, H. J.; Pack, J. D. Special Points for Brillouin-Zone Integrations. *Phys. Rev. B* **1976**, *13* (12), 5188–5192.

(38) Grimme, S.; Antony, J.; Ehrlich, S.; Krieg, H. A Consistent and Accurate Ab Initio Parametrization of Density Functional Dispersion Correction (DFT-D) for the 94 Elements H-Pu. *J. Chem. Phys.* **2010**, *132* (15), 154104.

(39) Zhu, Y. A.; Sui, Z. J.; Zhao, T. J.; Dai, Y. C.; Cheng, Z. M.; Yuan, W. K. Modeling of Fishbone-Type Carbon Nanofibers: A Theoretical Study. *Carbon N. Y.* **2005**, *43* (8), 1694–1699.

(40) Shan, N.; Zhou, M.; Hanchett, M. K.; Chen, J.; Liu, B. Practical Principles of Density Functional Theory for Catalytic Reaction Simulations on Metal Surfaces – from Theory to Applications. *Mol. Simul.* **2017**, *43* (10–11), 861–885.

(41) Dean, J. A. *Lange's Handbook of Chemistry*; McGraw-Hill: New York, 1985.

(42) Plimpton, S. Fast Parallel Algorithms for Short-Range Molecular Dynamics. *J. Comput. Phys.* **1995**, *117* (1), 1–19.

(43) Shin, Y. K.; Gai, L.; Raman, S.; van Duin, A. C. T. Development of a ReaxFF Reactive Force Field for the Pt–Ni Alloy Catalyst. *J. Phys. Chem. A* **2016**, *120* (41), 8044–8055.

(44) van Duin, A. C. T.; Dasgupta, S.; Lorant, F.; Goddard, W. A. ReaxFF: A Reactive Force Field for Hydrocarbons. *J. Phys. Chem. A* **2001**, *105* (41), 9396–9409.

(45) JCrystalSoft. Nanotube Modeler.

(46) Liu, S.; White, M. G.; Liu, P. Mechanism of Oxygen Reduction Reaction on Pt(111) in Alkaline Solution: Importance of Chemisorbed Water on Surface. *J. Phys. Chem. C* **2016**, *120* (28), 15288–15298.

(47) Xu, J.; Liu, B. Intrinsic Properties of Nitrogen-Rich Carbon Nitride for Oxygen Reduction Reaction. *Appl. Surf. Sci.* **2020**, *500*, 144020.

(48) Choi, C. H.; Lim, H.-K.; Chung, M. W.; Park, J. C.; Shin, H.; Kim, H.; Woo, S. I. Long-Range Electron Transfer over Graphene-Based Catalyst for High-Performing Oxygen Reduction Reactions: Importance of Size, N-Doping, and Metallic Impurities. *J. Am. Chem. Soc.* **2014**, *136* (25), 9070–9077.

(49) Cheng, H.-Y.; Zhu, Y.-A.; Åstrand, P.-O.; Chen, D.; Li, P.; Zhou, X.-G. Evolution of Pt Nanoparticles Supported on Fishbone-Type Carbon Nanofibers with Cone–Helix Structures: A Molecular Dynamics Study. *J. Phys. Chem. C* **2013**, *117* (27), 14261–14271.

Chapter 4 - Intrinsic Properties of Nitrogen-Rich Carbon Nitride for Oxygen Reduction Reaction

Chapter 4 is adapted with permission from:

Xu, J.; Liu, B. "Intrinsic properties of nitrogen-rich carbon nitride for oxygen reduction reaction", Applied Surface Science, 2020, 500, 144020.

4.1 Introduction

The kinetically sluggish cathodic oxygen reduction reaction (ORR) has long been recognized as a limiting factor in fuel cell applications.[1–3] Platinum (Pt) catalysts supported on high surface area Vulcan carbon (Pt/C) are regarded as the standard ORR electrocatalysts; however, the high cost hinders their ability to compete against current fossil-based energy conversion and transportation technologies.[4–6] The Pt/C catalysts are also susceptible to sintering, catalyst dissolution, and support corrosion.[7–9] Moreover, cathodes based on Pt are very sensitive to methanol crossover reaction as well as CO poisoning.[10,11]

Pt-free carbon materials such as graphene (denoted as GN) are one of the most studied ORR catalyst substitutes due to their tunable reactivity, low cost,[3] durability, and resistance to the interference of crossover methanol and CO.[12] Its characteristic sp^2 hybridized graphitic lattice facilitates the charge transfer needed for electrochemical reactions.

The graphitic carbon nitride (g-C_3N_4) is a two-dimensional (2D) semiconductor. g-C_3N_4 is also a nitrogen rich carbon material (with a N content of 57%), consisting of both graphitic (N_g) and pyridinic (N_p) nitrogen species (see Figure 4.1a).[13] Boosted by its emerging applications in photocatalysis,[14–17] and the fabrications of photoelectrochemical devices,[18] the properties of g-

C_3N_4 are being studied extensively. More recently, g-C_3N_4 is being explored in electrochemical ORR systems as well.[4,6,19–21] Zheng *et al.*[6] found that the 2 e^- ORR pathways are permitted for g-C_3N_4. However, with an energy band gap of 2.7 eV, one main challenge for g-C_3N_4 to be a viable ORR electrocatalyst is to overcome its rather poor electrical conductivity.

Both the intrinsic catalytic and electrical properties of g-C_3N_4 can be manipulated to achieve improved ORR performance. Toward this goal, various 2D g-C_3N_4 hybrid nanocomposites have been obtained through couplings with graphene (GN), carbon black, or mesoporous carbon, all of which resulted in promising electrocatalytic activities for ORR.[4,6,22] Specifically, Lyth *et al.*[4] reported that the current density collected from the g-C_3N_4/C mixture is more than twice as much as that obtained from g-C_3N_4 alone at zero applied potential. In addition, Zheng *et al.*[6] showed that the g-C_3N_4 incorporated into the highly ordered mesoporous carbon (CMK-3) enables the 4 e^- ORR pathway, and performs competitively against commercial Pt/C catalysts. The current density obtained using g-C_3N_4@CMK-3 (3.5mA/cm^2) is comparable with that on Pt/C (3.75 mA/cm^2). The ORR performance was also unaffected by the presence of methanol.[6] Electronically, Li *et al.*[23] demonstrated that, by stacking g-C_3N_4 on top of GN, the band gap of the heterostructure decreases by approximately 0.9 eV. Theoretically, Du *et al.*[24] showed that the g-C_3N_4 supported on the GN layer forms electron-hole puddles, which create electron-rich and hole-rich regions to drive electrons transfer from GN to g-C_3N_4 at the interface. As a result, both the electro- and photocatalytic activities improve.[23]

A number of studies also confirm that the unique Fe-N-C moiety, facilitated by Fe–N bond formation, possesses extraordinary ORR reactivity with the Fe being the primary ORR active site.[1,25–31] The X-ray absorption near edge structure microscopy further revealed that the actual active site in Fe-N-C can be described as a four-coordinated FeN_4 configuration.[1,25–31] Within the

g-C_3N_4 lattice, the N_p species located at the hollow sites (Figure 4.1a) provide a natural structure platform (without artificial N-doping) to stabilize metal ions (e.g., Fe, Co).[21,32,33] Nevertheless, neither the active site nor the relationship with ORR reactivity for g-C_3N_4-based materials has yet been fully elucidated.

In this work, we address this issue by employing the HSE06 hybrid functional and van der Waals corrections within the density functional theory (DFT) framework to probe the potential active site of the g-C_3N_4 lattice. We focused on how the properties most directly related to ORR performance by: (1) modulating the electronic structures of g-C_3N_4 with 2D materials (i.e., GN and hBN) as bilayer heterostructures; and (2) examining the interactions with ORR intermediates with and without the presence of single-atom transition metal site. Both of these aspects must be satisfied synergistically. DFT calculations revealed that the g-C_3N_4 energy band gap can indeed be reduced in the g-C_3N_4/GN bilayer to facilitate charge transfer. The electronic property was then used as a screening criterion to study the ORR molecular mechanism. For the g-C_3N_4 lattice, a Fe single atom site, in a resembling 4-coordinated Fe-N-C moiety, also exists. We predict that this active site structure exhibits comparable ORR reactivity to the experimentally verified FeN_4 catalysts.

4.2 Computational Method

Periodic DFT calculations were performed using the plane-wave based Vienna Ab initio Simulation Package (VASP).[34] The projector augmented wave (PAW) method was used to describe the wave function near the ionic cores.[35] The generalized-gradient approximation (GGA) PBE functional was employed to account for the electron exchange and correlation effects within the Kohn-Sham framework.[36] The energy cutoff for bulk optimization was set to 520 eV, with a 6 × 6 × 4 k-point mesh based on the Monkhorst-Pack scheme.[37] Convergence tests performed on g-

C_3N_4 showed that the lattices have converged to within 0.01 Å. The break condition for self-consistent iterations was 1×10^{-6} eV, and ionic relaxations were stopped when the residual forces on all atoms were less than -0.02 eV/Å. All calculations were spin polarized. The van der Waals interactions between heterostructures, as well as between reactants and substrates, were considered using the Grimme's PBE-D2 method.[38] To obtain the density of states (DOS), static calculations were performed based on the optimized structures using a k-point mesh of $5 \times 5 \times 1$ and the hybrid HSE06 functional (for more accurate energy band gaps).[39]

Table 4.1. Lattice parameters and interlayer spacing for g-C_3N_4, g-C_3N_4/GN, and g-C_3N_4/hBN. The PBE-D2 calculations from this work are highlighted in bold numbers.

	Method	Lattice parameter, Å	Interlayer spacing, Å	References
g-C_3N_4 monolayer	PBE-D2	7.06	-	[23]
	PBE	7.15	-	[40]
	PBE	7.20	-	[41]
	PBE	7.14	-	This work
	PBE-D2	**7.13**	-	This work
	BEEF-vdW	7.14	-	This work
	optB88	7.13	-	This work
g-C_3N_4 bulk	PBE	6.96	3.76	[21]
	PBE-D2	**7.13**	**3.16**	This work
g-C_3N_4/GN	PBE-D2	7.31	-	[42]
	PBE-D2	-	2.89	[23]
	HSE06	-	3.04	[43]
	PBE+U	-	3.03	[24]
	PBE-D2	**7.31**	**3.12**	This work
	BEEF-vdW	7.32	3.56	This work
	optB88	7.31	3.31	This work
g-C_3N_4/hBN	PBE-D2	**7.40**	**3.13**	This work

For the optimizations of g-C_3N_4 monolayer (Figure 4.1a), g-C_3N_4/GN (Figure 4.1c), and g-C_3N_4/hBN (Figure 4.1d), the entire structures were relaxed. For the g-C_3N_4 multilayer (Figure

4.1b), only the top layer was relaxed. The lattice parameters estimated for the g-C_3N_4 monolayer (7.13 Å) and the g-C_3N_4/GN bilayer (7.31 Å) are in good agreement with the values reported in literature (see Table 4.1). For the g-C_3N_4 multilayer, the predicted interlayer spacing predicted is 3.16 Å, smaller than the literature value (3.57 Å) obtained using the standard PBE function (Table 4.1). This is expected because of the van der Waals forces considered at the PBE-D2 level of theory. To determine the most optimal g-C_3N_4/GN and g-C_3N_4/hBN bilayer structures for ORR calculations, four stacking configurations (Figure A.1) were considered based on Ref. 23. The structure with the lowest cohesive energy was selected for ORR modeling. The cohesive energy ($E_{cohesive}$) is defined by eq. 4.1.

$$E_{cohesive} = E_{heterostructure} - E_{monolayer\ I} - E_{monolayer\ II}, \quad (4.1)$$

where monolayer I and monolayer II refer to respective g-C_3N_4 and GN (or hBN) layer, respectively.

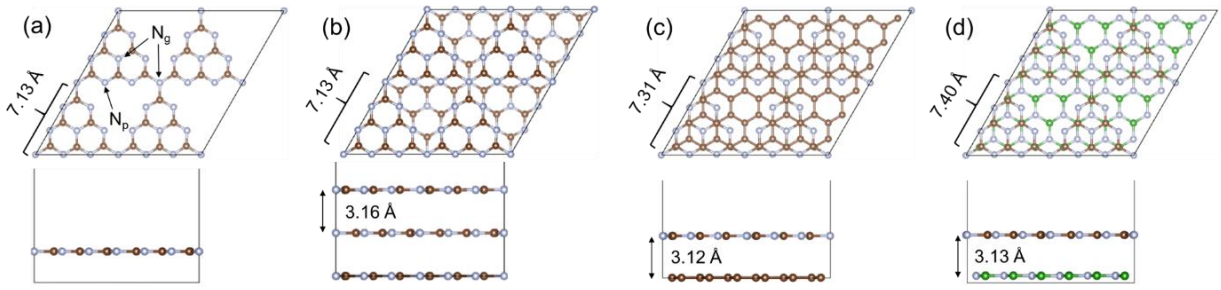


Figure 4.1. Optimized (2 × 2) supercells for g-C_3N_4 and its various bilayer heterostructures: (a) g-C_3N_4 monolayer, (b) g-C_3N_4 multilayer, (c) g-C_3N_4/GN, and (d) g-C_3N_4/hBN bilayer. C, N, B atoms are in brown, gray, and green, respectively. Black lines indicate the periodic cell boundaries. The lateral lattice parameters and the interlayer spacing are labeled on each structure.

The ORR free energy profiles were computed based on the 2 × 2 supercells of the structures shown above. Computationally, the cutoff energy and k-point mesh were adjusted to 440 eV and 2 × 2 × 1, respectively. Zero-point energy (ZPE) corrections were computed based on the simple harmonic approximation. The entropic contributions were estimated using the standard statistical mechanics approach.[44] The solvation energies of the liquid phase species such as H_2O(l) was obtained from the free energy differences between their respective gas-phase and aqueous-phase states based on Ref. 45. The adsorption free energy (ΔG_{ads}) and reaction free energy (ΔG_{rxn}) are defined by eqs. 4.2-4.3, respectively.

$$\Delta G_{ads} = G_{total} - (G_{surf} + G_{gas}) \tag{4.2}$$

$$\Delta G_{rxn} = \sum_i G_{Products,i} - \sum_j G_{Reactants,j} \tag{4.3}$$

To evaluate the electrocatalytic performance, the computational hydrogen electrode model, as in eq. 4.4, was employed.[44,46]

$$\Delta G_{(U)} = G_{rxn} + eU, \tag{4.4}$$

where U represents the applied potential bias.[33,46] The limiting potential was identified as the highest potential that maintains all the elementary steps in each reaction pathway exothermic (i.e., $\Delta G_{(U)} < 0$).

4.3 Results and Discussion

4.3.1 Electronic Properties of g-C_3N_4

The g-C_3N_4 crystal itself is a semiconductor, with an experimental energy band gap value of 2.7 eV.[47] The total density of states (DOS) (black) and the decomposed DOS based on the constituent elementals (orange and purple for the respective C and N atoms) for the g-C_3N_4 mono-

and multilayer structures are presented in Figure 4.2a and b, respectively. The calculated DOS using the HSE06 hybrid functional confirm that both materials are semiconductors. DFT calculations indicate that the g-C_3N_4 monolayer has a slightly larger energy band gap (2.79 eV) versus 2.34 eV for the multilayer g-C_3N_4. The HOMO of g-C_3N_4 monolayer, with significant contribution from its N_p (orange), is closer to the Fermi level. In fact, both the occupied and unoccupied states in the g-C_3N_4 monolayer shift upward, with the latter shifting to even higher energies.

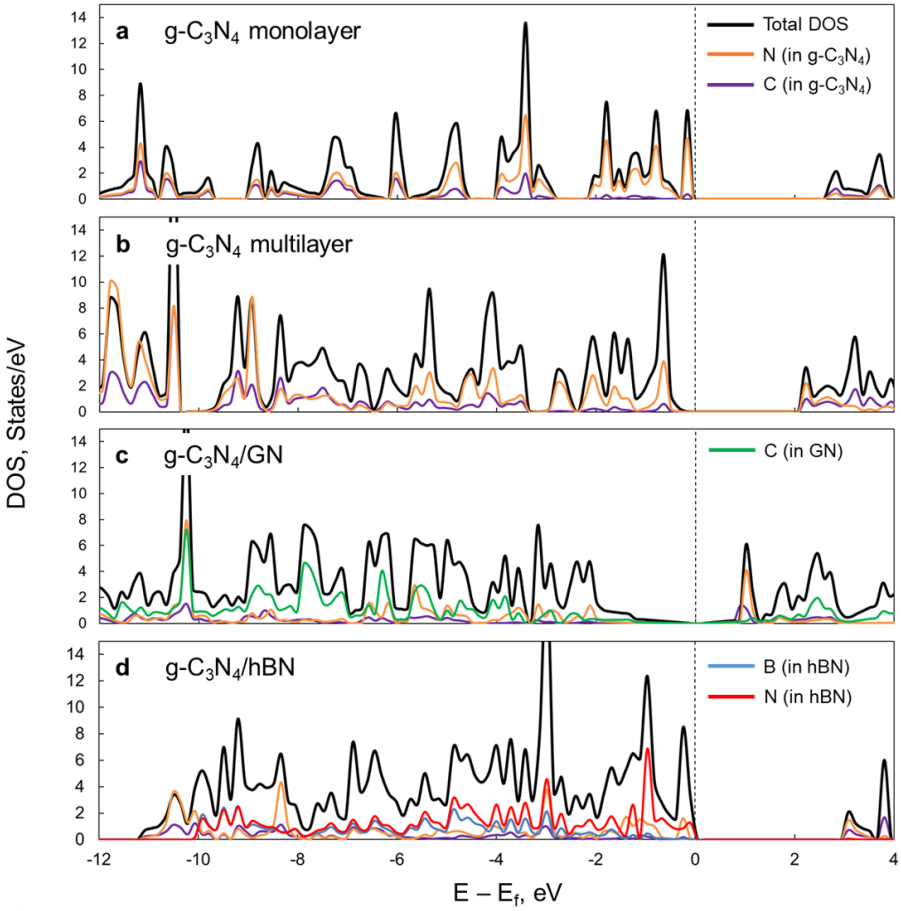


Figure 4.2**.** Density of states (DOS) of (a) g-C_3N_4 monolayer, (b) g-C_3N_4 multilayer, (c) g-C_3N_4/GN, (d) g-C_3N_4/hBN: entire structure (black); C in in g-C_3N_4 (orange); N in in g-C_3N_4 (purple); C in the GN layer (green); B in the hBN layer (blue); N in the hBN layer (red). Only the up-spin is shown, and the vertical dashed lines indicate the Fermi level.

By including a GN monolayer (Figure 4.1c), the electronic structures of g-C_3N_4 are substantially modified (Figure 4.2c). The highest occupied states (nearest to the Fermi level) become nearly absent, while the unoccupied states shift downward with increased magnitude. Overall, the gap within the g-C_3N_4/GN bilayer is almost closed. Du *et al.*[24] proposed that electron-hole puddles are formed due to the coupling between the g-C_3N_4 and GN layers. The GN monolayer layer has zero energy band gap, so the g-C_3N_4/GN bilayer is able to adapt and exhibits a similar electronic structure to GN, known as the band gap opening. Li *et al.*[23] reported an energy band gap of 0.11 eV for the GN/g-C_3N_4 bilayer and suggested the possibility of band structure engineering based on such observation.

The lattice mismatch occurring upon the formation of the bilayer could affect the electronic structure. As for g-C_3N_4/GN (Figure 4.1c), the g-C_3N_4 monolayer lattice is stretched laterally to 7.31 Å from 7.13 Å. To understand how the strain effect impacts the electronic structures of g-C_3N_4, the electronic structures corresponding to g-C_3N_4 monolayer with lattice parameters of 7.13 Å, 7.31 Å, and 7.40 Å were obtained as shown in Figure A.2 in the Appendix A. When the lattice is stretched laterally, the energy band gap increases from 2.79 eV to 3.15 eV. Therefore, the finding rules out that the band gap narrowing in the g-C_3N_4/GN bilayer results from the change in the g-C_3N_4 lattice; but is indeed due to the coupling with the GN layer underneath.

To broaden the scope, the g-C_3N_4 monolayer was also paired with hBN, another material with a 2D hexagonal structure (lattice parameter: 2.51 Å versus GN of 2.46 Å). Unlike GN, hBN has an indirect band gap of 5.96 eV. In the g-C_3N_4/hBN bilayer (Figure 4.1d), the calculated energy band gap is 2.75 eV. Moreover, the DOS of g-C_3N_4/hBN (Figure 4.2d) is distinct from both g-C_3N_4/GN and the g-C_3N_4 multilayer, where the occupied states show no apparent shift to the lower energy level, while the unoccupied states shift to the higher energy levels. Similarly, the effects on

the electronic structures associated with the change in lateral lattice of stand-alone g-C_3N_4 monolayer, which is elongated to 7.40 Å, were investigated. The band gap increases to 3.21 eV, close the energy band gap (3.20 eV) of the stand-alone g-C_3N_4 stretched laterally to the same distance. Hence, the good agreement shows that the coupling between g-C_3N_4 and the hBN layer is almost negligible.

4.3.2 ORR Intermediates on g-C_3N_4

Metal-free carbon nanomaterials, especially those consisting of N_p (or N_g) species, are catalytically active toward ORR.[3,48–51] The feasibility of g-C_3N_4 as ORR electrocatalysts has recently been demonstrated in the literature.[4,6] To elucidate the ORR molecular mechanism, the optimized structures of the reaction intermediates on different substrates (Figure 4.3) were first obtained. The binding energies (BE), calculated according to: $BE_A = E_A - E_* - E_{A(g)}$, where A refers to the adsorbate generically, E_A, E_*, $E_{A(g)}$ represent total energies of adsorbed state, clean substrate, and gas phase adsorbate, respectively. The total energies of the gas phase species are based on the stable molecules (i.e., H_2 and H_2O). The BE_A values are listed in Table 4.2.

Table 4.2. Binding energies (BE_A in eV) of ORR intermediates on g-C_3N_4 monolayer, g-C_3N_4 multilayer, g-C_3N_4/GN, and g-C_3N_4/hBN.

Species	g-C_3N_4 monolayer	g-C_3N_4 multilayer	g-C_3N_4/GN	g-C_3N_4/hBN
O_2	-1.34	-0.93	0.29	0.41
OOH	-1.91	-1.51	-0.21	-0.10
O	-1.35	-0.79	0.35	0.48
OH	1.01	1.32	2.29	2.28

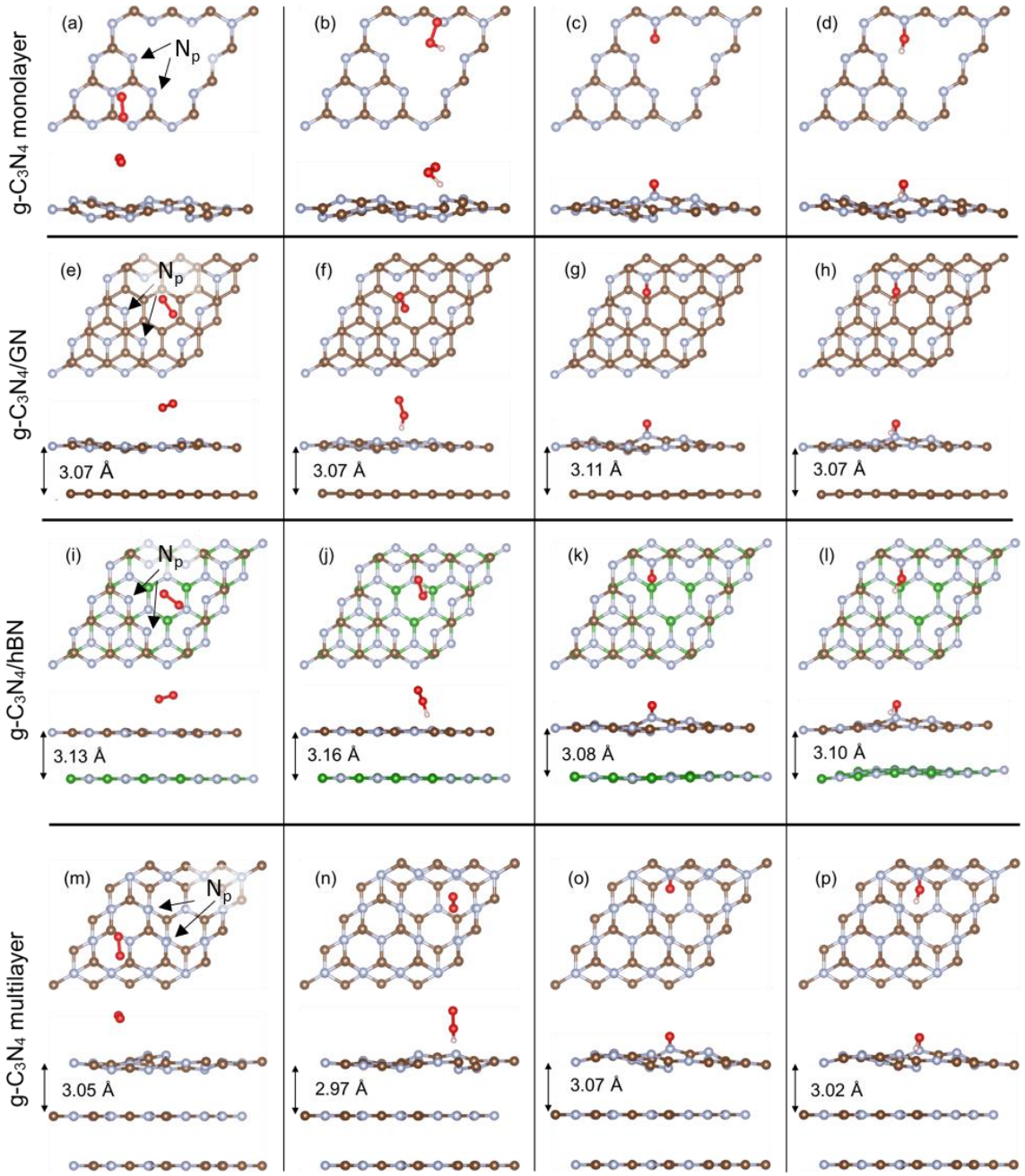


Figure 4.3. Optimized structures of O_2, OOH, O, and OH on g-C_3N_4 monolayer (a-d), g-C_3N_4/GN (e-h), g-C_3N_4/hBN (i-l), and g-C_3N_4 multilayer surface (m-p), respectively. The C, N, B atoms are in brown, blue, and green.

On the g-C_3N_4 mono- and multilayer, the O–O bond of the molecular O_2 is parallel to the C–N (an N_g species) bond (Figure 4.3a and m). Above the g-C_3N_4/GN and g-C_3N_4/h-BN

heterostructures, O_2 is also in a horizontal position located above the hollow site (Figure 4.3e and i). The BE_{O_2} on the g-C_3N_4 monolayer and multilayer are -1.34 eV and -0.93 eV, which are much stronger than those on the heterostructures, 0.29 eV for g-C_3N_4/GN, and 0.41 eV for g-C_3N_4/h-BN, respectively. The positive BE_{O_2} values are likely due to the structure change in the substrate from its natural planar state. On all substrate, as shown in Figure A.3, the *s*- and *p*-states of N_p do not overlap with the *s*- and *p*-states of the O atoms in O_2, suggesting that the primary interactions O_2 with all the substrates are essentially the long-range van der Waals forces, without physically binding at the substrate site. For ORR catalysis, recent studies have suggested that O_2 activation does not depend on the chemical bonding with the substrate necessarily.[52]

The O (Figure 4.3c, g, k, and o) and OH (Figure 4.3d, h, l, and k) intermediates prefer to bind at the N_p site at the g-C_3N_4 hollow site. Their preference to this site is expected since the highest occupied states reside in N_p in these structures (Figure 4.2). The OOH intermediate interacts weakly with all the substrates considered. As show in Figure 4.3b, f, j, and n, OOH interacts with the substrate via its H-end. In a previous study, He *et al*.[32] also observed a similar pattern at the N_p site.

As shown in Figure 4.3, the lattice relaxations have been observed for all structures upon adsorption, especially at the top g-C_3N_4 layer. The extents of relaxation are described in terms of the vertical displacements between the highest and lowest atoms within the top g-C_3N_4 layer, i.e., 1.05 Å, 0.89 Å, 0.45 Å, and 0.55 Å in a decreasing order for g-C_3N_4 monolayer, g-C_3N_4 multilayer, g-C_3N_4/GN, and g-C_3N_4/hBN, respectively. While the relaxation for the g-C_3N_4 monolayer can be understood as being free from structural restrictions, note that the top layer in the g-C_3N_4 multilayer structure also exhibits substantial relaxation (as in Figure 4.3m, n, o, and p) despite the presence

of g-C_3N_4 layers underneath. In comparison, g-C_3N_4/GN and g-C_3N_4/hBN exhibit the least amount of relaxation with the GN or hBN underneath.

4.3.3 Catalytic Performance of g-C_3N_4 and Heterostructures for ORR

The proposed ORR pathways are described by eqs. (A.1-A.4) in the Appendix A. For N-containing carbon-based ORR electrocatalysts, Choi *et al.*[52] suggested that the formation of OOH species from molecular O_2 (accompanied by the first electron transfer, eq. (A.1)) can proceed at the Outer Helmholtz Plane (ET-OHP), producing OOH and OH^-(aq). Here, we adopted the same mechanism due to weak O_2 and OOH adsorptions, where the cleavage of the O–O bond occurs through the OOH intermediate (i.e., the *associative* mechanism), producing O (bound at the N_p site) and OH^-(aq), as in eq. (A.2). In the following step, i.e., eq. (A.3), the O atom abstracts a H atom from H_2O to form OH (also bound at the N_p site) and an OH^-(aq). Lastly, OH accepts the 4th charge, as in eq. (A.4), and leaves the surface as OH^-(aq).

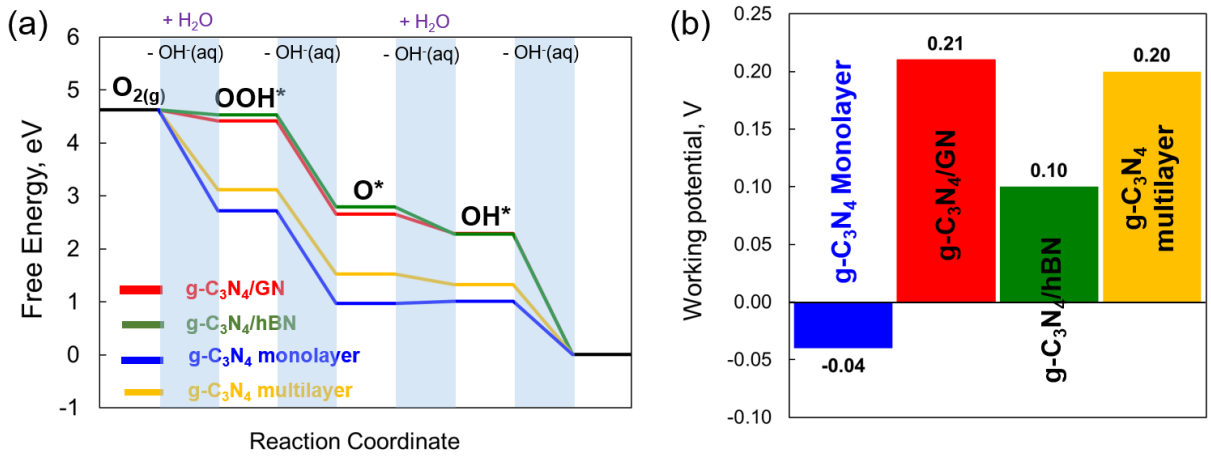


Figure 4.4. (a) Free energy diagrams of ORR on g-C_3N_4 monolayer (blue), g-C_3N_4/GN (red), g-C_3N_4/hBN (green), and g-C_3N_4 multilayer (yellow) at 298 K and 1 bar, with zero applied potential (U = 0 V); and (b) comparisons of limiting potentials for these materials. Each charge transfer step, associated with the formation of hydroxide ion, i.e., OH^-(aq), is highlighted in blue.

The free energy profiles for the g-C_3N_4 monolayer (blue), g-C_3N_4/GN (red), g-C_3N_4/hBN (green), and g-C_3N_4 multilayer (orange) are presented in Figure 4.4a. The above ORR steps are exoergic on all substrates due to strong O binding at the N_p site. In particular, the g-C_3N_4 monolayer and multilayer stabilize OOH more than the g-C_3N_4/GN and g-C_3N_4/hBN bilayers, and thus exhibit steeper slopes at the onset of the free energy profiles (in blue and orange) in Figure 4.4a. On the other hand, the formation of OH, eq. (A.3), becomes more facile on g-C_3N_4/GN and g-C_3N_4/hBN, while the formation of OH^-(aq) on the g-C_3N_4 monolayer is even slightly endothermic. Moreover, the formations of OH^-(aq) are also much more thermodynamically favorable on the two bilayer heterostructures.

The limiting potentials (U_{lim}) were extracted to further characterize the free energy profiles, as shown in Figure 4.4b. Furthermore, the overpotentials (η) were then calculated using $\eta = 1.23\ V - U_{lim}$, with 1.23 V being the equilibrium ORR potential. The highest η corresponds to the g-C_3N_4 monolayer, reflecting the slightly negative U_{lim} associated with the endothermic OH^-(ag) formation step. On the other hand, the lowest overpotentials were obtained on g-C_3N_4/GN and the g-C_3N_4 multilayer, closely followed by g-C_3N_4/hBN. Note the U_{lim}-determining mechanisms on various substrates may defer. On g-C_3N_4/GN, the WP is governed by OOH formation as in eq. (A.1); while on the g-C_3N_4 multilayer, the WP is decided by OH formation through eq. (A.3). The variation in the potential-determining step underscores the influences from the substrates on ORR intermediates despite similar WPs observed on g-C_3N_4/GN and the g-C_3N_4 multilayer.

Besides the similarity in WPs for g-C_3N_4/GN and the g-C_3N_4 multilayer, the energy band gap of g-C_3N_4 multilayer is much larger (still a semiconductor). Thus, the large band gap of pure g-C_3N_4 will likely be much less efficient for the charge transfer involved during ORR. This finding is supported by experimental studies reported in Refs. 4 and 6, which showed that, after mixing g-

C_3N_4 with carbon black or incorporating g-C_3N_4 into CMK-3 framework, the ORR activity improves significantly in the 4 e^- transfer process.

4.3.4 g-C_3N_4 with Fe Single Atom Site for ORR

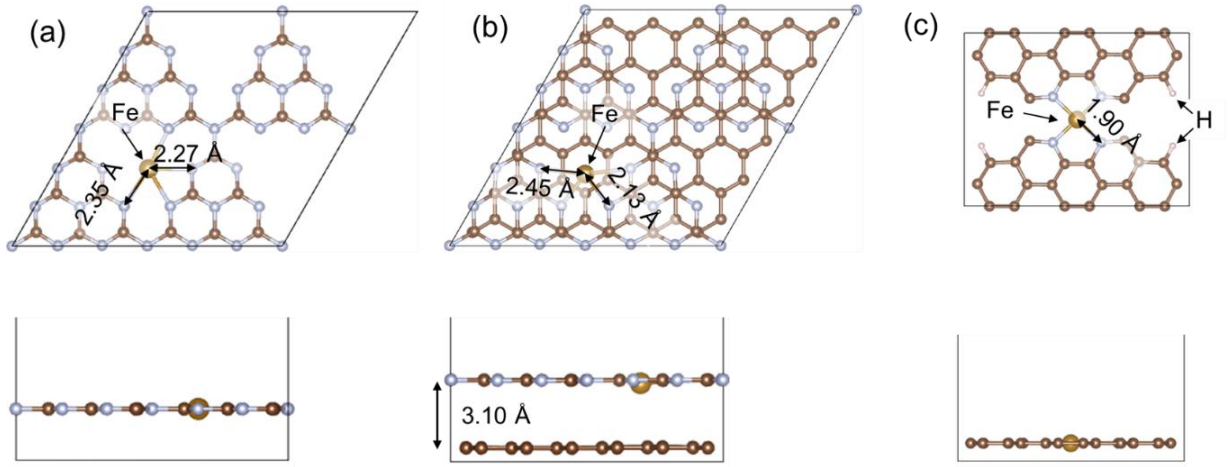


Figure 4.5. Optimized structures of (a) Fe/g-C_3N_4, (b) Fe/g-C_3N_4/GN (with an interlayer spacing of 3.10 Å), and (c) FeN_4 moiety in GN (edge passivated with H), adapted from Ref. [53]. The C, N, B, H atoms are in brown, gray, green, orange, and white, respectively. The black lines indicate the periodic cell boundaries. The distinct Fe–N bond lengths in each structure are labeled.

Iron-containing carbon materials are known to promote ORR.[25,26,29] The Fe species can be effectively stabilized by N species. Here, structures consisting of single-atom Fe were explored at various locations within the g-C_3N_4 lattice (Figure A.4). The most energetically favorable structure (Figure 4.5a) indicates that the Fe single atom is coordinated with 4 N_p atoms at the hollow site. The side view (Figure 4.5a) also shows that this Fe atom is *in-plane* with the g-C_3N_4 monolayer. A similar 4-coordinated configuration is preferred by the single-atom Fe species in the top layer of the g-C_3N_4 multilayer as well (Figure 4.5b). The four-coordinated Fe embedded in the graphene-like structure has been reported as the best Fe-N-C moiety (denoted as FeN_4) for ORR.[25,26,29] In

this study, the FeN_4 moiety suggested by Mun *et al*. and Liu *et al.*,[53,54] consisting of an Fe atom embedded among four N_p species in-between two GN armchair edges (Figure 4.5c adapted from Ref. 53), was adopted and used as a benchmark model. The four Fe–N bonds within the FeN_4 motif are symmetric (all at 1.90 Å), while the Fe–N bonds within g-C_3N_4 are stretched and unequal (at 2.35 Å and 2.27 Å as illustrated in Figure 4.5a). In Fe/g-C_3N_4/GN, the Fe–N bond lengths show an even more pronounced difference (2.45 Å and 2.13 Å in Figure 4.5b).

The electronic structures of the models depicted in Figure 4.5 are shown in Figure 4.6. Only the decomposed *sp*-states for N_p (green) and the *s*- and *d*-states for Fe (red and purple) that are directly responsible for the bonding are shown for clarity. The alignments between these states in Figure 4.6a and b confirm that the bonding between N_p and Fe atoms indeed exists, and, in turn, provides the primary support to stabilize the *in-plane* Fe atom in all the optimized structures. Also, the energy band gaps in both Fe/g-C_3N_4 and Fe/g-C_3N_4/GN are essentially eliminated. A closer examination suggests that the DOS for Fe/g-C_3N_4 shows a more pronounced occupied states near the Fermi level due to the Fe *d*-state, alluding the tendency to form stronger bonding with adsorbate with the frontier orbitals. The DOS profiles for Fe/g-C_3N_4/GN are more dispersive with a GN layer underneath than its Fe-free counterpart. As the benchmark, the DOS profiles of FeN_4 also feature excellent alignment at all the main peaks between the Fe *d*-state and the N_p *sp*-state. This is likely due to the shorter Fe–N_p bond length and symmetry within the FeN_4 configuration. The impact of the variations in the electronic structures on ORR is discussed in the following section.

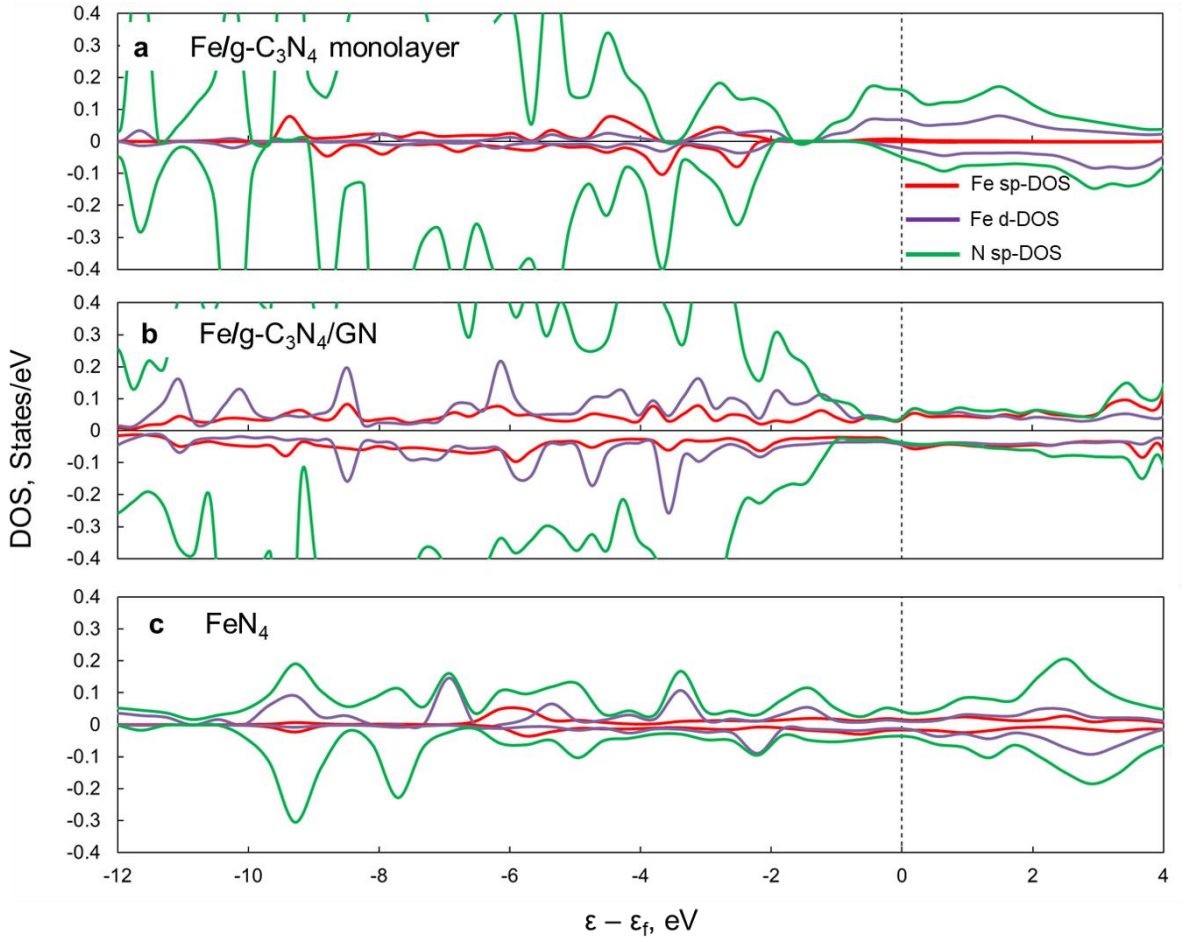


Figure 4.6**.** Projected density of states of (a) Fe/C_3N_4, (b) Fe/C_3N_4/GN, and (c) FeN_4. Only the decomposed *sp*-orbitals for N_p species (green) and the Fe valence electrons (s- and d-orbitals in red and purple respectively) are shown for clarity.

The Fe species is considered as the primary active site for ORR, although N_p species can still be available at the hollow site. The same set of species (O_2, OOH, O, and OH) was considered. The optimized structures at their preferred sites associated with Fe/g-C_3N_4 (a-d), g-C_3N_4/GN (e-h), and FeN_4 (i-l) are illustrated in Figure 4.7, and the corresponding BE_A values are listed in Table 4.3.

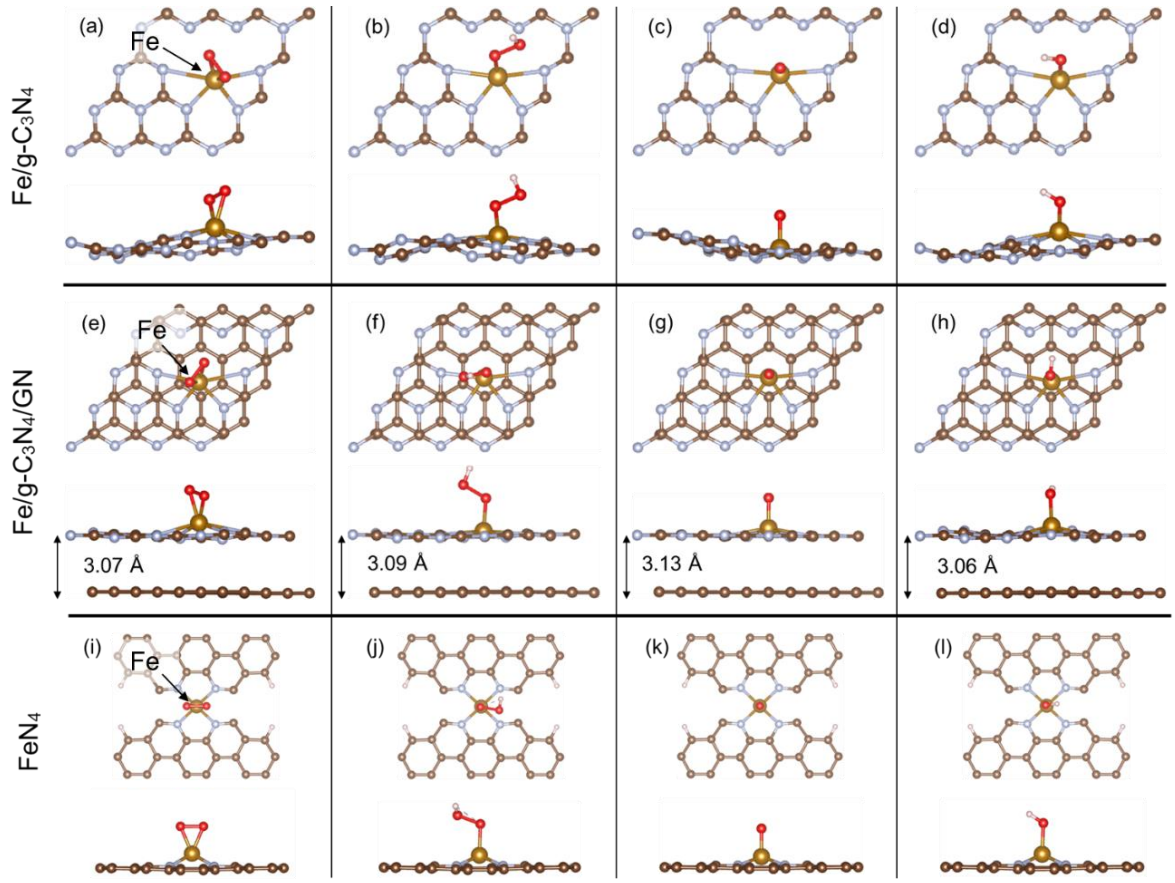


Figure 4.7. Optimized structures of O_2, OOH, O, and OH over Fe/C_3N_4 (a-d), Fe/C_3N_4/GN (e-h), and FeN_4 in GN (i-l). The C, N, B atoms are in brown, blue, and green, respectively.

Molecular O_2 binds with both its O atoms sharing the Fe atom (Figure 4.7a), accompanied by Fe being displaced out of a significantly relaxed g-C_3N_4 plane. The BE_{O_2} on Fe/g-C_3N_4 is -2.52 eV, which is 1.18 eV stronger than on the Fe-free layer. The enhanced O_2 binding on Fe/g-C_3N_4 is directly associated with the addition of Fe *d*-state. The calculated DOS profiles for O_2 adsorption are shown in Figure A.5(a-b) in the Appendix A, and the overlaps between the Fe *d*-state and the O *sp*-states on both Fe/g-C_3N_4 and Fe/g-C_3N_4/GN confirm O_2 chemisorption at the Fe site. Calculations performed on the fixed Fe/g-C_3N_4 monolayer produced a BE_{O_2} of -0.63 eV. This result suggests that, in addition to the Fe ion, substrate structural relaxation may also play a

significant role in further strengthening O_2 binding. With a GN layer underneath, the BE_{O_2} (-1.14 eV) is weaker than on the relaxed g-C_3N_4 monolayer (due to less extent of lattice relaxation, see Figure 4.7e), but significantly stronger than the Fe-free g-C_3N_4/GN bilayer. For comparison, BE_{O_2} on FeN_4 (-1.29 eV) is slightly stronger than on Fe/g-C_3N_4/GN. Since both Fe/g-C_3N_4/GN and FeN_4 do not display significantly different relaxations, the difference in O_2 binding strength should be attributed to the Fe site itself.

Table 4.3. Binding energies (BE_A in eV) of ORR intermediates on Fe/g-C_3N_4, Fe/g-C_3N_4/GN, and FeN_4.

Species	Fe/g-C_3N_4	Fe/g-C_3N_4/GN	FeN_4
O_2	-2.52	-1.14	-1.29
OOH	-3.24	-1.84	-1.54
O	-2.50	-1.41	-1.30
OH	-1.83	-0.40	-0.26

Regardless of the substrate, OOH binds with its open O-end at the Fe top site (Figure 4.7b, f, and j), as do O (Figure 4.7c, g, and k) and OH (Figure 4.7d, h, and i). The Fe atom always protrudes to facilitate bonding with the adsorbates. Similar to O_2 adsorption, all ORR intermediates exhibit strongest binding (Table 4.3), as well as the largest extent of relaxation for the g-C_3N_4 top layer. The BE_{O_2} for FeN_4 is slightly stronger, while the bindings for the remaining OOH, O, and OH species are consistently stronger on Fe/g-C_3N_4 instead.

Due to stronger O_2 binding, ORR proceeds with an explicit O_2 adsorption step, i.e., eq. (A.5), in the presence of an Fe site based on the 4 e^- pathway as proposed in Ref. 54. The remaining steps, eqs. (A.6-A.9) otherwise, resemble the process on the Fe-free g-C_3N_4. The free energy diagrams generated for ORR at Fe/g-C_3N_4, Fe/g-C_3N_4/GN, and FeN_4 are presented in Figure 4.8a.

The free energies corresponding to the Fe-free g-C_3N_4 monolayer (green) is also included for comparison. The ORR profile for Fe/g-C_3N_4 (orange) displays a steep free energy downhill until the OH formation step (eq. (A.8)) due to the strong bindings of O_2 and OH. However, the strong OH binding also produces a deep free energy *well*, making the OH removal step via eq. (A.9) very endothermic (1.83 eV). Hence, it is expected that the OH species will hinder the subsequent ORR steps by poisoning the Fe site. The predicted strong OH binding can also be reflected in term of the WP (-1.83 V) as shown in Figure 4.8b (orange bar). The free energy profile representing Fe/g-C_3N_4/GN is actually comparable to that of the Fe-free g-C_3N_4 monolayer, with the exception of OH removal. This is because the binding of OH at the Fe site is much stronger than at the N_p site (Fe-free). On the other hand, OH binding is weaker on Fe/g-C_3N_4/GN (Table 4.3). The ORR free energy profiles on Fe/g-C_3N_4/GN and FeN_4 are also in general good agreement. Both the potential-determining steps are the removal of OH. Thus, the respective WPs are determined by BE_{OH}, and are -0.4 V (red) for Fe/g-C_3N_4/GN and -0.26 V (blue) for FeN_4, The same potential-determining step on FeN_4 has been suggested previously in the literature.[54]

To further elucidate the difference between the Fe sites in Fe/g-C_3N_4 and Fe/g-C_3N_4/GN, the '*d*-band centers' of the Fe atom were calculated. The '*d*-band center' in Fe/g-C_3N_4/GN (-4.83 eV) has shifted away from the Fermi level when compared with Fe/g-C_3N_4 (-3.44 eV), the shift is consistent with the occupied states shown in Figure 4.6a. The consequence of such shift results in the lowering of the tendency for Fe to bond with adsorbates according to the *d*-band theory.[55,56] Herein, the theory is easily verified by weaker BE_{O_2} and BE_{OH} (Table 4.3) from the calculations. According to the finding of Pan *et al*.[57], a weaker OH binding is preferred in this case.

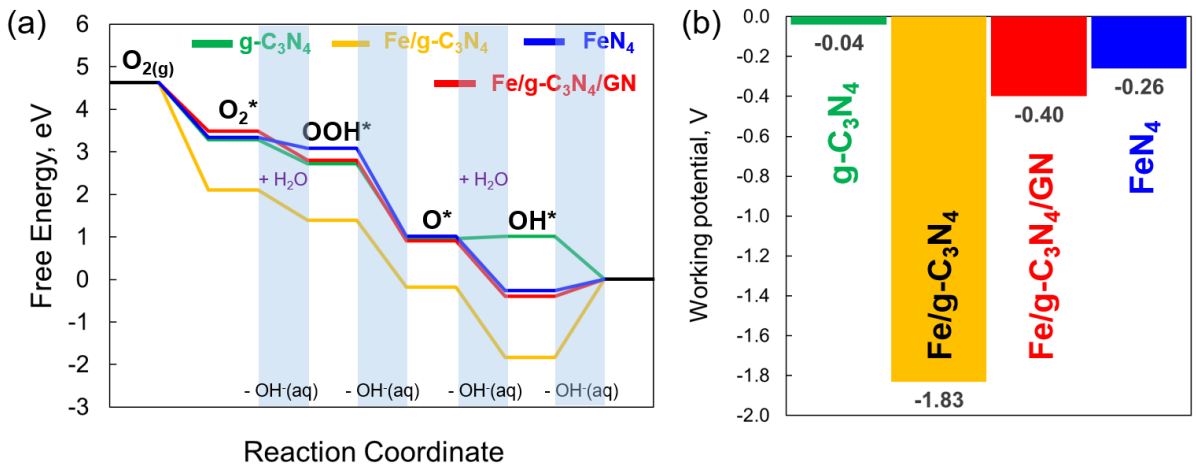


Figure 4.8. (a) Free energy diagrams of ORR on Fe-free g-C_3N_4 monolayer (green), Fe/g-C_3N_4 (yellow), Fe/g-C_3N_4/GN (red), and FeN_4 at 298 K and 1 bar, with zero applied potential; and (b) the limiting potentials (U_{lim}) corresponding to each system. Each charge transfer step, associated with the formation of hydroxide ion, i.e., OH^-(aq), is highlighted in blue.

In principle, without any free energy well in the ORR pathway, the WP should be negligible as for the case of the g-C_3N_4 monolayer in Figure 4.8b (green bar). It is the poor electronic property (large energy band gap) that limits its ORR application by hindering the charge transfer. In this work, we showed with DFT calculations that this intrinsic limitation can be overcome by the introduction of a GN layer or the Fe-dopants. Moreover, the overpotential associated with ORR can also be tuned. As shown in Figure 4.8b, the bindings of ORR intermediates also vary in the presence of either the Fe-dopant or the underneath layer. From this study, the g-C_3N_4/GN bilayer with the Fe species is found to be effective to enhance O_2 binding and for OH removal. As shown in Figure 4.8, the overall effect on ORR becomes comparable between Fe/g-C_3N_4/GN (red bar) and our FeN_4 benchmark (blue bar).

4.4 Conclusions

Periodic DFT calculations, performed using the HSE06 functional and the van der Waals corrections, showed that g-C_3N_4 lattices possess intrinsically reactivity toward ORR. However, the large energy band gap potentially is likely to hinder charge transfer. DFT calculations also revealed that the electronic structures of g-C_3N_4 can be tuned by pairing with 2D GN and hBN layers. In particular, the energy band gap for g-C_3N_4/GN can be significantly narrowed and becomes suitable for electrochemical applications. The energy band gap can be completely eliminated in the Fe-doped g-C_3N_4 and g-C_3N_4/GN bilayer. With DFT, the bindings of ORR reaction intermediates (i.e., O_2, OH) are tunable as well. While Fe/g-C_3N_4 binds O_2 too strongly, making OH removal difficult. Fe/g-C_3N_4/GN is predicted to weaken OH binding and enables similar ORR activity to some of the best Pt-free carbon-based ORR catalysts such as the GN-based FeN_4 structures.

References

(1) Wu, G.; More, K. L.; Johnston, C. M.; Zelenay, P. High-Performance Electrocatalysts for Oxygen Reduction Derived from Polyaniline, Iron, and Cobalt. *Science.* **2011**, *332* (6028), 443 – 447.

(2) Steele, B. C. H.; Heinzel, A. Materials for Fuel-Cell Technologies. *Nature* **2001**, *414* (6861), 345–352.

(3) Gong, K.; Du, F.; Xia, Z.; Durstock, M.; Dai, L. Nitrogen-Doped Carbon Nanotube Arrays with High Electrocatalytic Activity for Oxygen Reduction. *Science.* **2009**, *323* (5915), 760 – 764.

(4) Lyth, S. M.; Nabae, Y.; Moriya, S.; Kuroki, S.; Kakimoto, M.; Ozaki, J.; Miyata, S. Carbon Nitride as a Nonprecious Catalyst for Electrochemical Oxygen Reduction. *J. Phys. Chem. C* **2009**, *113* (47), 20148–20151.

(5) Yang, C.-J. An Impending Platinum Crisis and Its Implications for the Future of the Automobile. *Energy Policy* **2009**, *37* (5), 1805–1808.

(6) Zheng, Y.; Jiao, Y.; Chen, J.; Liu, J.; Liang, J.; Du, A.; Zhang, W.; Zhu, Z.; Smith, S. C.; Jaroniec, M.; Lu, G. Q. (Max); Qiao, S. Z. Nanoporous Graphitic-C3N4@Carbon Metal-Free Electrocatalysts for Highly Efficient Oxygen Reduction. *J. Am. Chem. Soc.* **2011**, *133* (50), 20116–20119.

(7) Yu, X.; Ye, S. Recent Advances in Activity and Durability Enhancement of Pt/C Catalytic

Cathode in PEMFC: Part I. Physico-Chemical and Electronic Interaction between Pt and Carbon Support, and Activity Enhancement of Pt/C Catalyst. *J. Power Sources* **2007**, *172* (1), 133–144.

(8) Yu, X.; Ye, S. Recent Advances in Activity and Durability Enhancement of Pt/C Catalytic Cathode in PEMFC: Part II: Degradation Mechanism and Durability Enhancement of Carbon Supported Platinum Catalyst. *J. Power Sources* **2007**, *172* (1), 145–154.

(9) Nie, Y.; Li, L.; Wei, Z. Recent Advancements in Pt and Pt-Free Catalysts for Oxygen Reduction Reaction. *Chem. Soc. Rev.* **2015**, *44* (8), 2168–2201.

(10) Joghee, P.; Pylypenko, S.; Wood, K.; Bender, G.; O'Hayre, R. High-Performance Alkaline Direct Methanol Fuel Cell Using a Nitrogen-Postdoped Anode. *ChemSusChem* **2014**, *7* (7), 1854–1857.

(11) Kolla, P.; Smirnova, A. Methanol Oxidation and Oxygen Reduction Activity of PtIrCo-Alloy Nanocatalysts Supercritically Deposited within 3D Carbon Aerogel Matrix. *Electrochim. Acta* **2015**, *182*, 20–30.

(12) Zou, X.; Wang, L.; Yakobson, B. I. Mechanisms of the Oxygen Reduction Reaction on B- and/or N-Doped Carbon Nanomaterials with Curvature and Edge Effects. *Nanoscale* **2018**, *10* (3), 1129–1134.

(13) Tan, C.; Cao, X.; Wu, X.-J.; He, Q.; Yang, J.; Zhang, X.; Chen, J.; Zhao, W.; Han, S.; Nam, G.-H.; Sindoro, M.; Zhang, H. Recent Advances in Ultrathin Two-Dimensional Nanomaterials. *Chem. Rev.* **2017**, *117* (9), 6225–6331.

(14) Xiang, Q.; Yu, J.; Jaroniec, M. Preparation and Enhanced Visible-Light Photocatalytic H2-Production Activity of Graphene/C3N4 Composites. *J. Phys. Chem. C* **2011**, *115* (15), 7355–7363.

(15) Low, J.; Cao, S.; Yu, J.; Wageh, S. Two-Dimensional Layered Composite Photocatalysts. *Chem. Commun.* **2014**, *50* (74), 10768–10777.

(16) Dai, K.; Lu, L.; Liu, Q.; Zhu, G.; Wei, X.; Bai, J.; Xuan, L.; Wang, H. Sonication Assisted Preparation of Graphene Oxide/Graphitic-C3N4 Nanosheet Hybrid with Reinforced Photocurrent for Photocatalyst Applications. *Dalt. Trans.* **2014**, *43* (17), 6295–6299.

(17) Li, H.; Wu, Y.; Li, C.; Gong, Y.; Niu, L.; Liu, X.; Jiang, Q.; Sun, C.; Xu, S. Design of Pt/t-ZrO2/g-C3N4 Efficient Photocatalyst for the Hydrogen Evolution Reaction. *Appl. Catal. B Environ.* **2019**, *251*, 305–312.

(18) Tian, J.; Liu, Q.; Ge, C.; Xing, Z.; Asiri, A. M.; Al-Youbi, A. O.; Sun, X. Ultrathin Graphitic Carbon Nitride Nanosheets: A Low-Cost, Green, and Highly Efficient Electrocatalyst toward the Reduction of Hydrogen Peroxide and Its Glucose Biosensing Application. *Nanoscale* **2013**, *5* (19), 8921–8924.

(19) Jin, H.; Guo, C.; Liu, X.; Liu, J.; Vasileff, A.; Jiao, Y.; Zheng, Y.; Qiao, S.-Z. Emerging Two-Dimensional Nanomaterials for Electrocatalysis. *Chem. Rev.* **2018**, *118* (13), 6337–6408.

(20) Mansor, N.; Miller, T. S.; Dedigama, I.; Jorge, A. B.; Jia, J.; Brázdová, V.; Mattevi, C.;

Gibbs, C.; Hodgson, D.; Shearing, P. R.; Howard, C. A.; Corà, F.; Shaffer, M.; Brett, D. J. L.; McMillan, P. F. Graphitic Carbon Nitride as a Catalyst Support in Fuel Cells and Electrolyzers. *Electrochim. Acta* **2016**, *222*, 44–57.

(21) An, S.; Zhang, G.; Wang, T.; Zhang, W.; Li, K.; Song, C.; Miller, J. T.; Miao, S.; Wang, J.; Guo, X. High-Density Ultra-Small Clusters and Single-Atom Fe Sites Embedded in Graphitic Carbon Nitride (g-C3N4) for Highly Efficient Catalytic Advanced Oxidation Processes. *ACS Nano* **2018**, *12* (9), 9441–9450.

(22) Wen, J.; Xie, J.; Chen, X.; Li, X. A Review on G-C3N4-Based Photocatalysts. *Appl. Surf. Sci.* **2017**, *391*, 72–123.

(23) Li, X.; Dai, Y.; Ma, Y.; Han, S.; Huang, B. Graphene/g-C3N4 Bilayer: Considerable Band Gap Opening and Effective Band Structure Engineering. *Phys. Chem. Chem. Phys.* **2014**, *16* (9), 4230–4235.

(24) Du, A.; Sanvito, S.; Li, Z.; Wang, D.; Jiao, Y.; Liao, T.; Sun, Q.; Ng, Y. H.; Zhu, Z.; Amal, R.; Smith, S. C. Hybrid Graphene and Graphitic Carbon Nitride Nanocomposite: Gap Opening, Electron–Hole Puddle, Interfacial Charge Transfer, and Enhanced Visible Light Response. *J. Am. Chem. Soc.* **2012**, *134* (9), 4393–4397.

(25) Hossen, M. M.; Artyushkova, K.; Atanassov, P.; Serov, A. Synthesis and Characterization of High Performing Fe-N-C Catalyst for Oxygen Reduction Reaction (ORR) in Alkaline Exchange Membrane Fuel Cells. *J. Power Sources* **2018**, *375*, 214–221.

(26) Wang, M.; Yang, Y.; Liu, X.; Pu, Z.; Kou, Z.; Zhu, P.; Mu, S. The Role of Iron Nitrides in the Fe–N–C Catalysis System towards the Oxygen Reduction Reaction. *Nanoscale* **2017**, *9* (22), 7641–7649.

(27) Jiang, W.-J.; Gu, L.; Li, L.; Zhang, Y.; Zhang, X.; Zhang, L.-J.; Wang, J.-Q.; Hu, J.-S.; Wei, Z.; Wan, L.-J. Understanding the High Activity of Fe–N–C Electrocatalysts in Oxygen Reduction: Fe/Fe3C Nanoparticles Boost the Activity of Fe–Nx. *J. Am. Chem. Soc.* **2016**, *138* (10), 3570–3578.

(28) Lee, D. H.; Lee, W. J.; Lee, W. J.; Kim, S. O.; Kim, Y.-H. Theory, Synthesis, and Oxygen Reduction Catalysis of Fe-Porphyrin-Like Carbon Nanotube. *Phys. Rev. Lett.* **2011**, *106* (17), 175502.

(29) Bezerra, C. W. B.; Zhang, L.; Lee, K.; Liu, H.; Marques, A. L. B.; Marques, E. P.; Wang, H.; Zhang, J. A Review of Fe–N/C and Co–N/C Catalysts for the Oxygen Reduction Reaction. *Electrochim. Acta* **2008**, *53* (15), 4937–4951.

(30) Zitolo, A.; Goellner, V.; Armel, V.; Sougrati, M.-T.; Mineva, T.; Stievano, L.; Fonda, E.; Jaouen, F. Identification of Catalytic Sites for Oxygen Reduction in Iron- and Nitrogen-Doped Graphene Materials. *Nat. Mater.* **2015**, *14* (9), 937–942.

(31) Lefèvre, M.; Proietti, E.; Jaouen, F.; Dodelet, J.-P. Iron-Based Catalysts with Improved Oxygen Reduction Activity in Polymer Electrolyte Fuel Cells. *Science.* **2009**, *324* (5923), 71 – 74.

(32) He, F.; Li, H.; Ding, Y.; Li, K.; Wang, Y.; Wu, Z. The Oxygen Reduction Reaction on Graphitic Carbon Nitride Supported Single Ce Atom and CexPt6-x Cluster Catalysts from

First-Principles. *Carbon N. Y.* **2018**, *130*, 636–644.

(33) He, F.; Li, K.; Yin, C.; Wang, Y.; Tang, H.; Wu, Z. Single Pd Atoms Supported by Graphitic Carbon Nitride, a Potential Oxygen Reduction Reaction Catalyst from Theoretical Perspective. *Carbon N. Y.* **2017**, *114*, 619–627.

(34) Kresse, G.; Furthmüller, J. Efficient Iterative Schemes for Ab Initio Total-Energy Calculations Using a Plane-Wave Basis Set. *Phys. Rev. B* **1996**, *54* (16), 11169–11186.

(35) Blöchl, P. E. Projector Augmented-Wave Method. *Phys. Rev. B* **1994**, *50* (24), 17953–17979.

(36) Perdew, J. P.; Burke, K.; Ernzerhof, M. Generalized Gradient Approximation Made Simple. *Phys. Rev. Lett.* **1996**, *77* (18), 3865–3868.

(37) Monkhorst, H. J.; Pack, J. D. Special Points for Brillouin-Zone Integrations. *Phys. Rev. B* **1976**, *13* (12), 5188–5192. https://doi.org/10.1103/PhysRevB.13.5188.

(38) Grimme, S. Semiempirical GGA-Type Density Functional Constructed with a Long-Range Dispersion Correction. *J. Comput. Chem.* **2006**, *27* (15), 1787–1799.

(39) Krukau, A. V; Vydrov, O. A.; Izmaylov, A. F.; Scuseria, G. E. Influence of the Exchange Screening Parameter on the Performance of Screened Hybrid Functionals. *J. Chem. Phys.* **2006**, *125* (22), 224106.

(40) Zhu, B.; Zhang, L.; Xu, D.; Cheng, B.; Yu, J. Adsorption Investigation of CO2 on G-C3N4 Surface by DFT Calculation. *J. CO2 Util.* **2017**, *21*, 327–335.

(41) Silva, A. M.; Rojas, M. I. Electric and Structural Properties of Polymeric Graphite Carbon Nitride (g-C3N4): A Density Functional Theory Study. *Comput. Theor. Chem.* **2016**, *1098*, 41–49.

(42) Zhi, X.; Jiao, Y.; Zheng, Y.; Qiao, S.-Z. Impact of Interfacial Electron Transfer on Electrochemical CO2 Reduction on Graphitic Carbon Nitride/Doped Graphene. *Small* **2019**, *15* (10), 1804224.

(43) Ghosh, D.; Periyasamy, G.; Pati, S. K. Transition Metal Embedded Two-Dimensional C3N4–Graphene Nanocomposite: A Multifunctional Material. *J. Phys. Chem. C* **2014**, *118* (28), 15487–15494.

(44) Shan, N.; Zhou, M.; Hanchett, M. K.; Chen, J.; Liu, B. Practical Principles of Density Functional Theory for Catalytic Reaction Simulations on Metal Surfaces – from Theory to Applications. *Mol. Simul.* **2017**, *43* (10–11), 861–885.

(45) Dean, J. A. *Lange's Handbook of Chemistry*; McGraw-Hill: New York, 1985.

(46) Nørskov, J. K.; Rossmeisl, J.; Logadottir, A.; Lindqvist, L.; Kitchin, J. R.; Bligaard, T.; Jónsson, H. Origin of the Overpotential for Oxygen Reduction at a Fuel-Cell Cathode. *J. Phys. Chem. B* **2004**, *108* (46), 17886–17892.

(47) Wang, X.; Blechert, S.; Antonietti, M. Polymeric Graphitic Carbon Nitride for Heterogeneous Photocatalysis. *ACS Catal.* **2012**, *2* (8), 1596–1606.

(48) Liu, X.; Dai, L. Carbon-Based Metal-Free Catalysts. *Nat. Rev. Mater.* **2016**, *1* (11), 16064.

(49) Qu, L.; Liu, Y.; Baek, J.-B.; Dai, L. Nitrogen-Doped Graphene as Efficient Metal-Free Electrocatalyst for Oxygen Reduction in Fuel Cells. *ACS Nano* **2010**, *4* (3), 1321–1326.

(50) Chen, X.; Chang, J.; Ke, Q. Probing the Activity of Pure and N-Doped Fullerenes towards Oxygen Reduction Reaction by Density Functional Theory. *Carbon N. Y.* **2018**, *126*, 53–57.

(51) Guo, D.; Shibuya, R.; Akiba, C.; Saji, S.; Kondo, T.; Nakamura, J. Active Sites of Nitrogen-Doped Carbon Materials for Oxygen Reduction Reaction Clarified Using Model Catalysts. *Science.* **2016**, *351* (6271), 361 – 365.

(52) Choi, C. H.; Lim, H.-K.; Chung, M. W.; Park, J. C.; Shin, H.; Kim, H.; Woo, S. I. Long-Range Electron Transfer over Graphene-Based Catalyst for High-Performing Oxygen Reduction Reactions: Importance of Size, N-Doping, and Metallic Impurities. *J. Am. Chem. Soc.* **2014**, *136* (25), 9070–9077.

(53) Liu, K.; Wu, G.; Wang, G. Role of Local Carbon Structure Surrounding FeN4 Sites in Boosting the Catalytic Activity for Oxygen Reduction. *J. Phys. Chem. C* **2017**, *121* (21), 11319–11324.

(54) Mun, Y.; Lee, S.; Kim, K.; Kim, S.; Lee, S.; Han, J. W.; Lee, J. Versatile Strategy for Tuning ORR Activity of a Single Fe-N4 Site by Controlling Electron-Withdrawing/Donating Properties of a Carbon Plane. *J. Am. Chem. Soc.* **2019**, *141* (15), 6254–6262.

(55) Hammer, B.; Nørskov, J. K. Electronic Factors Determining the Reactivity of Metal Surfaces. *Surf. Sci.* **1995**, *343* (3), 211–220.

(56) Norsko, J. K. Chemisorption on Metal Surfaces. *Reports Prog. Phys.* **1990**, *53* (10), 1253–1295.

(57) Pan, Y.; Sun, K.; Lin, Y.; Cao, X.; Cheng, Y.; Liu, S.; Zeng, L.; Cheong, W.-C.; Zhao, D.; Wu, K.; Liu, Z.; Liu, Y.; Wang, D.; Peng, Q.; Chen, C.; Li, Y. Electronic Structure and D-Band Center Control Engineering over M-Doped CoP (M = Ni, Mn, Fe) Hollow Polyhedron Frames for Boosting Hydrogen Production. *Nano Energy* **2019**, *56*, 411–419.

Chapter 5 - Graphene-Based Dual-Metal Sites for Oxygen Reduction Reaction

Chapter 5 is adapted with permission from:

Xu, J.; Elongovan, A.; Li, J.; Liu, B. "Graphene-Based Dual-Metal Sites for Oxygen Reduction Reaction: A Theoretical Study", Journal of Physical Chemistry C (Just accepted). DOI: https://doi.org/10.1021/acs.jpcc.0c10617.

5.1 Introduction

Fuel cell technology is an essential toolset to mitigate our dependence on fossil-based fuels and to better engage with sustainable energy sources.[1–3] The efficiency of direct methanol fuel cells (DMFCs) may reach up to 96.5%.[4,5] Currently, the choice for the electrocatalysts to carry out the cathodic oxygen reduction reaction (ORR) is primarily based on platinum group metals (PGMs);[6–8] however, the reliance on scarce catalytic materials poses severe limitation on achieving low-cost power generation (< $30/kW) for wide-ranging applications.[9]

Atomically dispersed transition metal single atom catalysts (SACs), containing PGM or non-PGM active centers (e.g., Fe, Co, and Mn), offer an appealing solution by enabling competitive ORR pathways under both acidic and alkaline conditions.[9–16] For example, the single Pt atom active site coordinated by N dopants has a half-wave potential (one key metric for ORR activity) of 0.87 V in alkaline solutions (versus 0.84 V on standard bulk Pt catalysts).[17] Even higher ORR activities have been reported on non-PGM single-atom Fe species anchored in N-doped graphitic carbon, with a half-wave potential that is 30 mV higher than the standard Pt/C in alkaline solutions.[18] The X-ray absorption near-edge structure (XANES) confirmed that single-atom Fe

active sites favor a FeN_4 configuration.[1,16,19–23] With single-atom Fe attributed to the active site, a maximal atomic utilization for ORR can be ensured.

A broader group of N-doped SACs based on the Metal-Nitrogen-Carbon (M-N-C) moieties are being discussed in the literature.[1,9,10,12,16,19,21,24,25] These M-N-C moieties display a rich variety in their central metal ions and ligand configurations. The ORR efficacy is also sensitive to the heteroatom co-dopants such as B,[14] P,[26] S,[13] or the presence of external ligands (e.g., OH,[24,27–30], O[28], Cl[31], NH_2[32], imidazole[33]) directly associated with the active centers.

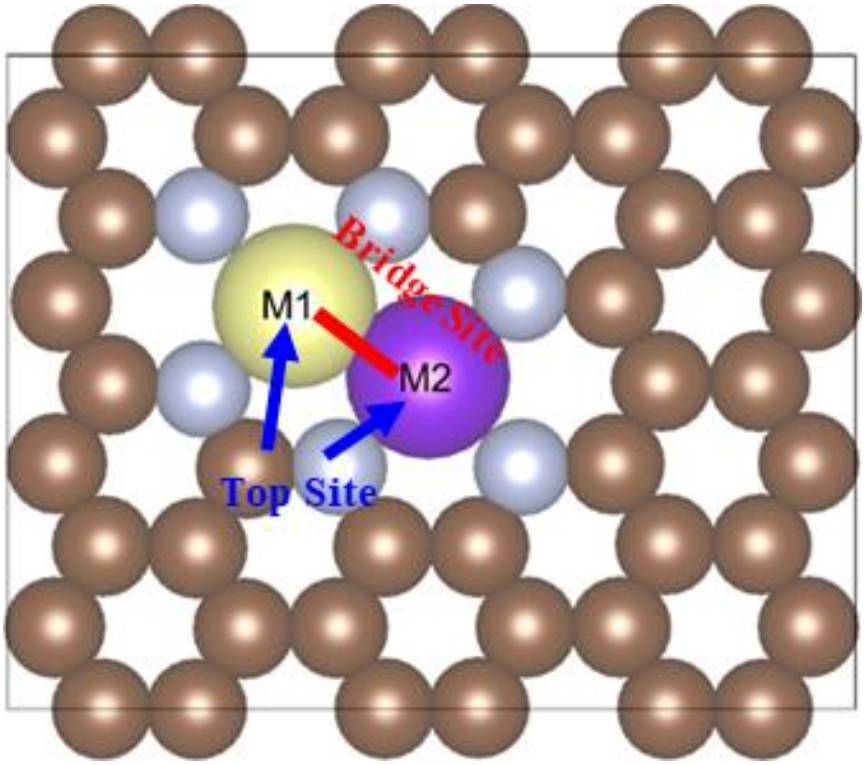


Figure 5.1. Molecular structure of dual-metal active center anchored with six pyridinic nitrogen atoms in a periodic monolayer graphene sheet. Color scheme: brown-graphitic carbon, gray-pyridinic nitrogen, yellow-Metal site 1 (M1), and purple-Metal site 2 (M2).

Dual-metal centers present extended forms of SAC.[10] It has been reported that Fe dimers retain high ORR activity and could be even more stable than the single-atom FeN_x configuration.[29,34] The investigation of ORR activity over a variety of dual-metal sites beyond Fe-Fe has also been carried out. Zinc,[35–37] iron,[38–42] or cobalt[36,37,40,43] containing dual-metal sites, paired with Ni, Cu, Pt, and Mn in characteristic MN_6 (see Figure 5.1) or MN_5-OH configurations, further enrich the repertoire of atomically dispersed electrocatalysts for ORR applications. On dual-metal sites, molecular O_2 binds frequently at the metal-metal bridge site.[26] The O–O bond cleavage is facilitated, and proceed at lower energy barriers as the dissociated species may occupy different metal sites that function synergistically.[39] The measured ORR activity on the Pt-Co dual-metal site catalyst is 267 times higher than the bulk Pt catalyst.[43] The Fe-Co is one remarkable dual-metal catalyst. The half-wave potentials obtained from the Fe-Co dual-metal system in respective acidic and alkaline solutions are 0.86 V and 0.95 V, versus 0.86 V and 0.84 V on Pt/C under comparable conditions.[39,44] The reported half-wave potentials for commercial Pt catalysts normally range from 0.8 to 0.9 V.[39,45,46] Therefore, the Fe-Co dual-metal catalyst are quite attractive for large-scale ORR applications.

One of the restraints in M-N-C moiety design is that the active sites must withstand potential structural decay or decomposition under harsh ORR reduction potentials during long-term operations.[9,10] Wang *et al*.[39] demonstrated that the Fe-Co dual-metal cathode showed almost no voltage loss over a period of 100 h in the $HClO_4$ (0.1 M) solution. Zhang *et al*.[40] also showed that the Fe-Co dual-metal site anchored in metal-organic frameworks exhibited negligible activity decay after 5000 voltage cycles in alkaline solutions (0.1 M KOH).

A number of theoretical dual-metal constructs have been proposed and investigated by Hunter *et al*. and Meng *et al*.[47,48] Here, we adopted a structure motif based on recent XANES and

extended C-ray adsorption fine structure (EXAFS) analyses, which revealed that the Fe-Co dual-metal site is coordinated with six pyridinic N atoms in direct contact binuclear metal center (see Figure 5.1).[39,44] Like single-metal sites (e.g., FeN_4), dual-metal configurations are also tunable through similar structure manipulation strategies. For instance, the potential-limiting step (PLS) (e.g., OH removal) is mitigated by including an external OH ligand due to the weakening of OH binding.[27,44] Density Functional Theory (DFT) calculations revealed that a weaker Fe-O bonding in $FeCoN_5$-OH leads to ORR activities surpassing that of FeN_4.[44] As reported by Holby and Taylor,[34] the limiting potential at the Fe-Fe center with a bridging OH ligand coordinated by five pyridinic N at the graphene edge improves to 0.8 V.

To systematically survey the potential of dual-metal ORR electrocatalysts, periodic DFT was employed to investigate the impact of pairing in dual-metal sites that consist of both PGM Pt, Pd, Fe, Co, Ni, and Cu elements. In particular, the influence of the external OH ligand on the ORR rate-limiting step will be understood. The trends and behaviors will be revealed through electronic structure calculations and mechanistic analyses.

5.2 Computational Methods

Periodic, spin-polarized DFT calculations were performed using the plane-wave based Vienna *Ab initio* Simulation Package (VASP).[49,50] The projector augmented wave (PAW) method was used to describe the wave functions of the ionic cores;[51] the generalized gradient approximation PBE functional was used to account for the electron exchange-correlation effects.[52] An energy cutoff of 520 eV was to determine the graphene (GN) lattice; 440 eV was applied for regular geometry optimizations of O_2, OOH, O, and OH adsorptions at the dual-metal sites. The Monkhorst-Pack *k*-point meshes of 6 × 6 × 4 was used for lattice optimization and 4 × 4 × 1 was used for regular geometry optimizations, correspondingly.[53] The convergence criterion for the self-

consistent iteration is 1×10^{-6} eV; the ionic relaxations stop when the force on each atom is less than 0.02 eV/Å. In this work, the Grimme's DFT-D3 theory was employed to account for the van der Waals interactions between adsorbates and substrates.[54]

As illustrated in Figure 5.1, the Fe-Co dual-metal site coordinated by 6 N atoms has been confirmed in nitrogen-doped carbon structures.[39,44] Here, all dual-metal sites were constructed in a similar fashion. The relative stabilities of dual-metal active sites (demoted as M1-M2) were evaluated with the formation energy defined by eq 5.1,[55] where the most stable crystal bulk of M1 and M2 elements, a pristine GN monolayer, and gas-phase N_2 were used as the reference state.

$$\Delta G_f = E_{dual-metal/GN} + 10\,\mu_C - E_{M1} - E_{M2} - E_{GN} - 3\mu_{N_2} \quad (5.1)$$

In eq 5.1, μ_C refers to the chemical potential of the carbon atom in a GN monolayer and its coefficient corresponds to the number of carbon atoms (10 atoms in total) removed to generate the vacancy to accommodate each dual-metal site. $E_{M1}$and E_{M2} are the total energies per atom in their respective bulk states. $E_{dual-metal/GN}$ and E_{GN} represent the total energies of GN monolayer with and without the dual-metal site, respectively. Lastly, μ_{N_2} represents the chemical potential of gas phase N_2 at 1 atm and 298 K. All gas-phase species were modeled in a large vacuum box (20 × 20 × 20 Å^3).

The adsorption energies of O_2*, OOH*, O*, and OH*, denoted $\Delta G_{O_2{}^*}$ ΔG_{OOH^*}, ΔG_{O^*}, and ΔG_{OH^*} were calculated based on eqs 5.2-5.5, using μ_{H_2O} and μ_{H_2} as references:

$$\Delta G_{O_2^*} = G_{O_2^*} - E_* - 2\left(\mu_{H_2O} - \mu_{H_2}\right) - 4.92 \quad (5.2)$$

$$\Delta G_{OOH^*} = G_{OOH^*} - E_* - (2\mu_{H_2O} - \frac{3}{2}\mu_{H_2}) \quad (5.3)$$

$$\Delta G_{O^*} = G_{O^*} - E_* - (\mu_{H_2O} - \mu_{H_2}) \quad (5.4)$$

$$\Delta G_{OH^*} = G_{OH^*} - E_* - (\mu_{H_2O} - \frac{1}{2}\mu_{H_2}) \quad (5.5)$$

$$\Delta G = \Delta E + \Delta ZPE - T\Delta S + \Delta G_U \quad (5.6)$$

Eq 5.6 was used to calculate the reaction free energy change for each elementary step, where ΔE represents the total energy change, ΔZPE and $T\Delta S$ represent the zero-point energy and entropy changes, respectively. For the former, we adopted the ΔZPE values reported by Nørskov and coworkers, i.e., 0.1, 0.4, 0.05, and 0.35 eV for O_2*, OOH*, O*, and OH*, respectively.[35,56–58] ΔG_U represents the energy contribution from the applied potential, $-neU$, where n is the number of electron transferred in each elementary step, and U is the applied electrode potential. The solvation energies of the liquid phase species, at 1 atm and room temperature, such as H_2O(l) were obtained from the free energy differences between its gas and aqueous phase according to Ref. [59].

$$O_2(g) + 2\,H_2O(l) + 4\,e^- \rightarrow 4\,OH^-(aq) \quad (R5.1)$$

$$O_2(g) + * \rightarrow O_2^* \quad (R5.2)$$

$$O_2^* + H_2O(l) + e^- \rightarrow OOH^* + OH^-(aq) \quad (R5.3)$$

$$O_2(g) + H_2O(l) + e^- + * \rightarrow OOH^* + OH^-(aq) \quad (R5.4)$$

$$OOH^* + e^- \rightarrow O^* + OH^-(aq) \quad (R5.5)$$

$$O^* + H_2O(l) + e^- \rightarrow OH^* + OH^-(aq) \quad (R5.6)$$

$$OH^* + e^- \rightarrow * + OH^-(aq) \quad (R5.7)$$

In this chapter, the ORR mechanism fitting for alkaline conditions is considered (R5.1). An outer-sphere electron transfer mechanism (as in R5.4) is frequently adopted if O_2 adsorption

on a crystalline catalyst surface is deemed weak.[46,60,61] However, for single atom active centers, the molecular O_2 adsorption state will play a more pronounced role in determining the rate-limiting potential.[60,62] Hence, the inner-sphere electron transfer mechanism(R5.2) will also be considered whenever $\Delta G_{O_2^*} < 0$.[60,61] Following R5.2, the adsorbed O_2 is converted into OOH via a H_2O-coupled charge transfer step (R5.3), producing one OH^- ion. If $\Delta G_{O_2^*} > 0$, R5.4 will still be used as the initial ORR step. In this step, weak OOH binding typically indicates that subsequent O–O bond cleavage will likely be the PLS. After forming OOH* by accepting a second charge (R5.5), the O–O bond cleavage occurs forming O* and another OH^-(aq). The O* species is then converted into OH* in a second H_2O-coupled charge transfer step (R5.6). Lastly, OH* desorbs as an OH^- ion by accepting the fourth charge to vacate the active site (R5.7), which has been widely recognized as the PLS when OH binding becomes too strong, as on the Fe-Fe or Co-Co dual-metal sites.[27]

The ORR limiting potential (U_{lim} in V), also referred as working potential[12,48,63] (or onset potential[47,64]) was employed to assess catalyst performance. Here, U_{lim} represents the largest free energy change among R5.3-R5.7,[14,35] and is expressed in eq 5.5.

$$U_{lim} = -\frac{max[\Delta G_{5.3}, \Delta G_{5.4}, \Delta G_{5.5}, \Delta G_{5.6}, \Delta G_{5.7}]}{e} \quad (5)$$

5.3 Results and Discussion

5.3.1 Stability of the Dual Metal Configurations

The structural stability of M-N-C motifs depends on specific metal-metal and/or metal-ligand configurations. The metal-ligand interactions will be mainly governed by the M–N type bonding (Figure 5.1). There is evidence showing that, even with subtle variations, such as the coordination numbers associated with the M–N bonding and the separations between metal ions, the ORR performance will be impacted.[47,48]

Table 5.1**.** Adsorption energies (in eV) of O_2, OOH, O, and OH, the dual-metal site formation energies (ΔG_f in eV), the limiting potentials (U_{lim} in V), and the corresponding PLS.

	$\Delta G_{O_2^*}$	ΔG_{OOH^*}	ΔG_{O^*}	ΔG_{OH^*}	ΔG_f	U_{lim}	PLS
Fe-Fe	-1.17	3.48	0.31	-0.13	4.07	-0.13	R7
Fe-Co	-0.94	3.96	0.46	0.35	4.00	0.02	R3
Fe-Ni	-0.62	3.97	0.77	0.34	3.92	0.33	R7
Fe-Cu	-0.94	3.70	1.00	0.27	4.24	0.27	R7
Co-Co	-1.05	1.94	0.48	0.02	4.40	0.02	R7
Co-Ni	-0.62	2.36	1.00	0.40	4.22	0.40	R7
Co-Cu	-0.31	4.12	1.54	0.70	4.34	0.48	R3
Ni-Ni	0.19	4.65	1.80	1.16	3.75	0.27	R4
Ni-Cu	0.21	4.66	2.24	1.21	4.12	0.26	R4
Cu-Cu	0.33	4.78	2.54	1.21	4.45	0.14	R4
Pt-Fe	-0.37	3.89	1.07	0.66	4.60	0.41	R6
Pt-Co	-0.27	3.98	1.14	0.55	4.98	0.55	R7
Pt-Ni	0.58	4.84	2.07	1.30	4.47	0.08	R4
Pt-Cu	0.61	4.93	2.64	1.42	4.64	-0.01	R4
Pd-Ni	0.34	4.79	2.12	1.28	4.46	0.13	R4
Pt-Pd	0.49	4.56	2.15	1.12	5.46	0.36	R4

The formation energies (ΔG_f) for the illustrated dual-metal sites (Figure 5.1) are presented in Table 5.1. Holby et al.[47] already showed that the FeN_4 site is less thermodynamically stable than the Fe-Fe dual-metal sites. According to eq 5.1, the lower formation energies indicate stronger cohesion for the overall system. The low ΔG_f values obtained for both Fe-Fe and Fe-Co dual-metal sites are supported by prior studies in the literature.[27,42,47] For instance, the formation energy of Fe-Co is slightly lower than that of Fe-Fe, which is consistent with Yang et al.[27,] and Hunter et al.[47] In an even broader context, the stability of Fe-Co under typical ORR conditions has been extensively confirmed with both experimental and theoretical approaches in these studies. Using the Fe-Co system as a benchmark, it can be learned that systems such as Fe-Ni, Fe-Cu, Co-Ni, and Ni-Cu also show comparable cohesive ΔG_f values to Fe-Co. On the other hand, Co-Co, Pt-Fe, Pt-

Co, and Pt-Pd are not as stable. Such information can be used as metric, in additional to their intrinsic ORR reactivity, for the purpose of future catalyst screening.

5.3.2 ORR at Dual Metal Sites

The preferred adsorptions of O_2, OOH, O, and OH at the top or the bridge site are illustrated in Figures B.1 and B.2 in Appendix B.. Molecular O_2 can bind in the di-σ, π, or η^1 configurations at these two-center dual-metal sites. The adsorption energies of O_2 will be used to determine the initial O_2 protonation in the $4e^-$ associative mechanism and are summarized in Table 5.1.

The hydroperoxyl (OOH) group always prefers the more oxophilic metal species at the dual-metal site, especially when a PGM atom (i.e., Pt, or Pd) is paired with Fe, Co, or Ni. For Fe-Ni and Fe-Cu, OOH preferers the top sites of Fe. In Pt-Pd, where both atoms are PGM species, OOH prefers the Pd site. The optimizations of OOH at the Co-Co and Co-Ni sites resulted in O-O cleavage, and in this case, the co-adsorptions of O and OH were considered instead. For the remaining dual-metal systems, their bridge or the tilted top site is preferred. As shown in Table 5.1, OOH binds the most strongly at the Fe-Fe site. The adsorption energy decreases for other Fe-containing hetero-nuclear dual-metal sites (i.e., one Fe is substituted by a different metal species). At Co-Cu, Ni-Ni, Ni-Cu, Cu-Cu, and the Pt(Pd)-containing dual-metal sites, the binding of OOH is much weaker.

The hydroxyl (OH) and atomic oxygen (O) always prefer the bridge site, but the calculated adsorption energies follow a similar pattern to OOH, that is, OH and O bind the most strongly at the Fe-Fe site, which is closely followed by Co-Co. The Ni-Cu, Cu-Cu, Pt-Cu, and Pd-Ni are among the weakest binding sites for OH and O.

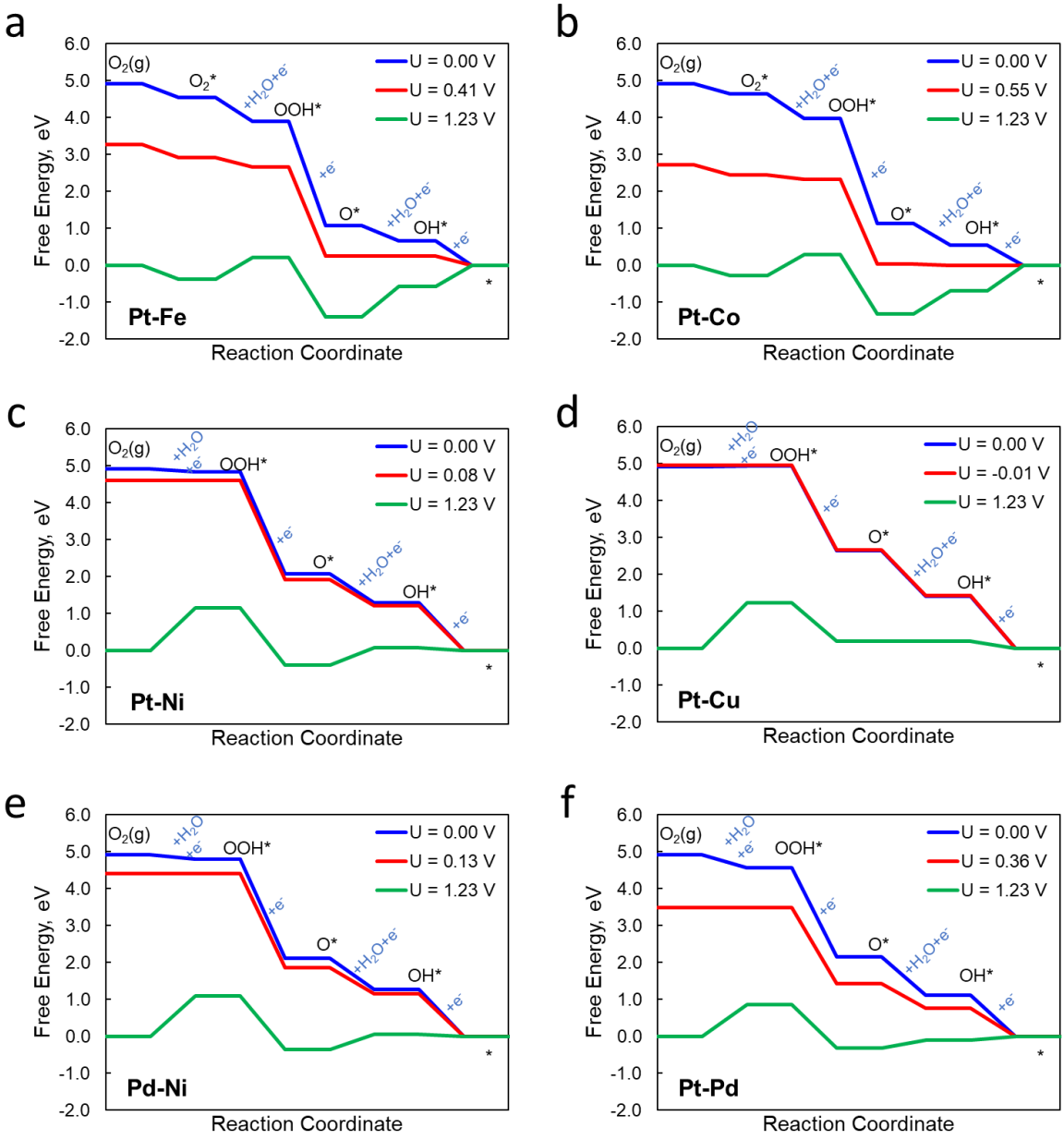


Figure 5.2. Free energy diagrams for six dual-metal sites: (a) Pt-Fe, (b) Pt-Co, (c) Pt-Ni, (d) Pt-Cu, (e) Pd-Ni, and (f) Pt-Pd, at U = 0 V (blue), U_{lim} (red), and U = 1.23 V (green). "*" indicates clean surface.

Dual-metal centers support the 4e$^-$ ORR pathways, as represented by R1.[27,44,65] The free energy diagrams for the six dual-metal systems containing Pt or Pd are summarized in Figure 5.2 at three applied potentials. The profiles at 0 V are shown in blue, and at their limiting potential

(U_{lim}) are shown in red. Also, the free energy profiles obtained at U = 1.23 V are shown in green. Based on $\Delta G_{O_2^*}$ listed in Table 5.1, ORR follows the outer-sphere electron transfer process (when $\Delta G_{O_2^*} > 0$) except at the Pt-Fe and Pt-Co sites. For Pt-Fe (Figures 5.2a) and Pt-Co (Figure 5.2b), the PLSs corresponds to the conversions of O* into OH* at the active site (R5.6) and the removal of OH* (R5.7), respectively. For Pt-Ni (Figure 5.2c), Pt-Cu (Figure 5.2d), Pd-Ni (Figure 5.2e), and Pt-Pd (Figure 5.2f), the protonation of gas-phase O_2 (R5.4) is the PLS, due to weak O_2 binding. For this group, the Pt-Co dual-metal site exhibits the highest limiting potential at 0.55 V.

The ORR free energy profiles representing the ten non-PGM dual-metal sites are summarized in Figure 5.3. On Fe-Fe (Figure 5.3a), O_2, OOH, O, and OH bind the strongest, and a negative U_{lim} (-0.13 V) is determined by the highly endothermic R7 step. At Fe-Co (Figure 5.3b) and Co-Cu (Figure 5.3g), U_{lim} is both determined by R3, involving the protonation of the adsorbed molecular O_2. The removal of OH* (R5.7) is the PLS for Fe-Ni (Figure 5.3c), Fe-Cu (Figure 5.3d), Co-Co (Figure 5.3e), and Co-Ni (Figure 5.3f). At the Ni-Ni (Figure 5.3h), Ni-Cu (Figure 5.3i), and Cu-Cu (Figure 5.3j) sites, ORR follows the outer-sphere electron transfer process, and it was shown that the U_{lim} is determined by R4 (the protonation of gas-phase O_2). Overall, a trend characterizing the ORR mechanism at the PGM-free dual-metal sites emerges: with decrease active site oxophilicity, the PLS transition from the late-stage OH* removal (R5.7), toward the protonation of adsorbed O (R5.6) and O_2 (R5.3), to the initial protonation of gas-phase O_2 (R5.4).

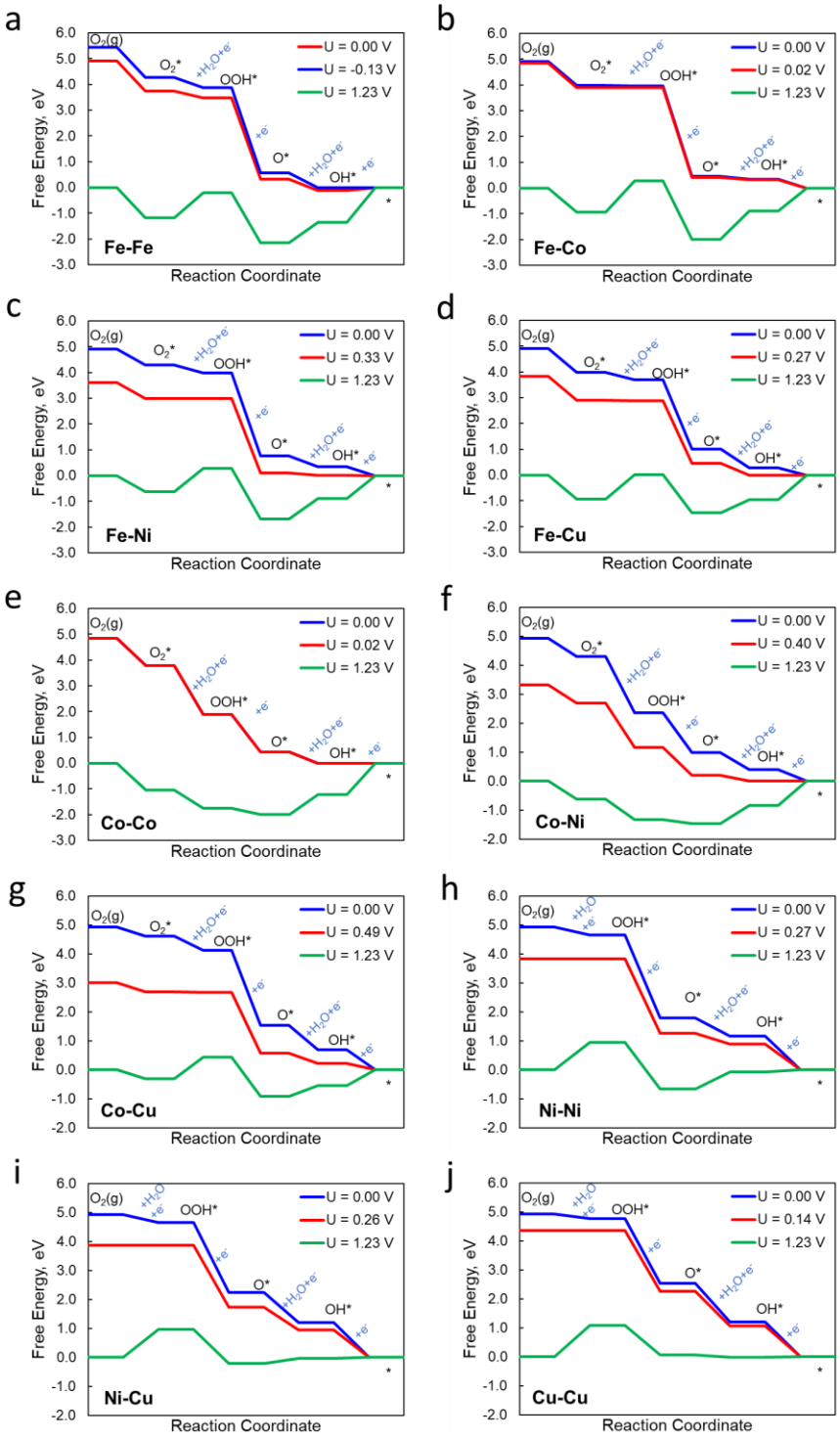


Figure 5.3. Free energy diagrams for ORR over PGM-free dual-metal sites: (a) Fe-Fe, (b) Fe-Co, (c) Fe-Ni, (d) Fe-Cu, (e) Co-Co, (f) Co-Ni, (g) Co-Cu, (h) Ni-Ni, (i) Ni-Cu, and (j) Cu-Cu, at U = 0 V (blue), U_{lim} (red), and U = 1.23 V (green). "*" indicates clean surface.

5.3.3 ORR at the Dual Metal Sites Modified by OH Ligands

It has been shown that the strong binding OH at the Fe single-atom site also modulate the active site electronic structures with implications to ORR performance.[10,24,27,28,30,34,44,66] As reported by Yang et al.,[67] the OH ligand originates either from the ORR intermediate (in acidic environments) or directly from alkaline solutions. In this work, assuming alkaline conditions, an OH group was left at those dual-metal sites (with R7 as the PLS), which are denoted as M1-M2(OH). Subscripts 'o' and 's' are added to indicate ORR intermediates bind at the opposite or the same side of the pre-adsorbed OH ligand. The adsorption energies of ORR intermediates at the modified M1-M2 dual-metal sites are shown in Tables 5.2 (for M1-M2(OH)$_o$) and S1 (for M1-M2(OH)$_s$).

The top and side views of the optimized O_2, OOH, O, and OH on M1-M2(OH)$_o$ are illustrated in Figure B.3 in Appendix B. As shown in Table 5.2, the $\Delta G_{O_2^*}$ for all six dual-metal systems favors a molecular adsorption state, that is, $\Delta G_{O_2^*} < 0$, and were included in the ORR mechanism. Molecular O_2 prefers the bridge or the top site of the more oxophilic metal species in M1-M2(OH)$_o$.

Table 5.2. Adsorption energies (in eV) of O_2, OOH, O, and OH, limiting potentials (U_{lim} in V), and the corresponding PLS for M1-M2(OH)$_o$. Subscription "o" indicates binding sites are on the opposite side of the OH ligand.

	$\Delta G_{O_2^*}$	ΔG_{OOH^*}	ΔG_{O^*}	ΔG_{OH^*}	U_{lim}	PLS
Fe-Fe(OH)$_o$	-0.83	4.07	1.13	0.70	0.02	R3
Fe-Co(OH)$_o$	-0.76	3.90	1.19	0.53	0.26	R3
Fe-Ni(OH)$_o$	-0.44	4.11	1.52	0.76	0.37	R3
Fe-Cu(OH)$_o$	-0.16	4.17	1.88	0.80	0.59	R3
Co-Co(OH)$_o$	-0.32	4.42	2.14	1.07	0.18	R3
Co-Ni(OH)$_o$	-0.15	4.42	2.14	1.04	0.35	R3
Pt-Co(OH)$_o$	-0.24	4.15	2.27	0.82	0.53	R3

The OOH species always prefer the top site of the more oxophilic metal species for M1-M2(OH)$_o$. As shown in Table 5.2, OOH binds the most strongly on Fe-Co(OH)$_o$, followed by Fe-Fe(OH)$_o$, Fe-Ni(OH)$_o$, Pt-Co(OH)$_o$, and Fe-Cu(OH)$_o$. On Fe-Fe(OH)$_o$, Fe-Co(OH)$_o$, Fe-Ni(OH)$_o$, Co-Co(OH)$_o$, Co-Ni(OH)$_o$, atomic O prefers the bridge site as a bridging oxygen; while on Fe-Cu(OH)$_o$ and Pt-Co(OH)$_o$, O prefers the Fe (or Co) top site as an oxo-group (Figure B.3). The O also binds the most strongly on Fe-Fe(OH)$_o$. For OH, the top sites of the more oxophilic metal atoms are preferred except for Fe-Fe(OH)$_o$ (Figure B.3). Just like OOH, OH binds most strongly on Fe-Co(OH)$_o$, followed by Fe-Fe(OH)$_o$, Fe-Ni(OH)$_o$, Fe-Cu(OH)$_o$, and Pt-Co(OH)$_o$. In fact, all ORR intermediates bind weaker than on ligand-free sites except for OOH at Fe-Co(OH)$_o$ (Table 5.2). Particularly, ΔG_{OH^*} universally shifts toward more positive values (i.e., weaker binding), compared with the bare dual-metal sites.

It has been previously shown that the singe-atom Fe-N-C motifs modified by the S, or P dopant in the π-bonded carbon supports exhibit enhanced ORR performance.[13,68] Functional groups with excess electrons in the proximity of the metal centers are shown to weaken the adsorbate binding by lowering the *d*-band center. Theoretically, the calculated net changes of the charges carried by the metal centers in all these systems changes inversely with the adsorption energies of OH.[48,68] The Bader charge analysis was performed on all M1-M2(OH) systems and is presented in Figure B.4 in Appendix B. Figure 5.4 shows that, with the non-participating OH ligand, charges are transferred away from the active sites (more positive Bader charge) when compared with the bare dual-metal centers. Furthermore, subsequent OH binding became weaker in the presence of an OH ligand. This observation further confirms that the electron withdrawing effects as ligands shifts the d-band centers downward.

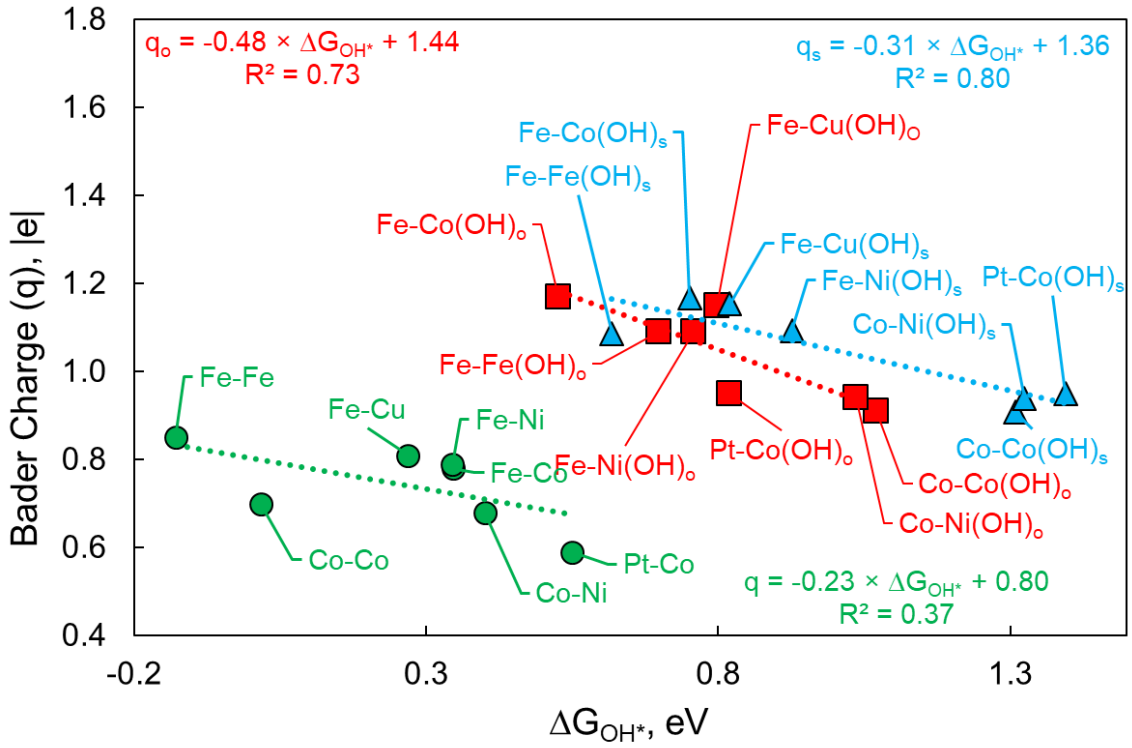


Figure 5.4. Relationship between ΔG_{OH^*} (eV) and the Bader charge (q, in |e|) at the OH binding site. The colored lines are used to guide the trend. Green indicates the relationship for the dual-metal sites without OH ligand, blue indicates the relationship on the same side with OH ligand, and red indicates the relationship on the opposite side of OH ligand.

Figure 5.5 summarizes the free energy diagrams for the ORR on M1-M2(OH)$_o$. At U = 0 V, the energy profiles of considered M1-M2(OH)$_o$ systems show exothermic behaviors. According to the respective limiting potentials (red), the OH ligand shifts the potential-limiting step from R7 to R3. The U_{lim} associated with Fe-Fe(OH)$_o$ (Figure 5.5a) has increased substantially to 0.02 V. In fact, all the variations in calculated U_{lim} indicate that the OH ligand plays an active role in facilitating OH desorption to varied extents. The U_{lim} values for Fe-Co(OH)$_o$ (Figure 5.5b), Fe-Ni(OH)$_o$ (Figure 5.5c), Fe-Cu(OH)$_o$ (Figure 5.5d), and Co-Co(OH)$_o$ (Figure 5.5e) have all risen, from 0.02 V 0.33 V, 0.27 V. and 0.02 to 0.26 V 0.37 V, 0.59 V, and 0.18 V, respectively. The

enhancement on ORR activity at these dual-metal sites associated with the OH ligand is consistent with the observations reported in recent literature.[24,28,30,34,44,66] However, for Co-Ni(OH)$_o$ and Pt-Co(OH)$_o$, the presence of a OH ligand weakens OOH binding, and will thus hinder ORR. Not surprisingly, the limiting potentials decrease from 0.40 V to 0.35 V, and from 0.55 V to 0.53 V correspondingly.

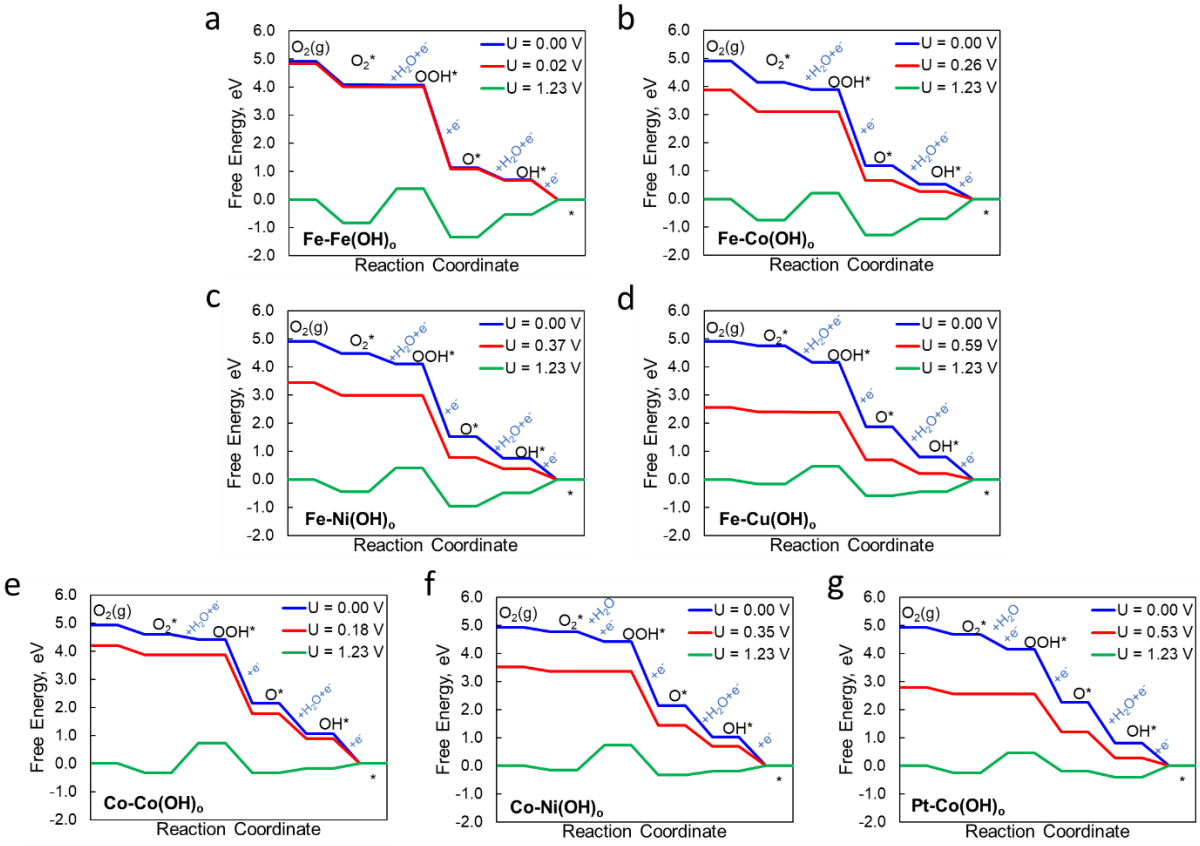


Figure 5.5. Free energy diagrams for (a) Fe-Fe(OH)$_o$, (b) Fe-Co(OH)$_o$, (c) Fe-Ni(OH)$_o$, (d) Fe-Cu(OH)$_o$, (e) Co-Co(OH)$_o$, (f) Co-Ni(OH)$_o$, and (g) Pt-Co(OH)$_o$ at U = 0 V (blue), U_{lim} (red), and U = 1.23 V (green). "*" indicates clean surface. The subscript 'o' indicates ORR happens at the opposite side of OH ligand.

Adsorptions of O_2, OOH, O, and OH on M1-M2$(OH)_s$ were also considered and are shown in Figure B.5 in Appendix B, and the adsorption energies are summarized in Table B.1 in Appendix B. Unlike the bare and M1-M2$(OH)_o$ systems, the OH ligand at the bridge site will potentially block the access of other intermediates to this site as their first choice. Geometry optimizations showed that O_2, OOH, O, and OH all will bind at the top sites of the oxophilic metal species. In general, the adsorptions of ORR intermediates are further weakened. This consequence is reflected that ORR now follows an inner-sphere electron transfer process that is only applicable for Fe-Fe$(OH)_s$ and Fe-Co$(OH)_s$.

The free energy profiles are summarized in Figure B.6 in Appendix B. The U_{lim} for Fe-Fe$(OH)_s$ is still determined by the OH removal step (R5.7), while the PLS for the remaining M1-M2$(OH)_s$ is the protonation of gas-phase O_2 forming OOH (R5.4). The highest U_{lim} were obtained from Fe-Fe$(OH)_s$, Fe-Co$(OH)_s$, Fe-Ni$(OH)_s$, and Fe-Cu$(OH)_s$, at 0.62 V, 0.73 V, 0.62 V, and 0.59 V, respectively. However, at the Co-Ni$(OH)_s$ and Pt-Co$(OH)_s$ sites, as shown in Figure 5.5, U_{lim} lower than that of the bare Co-Ni and Pt-Co sites were obtained due to weakened OOH binding.

Previous studies have established linear correlations among ORR intermediates for the purpose of ORR catalyst screening.[48,69,70] In this study, similar linear correlations were observed for O (ΔG_{O^*}), OOH (ΔG_{OOH^*}) (Figure 5.6a), as well as molecular O_2 ($\Delta G_{O_2^*}$) (Figure B.7) against ΔG_{OH^*} on the dual-metal sites with and without OH ligand. The slope for the correlation between OH and O (1.62, see Figure 3.6a) is in a good agreement the value (1.49) reported by Meng and coworkers.[48] The slope the correlation between OH and OOH is 0.92 (also see Figure 3.6a), which is also consistent extensively with previous reports (i.e., ~1).[48,70–73] Most notably, a decent correlation, with a slope of 1.11 (R^2 = 0.84), between OH and the adsorbed O_2 was also established as shown in Figure B.7 in Appendix B. A rather broad range of $\Delta G_{O_2^*}$ values (-1.2~0.5 eV) was

observed, indicating that the binding of molecular O_2 is sensitive to the compositions of the dual-metal sites. For systems such as Fe-Fe, Co-Co, such as stable O_2 adsorption state (without O-O bond cleavage) may not be completely neglected.

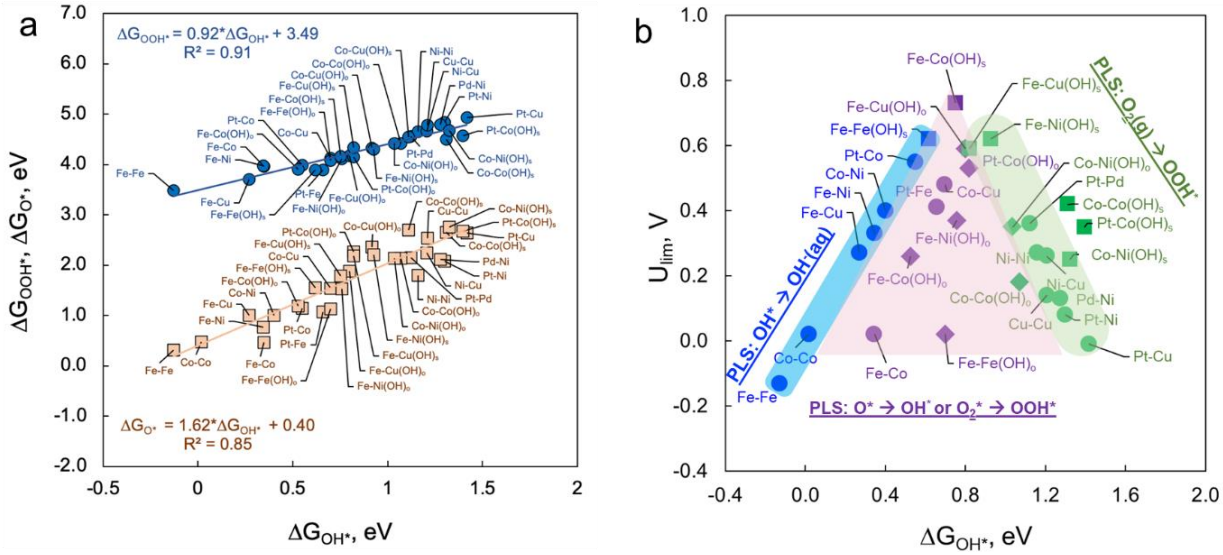


Figure 5.6. (a) Linear scaling relationships between ΔG_{OH} and ΔG_O (orange) and G_{OH} and G_{OOH} (blue). (b) Predicted U_{lim} as a function of G_{OH}. Systems associated with the potential-limiting step (PLS), $OH^* \rightarrow OH^-_{(aq)}$ (left side), are colored in blue; systems associated with the PLS, $O^* \rightarrow OH^*$ or $O_2^* \rightarrow OOH^*$ (middle), are colored in purple; and system associated with the PLS, $O_{2(g)} \rightarrow OOH^*$ (right side), are colored in green. In addition, the bare dual-metal centers are represented in dots; the dual-metal centers with ORR occurring on the same side with the OH ligand are represented by squares; and the dual-metal centers with ORR occurring on the opposite side of the OH ligand are represented by diamonds.

When the U_{lim} for all dual-metal systems are organized based on ΔG_{OH^*} (Figure 5.6b), U_{lim} peaks at the ΔG_{OH^*} value of approximately 0.8 V. Moreover, the dual-metal systems included in this *volcano*-like trend can be generally grouped in three regimes following the identified PLS: (I) strong OH binding dual-metal sites with R7 as the PLS; (II) intermediate OH binding dual-

metal sites with R3 or R6 as the PLS; and (III) weak OH binding dual-metal sites with R4 as the PLS. The dual-metal sites in regime I (blue) form a strictly linear left boundary, as shown Figure 5.6b. In this case, U_{lim} is purely dictated by ΔG_{OH^*}, which is also used as the ORR performance descriptor. Almost all the dual-metal systems in this regime are OH-ligand free (represented by dots) except for Fe-Fe$(OH)_s$. It is also evident that all these dual-metal sites contain at least one Fe or Co, which are both strong OH binding species. On the other hand, the right boundary formed by the dual-metal sites from regime III (green) is more scattered governed by $\Delta G_{O_2^*}$ instead. Hence, the less-define nature reflects the correlation between ΔG_{OH^*} and $\Delta G_{O_2^*}$ (Figure B.7). By inspection, common elemental species in these dual-metal sites are Pt, Pd, Cu, Ni, occasionally coupled with Fe, and Co. When Fe or Co is present, the dual-metal site always contains the OH ligand, as M1-M2$(OH)_s$ (square). In this case, as discussed previously, the OH ligand tends to weaken the bindings of O_2, O, OH, and OOH much more effectively. The ORR performance in the dual-metal systems in regimes I and III is governed by one of the two conventional mechanisms, that is, either the strong OH binding (left leg) or the protonation of free O_2 molecule (right leg).[35,47,48,69,70]

In Figure 5.6b, we also identified several dual-metal systems (highlighted in purple) located in regime II. These diverse group contains bare dual-metal sites (dots), such as Fe-Co, Pt-Fe, Co-Cu; same-side OH ligand (squares) such as Fe-Co$(OH)_s$; and opposite-side OH ligand (diamonds) such as Fe-Fe$(OH)_o$, Fe-Co$(OH)_o$, Fe-Ni$(OH)_o$, and Pt-Co$(OH)_o$. In this regime corresponding to intermediate ΔG_{OH^*}, the PLS that determines U_{lim} is the protonation of either O or O_2 adsorbed at the dual-metal sites.

Overall, the mechanistic study based on DFT suggest that dual-metal compositions, ligands, and locations of ORR allow molecular O_2 adsorption to play an influential role and to subsequently alter the potential limiting step. Ramaswamy[60] has also recognized the necessity to consider O_2

adsorption at SAC sites in their respective investigations. In our final analysis, we tracked the variations of U_{lim} for the Fe-Co system to further elucidate the impact from the OH ligand. Interestingly, all three Fe-Co, Fe-Co(OH)$_o$, and Fe-Co(OH)$_s$ systems are located in regime II. Also, the Fe-Co dual-metal site has already been reported for its promising ORR reactivity in a number of literature studies.[27,39,44,47,48] Without explicitly considering molecular O_2 adsorption at the Fe-Co site, the ORR has been suggested to be hindered by the difficulty in OH removal (i.e., R7).[27,31,47]

Molecular O_2 has a stable adsorption state on bare Fe-Co with a $\Delta G_{O_2^*}$ of -0.94 eV. The associated U_{lim} is 0.02 V (lower purple region in Figure 5.6b) with the protonation of adsorbed O_2 (R5.3) as the PLS. In Fe-Co(OH)$_o$, ΔG_{OH^*} becomes more positive. Nevertheless, the PLS remains the same despite a small shift toward right, but U_{lim} rises above 0.2 V. In Fe-Co(OH)$_s$, ΔG_{OH^*} continues to shift right (even more positive). At this point, the U_{lim} increases significantly to 0.73 V. This value matches the results predicted by Wang and coworkers.[44] Moreover, other PGM-free dual-metal sites, such as Fe-Fe, Co-Co, and Fe-Cu, also exhibit enhanced ORR activities by the OH ligand. By comparing with the FeN_4 motif,[74] which yields the limiting potential as 0.46 V, the dual-metal centers indeed display improved performance. The outstanding ORR activity of Fe-Co(OH)$_s$ shows good consistency with Wang's work.[39,44] It is very encouraging to note that PGM-free catalysts are capable of replacing PGM based ORR catalysts.

5.4 Conclusions

DFT calculations were performed on a variety of dual-metal active centers coordinated by six pyridinic nitrogen embedded in GN monolayer for 4e$^-$ ORR. Both PGM (Pt and Pd) and non-PGM (Fe, Co, Ni, and Cu) metal species were considered. Moreover, the OH group was deliberately considered as a modulating ligand for the charge redistribution at the dual-metal sites

that naturally bind OH strongly. The ORR reactivities at these dual-metal sites can be depicted in terms of a volcano diagram divided distinctively by multiple PLSs. Specifically, the traditional OH removal and the protonation of gas-phase O_2 remain as the two boundaries for the ORR reactivity volcano when too strong or weak OH binding occurs at the active sites, respectively. However, due to the strong molecular O_2 adsorption at the dual-metal sites, protonation of adsorbed O_2 and O species also emerge as likely the PLSs and thus enrich the electrochemistry for ORR. Among all dual-metal sites, Fe-Co$(OH)_s$ is predicted to have the highest limiting potential, with a U_{lim} of 0.73 V, which remains consistent with findings with literature findings. Also, the PGM-free dual-metal sites such as Fe-Fe(OH), Fe-Cu(OH), and Co-Co(OH) also appear to be competitive and could encourage further explorations for Pt-free ORR electrocatalysts.

References

(1) Lefèvre, M.; Proietti, E.; Jaouen, F.; Dodelet, J.-P. Iron-Based Catalysts with Improved Oxygen Reduction Activity in Polymer Electrolyte Fuel Cells. *Science.* **2009**, *324* (5923), 71 – 74.

(2) Debe, M. K. Electrocatalyst Approaches and Challenges for Automotive Fuel Cells. *Nature* **2012**, *486* (7401), 43–51.

(3) Staffell, I.; Scamman, D.; Velazquez Abad, A.; Balcombe, P.; Dodds, P. E.; Ekins, P.; Shah, N.; Ward, K. R. The Role of Hydrogen and Fuel Cells in the Global Energy System. *Energy Environ. Sci.* **2019**, *12* (2), 463–491.

(4) Tiwari, J. N.; Tiwari, R. N.; Singh, G.; Kim, K. S. Recent Progress in the Development of Anode and Cathode Catalysts for Direct Methanol Fuel Cells. *Nano Energy* **2013**, *2* (5), 553–578.

(5) Zou, L.; Fan, J.; Zhou, Y.; Wang, C.; Li, J.; Zou, Z.; Yang, H. Conversion of PtNi Alloy from Disordered to Ordered for Enhanced Activity and Durability in Methanol-Tolerant Oxygen Reduction Reactions. *Nano Res.* **2015**, *8* (8), 2777–2788.

(6) Elangovan, A.; Xu, J.; Brown, E.; Liu, B.; Li, J. Fundamental Electrochemical Insights of Vertically Aligned Carbon Nanofiber Architecture as a Catalyst Support for ORR. *J. Electrochem. Soc.* **2020**, *167* (6), 66523.

(7) Bing, Y.; Liu, H.; Zhang, L.; Ghosh, D.; Zhang, J. Nanostructured Pt-Alloy Electrocatalysts for PEM Fuel Cell Oxygen Reduction Reaction. *Chem. Soc. Rev.* **2010**, *39* (6), 2184–2202.

(8) Marković, N. M.; Schmidt, T. J.; Stamenković, V.; Ross, P. N. Oxygen Reduction Reaction on Pt and Pt Bimetallic Surfaces: A Selective Review. *Fuel Cells* **2001**, *1* (2), 105–116.

(9) He, Y.; Liu, S.; Priest, C.; Shi, Q.; Wu, G. Atomically Dispersed Metal–Nitrogen–Carbon Catalysts for Fuel Cells: Advances in Catalyst Design, Electrode Performance, and Durability Improvement. *Chem. Soc. Rev.* **2020**.

(10) Zhu, Y.; Sokolowski, J.; Song, X.; He, Y.; Mei, Y.; Wu, G. Engineering Local Coordination Environments of Atomically Dispersed and Heteroatom-Coordinated Single Metal Site Electrocatalysts for Clean Energy-Conversion. *Adv. Energy Mater.* **2019**, *n/a* (n/a), 1902844.

(11) Xu, J.; Liu, B. Intrinsic Properties of Nitrogen-Rich Carbon Nitride for Oxygen Reduction Reaction. *Appl. Surf. Sci.* **2020**, *500*, 144020.

(12) Zhao, J.; Wang, W.; Qu, X.; Meng, Y.; Wu, Z. M-Porphyrin (M = Mn, Co) Carbon Materials as Oxygen Reduction Catalysts from Density Functional Studies. *Mol. Phys.* **2019**, 1–9.

(13) Mun, Y.; Lee, S.; Kim, K.; Kim, S.; Lee, S.; Han, J. W.; Lee, J. Versatile Strategy for Tuning ORR Activity of a Single Fe-N4 Site by Controlling Electron-Withdrawing/Donating Properties of a Carbon Plane. *J. Am. Chem. Soc.* **2019**, *141* (15), 6254–6262.

(14) Saputro, A. G.; Fajrial, A. K.; Maulana, A. L.; Fathurrahman, F.; Agusta, M. K.; Akbar, F. T.; Dipojono, H. K. Dissociative Oxygen Reduction Reaction Mechanism on the Neighboring Active Sites of a Boron-Doped Pyrolyzed Fe–N–C Catalyst. *J. Phys. Chem. C* **2020**, *124* (21), 11383–11391.

(15) Liu, K.; Wu, G.; Wang, G. Role of Local Carbon Structure Surrounding FeN4 Sites in Boosting the Catalytic Activity for Oxygen Reduction. *J. Phys. Chem. C* **2017**, *121* (21), 11319–11324.

(16) Lee, D. H.; Lee, W. J.; Lee, W. J.; Kim, S. O.; Kim, Y.-H. Theory, Synthesis, and Oxygen Reduction Catalysis of Fe-Porphyrin-Like Carbon Nanotube. *Phys. Rev. Lett.* **2011**, *106* (17), 175502.

(17) Liu, J.; Jiao, M.; Lu, L.; Barkholtz, H. M.; Li, Y.; Wang, Y.; Jiang, L.; Wu, Z.; Liu, D.; Zhuang, L.; Ma, C.; Zeng, J.; Zhang, B.; Su, D.; Song, P.; Xing, W.; Xu, W.; Wang, Y.; Jiang, Z.; Sun, G. High Performance Platinum Single Atom Electrocatalyst for Oxygen Reduction Reaction. *Nat. Commun.* **2017**, *8* (1), 15938.

(18) Yang, L.; Cheng, D.; Xu, H.; Zeng, X.; Wan, X.; Shui, J.; Xiang, Z.; Cao, D. Unveiling the High-Activity Origin of Single-Atom Iron Catalysts for Oxygen Reduction Reaction. *Proc. Natl. Acad. Sci.* **2018**, *115* (26), 6626 – 6631.

(19) Zitolo, A.; Goellner, V.; Armel, V.; Sougrati, M.-T.; Mineva, T.; Stievano, L.; Fonda, E.; Jaouen, F. Identification of Catalytic Sites for Oxygen Reduction in Iron- and Nitrogen-Doped Graphene Materials. *Nat. Mater.* **2015**, *14* (9), 937–942.

(20) Wu, G.; More, K. L.; Johnston, C. M.; Zelenay, P. High-Performance Electrocatalysts for Oxygen Reduction Derived from Polyaniline, Iron, and Cobalt. *Science.* **2011**, *332* (6028), 443 – 447.

(21) Hossen, M. M.; Artyushkova, K.; Atanassov, P.; Serov, A. Synthesis and Characterization of High Performing Fe-N-C Catalyst for Oxygen Reduction Reaction (ORR) in Alkaline Exchange Membrane Fuel Cells. *J. Power Sources* **2018**, *375*, 214–221.

(22) Wang, M.; Yang, Y.; Liu, X.; Pu, Z.; Kou, Z.; Zhu, P.; Mu, S. The Role of Iron Nitrides in the Fe–N–C Catalysis System towards the Oxygen Reduction Reaction. *Nanoscale* **2017**, *9* (22), 7641–7649.

(23) Jiang, W.-J.; Gu, L.; Li, L.; Zhang, Y.; Zhang, X.; Zhang, L.-J.; Wang, J.-Q.; Hu, J.-S.; Wei, Z.; Wan, L.-J. Understanding the High Activity of Fe–N–C Electrocatalysts in Oxygen Reduction: Fe/Fe3C Nanoparticles Boost the Activity of Fe–Nx. *J. Am. Chem. Soc.* **2016**, *138* (10), 3570–3578.

(24) Martinez, U.; Holby, E. F.; Babu, S. K.; Artyushkova, K.; Lin, L.; Choudhury, S.; Purdy, G. M.; Zelenay, P. Experimental and Theoretical Trends of PGM-Free Electrocatalysts for the Oxygen Reduction Reaction with Different Transition Metals. *J. Electrochem. Soc.* **2019**, *166* (7), F3136–F3142.

(25) Szakacs, C. E.; Lefèvre, M.; Kramm, U. I.; Dodelet, J.-P.; Vidal, F. A Density Functional Theory Study of Catalytic Sites for Oxygen Reduction in Fe/N/C Catalysts Used in H2/O2 Fuel Cells. *Phys. Chem. Chem. Phys.* **2014**, *16* (27), 13654–13661.

(26) Ma, T. Y.; Ran, J.; Dai, S.; Jaroniec, M.; Qiao, S. Z. Phosphorus-Doped Graphitic Carbon Nitrides Grown In Situ on Carbon-Fiber Paper: Flexible and Reversible Oxygen Electrodes. *Angew. Chemie Int. Ed.* **2015**, *54* (15), 4646–4650.

(27) Yang, Y.; Zhang, H.; Liang, Z.; Yin, Y.; Mei, B.; Song, F.; Sun, F.; Gu, S.; Jiang, Z.; Wu, Y.; Zhu, Z. Role of Local Coordination in Bimetallic Sites for Oxygen Reduction: A Theoretical Analysis. *J. Energy Chem.* **2020**, *44*, 131–137.

(28) Anderson, A. B.; Holby, E. F. Pathways for O2 Electroreduction over Substitutional FeN4, HOFeN4, and OFeN4 in Graphene Bulk Sites: Critical Evaluation of Overpotential Predictions Using LGER and CHE Models. *J. Phys. Chem. C* **2019**, *123* (30), 18398–18409.

(29) Holby, E. F.; Zelenay, P. Linking Structure to Function: The Search for Active Sites in Non-Platinum Group Metal Oxygen Reduction Reaction Catalysts. *Nano Energy* **2016**, *29*, 54–64.

(30) Chung, H. T.; Cullen, D. A.; Higgins, D.; Sneed, B. T.; Holby, E. F.; More, K. L.; Zelenay, P. Direct Atomic-Level Insight into the Active Sites of a High-Performance PGM-Free ORR Catalyst. *Science (80-.).* **2017**, *357* (6350), 479 LP – 484.

(31) Han, Y.; Wang, Y.; Xu, R.; Chen, W.; Zheng, L.; Han, A.; Zhu, Y.; Zhang, J.; Zhang, H.; Luo, J.; Chen, C.; Peng, Q.; Wang, D.; Li, Y. Electronic Structure Engineering to Boost Oxygen Reduction Activity by Controlling the Coordination of the Central Metal. *Energy Environ. Sci.* **2018**, *11* (9), 2348–2352.

(32) Jia, Q.; Ramaswamy, N.; Hafiz, H.; Tylus, U.; Strickland, K.; Wu, G.; Barbiellini, B.; Bansil,

A.; Holby, E. F.; Zelenay, P.; Mukerjee, S. Experimental Observation of Redox-Induced Fe–N Switching Behavior as a Determinant Role for Oxygen Reduction Activity. *ACS Nano* **2015**, *9* (12), 12496–12505.

(33) Zhu, H.; Paddison, S. J.; Zawodzinski, T. A. The Effects of the Ligand, Central Metal, and Solvent on the O2 Binding of Non-Precious Metal Catalyst Model Systems: An Ab Initio Study. *Electrochim. Acta* **2013**, *101*, 293–300.

(34) Holby, E. F.; Taylor, C. D. Activity of N-Coordinated Multi-Metal-Atom Active Site Structures for Pt-Free Oxygen Reduction Reaction Catalysis: Role of *OH Ligands. *Sci. Rep.* **2015**, *5* (1), 9286.

(35) Cao, L.; Shao, Y.; Pan, H.; Lu, Z. Designing Efficient Dual-Metal Single-Atom Electrocatalyst TMZnN6 (TM = Mn, Fe, Co, Ni, Cu, Zn) for Oxygen Reduction Reaction. *J. Phys. Chem. C* **2020**, *124* (21), 11301–11307.

(36) Lu, Z.; Wang, B.; Hu, Y.; Liu, W.; Zhao, Y.; Yang, R.; Li, Z.; Luo, J.; Chi, B.; Jiang, Z.; Li, M.; Mu, S.; Liao, S.; Zhang, J.; Sun, X. An Isolated Zinc–Cobalt Atomic Pair for Highly Active and Durable Oxygen Reduction. *Angew. Chemie Int. Ed.* **2019**, *58* (9), 2622–2626.

(37) Liu, D.; Wang, B.; Li, H.; Huang, S.; Liu, M.; Wang, J.; Wang, Q.; Zhang, J.; Zhao, Y. Distinguished Zn,Co-Nx-C-Sy Active Sites Confined in Dentric Carbon for Highly Efficient Oxygen Reduction Reaction and Flexible Zn-Air Batteries. *Nano Energy* **2019**, *58*, 277–283.

(38) Chen, P.; Zhou, T.; Xing, L.; Xu, K.; Tong, Y.; Xie, H.; Zhang, L.; Yan, W.; Chu, W.; Wu, C.; Xie, Y. Atomically Dispersed Iron–Nitrogen Species as Electrocatalysts for Bifunctional Oxygen Evolution and Reduction Reactions. *Angew. Chemie Int. Ed.* **2017**, *56* (2), 610–614.

(39) Wang, J.; Huang, Z.; Liu, W.; Chang, C.; Tang, H.; Li, Z.; Chen, W.; Jia, C.; Yao, T.; Wei, S.; Wu, Y.; Li, Y. Design of N-Coordinated Dual-Metal Sites: A Stable and Active Pt-Free Catalyst for Acidic Oxygen Reduction Reaction. *J. Am. Chem. Soc.* **2017**, *139* (48), 17281–17284.

(40) Zhang, D.; Chen, W.; Li, Z.; Chen, Y.; Zheng, L.; Gong, Y.; Li, Q.; Shen, R.; Han, Y.; Cheong, W.-C.; Gu, L.; Li, Y. Isolated Fe and Co Dual Active Sites on Nitrogen-Doped Carbon for a Highly Efficient Oxygen Reduction Reaction. *Chem. Commun.* **2018**, *54* (34), 4274–4277.

(41) Wang, B.; Zou, J.; Shen, X.; Yang, Y.; Hu, G.; Li, W.; Peng, Z.; Banham, D.; Dong, A.; Zhao, D. Nanocrystal Supracrystal-Derived Atomically Dispersed Mn-Fe Catalysts with Enhanced Oxygen Reduction Activity. *Nano Energy* **2019**, *63*, 103851.

(42) Holby, E. F.; Wu, G.; Zelenay, P.; Taylor, C. D. Structure of Fe–Nx–C Defects in Oxygen Reduction Reaction Catalysts from First-Principles Modeling. *J. Phys. Chem. C* **2014**, *118* (26), 14388–14393.

(43) Zhang, L.; Fischer, J. M. T. A.; Jia, Y.; Yan, X.; Xu, W.; Wang, X.; Chen, J.; Yang, D.; Liu, H.; Zhuang, L.; Hankel, M.; Searles, D. J.; Huang, K.; Feng, S.; Brown, C. L.; Yao, X. Coordination of Atomic Co–Pt Coupling Species at Carbon Defects as Active Sites for

Oxygen Reduction Reaction. *J. Am. Chem. Soc.* **2018**, *140* (34), 10757–10763.

(44) Wang, J.; Liu, W.; Luo, G.; Li, Z.; Zhao, C.; Zhang, H.; Zhu, M.; Xu, Q.; Wang, X.; Zhao, C.; Qu, Y.; Yang, Z.; Yao, T.; Li, Y.; Lin, Y.; Wu, Y.; Li, Y. Synergistic Effect of Well-Defined Dual Sites Boosting the Oxygen Reduction Reaction. *Energy Environ. Sci.* **2018**, *11* (12), 3375–3379.

(45) Chung, S.; Ham, K.; Kang, S.; Ju, H.; Lee, J. Enhanced Corrosion Tolerance and Highly Durable ORR Activity by Low Pt Electrocatalyst on Unique Pore Structured CNF in PEM Fuel Cell. *Electrochim. Acta* **2020**, *348*, 136346.

(46) Ge, X.; Sumboja, A.; Wuu, D.; An, T.; Li, B.; Goh, F. W. T.; Hor, T. S. A.; Zong, Y.; Liu, Z. Oxygen Reduction in Alkaline Media: From Mechanisms to Recent Advances of Catalysts. *ACS Catal.* **2015**, *5* (8), 4643–4667.

(47) Hunter, M. A.; Fischer, J. M. T. A.; Yuan, Q.; Hankel, M.; Searles, D. J. Evaluating the Catalytic Efficiency of Paired, Single-Atom Catalysts for the Oxygen Reduction Reaction. *ACS Catal.* **2019**, *9* (9), 7660–7667.

(48) Meng, Y.; Yin, C.; Li, K.; Tang, H.; Wang, Y.; Wu, Z. Improved Oxygen Reduction Activity in Heteronuclear FeCo-Codoped Graphene: A Theoretical Study. *ACS Sustain. Chem. Eng.* **2019**, *7* (20), 17273–17281.

(49) Kresse, G.; Furthmüller, J. Efficient Iterative Schemes for Ab Initio Total-Energy Calculations Using a Plane-Wave Basis Set. *Phys. Rev. B* **1996**, *54* (16), 11169–11186.

(50) Kresse, G.; Furthmüller, J. Efficiency of Ab-Initio Total Energy Calculations for Metals and Semiconductors Using a Plane-Wave Basis Set. *Comput. Mater. Sci.* **1996**, *6* (1), 15–50.

(51) Kresse, G.; Joubert, D. From Ultrasoft Pseudopotentials to the Projector Augmented-Wave Method. *Phys. Rev. B* **1999**, *59* (3), 1758–1775.

(52) Perdew, J. P.; Burke, K.; Ernzerhof, M. Generalized Gradient Approximation Made Simple. *Phys. Rev. Lett.* **1996**, *77* (18), 3865–3868.

(53) Monkhorst, H. J.; Pack, J. D. Special Points for Brillouin-Zone Integrations. *Phys. Rev. B* **1976**, *13* (12), 5188–5192.

(54) Grimme, S.; Antony, J.; Ehrlich, S.; Krieg, H. A Consistent and Accurate Ab Initio Parametrization of Density Functional Dispersion Correction (DFT-D) for the 94 Elements H-Pu. *J. Chem. Phys.* **2010**, *132* (15), 154104.

(55) Kattel, S.; Wang, G. A Density Functional Theory Study of Oxygen Reduction Reaction on Me–N4 (Me = Fe, Co, or Ni) Clusters between Graphitic Pores. *J. Mater. Chem. A* **2013**, *1* (36), 10790–10797.

(56) Nørskov, J. K.; Rossmeisl, J.; Logadottir, A.; Lindqvist, L.; Kitchin, J. R.; Bligaard, T.; Jónsson, H. Origin of the Overpotential for Oxygen Reduction at a Fuel-Cell Cathode. *J. Phys. Chem. B* **2004**, *108* (46), 17886–17892.

(57) Zhao, S.; Wang, K.; Zou, X.; Gan, L.; Du, H.; Xu, C.; Kang, F.; Duan, W.; Li, J. Group VB

Transition Metal Dichalcogenides for Oxygen Reduction Reaction and Strain-Enhanced Activity Governed by p-Orbital Electrons of Chalcogen. *Nano Res.* **2019**, *12* (4), 925–930.

(58) Deng, Q.; Zhao, J.; Wu, T.; Chen, G.; Hansen, H. A.; Vegge, T. 2D Transition Metal–TCNQ Sheets as Bifunctional Single-Atom Catalysts for Oxygen Reduction and Evolution Reaction (ORR/OER). *J. Catal.* **2019**, *370*, 378–384.

(59) Dean, J. A. *Lange's Handbook of Chemistry*; McGraw-Hill: New York, 1985.

(60) Ramaswamy, N.; Mukerjee, S. Fundamental Mechanistic Understanding of Electrocatalysis of Oxygen Reduction on Pt and Non-Pt Surfaces: Acid versus Alkaline Media. *Adv. Phys. Chem.* **2012**, *2012*, 491604.

(61) Choi, C. H.; Lim, H.-K.; Chung, M. W.; Park, J. C.; Shin, H.; Kim, H.; Woo, S. I. Long-Range Electron Transfer over Graphene-Based Catalyst for High-Performing Oxygen Reduction Reactions: Importance of Size, N-Doping, and Metallic Impurities. *J. Am. Chem. Soc.* **2014**, *136* (25), 9070–9077.

(62) Anderson, A. B. Insights into Electrocatalysis. *Phys. Chem. Chem. Phys.* **2012**, *14* (4), 1330–1338.

(63) Liu, S.; Cheng, L.; Wang, W.; Li, K.; Wang, Y.; Wu, Z. Fe-Porphyrin Carbon Matrix as a Bifunctional Catalyst for Oxygen Reduction and CO2 Reduction from Theoretical Perspective. *Mol. Phys.* **2019**, *117* (14), 1805–1812.

(64) Nagaprasad Reddy, S.; Krishnamurthy, C. B.; Grinberg, I. First-Principles Study of the Ligand Substituent Effect on ORR Catalysis by Metallocorroles. *J. Phys. Chem. C* **2020**, *124* (21), 11275–11283.

(65) Singh, K.; Razmjooei, F.; Yu, J.-S. Active Sites and Factors Influencing Them for Efficient Oxygen Reduction Reaction in Metal-N Coordinated Pyrolyzed and Non-Pyrolyzed Catalysts: A Review. *J. Mater. Chem. A* **2017**, *5* (38), 20095–20119.

(66) Wang, Y.; Tang, Y.-J.; Zhou, K. Self-Adjusting Activity Induced by Intrinsic Reaction Intermediate in Fe–N–C Single-Atom Catalysts. *J. Am. Chem. Soc.* **2019**, *141* (36), 14115–14119.

(67) Yang, X.; Xia, D.; Kang, Y.; Du, H.; Kang, F.; Gan, L.; Li, J. Unveiling the Axial Hydroxyl Ligand on Fe□N4□C Electrocatalysts and Its Impact on the PH-Dependent Oxygen Reduction Activities and Poisoning Kinetics. *Adv. Sci.* **2020**, *7* (12), 2000176.

(68) Chen, Y.; Ji, S.; Zhao, S.; Chen, W.; Dong, J.; Cheong, W.-C.; Shen, R.; Wen, X.; Zheng, L.; Rykov, A. I.; Cai, S.; Tang, H.; Zhuang, Z.; Chen, C.; Peng, Q.; Wang, D.; Li, Y. Enhanced Oxygen Reduction with Single-Atomic-Site Iron Catalysts for a Zinc-Air Battery and Hydrogen-Air Fuel Cell. *Nat. Commun.* **2018**, *9* (1), 5422.

(69) Greeley, J.; Stephens, I. E. L.; Bondarenko, A. S.; Johansson, T. P.; Hansen, H. A.; Jaramillo, T. F.; Rossmeisl, J.; Chorkendorff, I.; Nørskov, J. K. Alloys of Platinum and Early Transition Metals as Oxygen Reduction Electrocatalysts. *Nat. Chem.* **2009**, *1* (7), 552–556.

(70) Kulkarni, A.; Siahrostami, S.; Patel, A.; Nørskov, J. K. Understanding Catalytic Activity Trends in the Oxygen Reduction Reaction. *Chem. Rev.* **2018**, *118* (5), 2302–2312.

(71) Viswanathan, V.; Hansen, H. A.; Rossmeisl, J.; Nørskov, J. K. Universality in Oxygen Reduction Electrocatalysis on Metal Surfaces. *ACS Catal.* **2012**, *2* (8), 1654–1660.

(72) Siahrostami, S.; Tsai, C.; Karamad, M.; Koitz, R.; García-Melchor, M.; Bajdich, M.; Vojvodic, A.; Abild-Pedersen, F.; Nørskov, J. K.; Studt, F. Two-Dimensional Materials as Catalysts for Energy Conversion. *Catal. Letters* **2016**, *146* (10), 1917–1921.

(73) Stephens, I. E. L.; Bondarenko, A. S.; Grønbjerg, U.; Rossmeisl, J.; Chorkendorff, I. Understanding the Electrocatalysis of Oxygen Reduction on Platinum and Its Alloys. *Energy Environ. Sci.* **2012**, *5* (5), 6744–6762.

(74) Liu, F.; Zhu, G.; Yang, D.; Jia, D.; Jin, F.; Wang, W. Systematic Exploration of N, C Configurational Effects on the ORR Performance of Fe–N Doped Graphene Catalysts Based on DFT Calculations. *RSC Adv.* **2019**, *9* (39), 22656–22667.

Chapter 6 - C-H Bond Activation and Oxidation of Alkane over Cu-MOR

Chapter 6 is adapted with permission from:

Xu, J.; Liu, B. "Modeling C-H Bond Activation and Oxidations of Alkanes over Cu-MOR Using First-Principles Methods", Journal of Physical Chemistry C. 2019, 123, 10356-10366.

6.1 Introduction

Methane and C2-C3 light hydrocarbons (i.e., ethane and propane) are abundant hydrocarbon feedstocks for catalytic upgrading to obtain value-added fuels and chemicals.[1–3] In particular, the focus has shifted toward selective partial oxidation to directly produce alcohols and oxygenated hydrocarbons.[2,4,5]

In nature, methane C-H bond activation can be achieved selectively by soluble methane monooxygenase (sMMO), or particulate methane monooxygenase (pMMO). The diiron center in sMMO and tri- and dicopper center in pMMO are all capable of producing methanol via partial methane oxidation at room temperature,[6–12] with the articipation of their active bridging oxygen species.[10–14]

Synthetic metal-oxo complexes, such as Cu-oxo and Fe-oxo, supported by zeolite frameworks show similar catalytic reactivities toward methane partial oxidation.[13,15–17] For instance, Groothaert and co-workers found that Cu-exchanged zeolites, such as ZSM-5 and mordenite (MOR), show great selectivity toward methanol.[18] In the past few years, a number of Cu-exchanged zeolitic (e.g., ZSM-5, MOR, CHA) catalysts have been intensively studied.[13,16,19–24]

The C-H bond activation of hydrocarbons is generally considered as the rate-limiting step and can be used as a measure of the reactivity of the active center. Table 6.1 summarizes the theoretical activation barriers over selected catalysts based on ZSM-5 and MOR frameworks. EXAFS analysis performed by Groothaert and co-workers indicated that the active center, within the ZSM-5 framework, has a bis (μ-oxo) dicopper configuration.[18,25] However, with resonance Raman spectroscopy and normal coordinate analysis (NCA) , Woertink and co-workers later suggested that the mono (μ-oxo) dicopper, $[Cu\text{-}O\text{-}Cu]^{2+}$, is the active site in ZSM-5.[16] To further elucidate the structure of the active center, density functional theory (DFT), at the B3LYP level of theory, was employed to calculate the methane activation energy barrier on a mono (μ-oxo) dicopper complex constructed from a cleaved ZSN-5 cluster model.[16] The calculations showed that the value of such a barrier is 0.80 eV, in a good agreement with the experimental data (0.96 eV).[16] Li and co-workers performed thermodynamic stablility evaluation, which further confirmed that the most stable site in ZSM-5 framework is indeed in the mono (μ-oxo) dicopper configuration.[26]

Groothaert and co-workers showed that even higher activity and selectivity can be achieved with Cu-exchanged MOR over Cu-exchanged ZSM-5.[18] Grundner and co-workers performed a similar thermodynamic stablility evaluation on various active center configurations compatible with the MOR framework.[20] The Cu-trioxo complex (Cu_3O_3), as shown in Figure 6.1c, has been identified as the most stable structure anchored in the eight-membered ring (8MR).[20] The C-H bond activation energy barrier obtained from DFT calculations is 0.77 eV using the GGA-PBE functional. The lower energy barrier suggests the catalytic reactivity can be further improved over the Cu-exchanged ZSM-5 catalysts.[16,20,26] Since mono (μ-oxo) dicopper and Cu-trioxo are both active for methane-to methanol conversion, Mahyuddin and co-workers investigated and proposed

relevant mechanisms describing the formation of these active centers.[29] Computationally, Dandu and co-workers studied methane partial oxidation over $[Cu_3O_3(H_2O)_6]^{2+}$, reminiscent of Cu-trioxo sitting in MOR, using 31 exchange-correlation functionals. The energy barrier of methane activation is about 0.87 eV, which gives similar energy barrier as Cu-trioxo sitting in 8MR of MOR, 0.77 eV.[30] The methane partial oxidation mechanism in the 12MR of MOR was investigated by Zhao and co-workers,[28] who showed that mono (μ-oxo) dicopper is also likely responsible for the conversion, with an energy barrier of 0.70 eV for the C-H bond activation. This value is comparable to the work reported by Grundner and co-workers.[20,28]

Table 6.1. Selected theoretical works on C-H bond activation by Cu-oxo complexes in ZSM-5 or MOR frameworks.

Active Center	Framework	Program	Functional	Transition State Spin State	C-H Activation Barrier, eV	Ref.
Cu-trioxo	ZSM-5/8MR	VASP	PBE	doublet	0.56	26
Cu-trioxo	MOR/8MR(I)	VASP	PBE	doublet	0.77	20
Cu-trioxo	MOR/8MR(I)	VASP	PBE-D2	quartet	0.59	27
Cu-trioxo	MOR/8MR(II)	VASP	PBE-D2	quartet	0.33	27
Mono (μ-oxo) dicopper	ZSM-5/8MR	VASP	PBE	triplet	0.96	26
Mono (μ-oxo) dicopper	MOR/12MR	VASP	BEEF-vdW	triplet	1.03	28
Mono (μ-oxo) dicopper	MOR/8MR	VASP	PBE-D2	triplet	0.47	27

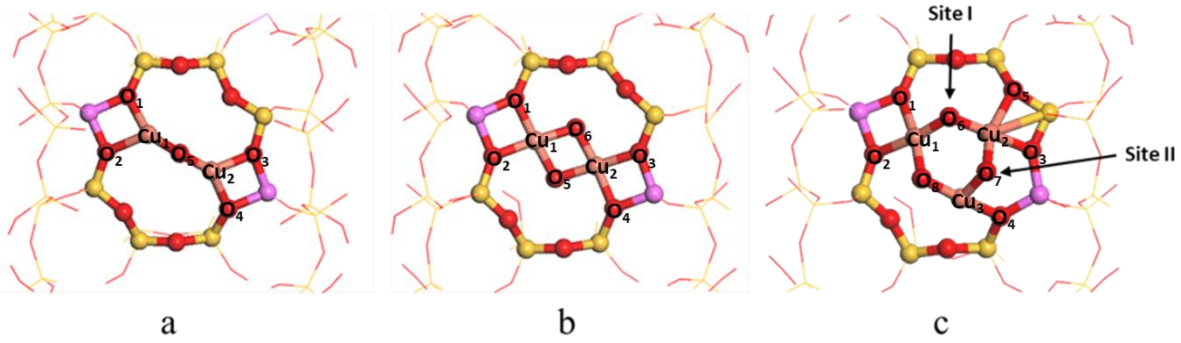


Figure 6.1. Optimized structures of Cu-oxo clusters. (a) mono (μ-oxo) dicopper, (b) bis (μ-oxo) dicopper, and (c) Cu-trioxo complex. The ball-and-stick style is used to emphasize each active center for C-H bond activation. The line style is used to represent the MOR framework for clarity. (Color code: red-O, purple-Al, yellow-Si, and orange-Cu).

To explore other possible Cu-oxo clusters in the 8MR of MOR, Palagin and co-workers studied the stability of a series of Cu-oxo complexes, ranging from dicopper to pentacopper.[31] The investigation revealed that the bigger the Cu-oxo complex, the more thermodynamically stable they will become as indicated by Grundner and co-workers.[20,31] Also, the formation of Cu-O-H and CH_3 fragments from methane activation becomes more favorable as well.[31] However, neither of the above computation included the long-range van der Waals interactions, which may impact the methane and methyl radical interactions with the active sites in both the initial and transition states of C-H bond activation.[32]

Over Cu-oxo complexes, spin crossing either from singlet to triplet or from doublet to quartet can occur during H-subtraction from methane.[20,26–28,33–36] Since spin crossing is a relatively fast process (microseconds), C-H bond activation is likely to proceed at the spin state corresponding to the lower energy barrier process.[37–39] Grundner and co-workers found that, over Cu-trioxo/MOR, the spin state crosses from doublet to quartet at the transitions state based on the

GGA-PBE level of theory.[20] However, using the PBE-D2 method, Mahyuddin and co-workers showed that the reaction starts with a quartet and then changes to a doublet after the homolytic C-H bond cleavage.[27] Since both the bare cluster and methane adsorption would be at the quartet spin state, whether the unpaired electron of the H atom subtracted from methane would impact the spin state remains unclear. More importantly, the associated energy barrier of C-H bond cleavage can be affected.

In this paper, we re-examined the relative thermodynamic stability of three Cu-oxo active centers, i.e mono (μ-oxo) dicopper (Figure 6.1a), bis (μ-oxo) dicopper (Figure 6.1b), and Cu-trioxo (Figure 6.1c), using the BEEF-vdW functional to account for the long-range van der Waals effects.[40] The reactivity of each Cu-oxo complex was then evaluated by identifying the lowest energy barrier for the first C-H bond activation of methane with the consideration of spin crossing. The computational uncertainties associated with methane partial oxidation pathway were estimated within the BEEF-vdW framework.[40] Finally, analyses for ethane and propane were included to gain a boarder understanding of the partial oxidation chemistries for C1-C3 light hydrocarbons.

6.2 Computational Methods

Periodic DFT calculations were performed using the plane-wave-based Vienna ab initio simulation package (VASP).[41] The generalized-gradient approximation (GGA) was adopted in the form of Bayesian error estimation functional including van der Waals correlations (BEEF-vdW) to account for the van der Waals interactions.[42] An energy cutoff of 400 eV was used for the plane wave-based wave function. The Brillouin zone was sampled by a single Γ *k*-point, as suggested by Zhao and co-workers.[28] The break condition for self-consistent iterations is 1×10^{-6} eV, and ionic relaxation is stopped when the forces on all atoms are less than −0.05 eV/Å. The lattice parameters

(Table 6.2) are in good agreement with reported experimental data and computational values.[28,43] All calculations were performed with spin polarization. Therefore, molecular species with unpaired electrons are treated as open shell systems. The numerical uncertainties were estimated using the BEEF-vdW ensemble of exchange-correlation functionals.[44]

Table 6.2. Lattice Parameters of MOR

	a = b	c	γ
PBE	13.60	7.51	96.92
BEEF-dW	13.58	7.51	96.84
PW91[a]	13.65	7.51	97.20
Exp.[b]	13.73	7.54	-

[a]Reference [43]
[b]Reference [28]

The orthogonal unit cell of MOR, as shown in Figure 6.2a, contains 144 atoms (i.e., 48 Si and 96 O).[45] A smaller monoclinic primitive cell containing 72 atoms (24 Si and 48 O) can be used to achieve higher computational efficiency, as suggested by Pidko and co-workers.[43] Thus, the monoclinic cell, as shown in Figure 6.2b, was used. In this work, we focus only on the 8MR side-pocket of the MOR framework, as shown in Figure 6.2c. The number of Al substituents (Si/Al = 11) and their locations were determined based on the suggestion by Pidko and co-workers, as illustrated in Figure 6.2d.[20,43] Specifically, the two Si atoms in the 8MR and two Si atoms in the 12 MR were substituted with Al. The unit cell with Al substitution was further optimized while keeping lattice parameters of the framework fixed this time.

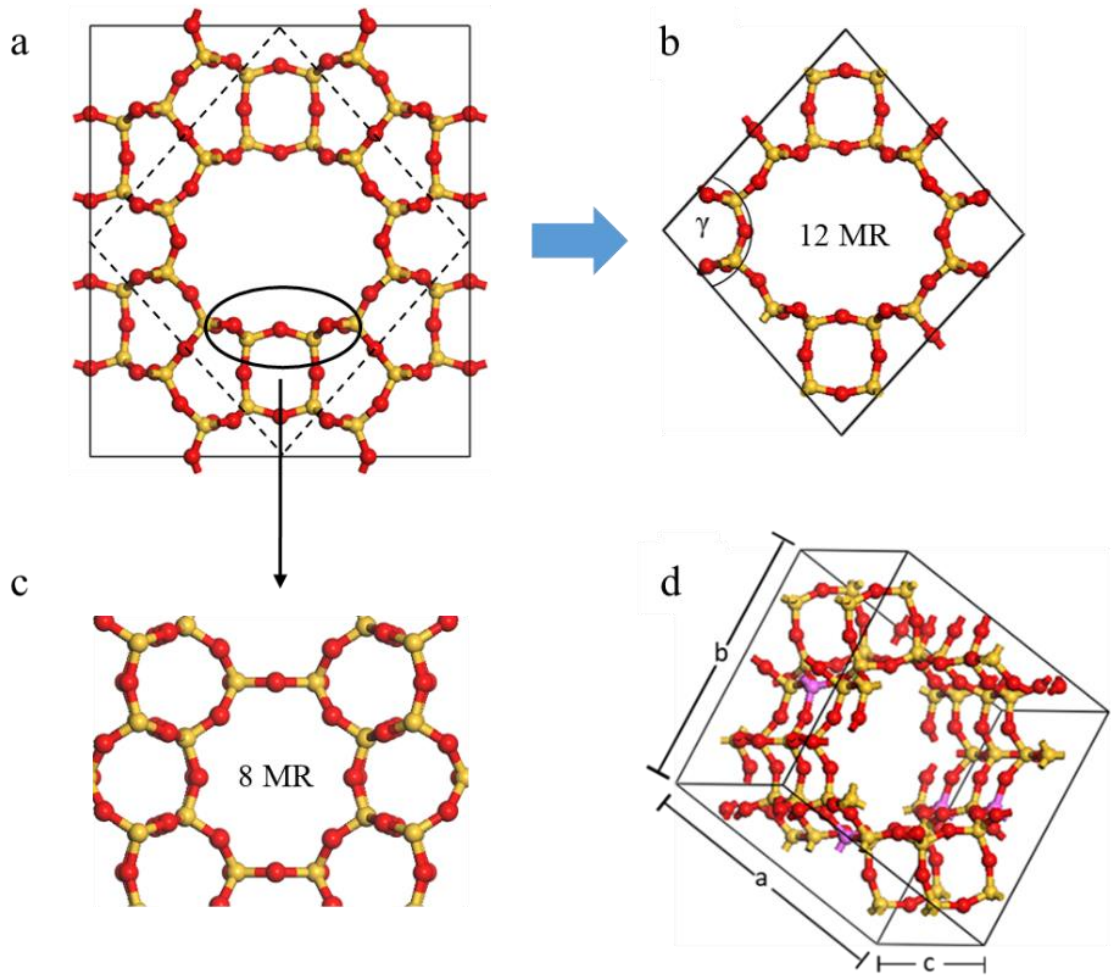


Figure 6.2. Optimized MOR zeolite framework structures. (a) the orthogonal MOR unit cell; (b) a view of the 12 MR along the [001] (c-axis) of the monoclinic unit cell cleaved from (a) indicated by dashed line; (c) a view of the 8MR of MOR framework; (d) the supercell of (b) along the z-axis with Al substitutions. (Color code: red-O, yellow-Si, and purple-Al)

The targeted mono (μ-oxo) dicopper, bis (μ-oxo) dicopper, and Cu-trioxo active sites, Figure 6.1a-c, were constructed within the optimized 8MR side pockets. The evaluation procedure for the relative thermodynamic stability was adopted from ref 20 as explained by eqs. C.1-C.7 in the Appendix C.

The energy barriers for the C-H bond activation at different active sites were calculated using the climbing image nudged elastic band (CI-NEB) method.[46] The transition state structures were then refined with the dimer method.[47] The optimized transition state structures were eventually confirmed by the single imaginary frequency from the harmonic vibrational frequency analysis.

The adsorption energy, E_{ad}, was defined using eq. (6.1),

$$E_{ad} = E_{total} - (E_{surf} + E_{gas}) \tag{6.1}$$

where E_{total} , E_{surf}, and E_{gas} represent the total energies of the relaxed adsorbate, adsorbate-free active center, and gas phase adsorbate species, respectively.

The reaction energies, E_{rxn}, were calculated using eq. (6.2),

$$E_{rxn} = \sum E_{Products} - \sum E_{Reactants} \tag{6.2}$$

where E_{rxn}, $E_{Products}$, and $E_{Reactants}$ represent the reaction energy of an elementary step, the summation of the total energies of all the product and reactant states, respectively.

To investigate the spin crossing associated with C-H bond activation, the total energies for the reactant, transition state, and product molecular species were evaluated with different spin multiplicities using the hybrid B3LYP functional and the aug-cc-pvdz basis set in the NWChem package at explicit spin states.[48–51] To reduce the computational cost, active centers and the 8MR with surrounding O atoms were cleaved from the periodic structures optimized with the BEEF-vdW functional previously. It is important to use the transition state structure that corresponds to respective spin multiplicity since different spin multiplicities result in slightly different C−H and O−H bond distances. Therefore, only passivating H atoms were optimized by keeping transition

state structure at fixed positions. Once the passivating H atoms were relaxed, the structures were used to estimate the total energies at different spin multiplicities with single point energy calculations.

Active site spin densities were calculated using GAMESS, which conveniently produces spin density results.[52] Similarly, the 8MR MOR clusters were cleaved from periodic MOR framework as before. The B3LYP functional and Pople's N-31G split-valence basis set were used in unrestricted Hartree-Fock calculations.[49,50,53,54] The level of theory is comparable to that used in the NWChem calculations.

6.3 Results and Discussion

6.3.1 Cu-Oxo Models for C-H Bond Activations

The stability of Cu−oxo complexes in MOR (with the Si/Al of 11) were evaluated using eq. C.7 in the Appendix C. All the clusters are anchored in the 8MR location through 4 O atoms (red) adjacent to the Al sites (purple). The bond distances and bond angles of the optimized active centers (Figure 6.1a−c) are summarized in Table C.2 in Appendix C.

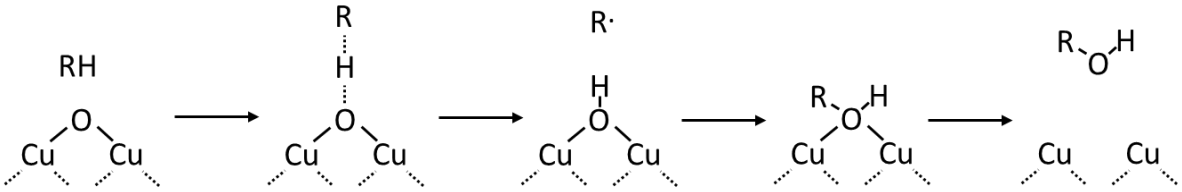
The 3-D phase diagram (Figure C.1 in Appendix C) reveals the most stable phases corresponding to $\Delta\mu_{H_2O}$ and $\Delta\mu_O$ in the range of -3.5 to -0.5 and -1.8 to -0.3 eV. Experimentally, the ion-exchanged zeolites are calcined at 700 K under 1 atm O_2 and 10 ppm of H_2O.[20] Hence, the corresponding to $\Delta\mu_{H_2O}$ and $\Delta\mu_O$ are -1.97 eV and -0.7 eV, which are located in the regions of bis (μ-oxo) dicopper (yellow), as indicated by the red triangle in Figure C.1b. However, Grundner et al. reported that Cu-trioxo is the most stable structure, based on the GGA-PBE functional.[20] The free energy planes for Cu-trioxo and bis (μ-oxo) dicopper are parallel and very close to each other

(Figure C.1a). Therefore, the relative stability of Cu-oxo complexes can be sensitive to the DFT functionals being used.

Within the Cu-trioxo complex, there are two types of active sites, site I and site II. As illustrated in Figure 6.1c, the distance between site I and the adjacent Al site is 4.23 Å, while the distance between site II and its adjacent Al site is 3.13 Å. The ∠Cu-O-Cu at site II is sharper than that at site I, i.e. 99.64º versus 117.22º. Site I is more negatively charged than site II, i.e., -0.76e versus -0.63e.[20] However, according to Mahyuddin et al.,[27] site II has a higher spin density than that of site I at the quartet state. In the following sections, both sites will be investigated to understand their reactivities for the C-H bond activation.

6.3.2 CH_4-to-CH_3OH Conversion over Cu-Oxo Complexes

Scheme 6.1. Reaction mechanism for direct hydrocarbon (RH)-to-alcohol (ROH) conversion via O insertion, where M-O represents metal-oxo in general (in this case is Cu-trioxo).



The general reaction scheme for partial oxidation of methane, a representative of light alkane (RH), is represented in Scheme 6.1, as well as eqs. 6.3-6.6. The reaction is initiated by a homolytic C-H bond activation of an adsorbed methane, parts a, e, and i of Figure 6.3, followed by the direct radical (CH_3 ·) rebound from the first C-H bond activation, parts b, f, and j of Figure 6.3. Before methanol formation, as shown in parts c, g, and k of Figure 6.3, an intermediate step involves the planar methyl radical species, which stays above the newly formed OH group momentarily.[20,26,27,33,34] The recombination of the methyl radical and the OH group results in the

formation of CH_3OH parts d, h, and l of Figure 6.3, which is a barrierless step.[20,26] O_{vac} in eq. 6.5 denotes a reduced site once the reactive O species is inserted into the C-H bond.[20,26]

$$CH_4(g) + * \rightarrow CH_4^* \quad (6.3)$$

$$CH_4^* \rightarrow CH_3\cdot + H^* \quad (6.4)$$

$$CH_3\cdot + H^* \rightarrow CH_3OH^* + O_{vac} \quad (6.5)$$

$$CH_3OH^* \rightarrow CH_3OH + * \quad (6.6)$$

The potential energy surfaces (PES) for all three Cu-ox complexes are shown in Figure 6.4. Different spin states were considered so that the lowest possible methane partial oxidation pathways can be determined. Additional computational at different spin multiplicities is shown in Figure C.2 in the Appendix C. For Cu-trioxo, site I has been proposed to be catalytically active for C-H bond activation since it is more negatively charged.[20] However, recent studies suggested that site II would have even better activity due to its higher spin density. The stronger electronegativity enables stronger O−H bond formation.[20,27,55] The PES over Cu−trioxo (blue in Figure 6.4) was produced over site II. The same mechanism over site I will be discussed in section 3.4. Over site II of Cu−trioxo, the adsorption energy of methane (Figure 6.3a) is −0.21 ± 0.34 eV, at a quartet spin state. This is in a very good agreement with the methane adsorption energy (−0.24 eV) estimated at the quartet spin state obtained by Mahyuddin and co-workers using the GGAPBE functional with the D2-level correction.[27] The transition state structure, Figure 6.3b, remains at the quartet spin state. The C−H bond distance is 1.32 Å, and the O−H bond distance is 1.23 Å. The corresponding energy barrier is 0.45 ± 0.08 eV, which also compares well with a barriers of 0.33 eV, reported by Mahyuddin et al, and 0.4 eV, reported by Vogiatzis et al., respectively.[27,55] The intermediate structure, Figure 6.3c, remains at the quartet spin state and is 0.14 ± 0.15 eV higher

than the adsorbed CH_4 state. The CH_3OH formation, Figure 6.3d, is highly exothermic by −2.45 ± 0.13 eV. The desorption energy of methanol is rather endothermic (0.82 ± 0.49 eV). Both methanol formation and desorption are at the doublet spin state. Therefore, we deduce that the spin crossing (from quartet to doublet) should occur during radical rebound (eq. 6.5), after the C−H bond cleavage.

The pathway for methane partial oxidation over mono (μ-oxo) dicopper is shown in red in Figure 6.4. At the reference state, the triplet spin state is 0.02 eV higher in energy than the singlet spin state. The adsorption energy of methane (Figure 6.3e) is −0.21 ± 0.32 eV, with a singlet spin state, while the triplet spin state is only slightly higher in energy by 0.002 eV than the singlet state. The transition state (Figure 6.3f) has an energy barrier of 0.65 ± 0.06 eV, which is at the triplet spin state. It is 0.1 eV lower than the corresponding singlet spin state. The C−H and O−H bond distances at the transition state are 1.37 Å, and 1.19 Å, respectively. The formation of the planar methyl group (Figure 6.3g) is endothermic by 0.39 ± 0.19 eV relative to the adsorbed CH4 state. This step is also at a triplet spin state. The formation of CH_3OH via radical rebound (Figure 6.3h) is exothermic by −1.15 ± 0.11 eV relative to the intermediate state. Methanol desorption is endothermic by 1.36 ± 0.26 eV. Both the formation and desorption of methanol are at the singlet spin state. According to Figure C.2b in Appendix C, the singlet and triplet spin states are close in potential energies upon methane adsorption. Such a small difference between singlet and triplet spins state suggests two scenarios. One is that the reaction starts with the singlet spin state, and during the C−H bond cleavage, the spin crosses to the triplet spin state. The other scenario is that the system starts with the triplet spin state up until the radical rebound step, in agreement with Mahyuddin's study.[27] During methanol formation, the singlet spin state becomes more favored.

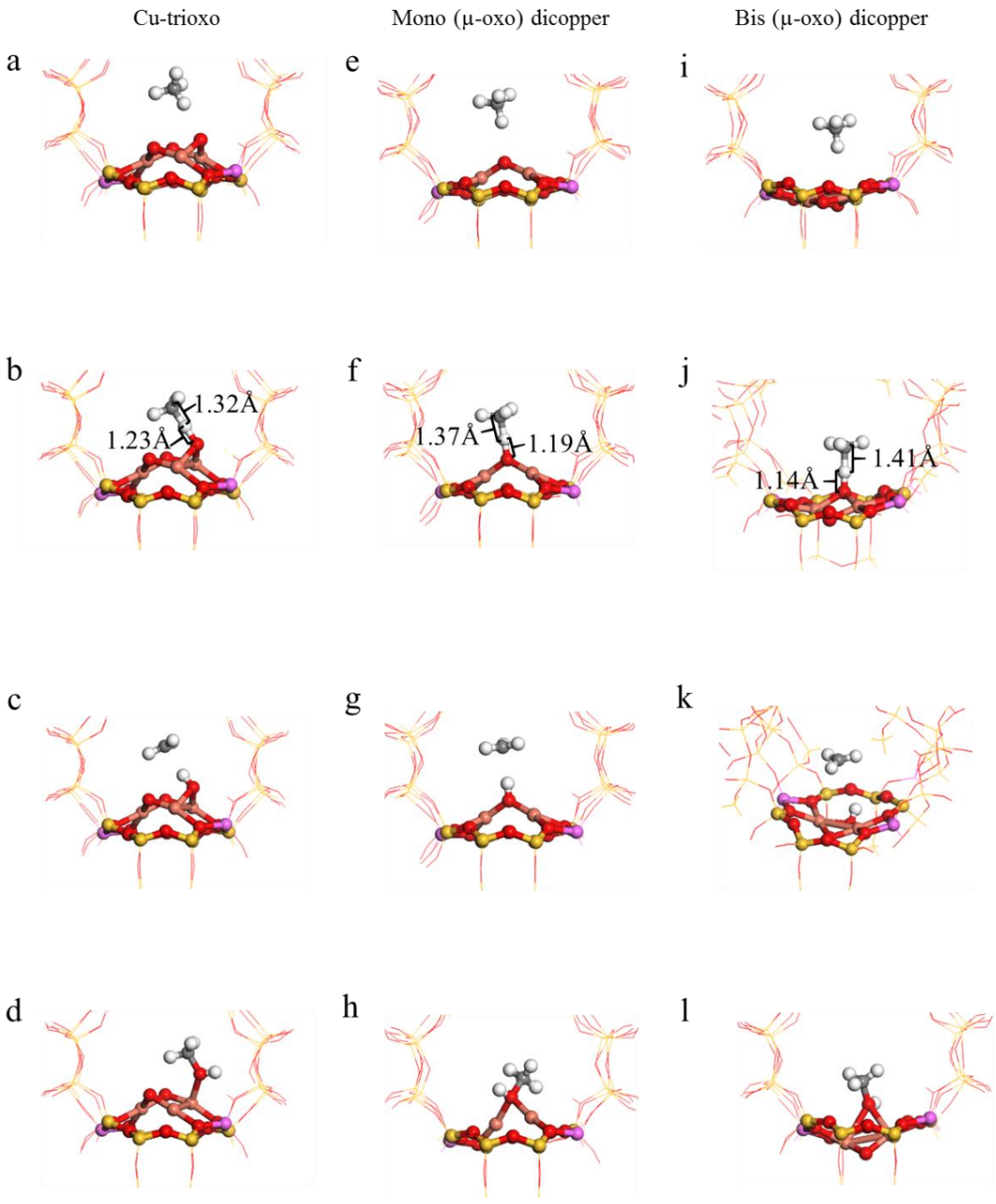


Figure 6.3. Optimized structures of various reaction intermediates. (a)-(d) correspond to methane adsorption, transition state (TS) of methane activation, CH_3+H*, and methanol adsorption over the site II of Cu-trioxo; (e)-(h) correspond to methane adsorption; TS of methane activation, CH_3+H*, and methanol adsorption over mono (μ-oxo) dicopper; (i)-(l) correspond to methane adsorption; TS of methane activation; CH_3+H*; methanol adsorption over bis (μ-oxo) dicopper. (Color code: red-O, yellow-Si, purple-Al, and orange-Cu)

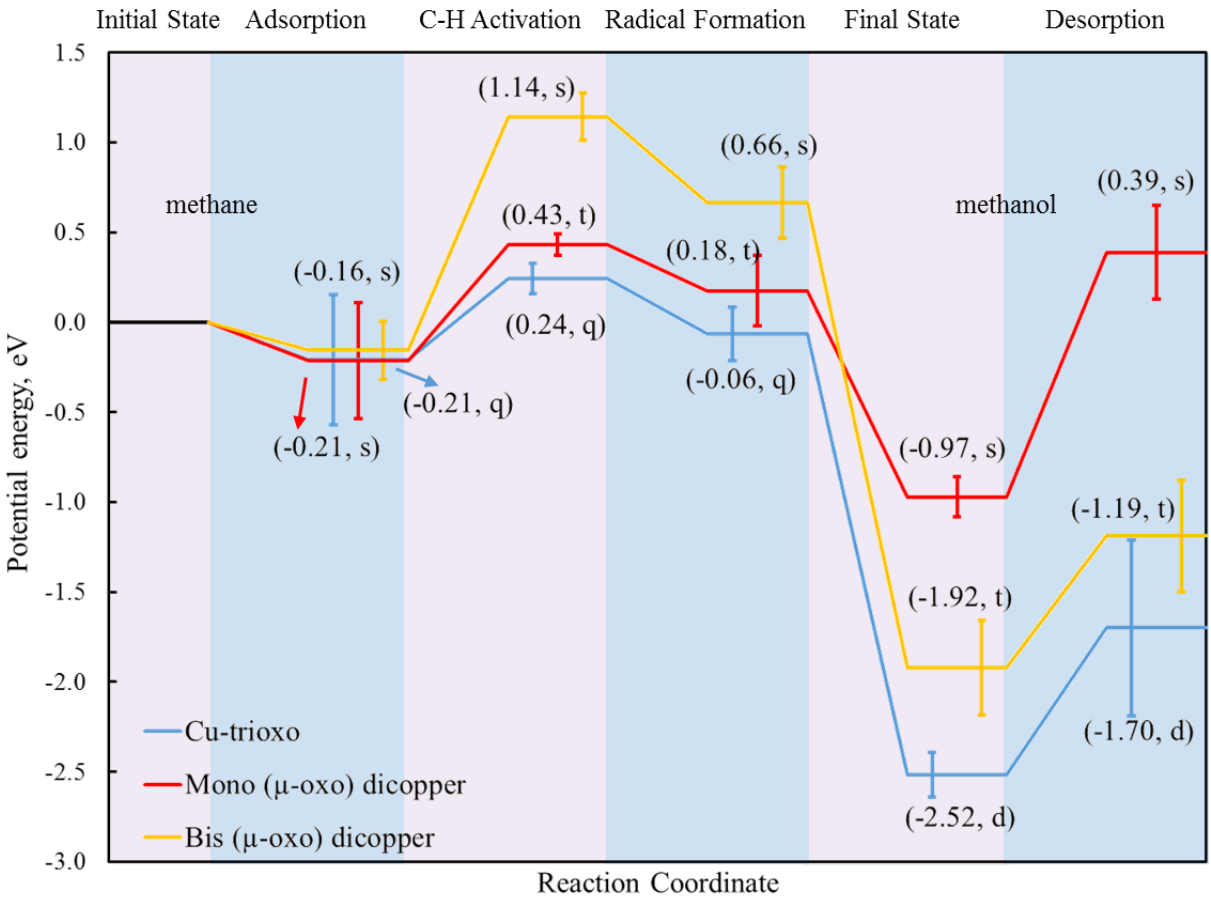


Figure 6.4. Potential energy surfaces of methane-to-methanol conversion over site II of Cu-trioxo (blue), mono (μ-oxo) dicopper (red), and bis (μ-oxo) dicopper (yellow), where s, d, t, q, indicates the singlet, doublet, triplet, and quartet spin states. Computational errors are based on the Bayesian error estimation.

Over the bis (μ-oxo) dicopper, (yellow in Figure 6.4), the adsorption energy of methane (Figure 6.3i) is -0.16 ± 0.16 eV, which is at a singlet spin state. The transition state (Figure 6.3j) has an energy barrier of 1.30 ± 0.13 eV, which is at singlet spin state. At the transition state, the C-H and O-H distances are 1.41 Å, and 1.14 Å, respectively. A stabilized planar methyl group cannot be observed over the bis (μ-oxo) dicopper. Instead, the OH group points away from the

methyl group (Figure 6.3k) was found, and the formation of this intermediate is 0.82 ± 0.20 eV higher relative to the adsorbed CH_4 state. The intermediate step is also singlet. The CH_3OH formation (Figure 6.3l) is highly exothermic (-2.59 ± 0.26 eV), relative to the reaction intermediate state. At this stage, the spin state becomes triplet. Methanol desorption energy is 0.73 ± 0.31 eV, which is also at triplet spins state. According to Figure C.2c, the spin crossing (from singlet to triplet) occurs during methanol formation.

By comparing the results of methane partial oxidation over Cu-trioxo, mono (μ-oxo) dicopper, and bis (μ-oxo) dicopper shown in Figure 6.4, it becomes clear that methane binds to the Cu-trioxo and mono (μ-oxo) dicopper stronger than on the bis (μ-oxo). The energy barrier over Cu-trioxo is also lower. Furthermore, the methanol formation step is a highly exothermic step. Hence, Cu-rioxo is expected to be the most active toward CH_4 oxidation. In addition, a comparison of the optimized TS structures over all three Cu-oxo active sites reveals that the C-H activation energy barrier decreases as C-H distance increases and O-H distance decreases.

6.3.3 C2 and C3 Conversions at Cu-Trioxo Site II

The oxidation of ethane and propane to respective ethanol and propanol (1-propanol and 2-propanol) are considered in this section. The reaction scheme for ethane partial oxidation over Fe-oxo complexes can also be described by Scheme 6.1.[56] Here, the same reaction mechanism is adopted for the Cu-oxo based active sites.

As shown in Figure 6.5 (blue), the adsorption (Figure 6.6a) at site I is -0.18 ± 0.54 eV, followed by a 0.19 ± 0.06 eV energy barrier for its C-H bond activation (Figure 6.6b). Both the adsorption and transition states are quartet, where the C-H and O-H bond distances (in the TS) are 1.29 Å and1.30 Å, respectively. Then the spin multiplicity shifts back to the doublet state. The formation of the ethyl radical (the intermediate state in Figure 6.6c) is exothermic by -2.23 ± 0.17

eV relative to the intermediate state. The desorption energy of ethanol is 0.78 ± 0.60 eV, endothermic, while the spin multiplicity remains doublet.

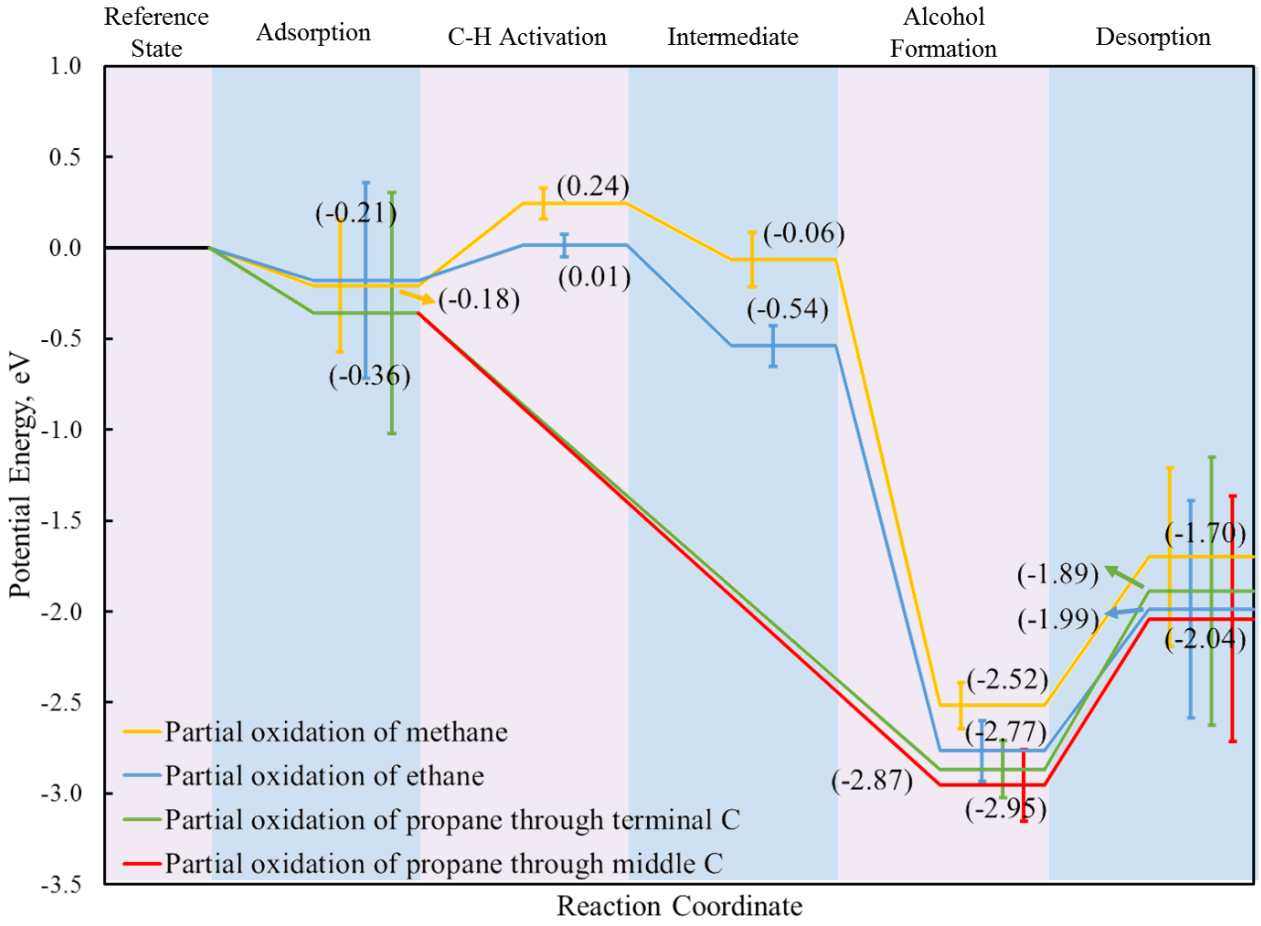


Figure 6.5. Potential energy surfaces of partial oxidation of methane, ethane, propane forming methanol (yellow), ethanol (blue), 1-propanol (green), and isopropanol (red) over site II of Cu-trioxo. Computational errors are based on the Bayesian error estimation.

The adsorption of propane (Figure 6.6e) is -0.36 ± 0.66 eV. However, the transition states for the first C-H bond activation at both the terminal and the middle carbon cannot be located. We believe this is because the TS is too metastable within the 8MR side pocket model. In addition, the

reaction intermediate (a propyl radical) is also unstable and will spontaneously form either 1-propanol or 2-propanol. Thus, we claim that the activation of propane over site II is barrierless. The formation of 1-propanol (Figure 6.6f) and 2-propanol (Figure 6.6g) are -2.51 ± 0.16 eV and -2.60 ± 0.20 eV, respectively, exothermic. The desorption energies of 1-propanol and 2-propanol are 0.98 ± 0.73 and 0.91 ± 0.68 eV, respectively. According to Figure C.3b and c in Appendix C, the initial spin multiplicity is quartet, which then becomes doublet upon 1-propanol and 2-propanol formation.

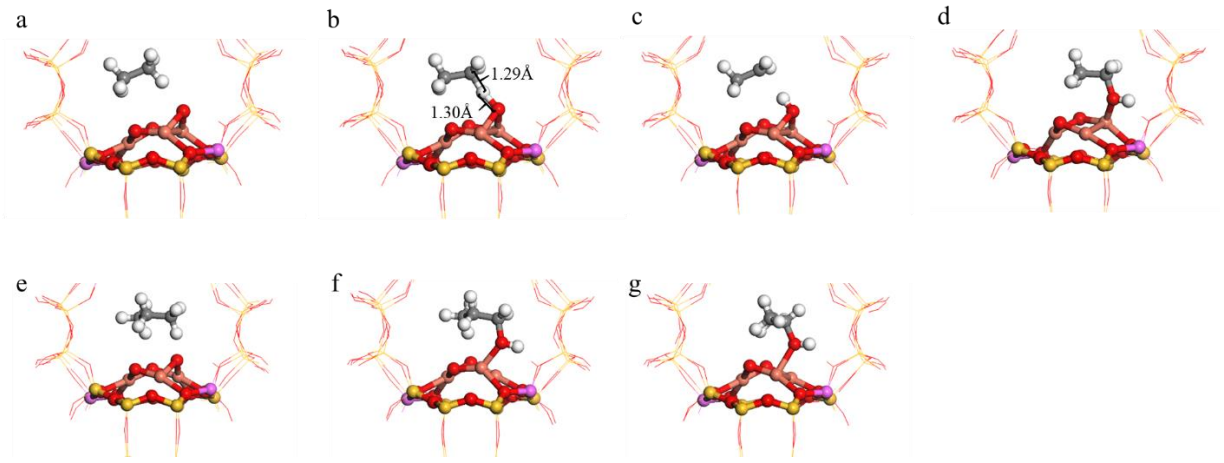


Figure 6.6. Optimized structure over Cu-trioxo site II. (a)-(d) are ethane adsorption, TS for ethane activation, C_2H_5+H*, ethanol; (e)-(g) illustrates the adsorptions of propane, 1 propanol, and isopropanol. (Color code: red-O, yellow-Si, purple-Al, and orange-Cu)

Overall, we have observed a trend where the energy barriers for C1 to C3 C−H bond activation gradually decrease; meanwhile, the formation of the radical intermediate becomes less endothermic. The formation of 2-propanol is more favorable than 1-propanol. The spin crossing over site II of Cu−trioxo occurs after the transition state of the first C−H bond activation. The spin

multiplicity shifts back from quartet to doublet (see Figure C.3 in Appendix C), consistent with the report by Mahyuddin et al.[27]

6.3.4 Alkane Partial Oxidations over Site I of Cu-Trioxo

The partial oxidation of methane, ethane, and propane over Cu−trioxo site I is considered in this section using a similar approach. The partial oxidation pathways corresponding to C1−C3 alkanes over site I of Cu−trioxo with spin crossing are presented in Figure 6.7.

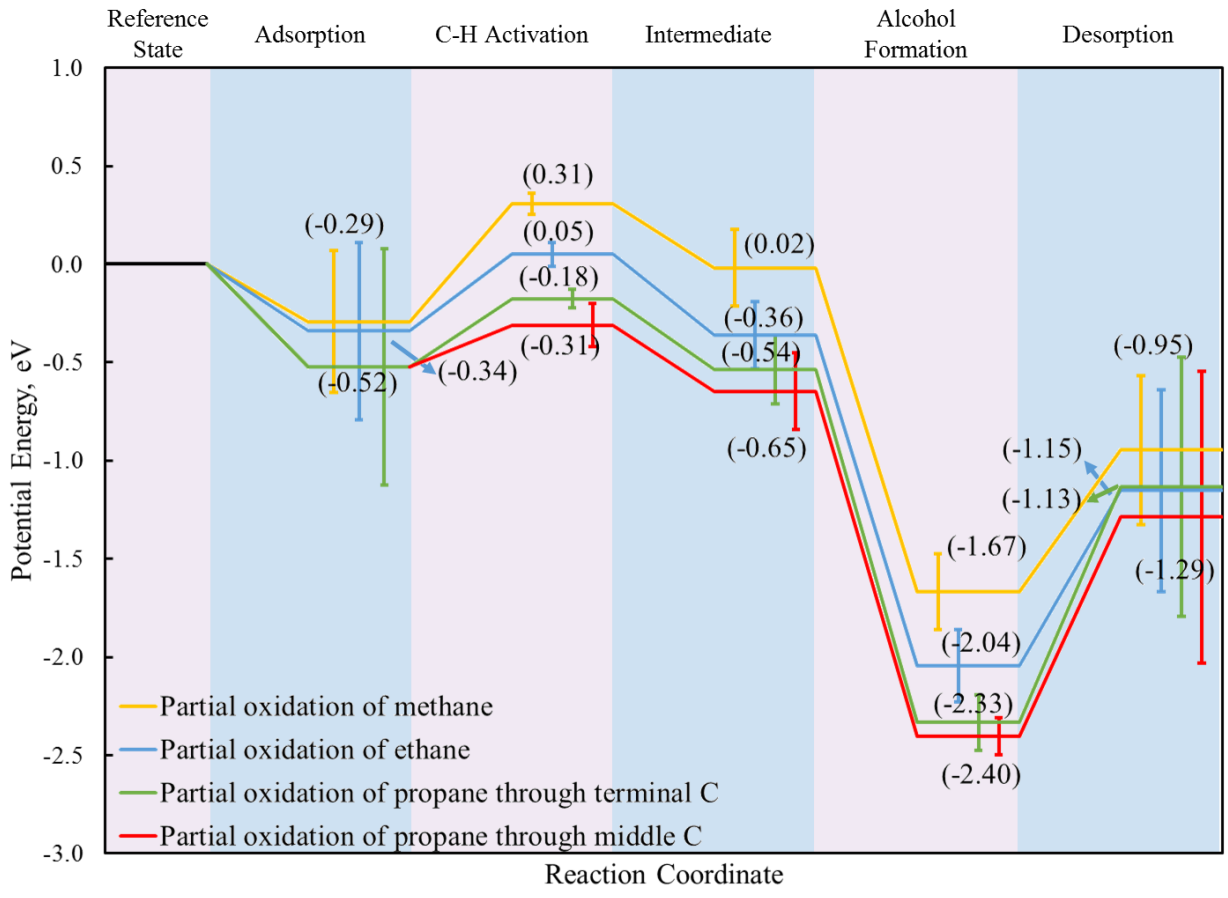


Figure 6.7. Potential energy surfaces for the partial oxidation of methane, ethane, propane forming methanol (yellow), ethanol (blue), 1-propnol (green), and isopropanol (red) over site I of Cu-trioxo, respectively. Computational errors are based on the Bayesian error estimation.

As shown in Figure 6.7 (yellow), the adsorption energy of methane, over site I of Cu−trioxo (Figure 6.8a), is −0.29 ± 0.36 eV. The adsorption step is at the quartet spin state, which is consistent with Mahyuddin's work.[27] By comparing with the adsorption energies estimated from the PBE-D2 (−0.25 eV) and PBE (-0.1 eV) calculations, we consider the adsorption energies are well within the predicted uncertainty range.[20,27] The transition state, Figure 6.8b has an energy barrier of 0.60 ± 0.05 eV, with a spin multiplicity of sextet. The C−H bond distance is 1.31 Å, and the O−H bond distance is 1.24 Å. PBED2 calculations suggest that the energy barrier is 0.59 eV. A slightly higher energy barrier (0.77 eV) was obtained from the GGA-PBE functional. The intermediate methyl radical, remaining at the sextet spin state, Figure 6.8c, is 0.27 ± 0.20 eV higher than the adsorbed methane state. The methanol formation, Figure 6.8d, is exothermic by −1.65 ± 0.19 eV, and the spin state can be either quartet or doublet. Methanol desorption is endothermic by 0.72 ± 0.38 eV.

As shown in Figure 6.7, the partial oxidation of methane starts with a quartet spin state, and it is likely to cross over to the sextet state during the first C−H bond activation, which gives a lower energy barrier. Mahyuddin *et al*.[27] only considered the doublet and quartet spin states, in which the former provides the lower energy barrier. However, since the initial state, CH_4*, is at quartet spin state, we suspect that during H abstraction, an unpaired electron from H could induce the sextet spin state, which has been shown to give an even lower energy barrier for the C-H bond activation (Figure 6.9). In order to further verify the energy barrier at sextet spin state, calculations were performed with designated spin multiplicities using NWChem. The results, Figure C.5 in Appendix C, confirmed that the energy barrier corresponding to the sextet is indeed lower than both quartet and doublet spin states. Since the reaction is likely to follow the pathway at the lowest energy, we conclude that spin crosses from quartet to sextet are more probable.

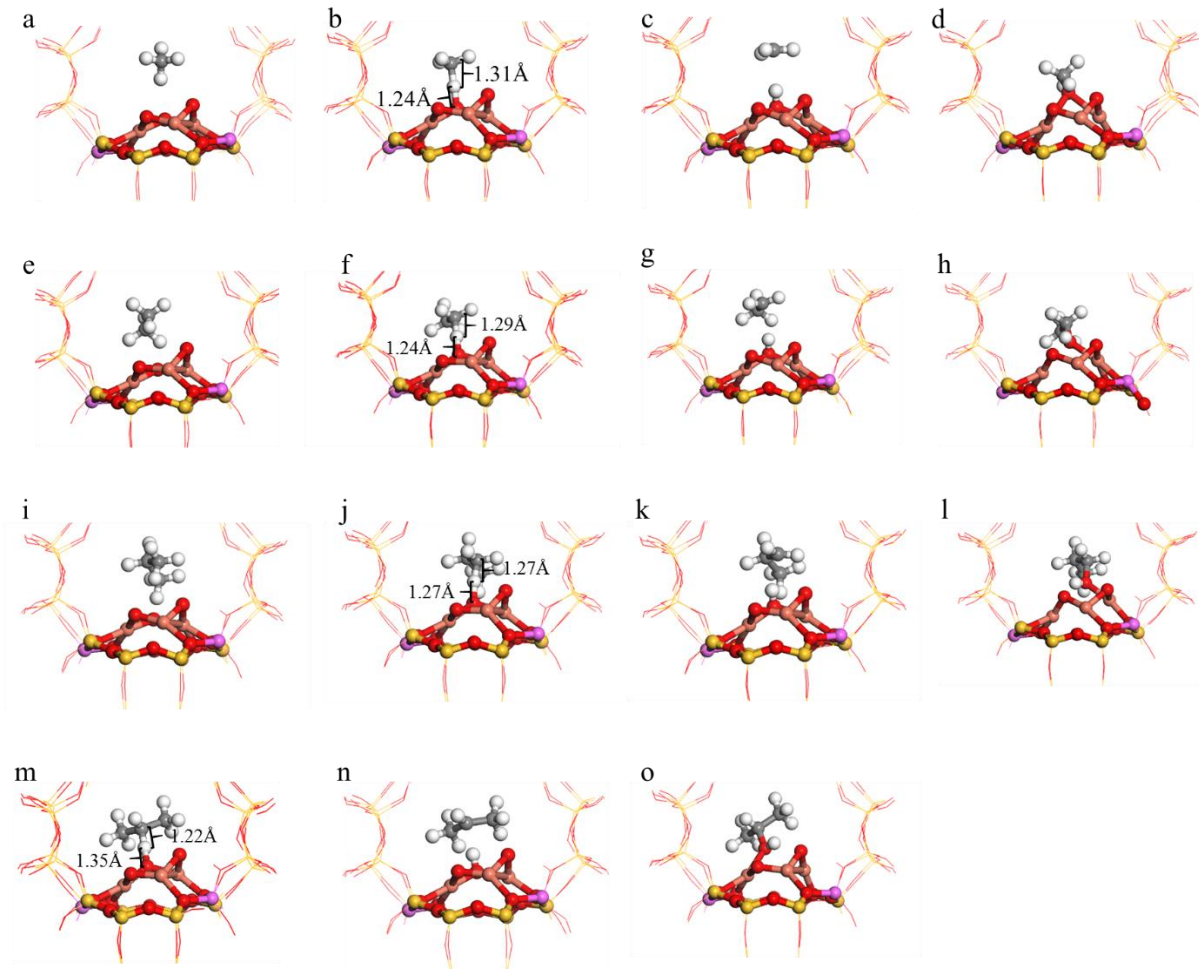


Figure 6.8. Optimized structures over Cu-trioxo site I. (a)-(d) correspond to methane adsorption, TS for methane activation, CH_3 + H*, and methanol adsorption; (e)-(h) correspond to ethane adsorption, TS for ethane activation, C_2H_5 + H*, and ethanol adsorption; (i)-(o) correspond to propane adsorption, TS for C-H bond activation at the terminal carbon, $CH_3CH_2CH_2$ + H*, 1-propanol, TS for C-H bond activation at the secondary carbon, CH_3CHCH_3 + H*, and isopropanol adsorption.(Color code: red-O, yellow-Si, purple-Al, and orange-Cu)

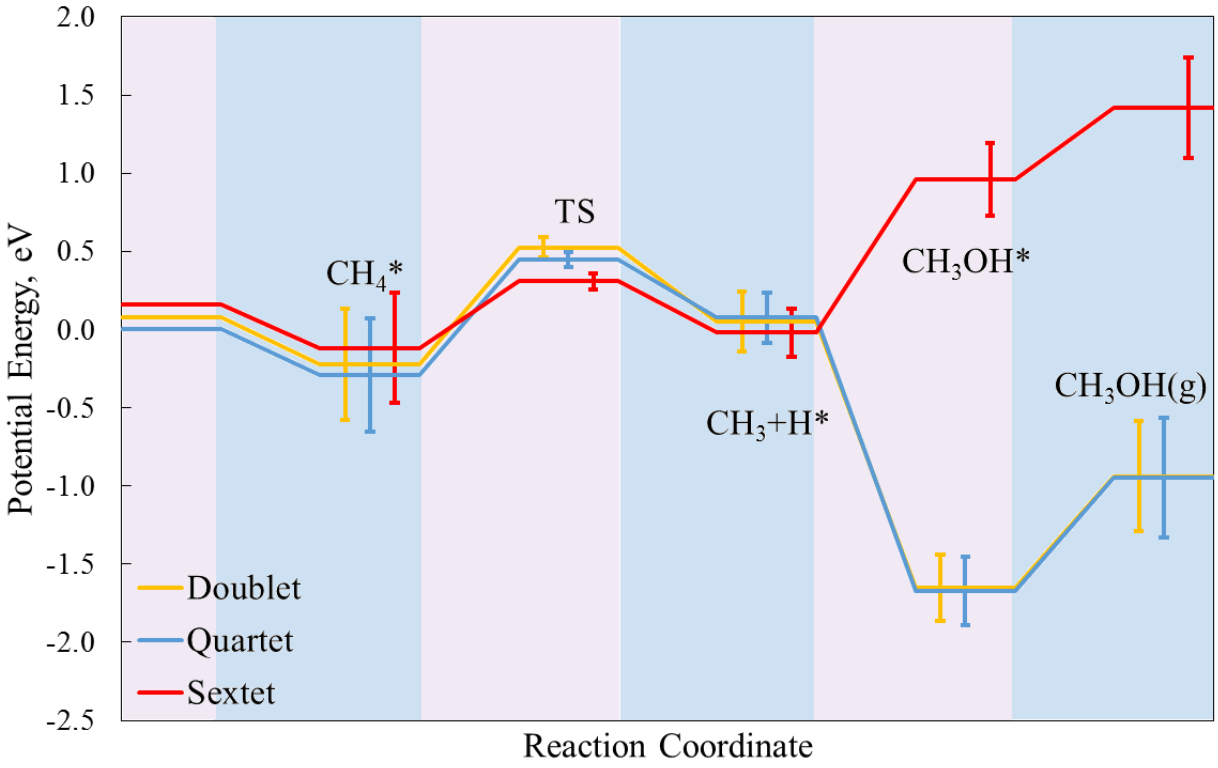


Figure 6.9. Potential energy surfaces of methane partial oxidation over Cu-trioxo site I at the doublet (yellow), quartet (blue), and sextet (red) spin multiplicities. Computational errors are based on the Bayesian error estimation.

Partial oxidation of ethane was depicted in Figure 6.7 (blue). The adsorption of ethane (Figure 6.8e) is −0.34 ± 0.45 eV. Like methane, the initial spin state is quartet. The C−H bond activation (Figure 6.8f) energy barrier of ethane is 0.39 ± 0.05 eV, which is also at the sextet spin state. At this transition state, the C−H bond distance is 1.29 Å, and the O−H bond distance is 1.24 Å. The formation of the ethyl radical, Figure 6.8g, and is exothermic by −0.02 ± 0.17 eV, relative to the adsorbed ethane. The spin state remains sextet. The radical rebound forming ethanol (Figure 6.8h) is also exothermic by −1.68 ± 0.18 eV relative to the intermediate state, while the spin multiplicity changes to either the doublet or quartet (Figure C.4a). The ethanol desorption energy is 0.89 ± 0.51 eV.

Propane partial oxidations, at either the terminal or secondary carbon, are illustrated in Figure 6.7, in green and red, respectively. The adsorption energy of propane (Figure 6.8i) is −0.52 ± 0.60 eV. The C−H bond activation barrier at the terminal carbon (Figure 6.8j) is 0.35 ± 0.05 eV. The barrier for C−H bond activation at the middle carbon (Figure 6.8m) is lower, at 0.21 ± 0.11 eV. Similar to its C1 and C2 counterparts, the spin multiplicities for the reference state and adsorbed state are quartet, while transition states are sextet. At the transition state of terminal C−H bond cleavage, the C−H bond and O−H bond distances are both 1.27 Å, while the C−H and C−H bond distances are 1.22 and 1.35 Å, respectively. The potential energy of forming the propyl radical structure through terminal C−H bond cleavage (Figure 6.8k) is 0.01 ± 0.17 eV lower relative to the adsorbed propane state. The spin multiplicity remains sextet. Furthermore, the formation of 1-propanol (Figure 6.8l) is exothermic by −1.80 ± 0.14 eV relative to the intermediate state, with lower spin multiplicities (either doublet or quartet) (see Figure C.4b in Appendix C). The intermediate for 2-propanol formation (Figure 6.8n) is −0.13 ± 0.20 eV relative to the adsorbed state. The evolution of spin multiplicity is the same as that for the 1-propanol formation. The formation of 2-propanol (Figure 6.8o) is exothermic by −1.76 ± 0.09 eV relative to the intermediate state, at a lower spin state (see Figure C.4c).

The BEEF-vdW calculations showed that the adsorption energies of C1−C3 follow an increasing order, with propane binding the most strongly at the Cu−trioxo site. From C1 to C3, the corresponding energy barrier decreases, with decreasing C−H bond distance and increasing O−H bond distance. Since the C−H bond activation barrier at the middle carbon is lower than that at the terminal carbon, we predict that the propane-to-2-propanol conversion should be preferred. At the Cu−trioxo site, all partial oxidations consistently start with a quartet spin state and then cross to the sextet state during the C−H bond activation, which also leads to the sextet transition state and

intermediate states. During radical rebound, the spin multiplicity shifts back to the quartet or the doublet state.

By comparison of site I and site II, the adsorption of hydrocarbons becomes a little bit less stable at site II. Bader charge analysis shows that site I and site II are both negatively charged, −0.71e (site I) and −0.67e (site II). At the transition state for methane, the C−H bond distances at site I and site II are also quite similar (1.31 vs 1.32 Å). A similar trend can be observed for ethane activation as well, in which the C−H bond distance is 1.29 Å for both site I and site II. However, the energy barriers over site II for alkane activation are consistently lower than that over site I. The propane-to-propanol conversion over site II is even barrierless. Therefore, site II should be more active for C−H bond activation, which agrees well with the results reported by Mahyuddin and Vogiatzis.[27,55] In regarding to spin crossing, over site I, spin crosses from quartet to sextet before transitions state, and it crosses back to quartet or doublet during radical rebound, while over site II, spin crosses from quartet to doublet after transition state.

According to Schwarz et al.,[57] higher spin density can significantly increase the reactivity towards methane activation. Therefore, the spin densities of considered active sites at different spin states were investigated using GAMESS. The computational results are shown in Table C.3 in the Appendix C. In Cu−trioxo, site I at the sextet spin state gives the lowest energy barrier, and it can be seen that the corresponding spin density is also the highest among all the spin states considered. For site II, Cu−trioxo at the quartet spin state is considered the most active. Similarly, the corresponding spin density is also the highest (Table C.3). This is consistent with the anticipated relationship between reactivity with the corresponding spin density; i.e., higher spin density is likely associated with higher reactivity. For mono(μoxo)dicopper, the triplet state with lowest energy barrier for C−H bond activation also shows the highest spin density (Table C.3).

For bis(μ-oxo)dicopper, the quintet state has the highest spin density and the lowest energy barrier as shown in Figure C.2c in Appendix C. However, at the reference state, the singlet state is much more active than the triplet and the quintet spin state; during methane activation, the spin states do not cross until the radical rebound step.

6.4 Conclusions

In this study, DFT calculations were performed using the BEEF-vdW functional to systematically investigate the stability of Cu−oxo complexes, as well as C1−C3 partial oxidation pathways over these active centers. Thermodynamic stability tests show that bis(μ-oxo)dicopper is more stable than Cu− trioxo. Overall, both configurations are close in free energies under realistic reaction conditions. Nevertheless, Cu−trioxo is more active toward partial oxidation based on the C−H bond activation energy barriers identified at both BEEF-vdW and B3LYP levels of theory and the consideration of spin crossing. In particular, spin crossing shows significant impact on the calculations of both reaction energetics and C−H activation energy barriers. Between site I and site II of Cu−trioxo, C1− C3 hydrocarbons all bind stronger at site I; however, the C−H bond activation energy barriers are generally lower at site II. For ethane and propane, partial oxidation to respective ethanol and propanols and, from C1 to C3, a trend of stronger adsorption and lower energy barrier can be observed over Cu− trioxo/MOR. This work also confirms that higher spin density is associated with higher activity toward C−H bond activation.

References

(1) Bao, B.; El-Halwagi, M. M.; Elbashir, N. O. Simulation, Integration, and Economic Analysis of Gas-to-Liquid Processes. *Fuel Process. Technol.* **2010**, *91* (7), 703–713.

(2) Arakawa, H.; Aresta, M.; Armor, J. N.; Barteau, M. A.; Beckman, E. J.; Bell, A. T.; Bercaw, J. E.; Creutz, C.; Dinjus, E.; Dixon, D. A.; Domen, K.; DuBois, D. L.; Eckert, J.; Fujita, E.; Gibson, D. H.; Goddard, W. A.; Goodman, D. W.; Keller, J.; Kubas, G. J.; Kung, H. H.; Lyons, J. E.; Manzer, L. E.; Marks, T. J.; Morokuma, K.; Nicholas, K. M.; Periana, R.; Que, L.; Rostrup-Nielson, J.; Sachtler, W. M. H.; Schmidt, L. D.; Sen, A.; Somorjai, G. A.; Stair, P. C.; Stults, B. R.; Tumas, W. Catalysis Research of Relevance to Carbon Management: Progress, Challenges, and Opportunities. *Chem. Rev.* **2001**, *101* (4), 953–996.

(3) Elia, J. A.; Baliban, R. C.; Xiao, X.; Floudas, C. A. Optimal Energy Supply Network Determination and Life Cycle Analysis for Hybrid Coal, Biomass, and Natural Gas to Liquid (CBGTL) Plants Using Carbon-Based Hydrogen Production. *Comput. Chem. Eng.* **2011**, *35* (8), 1399–1430.

(4) Lunsford, J. H. Catalytic Conversion of Methane to More Useful Chemicals and Fuels: A Challenge for the 21st Century. *Catal. Today* **2000**, *63* (2), 165–174. ht

(5) Himes, R. A.; Karlin, K. D. A New Copper-Oxo Player in Methane Oxidation. *Proc. Natl. Acad. Sci.* **2009**, *106* (45), 18877 LP – 18878.

(6) Lieberman, R. L.; Rosenzweig, A. C. Crystal Structure of a Membrane-Bound Metalloenzyme That Catalyses the Biological Oxidation of Methane. *Nature* **2005**, *434* (7030), 177–182.

(7) Rosenzweig, A. C. The Metal Centres of Particulate Methane Mono-Oxygenase. *Biochem. Soc. Trans.* **2008**, *36* (6), 1134–1137.

(8) Rosenzweig, A. C.; Frederick, C. A.; Lippard, S. J.; Nordlund, P. auml;r. Crystal Structure of a Bacterial Non-Haem Iron Hydroxylase That Catalyses the Biological Oxidation of Methane. *Nature* **1993**, *366* (6455), 537–543.

(9) Chan, S. I.; Wang, V. C.-C.; Lai, J. C.-H.; Yu, S. S.-F.; Chen, P. P.-Y.; Chen, K. H.-C.; Chen, C.-L.; Chan, M. K. Redox Potentiometry Studies of Particulate Methane Monooxygenase: Support for a Trinuclear Copper Cluster Active Site. *Angew. Chemie Int. Ed.* **2007**, *46* (12), 1992–1994.

(10) Liakos, D. G.; Neese, F. Interplay of Correlation and Relativistic Effects in Correlated Calculations on Transition-Metal Complexes: The (Cu2O2)2+ Core Revisited. *J. Chem. Theory Comput.* **2011**, *7* (5), 1511–1523.

(11) Snyder, B. E. R.; Bols, M. L.; Schoonheydt, R. A.; Sels, B. F.; Solomon, E. I. Iron and Copper Active Sites in Zeolites and Their Correlation to Metalloenzymes. *Chem. Rev.* **2018**, *118* (5), 2718–2768.

(12) Hori, Y.; Shiota, Y.; Tsuji, T.; Kodera, M.; Yoshizawa, K. Catalytic Performance of a Dicopper–Oxo Complex for Methane Hydroxylation. *Inorg. Chem.* **2018**, *57* (1), 8–11.

(13) Alayon, E. M.; Nachtegaal, M.; Ranocchiari, M.; van Bokhoven, J. A. Catalytic Conversion of Methane to Methanol over Cu–Mordenite. *Chem. Commun.* **2012**, *48* (3), 404–406.

(14) Balasubramanian, R.; Smith, S. M.; Rawat, S.; Yatsunyk, L. A.; Stemmler, T. L.; Rosenzweig, A. C. Oxidation of Methane by a Biological Dicopper Centre. *Nature* **2010**, *465* (7294), 115–119.

(15) Vanelderen, P.; Snyder, B. E. R.; Tsai, M.-L.; Hadt, R. G.; Vancauwenbergh, J.; Coussens, O.; Schoonheydt, R. A.; Sels, B. F.; Solomon, E. I. Spectroscopic Definition of the Copper Active Sites in Mordenite: Selective Methane Oxidation. *J. Am. Chem. Soc.* **2015**, *137* (19), 6383–6392.

(16) Woertink, J. S.; Smeets, P. J.; Groothaert, M. H.; Vance, M. A.; Sels, B. F.; Schoonheydt, R. A.; Solomon, E. I. A [Cu2O]2+ Core in Cu-ZSM-5, the Active Site in the Oxidation of Methane to Methanol. *Proc. Natl. Acad. Sci.* **2009**, *106* (45), 18908 LP – 18913.

(17) Dinh, K. T.; Sullivan, M. M.; Serna, P.; Meyer, R. J.; Dincă, M.; Román-Leshkov, Y. Viewpoint on the Partial Oxidation of Methane to Methanol Using Cu- and Fe-Exchanged Zeolites. *ACS Catal.* **2018**, *8* (9), 8306–8313. https://doi.org/10.1021/acscatal.8b01180.

(18) Groothaert, M. H.; Smeets, P. J.; Sels, B. F.; Jacobs, P. A.; Schoonheydt, R. A. Selective Oxidation of Methane by the Bis(μ-Oxo)Dicopper Core Stabilized on ZSM-5 and Mordenite Zeolites. *J. Am. Chem. Soc.* **2005**, *127* (5), 1394–1395.

(19) Sushkevich, V. L.; Palagin, D.; Ranocchiari, M.; van Bokhoven, J. A. Selective Anaerobic Oxidation of Methane Enables Direct Synthesis of Methanol. *Science.* **2017**, *356* (6337), 523 – 527.

(20) Grundner, S.; Markovits, M. A. C.; Li, G.; Tromp, M.; Pidko, E. A.; Hensen, E. J. M.; Jentys, A.; Sanchez-Sanchez, M.; Lercher, J. A. Single-Site Trinuclear Copper Oxygen Clusters in Mordenite for Selective Conversion of Methane to Methanol. *Nat. Commun.* **2015**, *6* (1), 7546.

(21) Wulfers, M. J.; Teketel, S.; Ipek, B.; Lobo, R. F. Conversion of Methane to Methanol on Copper-Containing Small-Pore Zeolites and Zeotypes. *Chem. Commun.* **2015**, *51* (21), 4447–4450.

(22) Beznis, N. V; Weckhuysen, B. M.; Bitter, J. H. Cu-ZSM-5 Zeolites for the Formation of Methanol from Methane and Oxygen: Probing the Active Sites and Spectator Species. *Catal. Letters* **2010**, *138* (1), 14–22.

(23) Xu, J.; Armstrong, R. D.; Shaw, G.; Dummer, N. F.; Freakley, S. J.; Taylor, S. H.; Hutchings, G. J. Continuous Selective Oxidation of Methane to Methanol over Cu- and Fe-Modified ZSM-5 Catalysts in a Flow Reactor. *Catal. Today* **2016**, *270*, 93–100.

(24) Pappas, D. K.; Borfecchia, E.; Dyballa, M.; Pankin, I. A.; Lomachenko, K. A.; Martini, A.; Signorile, M.; Teketel, S.; Arstad, B.; Berlier, G.; Lamberti, C.; Bordiga, S.; Olsbye, U.; Lillerud, K. P.; Svelle, S.; Beato, P. Methane to Methanol: Structure–Activity Relationships for Cu-CHA. *J. Am. Chem. Soc.* **2017**, *139* (42), 14961–14975.

(25) Groothaert, M. H.; Lievens, K.; Leeman, H.; Weckhuysen, B. M.; Schoonheydt, R. A. An Operando Optical Fiber UV–Vis Spectroscopic Study of the Catalytic Decomposition of

NO and N2O over Cu-ZSM-5. *J. Catal.* **2003**, *220* (2), 500–512.

(26) Li, G.; Vassilev, P.; Sanchez-Sanchez, M.; Lercher, J. A.; Hensen, E. J. M.; Pidko, E. A. Stability and Reactivity of Copper Oxo-Clusters in ZSM-5 Zeolite for Selective Methane Oxidation to Methanol. *J. Catal.* **2016**, *338*, 305–312.

(27) Mahyuddin, M. H.; Tanaka, T.; Shiota, Y.; Staykov, A.; Yoshizawa, K. Methane Partial Oxidation over [Cu2(μ-O)]2+ and [Cu3(μ-O)3]2+ Active Species in Large-Pore Zeolites. *ACS Catal.* **2018**, *8* (2), 1500–1509.

(28) Zhao, Z.-J.; Kulkarni, A.; Vilella, L.; Nørskov, J. K.; Studt, F. Theoretical Insights into the Selective Oxidation of Methane to Methanol in Copper-Exchanged Mordenite. *ACS Catal.* **2016**, *6* (6), 3760–3766.

(29) Mahyuddin, M. H.; Tanaka, T.; Staykov, A.; Shiota, Y.; Yoshizawa, K. Dioxygen Activation on Cu-MOR Zeolite: Theoretical Insights into the Formation of Cu2O and Cu3O3 Active Species. *Inorg. Chem.* **2018**, *57* (16), 10146–10152.

(30) Dandu, N. K.; Reed, J. A.; Odoh, S. O. Performance of Density Functional Theory for Predicting Methane-to-Methanol Conversion by a Tri-Copper Complex. *J. Phys. Chem. C* **2018**, *122* (2), 1024–1036.

(31) Palagin, D.; Knorpp, A. J.; Pinar, A. B.; Ranocchiari, M.; van Bokhoven, J. A. Assessing the Relative Stability of Copper Oxide Clusters as Active Sites of a CuMOR Zeolite for Methane to Methanol Conversion: Size Matters? *Nanoscale* **2017**, *9* (3), 1144–1153.

(32) Wu, Q.; Yang, W. Empirical Correction to Density Functional Theory for van Der Waals Interactions. *J. Chem. Phys.* **2001**, *116* (2), 515–524.

(33) Mahyuddin, M. H.; Staykov, A.; Shiota, Y.; Miyanishi, M.; Yoshizawa, K. Roles of Zeolite Confinement and Cu–O–Cu Angle on the Direct Conversion of Methane to Methanol by [Cu2(μ-O)]2+-Exchanged AEI, CHA, AFX, and MFI Zeolites. *ACS Catal.* **2017**, *7* (6), 3741–3751.

(34) Mahyuddin, M. H.; Staykov, A.; Shiota, Y.; Yoshizawa, K. Direct Conversion of Methane to Methanol by Metal-Exchanged ZSM-5 Zeolite (Metal = Fe, Co, Ni, Cu). *ACS Catal.* **2016**, *6* (12), 8321–8331.

(35) Mahyuddin, M. H.; Shiota, Y.; Staykov, A.; Yoshizawa, K. Theoretical Overview of Methane Hydroxylation by Copper–Oxygen Species in Enzymatic and Zeolitic Catalysts. *Acc. Chem. Res.* **2018**, *51* (10), 2382–2390.

(36) Yoshizawa, K.; Shiota, Y. Conversion of Methane to Methanol at the Mononuclear and Dinuclear Copper Sites of Particulate Methane Monooxygenase (PMMO): A DFT and QM/MM Study. *J. Am. Chem. Soc.* **2006**, *128* (30), 9873–9881.

(37) Saouma, C. T.; Mayer, J. M. Do Spin State and Spin Density Affect Hydrogen Atom Transfer Reactivity? *Chem. Sci.* **2014**, *5* (1), 21–31.

(38) Manner, V. W.; Lindsay, A. D.; Mader, E. A.; Harvey, J. N.; Mayer, J. M. Spin-Forbidden Hydrogen Atom Transfer Reactions in a Cobalt Biimidazoline System. *Chem. Sci.* **2012**, *3* (1), 230–243.

(39) Hirao, H.; Kumar, D.; Que, L.; Shaik, S. Two-State Reactivity in Alkane Hydroxylation by Non-Heme Iron−Oxo Complexes. *J. Am. Chem. Soc.* **2006**, *128* (26), 8590–8606.

(40) Wellendorff, J.; Lundgaard, K. T.; Møgelhøj, A.; Petzold, V.; Landis, D. D.; Nørskov, J. K.; Bligaard, T.; Jacobsen, K. W. Density Functionals for Surface Science: Exchange-Correlation Model Development with Bayesian Error Estimation. *Phys. Rev. B* **2012**, *85* (23), 235149.

(41) Kresse, G.; Furthmüller, J. Efficient Iterative Schemes for Ab Initio Total-Energy Calculations Using a Plane-Wave Basis Set. *Phys. Rev. B* **1996**, *54* (16), 11169–11186.

(42) Perdew, J. P.; Wang, Y. Accurate and Simple Analytic Representation of the Electron-Gas Correlation Energy. *Phys. Rev. B* **1992**, *45* (23), 13244–13249.

(43) Pidko, E. A.; van Santen, R. A.; Hensen, E. J. M. Multinuclear Gallium-Oxide Cations in High-Silica Zeolites. *Phys. Chem. Chem. Phys.* **2009**, *11* (16), 2893–2902.

(44) Medford, A. J.; Wellendorff, J.; Vojvodic, A.; Studt, F.; Abild-Pedersen, F.; Jacobsen, K. W.; Bligaard, T.; Nørskov, J. K. Assessing the Reliability of Calculated Catalytic Ammonia Synthesis Rates. *Science.* **2014**, *345* (6193), 197 – 200.

(45) Rudolf, P. R.; Garcés, J. M. Rietveld Refinement of Several Structural Models for Mordenite That Account for Differences in the X-Ray Powder Pattern. *Zeolites* **1994**, *14* (2), 137–146.

(46) Henkelman, G.; Uberuaga, B. P.; Jónsson, H. A Climbing Image Nudged Elastic Band Method for Finding Saddle Points and Minimum Energy Paths. *J. Chem. Phys.* **2000**, *113* (22), 9901–9904.

(47) Henkelman, G.; Jónsson, H. A Dimer Method for Finding Saddle Points on High Dimensional Potential Surfaces Using Only First Derivatives. *J. Chem. Phys.* **1999**, *111* (15), 7010–7022.

(48) Valiev, M.; Bylaska, E. J.; Govind, N.; Kowalski, K.; Straatsma, T. P.; Van Dam, H. J. J.; Wang, D.; Nieplocha, J.; Apra, E.; Windus, T. L.; de Jong, W. A. NWChem: A Comprehensive and Scalable Open-Source Solution for Large Scale Molecular Simulations. *Comput. Phys. Commun.* **2010**, *181* (9), 1477–1489.

(49) Becke, A. D. Density-functional Thermochemistry. III. The Role of Exact Exchange. *J. Chem. Phys.* **1993**, *98* (7), 5648–5652.

(50) Lee, C.; Yang, W.; Parr, R. G. Development of the Colle-Salvetti Correlation-Energy Formula into a Functional of the Electron Density. *Phys. Rev. B* **1988**, *37* (2), 785–789.

(51) Dunning, T. H. Gaussian Basis Sets for Use in Correlated Molecular Calculations. I. The Atoms Boron through Neon and Hydrogen. *J. Chem. Phys.* **1989**, *90* (2), 1007–1023.

(52) Schmidt, M. W.; Baldridge, K. K.; Boatz, J. A.; Elbert, S. T.; Gordon, M. S.; Jensen, J. H.; Koseki, S.; Matsunaga, N.; Nguyen, K. A.; Su, S.; Windus, T. L.; Dupuis, M.; Montgomery Jr, J. A. General Atomic and Molecular Electronic Structure System. *J. Comput. Chem.* **1993**, *14* (11), 1347–1363.

(53) Ditchfield, R.; Hehre, W. J.; Pople, J. A. Self-Consistent Molecular-Orbital Methods. IX. An Extended Gaussian-Type Basis for Molecular-Orbital Studies of Organic Molecules. *J. Chem. Phys.* **1971**, *54* (2), 724–728.

(54) Kitaura, K.; Morokuma, K. A New Energy Decomposition Scheme for Molecular Interactions within the Hartree-Fock Approximation. *Int. J. Quantum Chem.* **1976**, *10* (2), 325–340.

(55) Vogiatzis, K. D.; Li, G.; Hensen, E. J. M.; Gagliardi, L.; Pidko, E. A. Electronic Structure of the [Cu3(μ-O)3]2+ Cluster in Mordenite Zeolite and Its Effects on the Methane to Methanol Oxidation. *J. Phys. Chem. C* **2017**, *121* (40), 22295–22302.

(56) Verma, P.; Vogiatzis, K. D.; Planas, N.; Borycz, J.; Xiao, D. J.; Long, J. R.; Gagliardi, L.; Truhlar, D. G. Mechanism of Oxidation of Ethane to Ethanol at Iron(IV)–Oxo Sites in Magnesium-Diluted Fe2(Dobdc). *J. Am. Chem. Soc.* **2015**, *137* (17), 5770–5781.

(57) Schwarz, H.; González-Navarrete, P.; Li, J.; Schlangen, M.; Sun, X.; Weiske, T.; Zhou, S. Unexpected Mechanistic Variants in the Thermal Gas-Phase Activation of Methane. *Organometallics* **2017**, *36* (1), 8–17.

Chapter 7 - Conclusions and Future Work

As discussed in this dissertation, functional catalytic materials for oxygen reduction reaction (ORR) and methane partial oxidation, both of which will dictate the performance and feasibility of direct methanol fuel cells (DMFCs), were modeled and investigated using Density Functional Theory (DFT) and molecular dynamics (MD) simulation techniques.

Vertically aligned carbon nanofibers (VACNF) are effective and tunable 3-D functional support for both ORR and methanol oxidation reactions (MOR). However, the molecular Pt structures on such multi-edged support remain unclear and will hinder the understanding of the fundamental structure-property relationship. This thesis also made efforts to broaden the scope in search of the catalysts that are free from Pt. DFT-based catalyst screening was performed on a class of atomically dispersed dual-metal ORR catalysts (consisting of Fe, Co, Ni) embedded in graphene (GN) frameworks. In addition, monolayer 2-D graphitic carbon nitride (g-C_3N_4) was also considered as a potential functional catalytic material with targeted structure manipulations.

Major findings from these studies are summarized as below:

- Two models were employed to understand ORR performance of Pt catalyst supported on VACNF. For both models, VACNF stabilizes Pt catalysts at its open carbon edges thanks to the strong Pt–C bond. According to the Pt/VACNF model, the exposed low coordination sites bind ORR intermediates strongly compared with Pt(111), leading to lower ORR limiting potential. Moreover, due to the change in adsorption behavior, the ORR potential-determining step shifts from OH* formation (from O*) to OH* desorption.
- A class of dual-metal active configurations, consisting of both PGM (Pt and Pd) and non-PGM (Fe, Co, Ni, and Cu), anchored by six N atoms embedded in monolayer GN

framework were screened using first-principles methods for their ORR performance. Dual-metal sites consisting of Fe and Co tend to overbind the OH species and, in principle, should severely lower the limiting potentials. Nevertheless, DFT modeling discovered that, when treated as an external ligand, the strong binding OH at these dual metal sites actually allows ORR to proceed. By modulating the charge distribution, the OH ligand can enhance ORR activity. In fact, Fe-Co$(OH)_s$ shows one of the highest ORR limiting potentials (0.73 V), outperforming both Pt (111) and FeN_4.

- Metal-free N-rich g-C_3N_4 itself is active for ORR at its abundant pyridinic N sites. However, the poor electrical conductivity (with an intrinsic energy band gap of 2.70 eV) makes it a poor electrocatalytic material. By coupling with GN underlayer, the energy band gap of g-C_3N_4 can be reduced to 0.11 eV. Furthermore, the ORR activity can also be tuned by introducing a single Fe atom. Therefore, Fe/g-C_3N_4/GN hetero-structure was predicted to show similar ORR activity to FeN_4.

The stability of Cu-oxo clusters in the mordenite zeolitic framework, as well as their catalytic activity at different spin multiplicity, were evaluated for methanol production via partial methane oxidation. The main findings from this thesis work are shown as below:

- DFT calculations were carried out to determine various configurations of Cu-oxo clusters in the mordenite zeolitic framework. The bis (μ-oxo) dicopper and copper trioxo are the most thermodynamically stable under synthesis conditions. However, the site II in copper trioxo is the most active towards C–H bond activation due to its high spin density. Similar trends were also observed for ethane and propane activation as well.

The work in this thesis implies that the data extracted with the employed modeling techniques at the molecular level will make tremendous impact on future catalyst search, design,

and development. Therefore, additional work is still needed to provide a theoretical guidance to further enhance catalytic activity and stability of Pt NPs supported by VACNF, single atom catalysts, and Cu-oxo clusters.

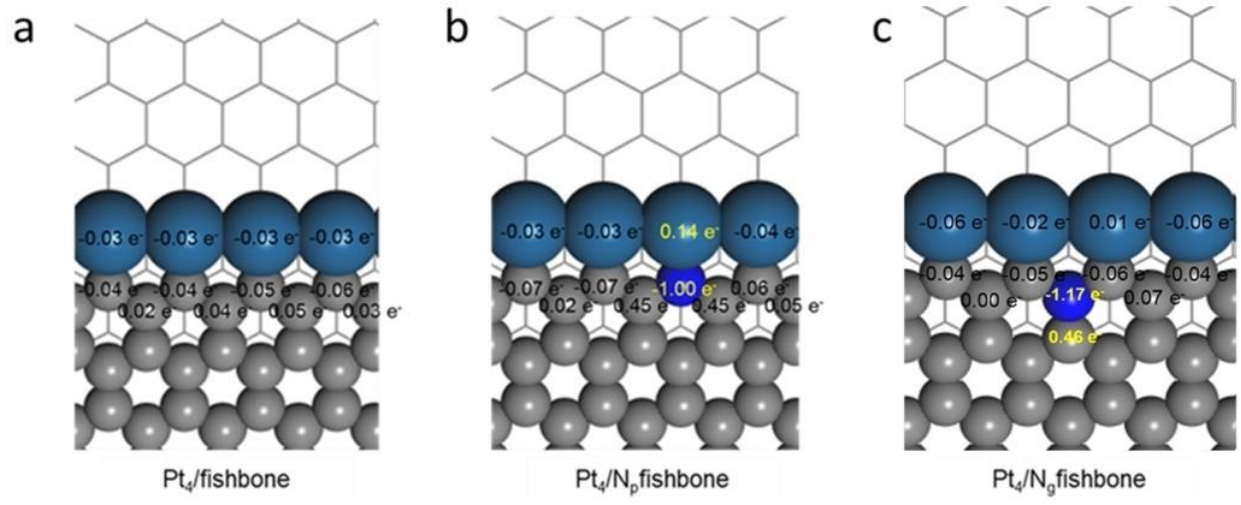


Figure 7.1. Semi-periodic Pt_4 supported on undoped (a), N_p-doped (b), and N_g-doped (c) graphitic edges in a modified fishbone model. The second layer GN network is rendered by grey lines. Numerical values labeled on Pt and edge C atoms are net charges based on Bader charge analyses. Color code: blue-Pt, gray-C, and blue-N. Adapted from Ref [1].

The VACNF architecture is capable of stabilizing Pt NPs. Numerous studies have also suggested that modified graphitic carbon frameworks by heteroatom dopants (e.g., N) display tunable ORR activities.[2–6] From this work, N-dopants (e.g., graphitic and pyridinic N species) will be readily incorporated into both developed VACNF models (i.e., Pt/fishbone and Pt/VACNF) to acquire molecular understanding related to ORR and methanol oxidation reaction. In fact, the Pt/fishbone model has already been utilized to reveal the electronic effect of pyridinic and graphitic N on CO binding and conversions (see Figure 7.1).[1] Pyridinic N (in Figure 7.1b) is capable of

withdrawing charges from adjacent Pt atom. However, graphitic N species (in Figure 7.1c) do not show the same effect. DFT calculations revealed that the charge transfer occurs between N-doped edges and Pt will impact the MOR activity by modulating the adsorption energy differences between CO and OH, which shrinks when compared with the N-free model (Figure 7.1a), suggesting that graphitic N could improve Pt tolerance toward CO poisoning.[1] In the future, a full assessment on methanol oxidation reaction will be considered.

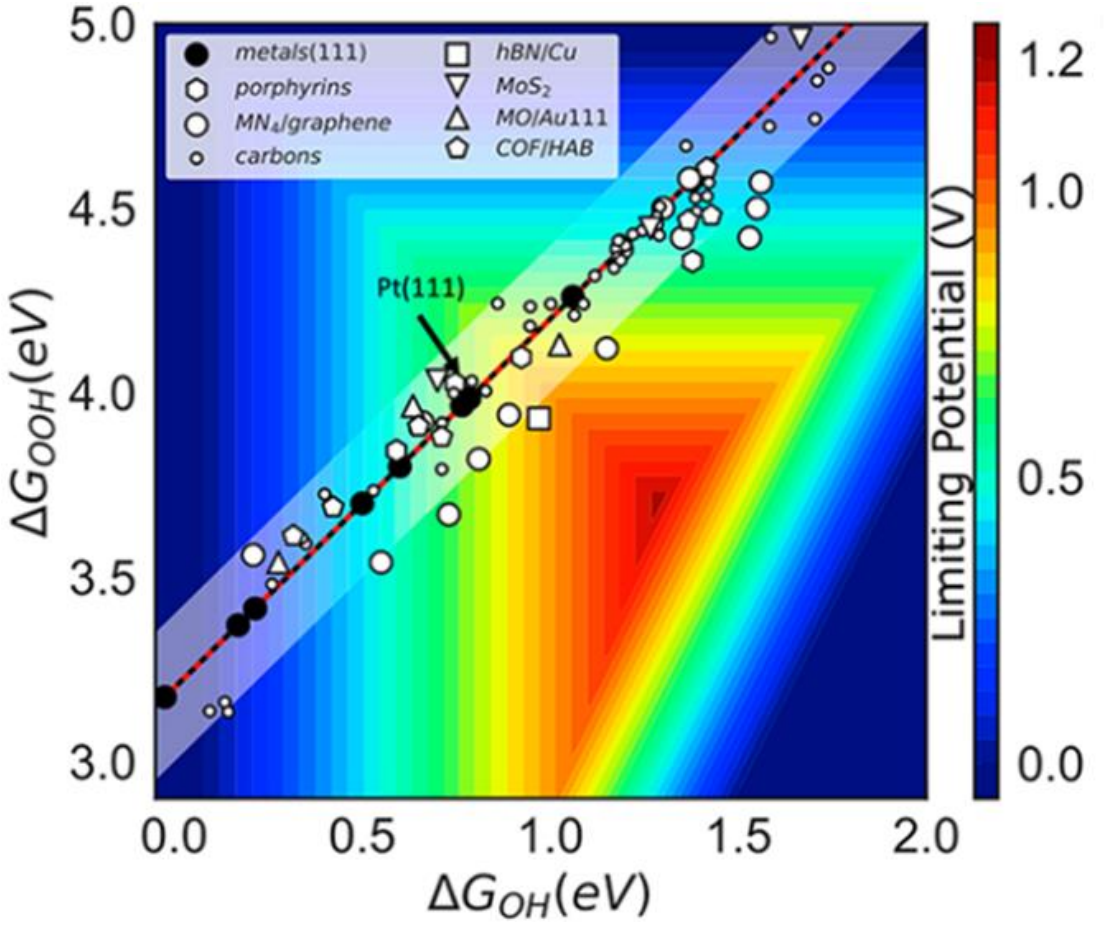


Figure 7.2. Limiting potential volcano plot for different classes of ORR electrocatalysts. The straight line indicates the linear constraint between ΔG_{OOH^*} and ΔG_{OH^*}. Adapted from Ref.[7]

Up to this point, the linear scaling relationship between ΔG_{OOH^*}vs ΔG_{OH^*} (see Figure 7.2) still governs intrinsic properties of the majority identified catalytic materials. The optimal ORR activity, with U_{lim} = 1.23 V, is off from the governing linear scaling relationship. Recently, Kulkarni *et al.*[7] pointed out that the linear scaling between ΔG_{OH^*} and ΔG_{OOH^*} needs to be broken in order to achieve the optimal ORR activity, red region in Figure 7.2. For instance, this would require simultaneous weakening of OH binding and strengthening of OOH binding. Strategies to break the linear scaling relationship include designing catalysts consisting of two distinct sites for separate OOH and OH adsorptions. In practice, different C_xN_y matrices (i.e. triazine, porphyrins, etc.) are the promising starting point. For ORR active site engineering, dimer, trimer, or cluster metal configurations will also present the opportunities to break away from current ORR performance constraint. Furthermore, advanced experimental synthesis, characterization, and data science methodologies are also integral components in future catalyst design paradigm.

DFT calculations also showed that Cu-trioxo is very active for ORR, however, continuous effort is needed to explore other catalyst structures to further enhance catalytic reactivities. One area is to understand if the dependence of C-H bond activation barriers on the size Cu-oxo cluster, or the Cu loading. In addition, Fe-oxo complexes have been extensive reported to be effective for methane partial oxidation as well, for instance, in enzymatic bicatalysts.[8] Our established approach, again, can be readily used for the elucidation of the catalyst stability and the preferred stable phases. Spin-polarized DFT calculations will then be performed to map out the thermodynamic and kinetic profiles for the catalytic conversions of methane into methanol, CO, CO_2, and other possible value-added oxidation products.

References

(1) Elangovan, A.; Xu, J.; Sekar, A.; Liu, B.; Li, J. Enhancing Methanol Oxidation Reaction with Platinum-Based Catalysts Using a N-Doped Three-Dimensional Graphitic Carbon Support. *ChemCatChem* **2020**, *12* (23), 6000–6012.

(2) Zhou, Y.; Neyerlin, K.; Olson, T. S.; Pylypenko, S.; Bult, J.; Dinh, H. N.; Gennett, T.; Shao, Z.; O'Hayre, R. Enhancement of Pt and Pt-Alloy Fuel Cell Catalyst Activity and Durability via Nitrogen-Modified Carbon Supports. *Energy Environ. Sci.* **2010**, *3* (10), 1437–1446.

(3) Saha, M. S.; Li, R.; Sun, X.; Ye, S. 3-D Composite Electrodes for High Performance PEM Fuel Cells Composed of Pt Supported on Nitrogen-Doped Carbon Nanotubes Grown on Carbon Paper. *Electrochem. commun.* **2009**, *11* (2), 438–441.

(4) Chen, Y.; Wang, J.; Liu, H.; Banis, M. N.; Li, R.; Sun, X.; Sham, T.-K.; Ye, S.; Knights, S. Nitrogen Doping Effects on Carbon Nanotubes and the Origin of the Enhanced Electrocatalytic Activity of Supported Pt for Proton-Exchange Membrane Fuel Cells. *J. Phys. Chem. C* **2011**, *115* (9), 3769–3776.

(5) Chen, Y.; Wang, J.; Liu, H.; Li, R.; Sun, X.; Ye, S.; Knights, S. Enhanced Stability of Pt Electrocatalysts by Nitrogen Doping in CNTs for PEM Fuel Cells. *Electrochem. commun.* **2009**, *11* (10), 2071–2076.

(6) Ma, J.; Habrioux, A.; Luo, Y.; Ramos-Sanchez, G.; Calvillo, L.; Granozzi, G.; Balbuena, P. B.; Alonso-Vante, N. Electronic Interaction between Platinum Nanoparticles and Nitrogen-Doped Reduced Graphene Oxide: Effect on the Oxygen Reduction Reaction. *J. Mater. Chem. A* **2015**, *3* (22), 11891–11904.

(7) Kulkarni, A.; Siahrostami, S.; Patel, A.; Nørskov, J. K. Understanding Catalytic Activity Trends in the Oxygen Reduction Reaction. *Chem. Rev.* **2018**, *118* (5), 2302–2312.

(8) Ross, M. O.; Rosenzweig, A. C. A Tale of Two Methane Monooxygenases. *JBIC J. Biol. Inorg. Chem.* **2017**, *22* (2), 307–319.

Appendix A - Physical Properties of g-C_3N_4 and Heterostructures

Associative ORR Mechanism (without Fe)

$$O_2(g) + H_2O(l) + e^- + * \rightarrow OOH^* + OH^-(aq) \quad \text{(A.1)}$$

$$OOH^* + e^- \rightarrow O^* + OH^-(aq) \quad \text{(A.2)}$$

$$O^* + H_2O(l) + e^- \rightarrow OH^* + OH^-(aq) \quad \text{(A.3)}$$

$$OH^* + e^- \rightarrow * + OH^- \quad \text{(A.4)}$$

Associative ORR Mechanism (with Fe single atom)

$$O_2(g) + * \rightarrow O_2^* \quad \text{(A.5)}$$

$$O_2^* + H_2O(l) \rightarrow OOH^* + OH^-(aq) \quad \text{(A.6)}$$

$$OOH^* + e^- \rightarrow O^* + OH^-(aq) \quad \text{(A.7)}$$

$$O^* + H_2O(l) + e^- \rightarrow OH^* + OH^-(aq) \quad \text{(A.8)}$$

$$OH^* + e^- \rightarrow * + OH^- \quad \text{(A.9)}$$

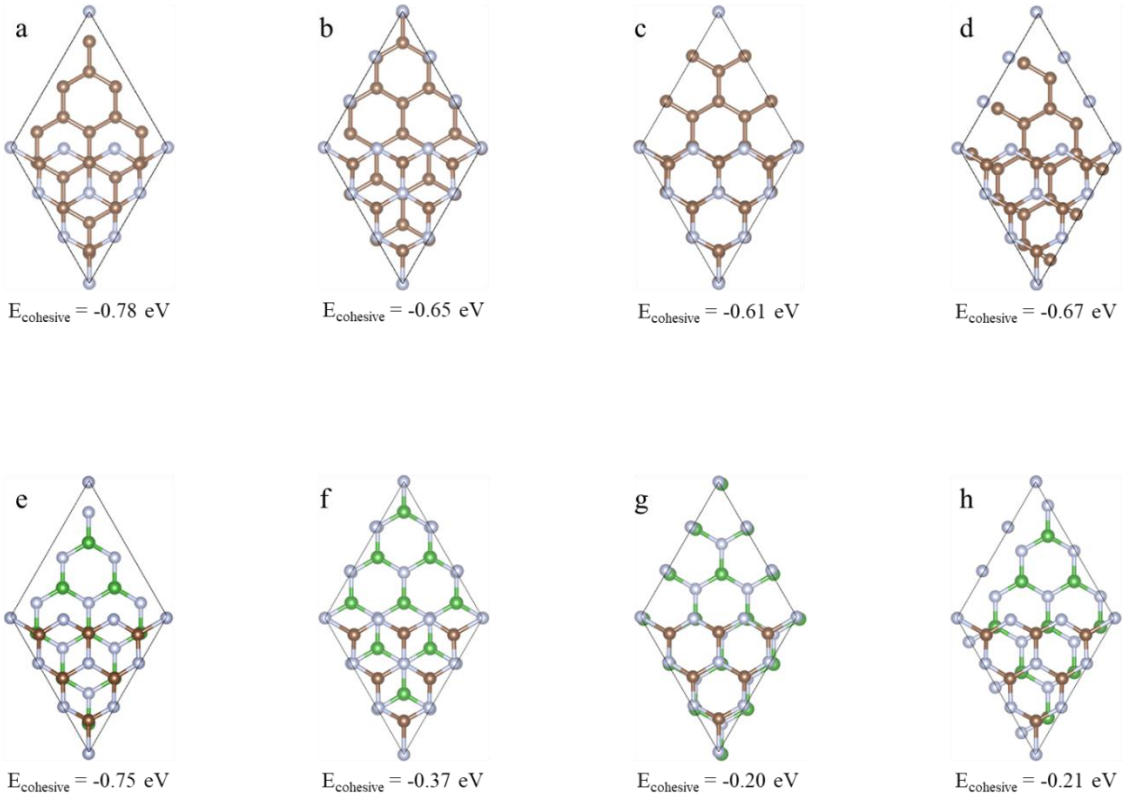


Figure A.1. Different stacking configurations of g-C_3N_4/GN (a-d) and g-C_3N_4/hBN (e-h). The corresponding cohesive energies are also shown. (Color code: blue-N, green-B, brown-C)

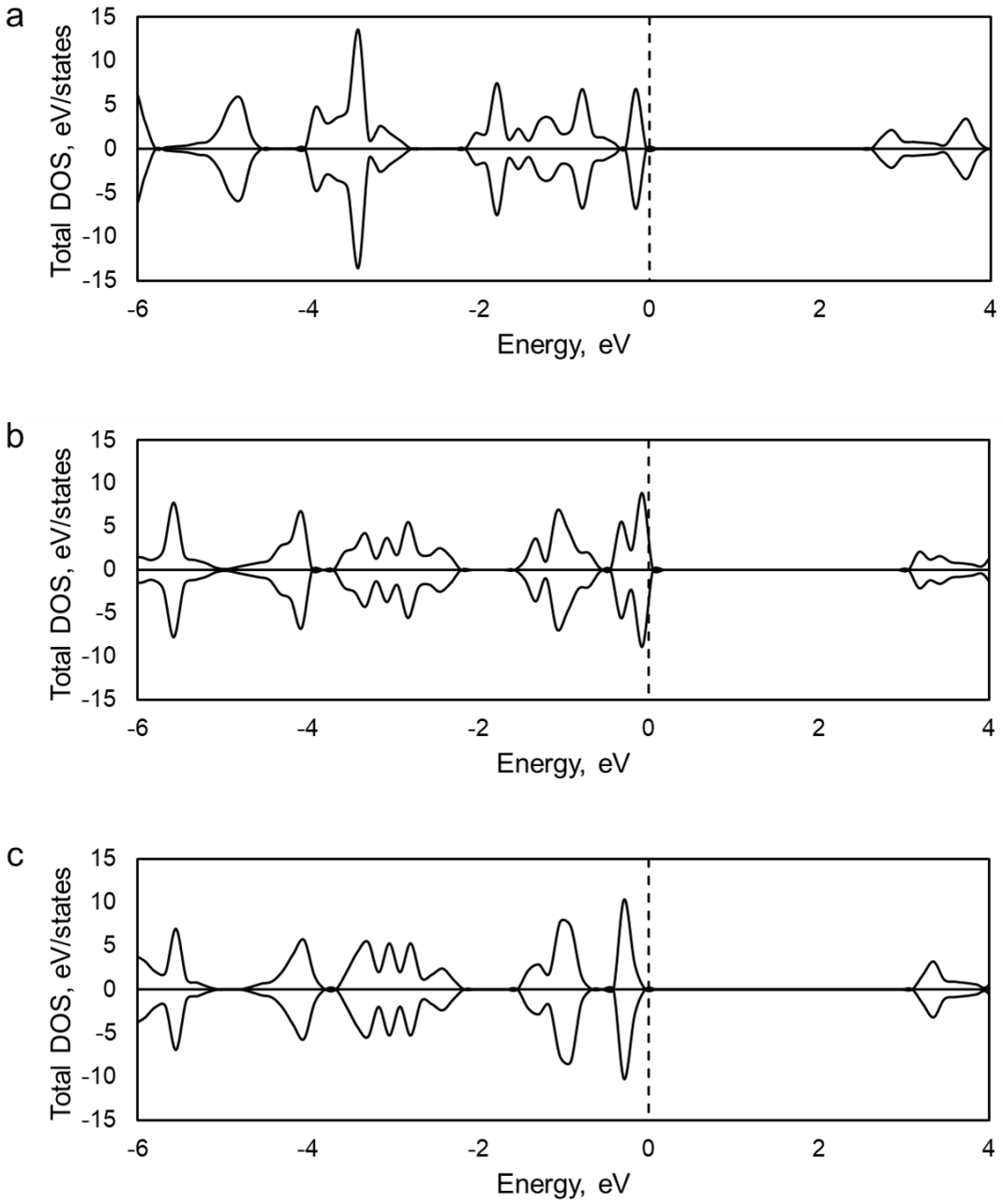


Figure A.2. Total DOS of g-C_3N_4 at lattice parameter of (a) 7.13 Å, (b) 7.31 Å, and (c) 7.40 Å with the corresponding energy band gap of 2.79 eV, 3.15 eV, and 3.20 eV.

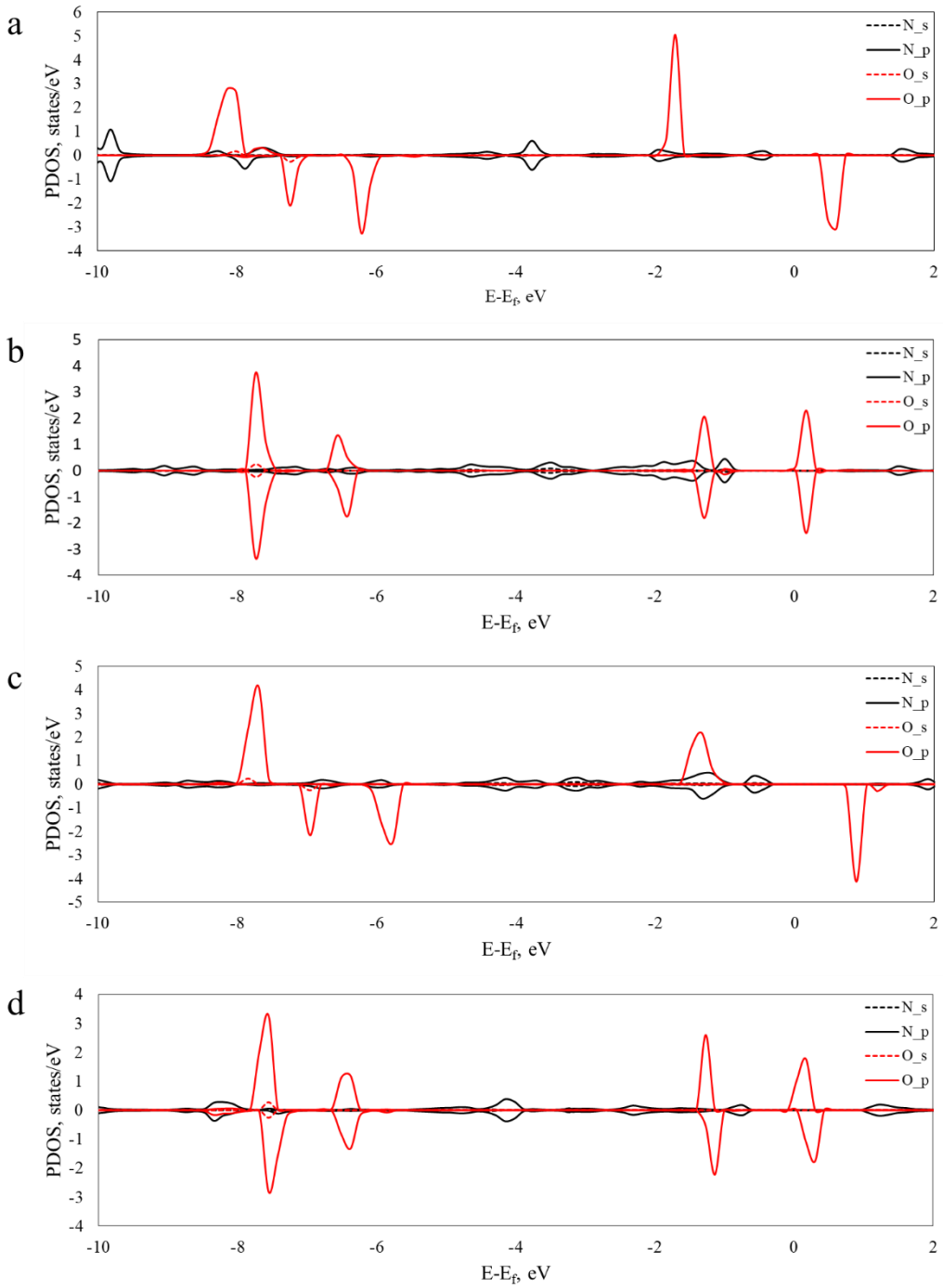
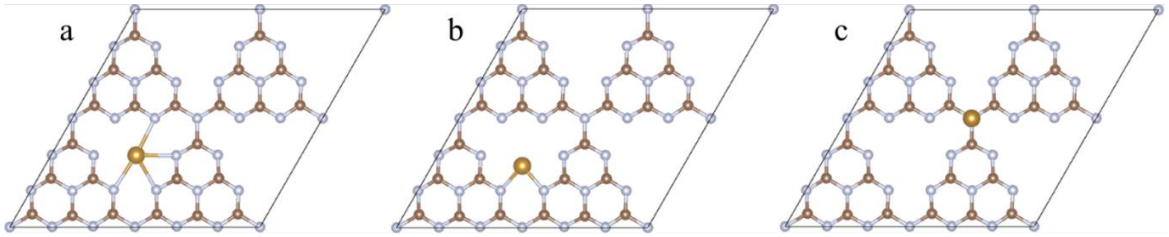


Figure A.3. Total DOS of O_2 adsorption over (a) g-C_3N_4 monolayer, (b) g-C_3N_4/GN, (c) g-C_3N_4/hBN, and (d) g-C_3N_4 multilayer.



$E_{relative}$ = 0.00 eV $E_{relative}$ = 0.79 eV $E_{relative}$ = 3.45 eV

Figure A.4. Optimized structures of Fe at different locations of the g-C_3N_4 substrate. (a) Hollow site coordinated with 4 N_p; (b) hollow site coordinated with 2 N_p; and (3) Fe on top of N_g. The lowest energy structure (a) is set to be at 0 eV. (Color code: blue-N, brown-C, and yellow-Fe)

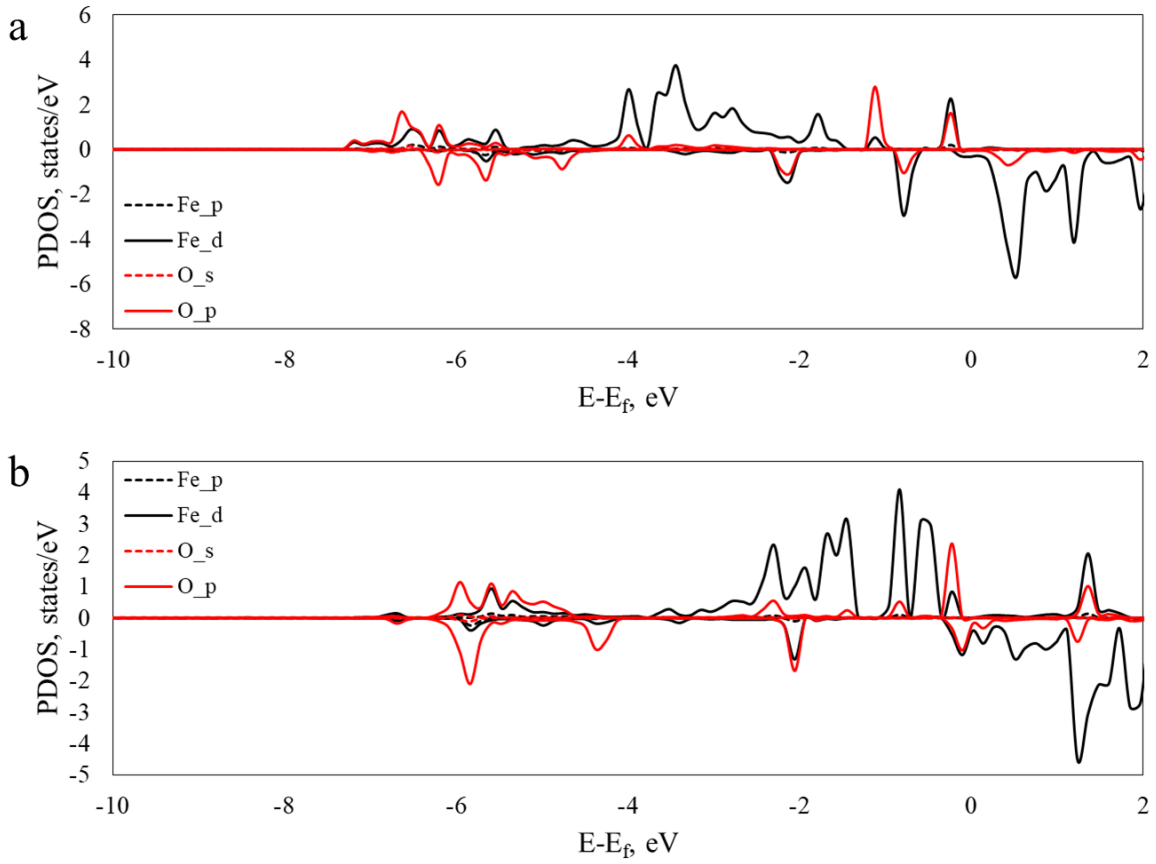


Figure A.5. DOS of O_2 adsorption on (a) Fe/g-C_3N_4 and (b) Fe/g-C_3N_4/GN.

Appendix B - Atomic Structures of ORR Intermediates at Dual Metal Centers

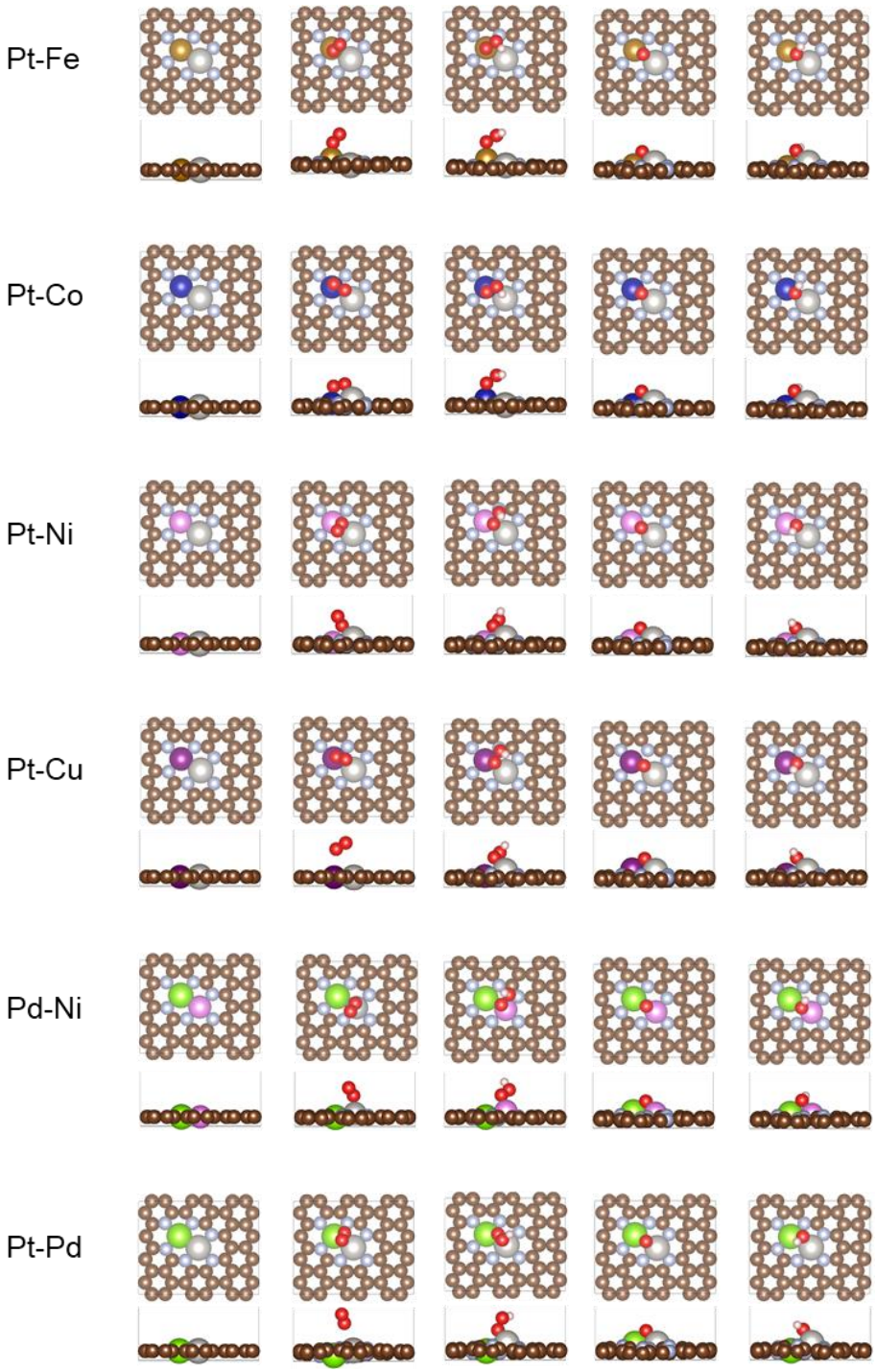


Figure B.1. Optimized dual-metal sites (consisting of PGM) and configurations of O_2, OOH, O, and OH adsorbates. Color code: brown-C, light blue-N, yellow-Fe, dark blue-Co, pink-Ni, purple-Cu, silver-Pt, green-Pd, red-O, and white, H.

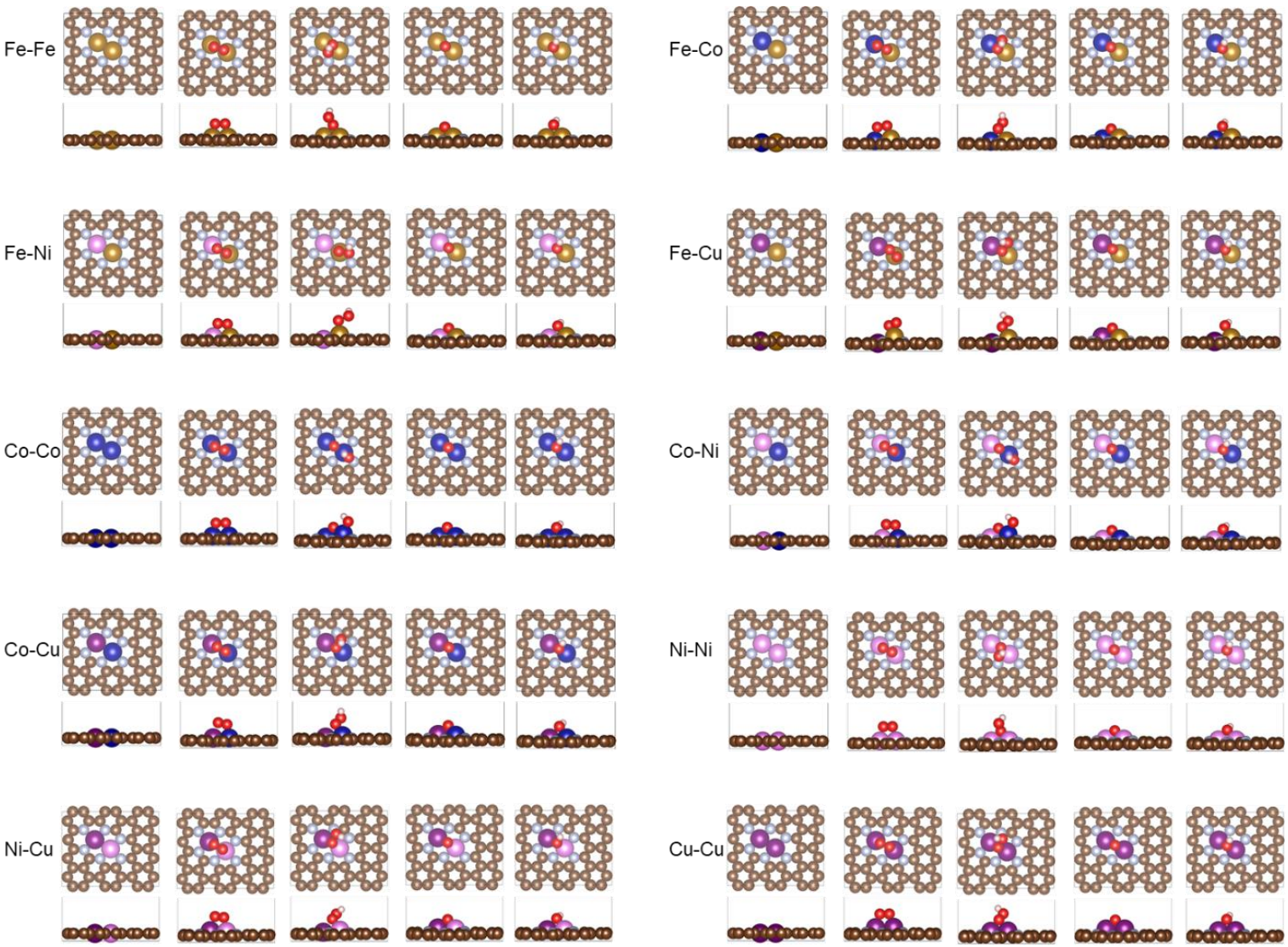


Figure B.2. Optimized dual-metal sites (consisting of non-PGM only) and configurations of O_2, OOH, O, and OH. Color code: brown-C, light blue-N, yellow-Fe, dark blue-Co, pink-Ni, purple-Cu, red-O, and white, H.

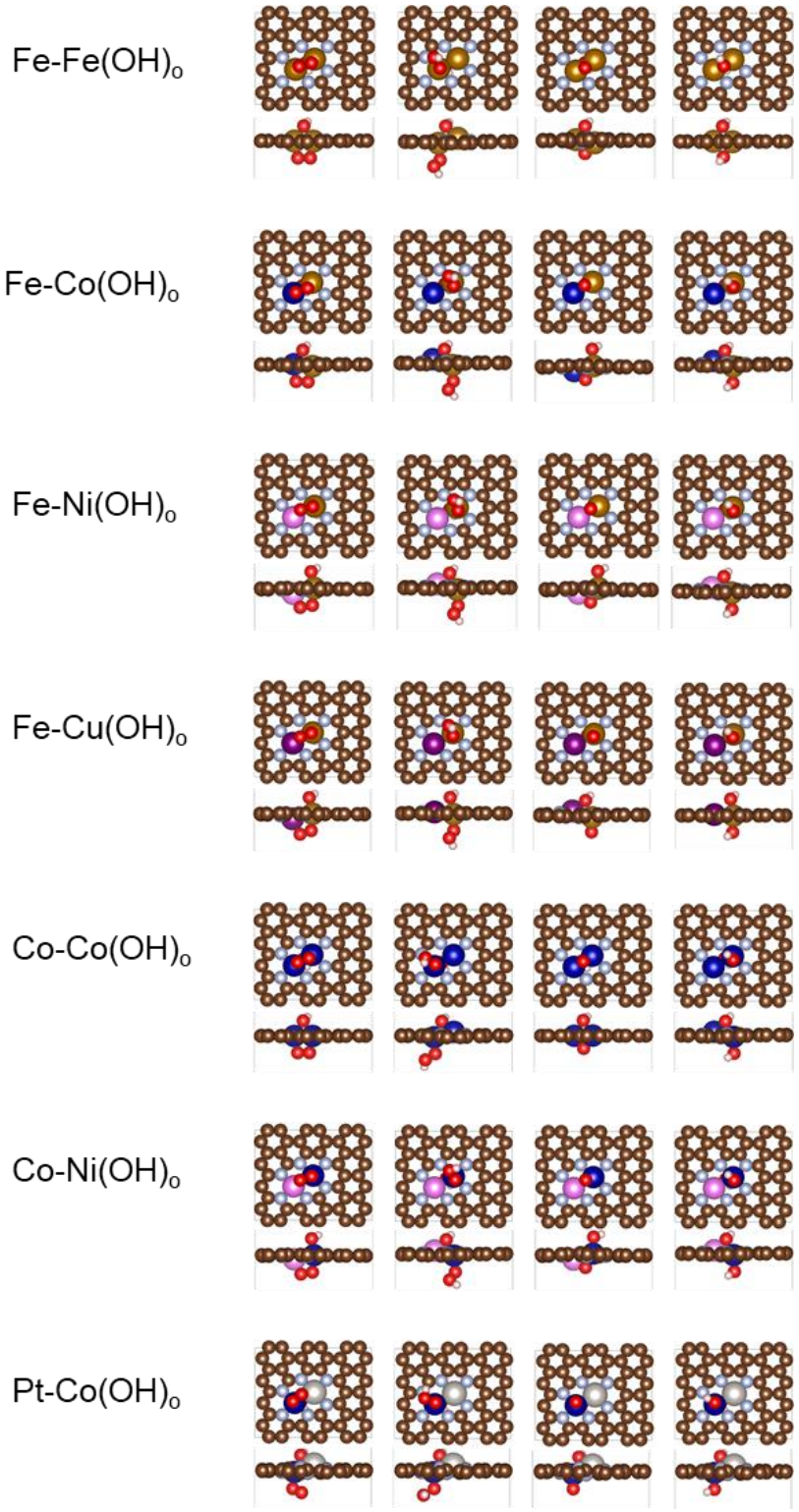
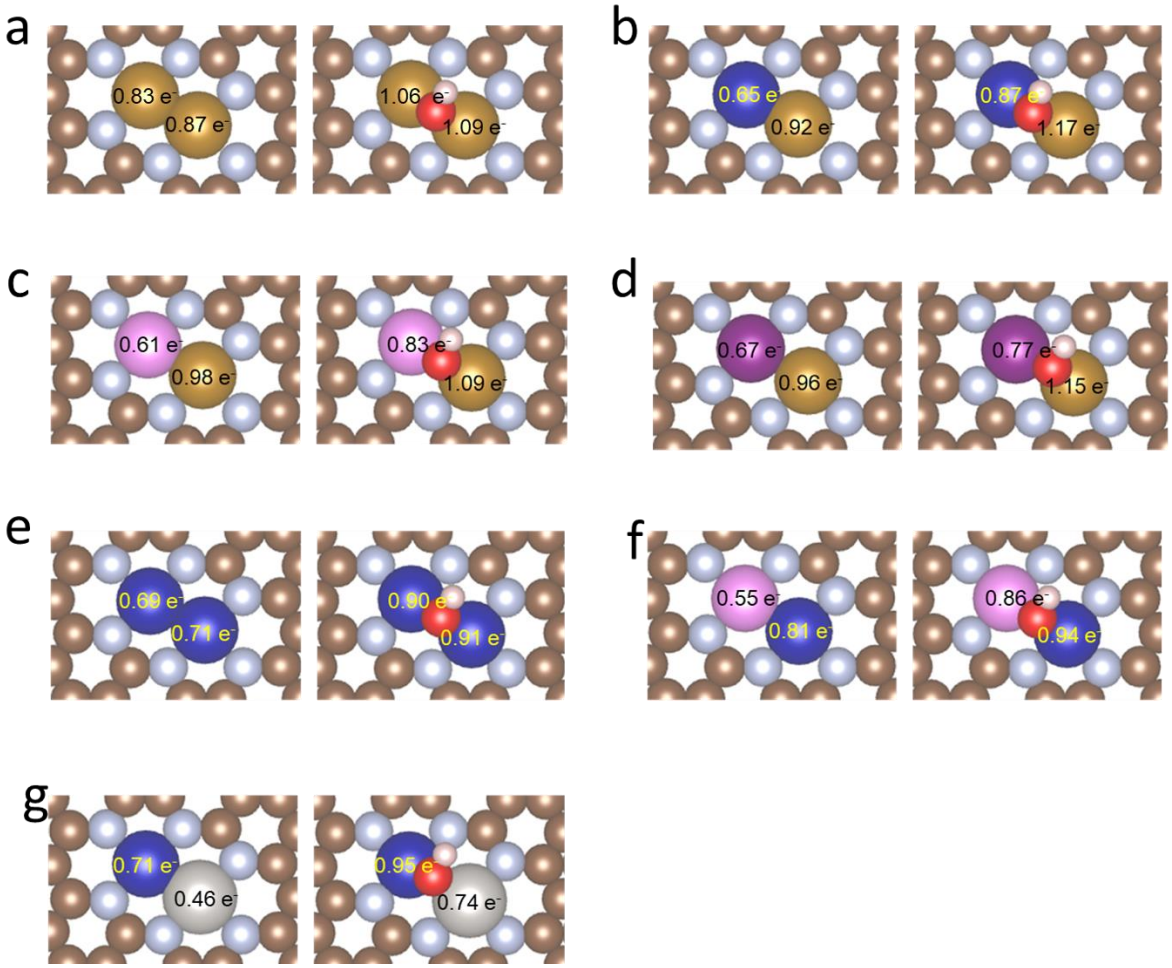


Figure B.3.Optimized dual-metal site and configurations O_2, OOH, O, and OH that bind on the opposite side of the pre-adsorbed OH ligand. Color code: brown-C, light blue-N, yellow-Fe, dark blue-Co, pink-Ni, purple-Cu, silver-Pt, red-O, and white-H.



.

Figure B.4. Bader charge analysis of Fe-Fe (a), Fe-Co (b), Fe-Ni (c), Fe-Cu (d), Co-Co (e), Co-Ni (f), and Pt-Co (g) with (right) and without (left) the pre-adsorbed OH ligand. Color code: brown-C, light blue-N, yellow-Fe, dark blue-Co, pink-Ni, purple-Cu, silver-Pt, red-O, and white, H.

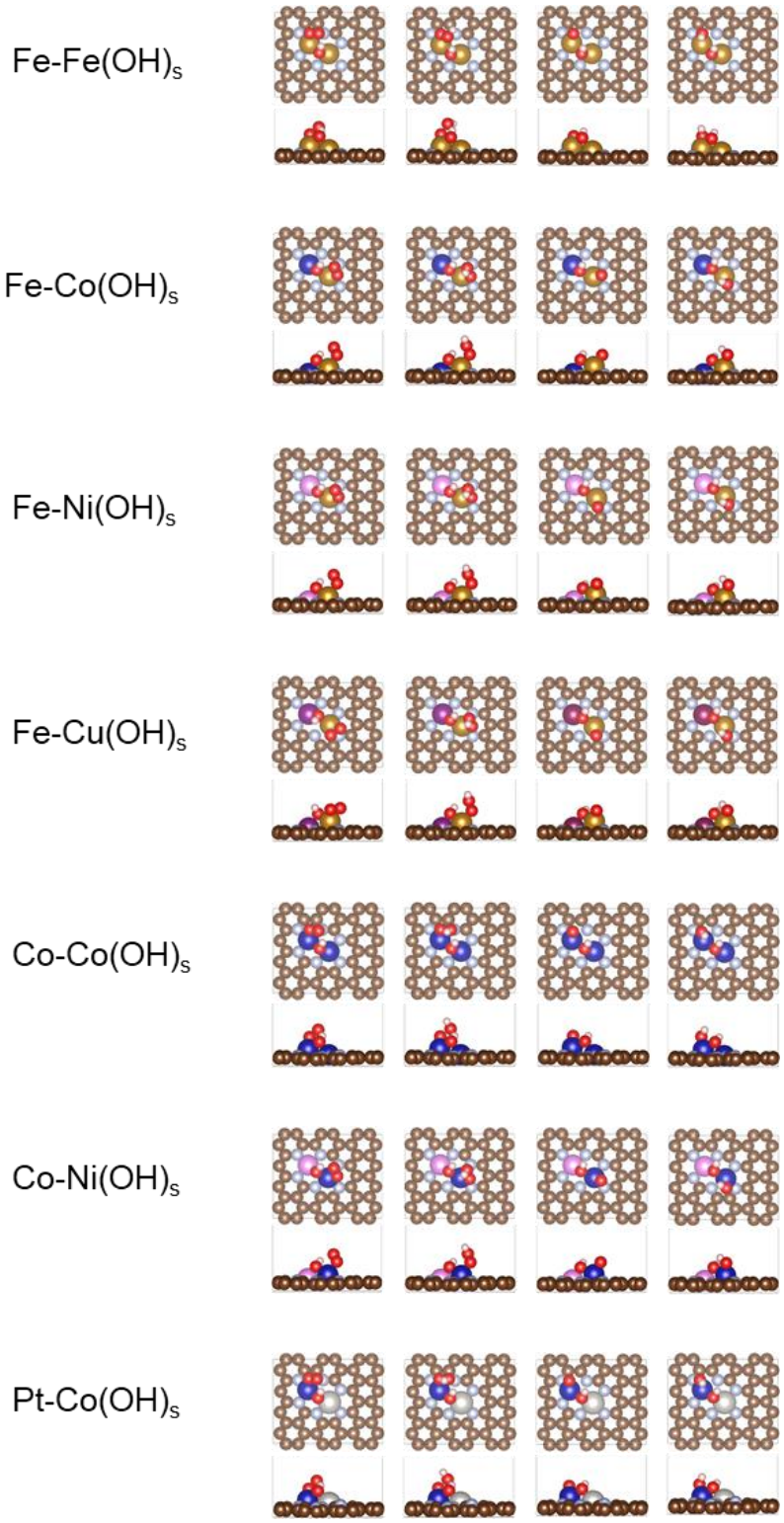


Figure B.5. Optimized dual-metal site and configurations O_2, OOH, O, and OH that bind on the same side of the pre-adsorbed OH ligand. Color code: brown-C, light blue-N, yellow-Fe, dark blue-Co, pink-Ni, purple-Cu, silver-Pt, red-O, and white-H.

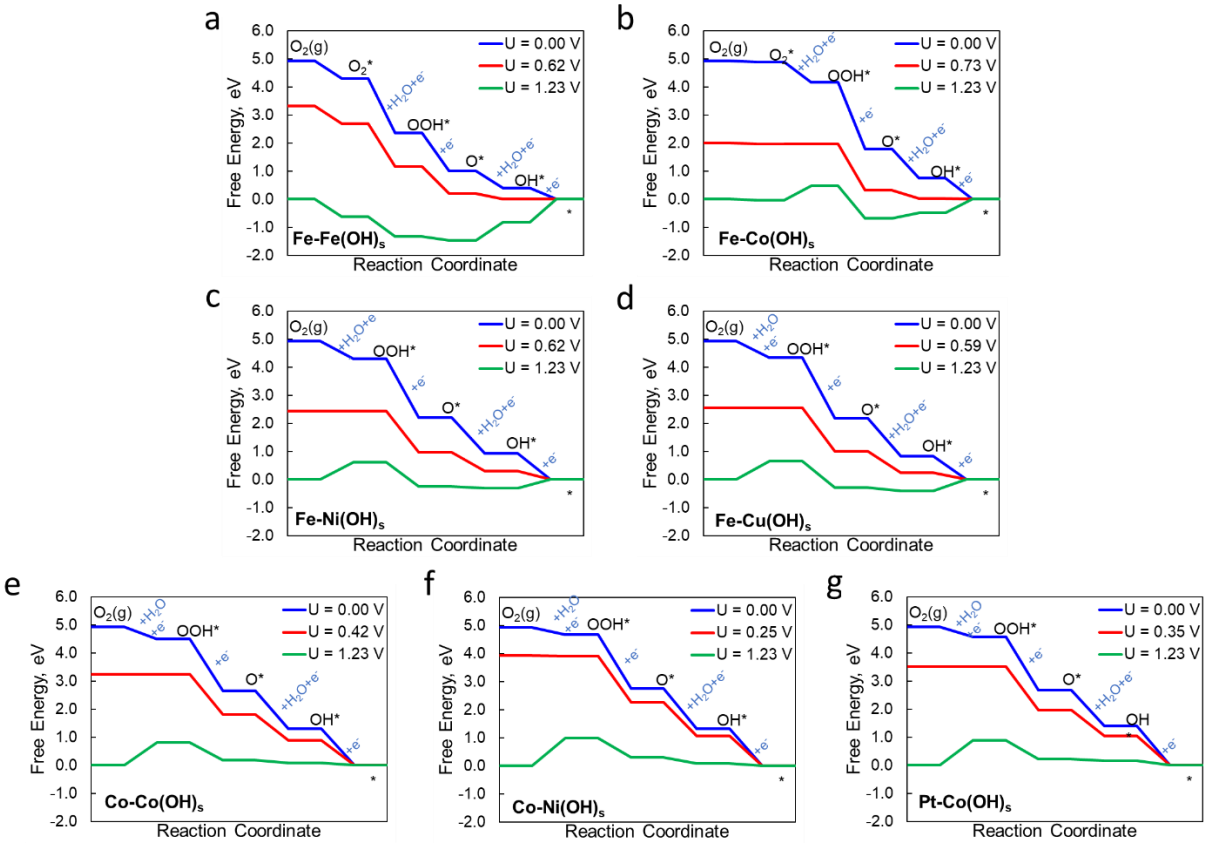


Figure B.6. Free energy diagrams of ORR over (a) Fe-Fe$(OH)_s$, (b) Fe-Co$(OH)_s$, (c) Fe-Ni$(OH)_s$, (d) Fe-Cu$(OH)_s$, (e) Co-Co$(OH)_s$, (f) Co-Ni$(OH)_s$, and (g) Pt-Co$(OH)_s$ at the same side of OH ligand. "*" indicates clean surface.

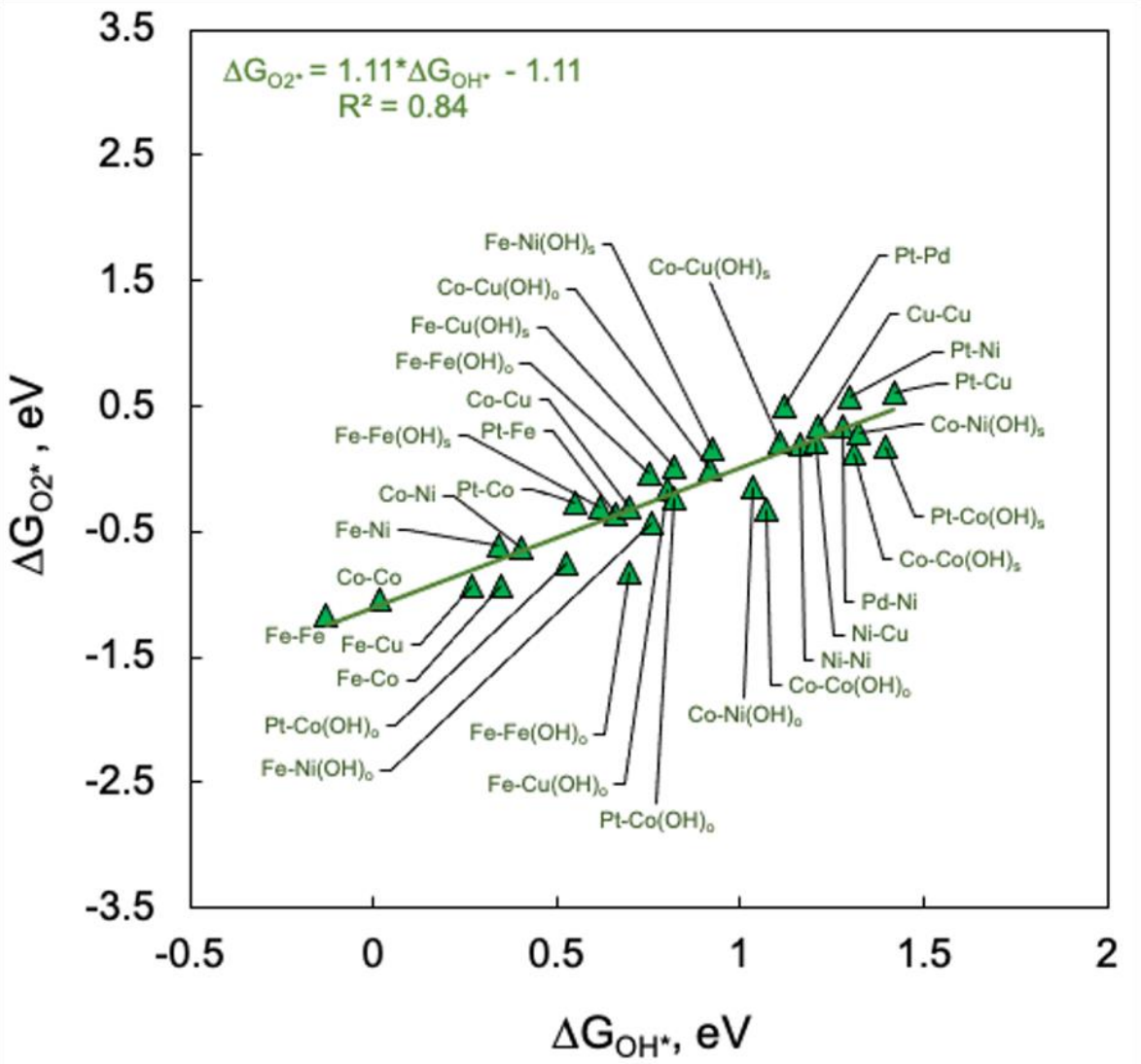


Figure B.7. The relationship between the adsorptions of OH and O_2 (i.e., ΔG_{OH^*} and $\Delta G_{O_2^*}$).

Table B.1.. Adsorption free energies (in eV) of ORR intermediates and onset potential (U_{lim} in V) on the same side of pre-adsorbed OH.

	$\Delta G_{O_2^*}$	ΔG_{OOH^*}	ΔG_{O^*}	ΔG_{OH^*}	U_{lim}	RLS
Fe-Fe$(OH)_s$	-0.31	3.90	1.55	0.62	0.62	R7
Fe-Co$(OH)_s$	-0.03	4.16	1.78	0.75	0.73	R3
Fe-Ni$(OH)_s$	0.16	4.30	2.21	0.93	0.62	R4
Fe-Cu$(OH)_s$	0.02	4.33	2.18	0.82	0.59	R4
Co-Co$(OH)_s$	0.12	4.50	2.65	1.31	0.42	R4
Co-Ni$(OH)_s$	0.29	4.67	2.75	1.32	0.25	R4
Pt-Co$(OH)_s$	0.18	4.57	2.68	1.39	0.35	R4

Appendix C - Stabilities of Cu-Oxo Clusters in 8MR and Free Energy Diagrams of Methane Partial Oxidation at Different Spin Multiplicities

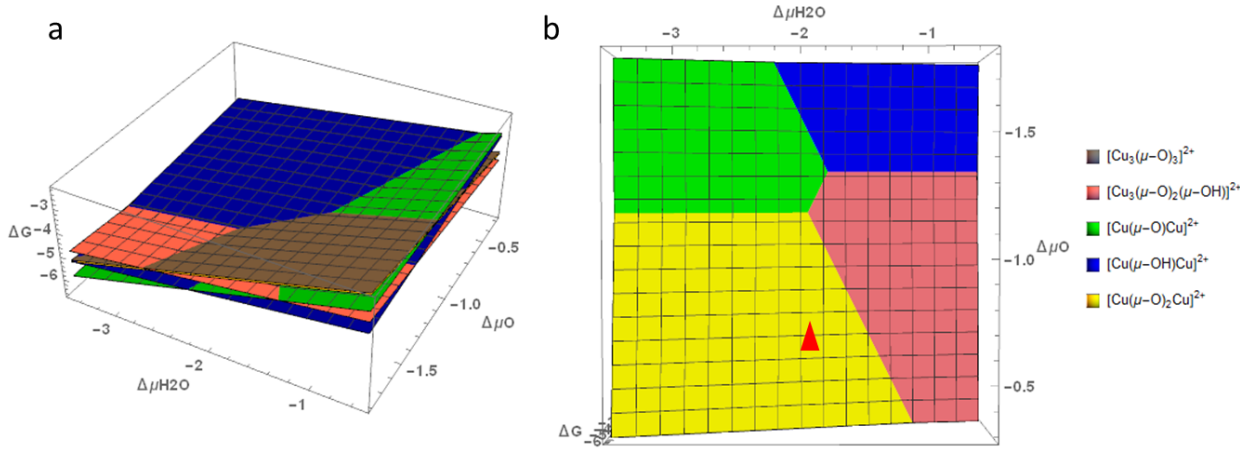


Figure C.1. Phase diagram (a) of Cu-oxo active centers as a function of μ_{H_2O} and μ_O, and (b) the most stable active center configuration (indicated by the red triangle) from the bottom view.

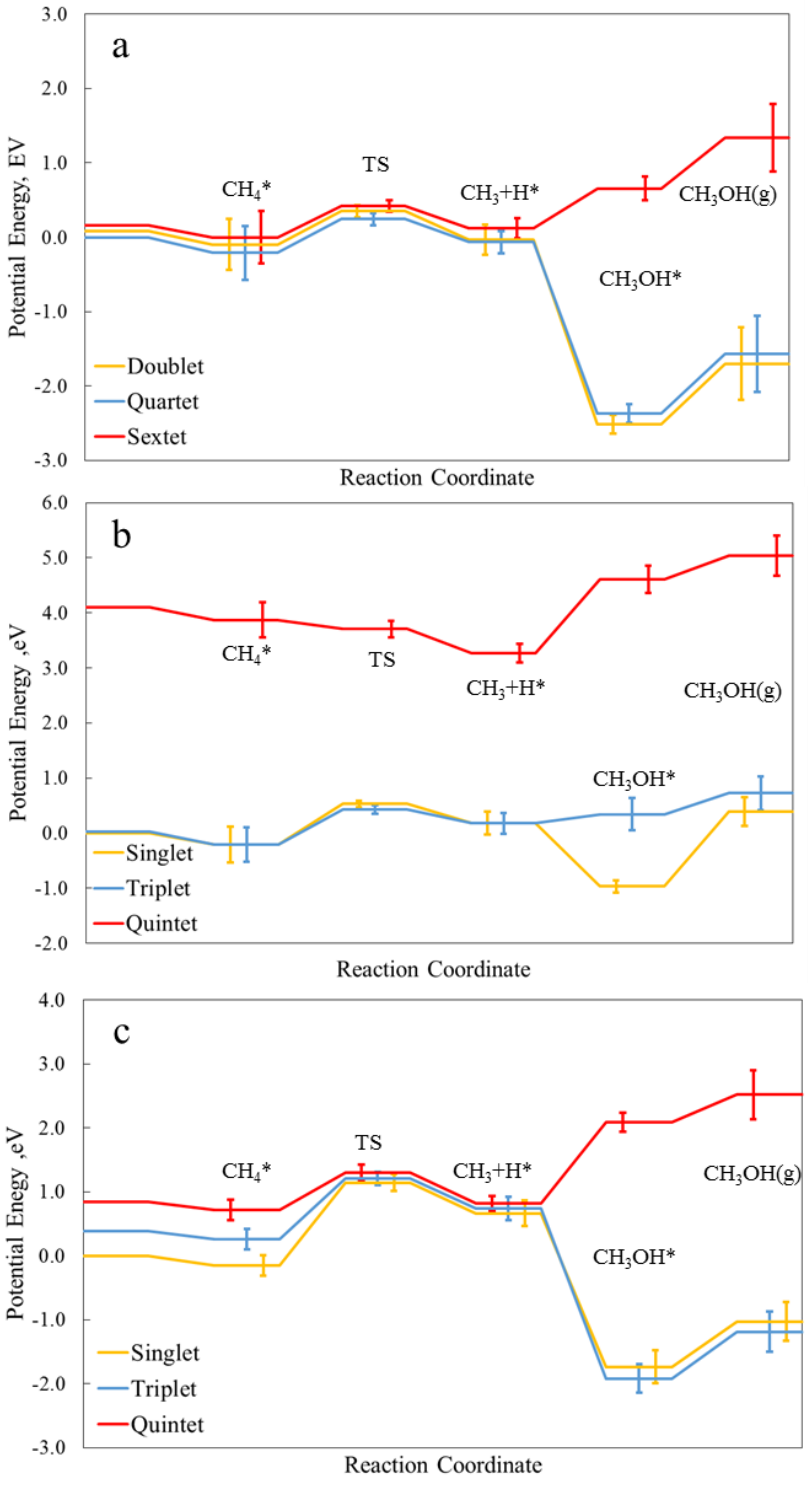


Figure C.2. Energetics of methane partial oxidation over (a) site II of Cu-trioxo, (b) mono (μ-oxo) dicopper, and (c) bis (μ-oxo) dicopper with different spin multiplicities. Computational errors are based on the Bayesian error estimation.

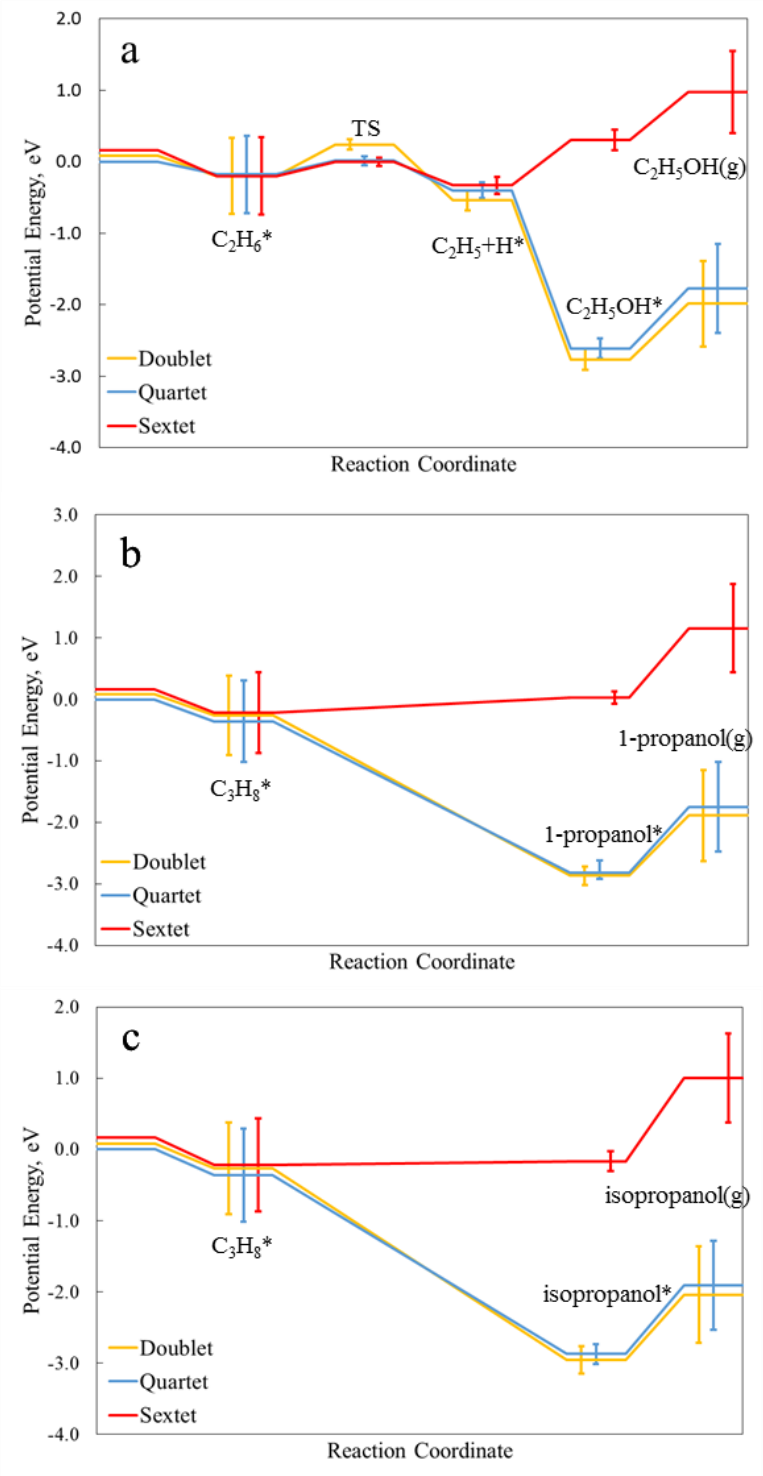


Figure C.3. Potential energy surfaces of respective ethane and propane conversions into ethanol (a), 1-propanol (b), and isopropanol (c) over site II of Cu-trioxo active site at doublet (yellow), quartet (blue), and sextet (red) spin multiplicities. Computational errors are based on the Bayesian error estimation.

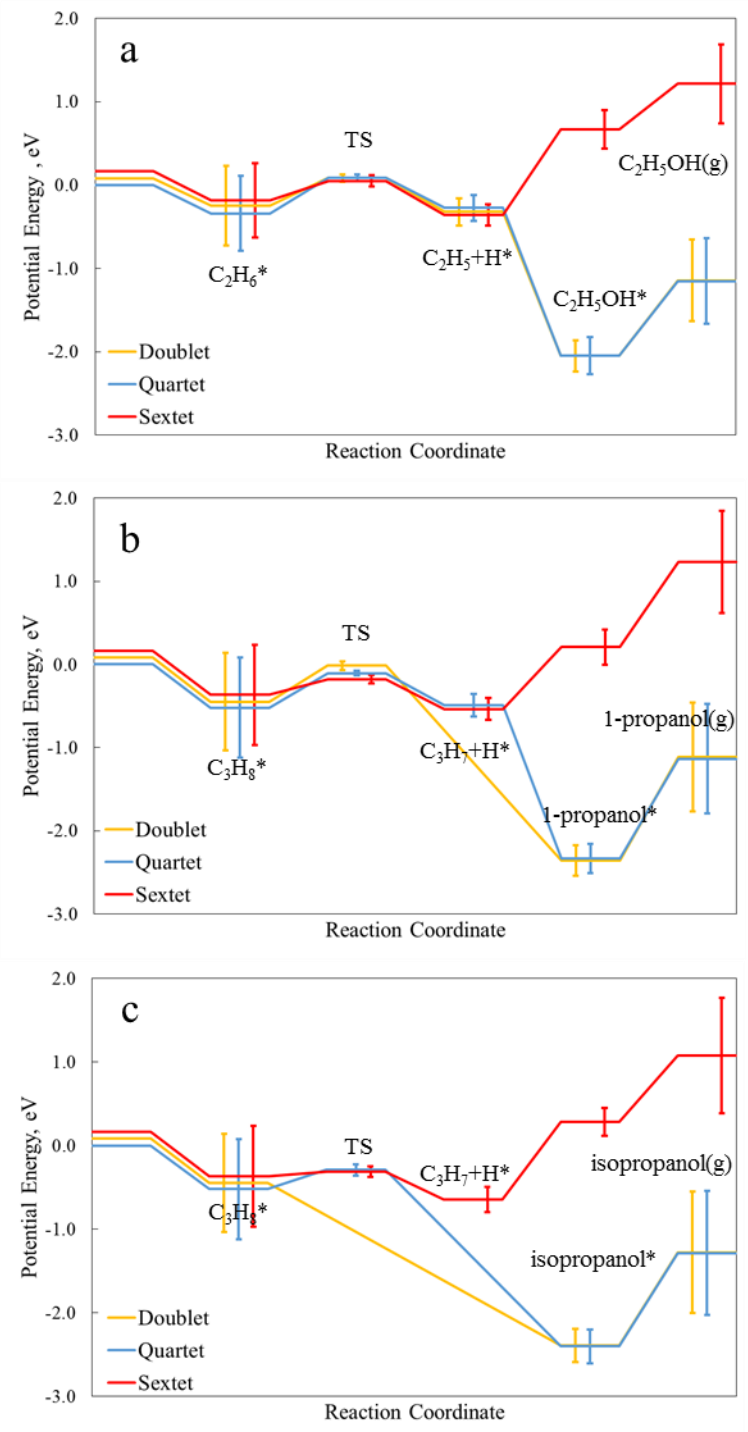


Figure C.4. Potential energy surfaces of respective ethane and propane conversions into ethanol (a), 1-propanol (b), and isopropanol (c) over site I of Cu-trioxo active site at doublet (yellow), quartet (blue), and sextet (red) spin multiplicities. Computational errors are based on the Bayesian error estimation.

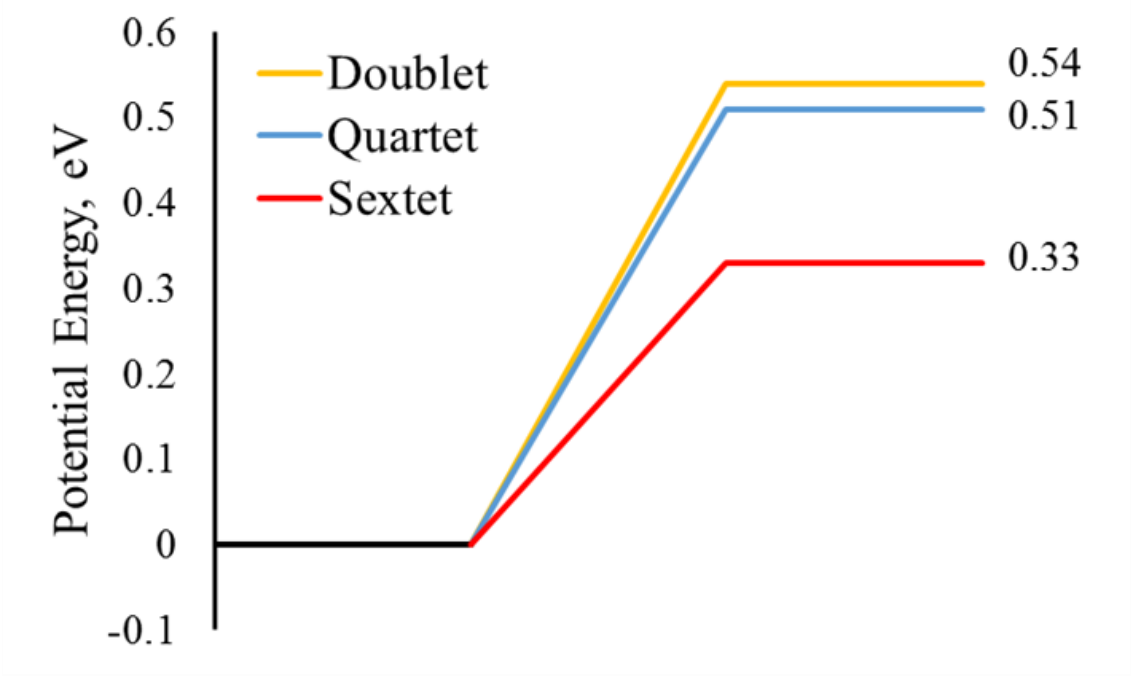


Figure C.5. Methane C-H bond activation considering doublet (yellow), quartet (blue), and sextet (red) spin multiplicities. The energy barriers (in eV) are also labeled numerically.

Table C.1. Lattice parameters and magnetic moments of bulk CuO.

Method	a	b	c	γ	Magnetic moment
PBE	4.60	3.60	5.12	99.25	0.00
LDA+U	4.60	3.45	5.09	99.51	0.67
LDA+U[a]	4.59	3.35	5.04	99.39	0.66
BEEF-vdW+U	4.66	3.44	5.12	100.1	0.67
Expt. values[a]	4.68	3.42	5.13	99.54	0.68

[a]Reference [2]

Table C.2. Bond distance and band angles of optimized Cu-oxo clusters.

Active center	Descriptor	Bond distance (Å) /angle (°)
Mono (μ-oxo) dicopper	O_1-Cu_1	1.96
	O_2-Cu_1	2.12
	O_3-Cu_2	2.05
	O_4-Cu_2	1.98
	O_5-Cu_1	1.75
	O_5-Cu_2	1.76
	∠Cu_1-O_5-Cu_2	131.46
Bis (μ-oxo) dicopper	O_1-Cu_1	1.96
	O_2-Cu_1	1.97
	O_3-Cu_2	1.95
	O_4-Cu_2	1.93
	O_5-Cu_1	1.80
	O_5-Cu_2	1.81
	O_6-Cu_1	1.81
	O_6-Cu_2	1.81
	∠Cu_1-O_5-Cu_2	99.66
	∠Cu_1-O_6-Cu_2	99.28
Cu-trioxo	O_1-Cu_1	2.05
	O_2-Cu_1	2.00
	O_3-Cu_2	2.04
	O_4-Cu_3	2.03
	O_5-Cu_2	2.26
	O_6-Cu_1	1.81
	O_6-Cu_2	1.78
	O_7-Cu_2	1.81
	O_7-Cu_3	1.84
	O_8-Cu_1	1.83
	O_8-Cu_3	1.79
	∠Cu_1-O_6-Cu_2	117.22
	∠Cu_2-O_7-Cu_3	99.64
	∠Cu_1-O_8-Cu_3	119.49

Table C.3. Spin densities of each active sites at different spin multiplicities

Spin States	Cu-trioxo	
	site I	site II
doublet	0.020	0.010
quartet	0.035	0.205
sextet	0.196	0.197
	Mono (μ-oxo) dicopper	
singlet	0.000	
triplet	0.077	
quintet	0.001	
	Bis (μ-oxo) dicopper	
singlet	0.000	
triplet	0.092	
quintet	0.236	

Computational methods for thermodynamic properties

The thermodynamic stability of different active sites was evaluated according to reaction. (1), in which the bulk copper oxide (CuO), O_2, H_2O, and , protonated MOR framework were chosen to be the reference state as reported in Ref [1]. $Cu_xO_mH_n$(MOR-2H) represents the active site in MOR with two protons.

$$\frac{2m-2x-n+2}{4}O_2+\frac{n-2}{2}H_2O+x(CuO)+(MOR-4H) \leftrightarrow Cu_xO_mH_n(MOR-2H) \quad (1)$$

Hence, the reaction Gibbs free energies, ΔG, for reaction (1) is calculated using eqn (2):

$$\Delta G(T,P)=G_{Cu_xO_mH_n(MOR-2H)}-G_{(MOR-4H)}-xG_{CuO}-\frac{2m-2x-n+2}{2}\mu_O-\frac{n-2}{2}\mu_{H_2O} \quad (2)$$

where $G_{Cu_xO_mH_n(MOR-2H)}$, $G_{(MOR-4H)}$, G_{CuO}, μ_O, and μ_{H_2O} are free energies of Cu-oxo active center located in MOR, the protonated MOR framework, bulk copper oxide, the chemical potential of O, and the chemical potential of H_2O.

The entropies, mainly due to lattice vibrations, for solid-state CuO, MOR-4H, and $Cu_xO_mH_n$(MOR-2H), have been neglected.[1] Hence, the Gibbs free energies for these three terms in eqn. (2) approximately equals to the total energies estimated by performing BEEF-vdW calculations.

The calculations of the Gibbs free energy of CuO can be sensitive to the initial guess of its magnetic moment. LDA+U was also considered for the bulk calculation. In this study, the U-J =7 eV was adopted for CuO.[2,3] The lattice parameters and magnetic moments of optimized CuO are

shown in Table C.1. The lattice parameters and magnetic moments were in good agreements with the literature.

The chemical potentials of gas phase O and H_2O at specific T, and P were calculated from eqns. (3) and (4) as

$$\mu_{gas}(T,P) = E_{gas} + \Delta\mu_{gas}(T,P) \quad (3)$$

$$\Delta\mu_{gas}(T,P) = H(T,P^0) - H(0K,P^0) - T\big(S(T,P^0) - S(0K,P^0)\big) + \frac{1}{2}RTln(\frac{P_{partial}}{P_{total}}) \quad (4)$$

where the total energies of gas phase species were obtained again using the BEEF-vdW functional. The molecules were placed in a box with dimensions of 20 × 20 × 25 Å. A Γ-k-point was employed. All the gas phase calculations were spin polarized. $\Delta\mu_{gas}(T,P)$ was calculated rom Eqn. (4), where $H(T,P^0) - H(0K,P^0)$ represents the enthalpy change from reference state (0 K) to any temperature, which are estimated from eqns. (5) and (6).

$$\Delta H = \int_0^T C_p\, dT, \quad (5)$$

$$C_p = a + bT + cT^2 + dT^3, \quad (6)$$

where C_p was evaluated from eqn. (6).

Parameters a, b, c, and d in eqn. (6) were obtained from the NIST website.[4] The entropy change from the reference state (0 K) at specified temperature (T) was calculated based on standard statistical mechanics treatment.[5] Hence, eqn. (2) becomes

$$\Delta G(T,P) = E_{Cu_xO_mH_n(MOR-2H)} - E_{(MOR-4H)} - xE_{CuO} - \frac{2m-2x-n+2}{2}E_O - \frac{n-2}{2}E_{H_2O} - \frac{2m-2x-n+2}{2}\Delta\mu_O - \frac{n-2}{2}\Delta\mu_{H_2O}. \quad (7)$$

With $\Delta\mu_{H_2O}$ and, $\Delta\mu_O$, the equilibrium phase diagram for Cu-oxo clusters (Figure 2) at the 8MR of MOR can be generated, as shown in Figure C.1.

References

1. Grundner, S.; Markovits, M. A. C.; Li, G.; Tromp, M.; Pidko, E. A.; Hensen, E. J. M.; Jentys, A.; Sanchez-Sanchez, M.; Lercher, J. A. Single-site trinuclear copper oxygen clusters in mordenite for selective conversion of methane to methanol. **2015**, *6*, 7546.

2. Heinemann, M.; Eifert, B.; Heiliger, C. Band structure and phase stability of the copper oxides Cu_2O, CuO, and Cu_4O_3. *Phys. Rev. B* **2013**, *87*, 115111.

3. Tang, J.; Liu, B. Reactivity of the Fe2O3(0001) Surface for Methane Oxidation: A GGA + U Study. *J. Phys. Chem. C* **2016**, *120*, 6642-6650.

4. U.S. Department of Commerce NIST Chemistry WebBook. *https://webbook.nist.gov/*.

5. Shan, N.; Zhou, M.; Hanchett, M. K.; Chen, J.; Liu, B. Practical principles of density functional theory for catalytic reaction simulations on metal surfaces – from theory to applications. *Molecular Simulation* **2017**, *43*, 861-885.

Appendix D- Reprint Permissions

Order Number: 1093745
Order Date: 28 Jan 2021

Print order

Payment Information

Jiayi Xu
jasonxjy@ksu.edu
Payment method: Invoice

Billing Address:
Jiayi Xu
Kansas State University
3404 Sioux Cir.
Manhattan, KS 66503
United States

+1 (646) 920-5051
jasonxjy@ksu.edu

Customer Location:
Jiayi Xu
Kansas State University
3404 Sioux Cir.
Manhattan, KS 66503
United States

Order Details

1. Journal of the Electrochemical Society

Billing Status:
Open

Print License

Order license ID	1093745-1	**Type of use**	Republish in a thesis/dissert...
Order detail status	Completed	**Publisher**	IOP Publishing
ISSN	1945-7111	**Portion**	Chapter/article

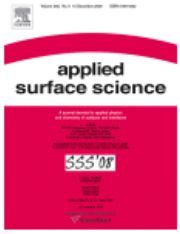
0.00 USD
Republication Permission
Publisher Terms and Conditions

View Details

Total Items: 1

Subtotal: 0.00 USD
Order Total: 0.00 USD

Back To Orders



Intrinsic properties of nitrogen-rich carbon nitride for oxygen reduction reaction

Author: Jiayi Xu,Bin Liu

Publication: Applied Surface Science

Publisher: Elsevier

Date: 15 January 2020

© 2019 Elsevier B.V. All rights reserved.

Please note that, as the author of this Elsevier article, you retain the right to include it in a thesis or dissertation, provided it is not published commercially. Permission is not required, but please ensure that you reference the journal as the original source. For more information on this and on your other retained rights, please visit: https://www.elsevier.com/about/our-business/policies/copyright#Author-rights

BACK

CLOSE WINDOW

ACS Publications
Most Trusted. Most Cited. Most Read.

Graphene-Based Dual-Metal Sites for Oxygen Reduction Reaction: A Theoretical Study

Author: Jiayi Xu, Ayyappan Elangovan, Jun Li, et al
Publication: The Journal of Physical Chemistry C
Publisher: American Chemical Society
Date: Jan 1, 2021

Copyright © 2021, American Chemical Society

PERMISSION/LICENSE IS GRANTED FOR YOUR ORDER AT NO CHARGE

This type of permission/license, instead of the standard Terms & Conditions, is sent to you because no fee is being charged for your order. Please note the following:

- Permission is granted for your request in both print and electronic formats, and translations.
- If figures and/or tables were requested, they may be adapted or used in part.
- Please print this page for your records and send a copy of it to your publisher/graduate school.
- Appropriate credit for the requested material should be given as follows: "Reprinted (adapted) with permission from (COMPLETE REFERENCE CITATION). Copyright (YEAR) American Chemical Society." Insert appropriate information in place of the capitalized words.
- One-time permission is granted only for the use specified in your request. No additional uses are granted (such as derivative works or other editions). For any other uses, please submit a new request.

BACK CLOSE WINDOW

ACS Publications
Most Trusted. Most Cited. Most Read.

Modeling C–H Bond Activation and Oxidations of Alkanes over Cu–MOR Using First-Principles Methods

Author: Jiayi Xu, Bin Liu

Publication: The Journal of Physical Chemistry C

Publisher: American Chemical Society

Date: Apr 1, 2019

Copyright © 2019, American Chemical Society

PERMISSION/LICENSE IS GRANTED FOR YOUR ORDER AT NO CHARGE

This type of permission/license, instead of the standard Terms & Conditions, is sent to you because no fee is being charged for your order. Please note the following:

- Permission is granted for your request in both print and electronic formats, and translations.
- If figures and/or tables were requested, they may be adapted or used in part.
- Please print this page for your records and send a copy of it to your publisher/graduate school.
- Appropriate credit for the requested material should be given as follows: "Reprinted (adapted) with permission from (COMPLETE REFERENCE CITATION). Copyright (YEAR) American Chemical Society." Insert appropriate information in place of the capitalized words.
- One-time permission is granted only for the use specified in your request. No additional uses are granted (such as derivative works or other editions). For any other uses, please submit a new request.

BACK CLOSE WINDOW